Shadow Mask assisted Heteroepitaxy of Compound Semiconductor Nanostructures

Dissertation zur Erlangung des
naturwissenschaftlichen Doktorgrades der
Bayerischen Julius-Maximilians-Universität
Würzburg

vorgelegt von
Timo Schallenberg
aus Coburg

Würzburg
2004

Eingereicht am:

bei der Fakultät für Physik und Astronomie

1. Gutachter: Professor Dr. L. W. Molenkamp

2. Gutachter: Professor Dr. G. Karczewski

1. Prüfer: Professor Dr. L. W. Molenkamp

2. Prüfer: Priv. Doz. Dr. M. Biehl

Tag der mündlichen Prüfung:

Doktorurkunde ausgehändigt am:

Index

1 **Fundamentals of Semiconductor Nanostructures** 8

1.1 Compound semiconductors 8
1.2 Mesoscopic structures 12

2 **Epitaxial Growth** 15

2.1 Molecular beam epitaxy 15
2.2 Reflection high-energy electron diffraction 17

3 **Fabrication of Quantum Structures** 21

3.1 Lithography techniques 21
3.2 Self-assembly techniques 23
3.2.1 Crystal shape
3.2.2 Step bunching
3.2.3 Self-assembly of 3D islands in heteroepitaxial growth
3.3 Selected area epitaxy 26
3.3.1 Growth on patterned substrates
3.3.2 Growth through shadow masks

4 **Technological Aspects** 33

4.1 Shadow mask technology 33
4.1.1 Epitaxial shadow mask layers
4.1.2 Preparation of the shadow masks
4.1.3 Loading of the samples
4.1.4 New mask concept
4.1.5 Lift-off of the mask
4.2 Growth control 39
4.2.1 Control of the incidence angles
4.2.2 Limitations of the beam control
4.2.3 Calibration of the incidence angles
4.2.4 Variation of the fluxes

5 Theory of SMMBE Growth 47

5.1 Previous studies 47
5.2 SMMBE growth model 49
5.2.1 Single component material
5.2.2 Two component material
5.2.3 Two interacting fluxes
5.2.4 Surface diffusion and effective flux
5.3 Predictions from the model 54
5.3.1 Interacting fluxes
5.3.2 Change of the flux ratio
5.3.3 Change of the growth geometry
5.3.4 Effects of surface diffusion

6 SMMBE of II-VI and III-V Compounds 61

6.1 Growth of II-VI compounds through shadow masks 61
6.1.1 Partial shadow
6.1.2 Facet formation
6.1.3 Formation of a shoulder structure
6.2 Growth of III-V compounds through shadow masks 68
6.2.1 Facet formation
6.2.2 Surface diffusion induced by the arsenic beam
6.2.3 Surface diffusion as a function of Ga and As beams
6.2.4 Surface diffusion dependent on In and As beams

7 SMMBE of Quantum Structures 77

7.1 Fabrication of quantum structures by SAE of a lateral barrier 78
7.1.1 Experiments
7.1.2 Lattice matched system - ZnSe QWR
7.1.3 Lattice unmatched system - CdSe QDs
7.2 SMMBE exploiting multiple, nanoscale apertures 82
7.2.1 Experiments
7.2.2 SEM and AFM on the reference sample
7.2.3 Self-assembly of QDs in nanoscale CdSe deposits
7.2.4 CdZnSe QW islands
7.2.5 Growth of CdSe without direct Se flux
7.3 Shadow mask assisted self-organized growth of nanostructures 94
7.3.1 Experiments
7.3.2 SEM investigations on the reference sample
7.3.3 CL investigations on the InAs QWR sample
7.3.4 Discussion
7.3.5 Growth on the mask-cap
7.3.6 III-V SMMBE exploiting multiple, nanoscale apertures

8 **Potential and Limitations of SMMBE** **102**

8.1 Limitations due to the geometry 103
8.1.1 Dependent incidence angles of the molecular beams
8.1.2 Finite diameter of source and sample
8.1.3 Imprecision and limited spatial range
8.1.4 Limitations of the shapes of the mask apertures
8.2 Potential of advanced mask geometry 107
8.2.1 Freestanding mask
8.2.2 Advanced mask pattern
8.3 Limitations due to surface kinetic processes 109
8.3.1 Secondary flux
8.3.1 Surface diffusion
8.4 Prospective shadow masks assisted processes 112
8.4.1 Strain and orientation dependent growth
8.4.2 Non-local growth
8.4.3 In situ etching in selected areas
8.4.4 Electronic doping in selected areas
8.4.5 In situ contact formation in selected areas
8.4.6 Magnetic doping in selected areas
8.4.7 Complex quantum devices

Summary 121

References 123

Appendix 128

Abbreviations

AFM	atomic force microscopy
BEP	beam equivalent pressure
CL	cathodoluminescence
FWHM	full width at half maximum
MBE	molecular beam epitaxy
ML	monolayer
PL	photoluminescence
QD	quantum dot
QW	quantum well
QWR	quantum wire
RHEED	reflection high-energy electron diffraction
UHV	ultra high vacuum
SAE	selected area epitaxy
SEM	scanning electron microscopy
SMMBE	shadow mask assisted molecular beam epitaxy
SPSL	short-period superlattices

Foreword

This work investigates a novel approach for the fabrication of compound semiconductor nanostructures by means of molecular beam epitaxy through stationary shadow masks.

In recent years, the physics of *semiconductor nanostructures* has become one of the most important topics of basic research (see Sect. 1.2). This is motivated on one hand, by the ongoing miniaturization and high-density integration of semiconductor devices following Moore's Law.[A] This development will reach a natural limit due to size-quantization effects, which affect the functionality of classical semiconductor devices with nanoscale structure dimensions. On the other hand, the investigations performed on semiconductor nanostructures have revealed a number of quantum mechanical effects opening up the possibility of building quantum devices. Quantum devices with prospective applications are, e.g., single-electron,[0D] quantum wire,[1D] and high electron mobility transistors,[2D] which can operate at very high frequencies, and quantum logic gates [0D] for solid-state quantum computing; single-photon emitters,[0D] enabling unconditionally secret communications, and the laser diode,[0D,2D] which has found its way in our everyday life in a multitude of applications such as data storage (CD, DVD), optical communications (fibre-optics), medicinal and analytical equipments (laser scalpels, molecule sensors, meters).

Unlike classical semiconductor devices, quantum devices often rely on specific properties of *compound semiconductors* from the II-VI and III-V systems (see Sect. 1.1). Advantages of compounds over the usual elemental semiconductor Si imply a direct band gap, which is crucial for certain opto-electronic devices, and a wide adjustable range of material properties, which enables the fabrication of novel band-engineered heterostructures. Moreover, compound semiconductors are prospective materials for applications in the field of semiconductor spintronics.

The development of compound semiconductor hetero- and nanostructures has been supported by the invention of the *molecular beam epitaxy* (MBE) technique in the 1970s' (see Chap. 2).[Cho71] This crystal growth technique allowed for the first time the defect-free production of single-crystal heterostructures with layer thicknesses controlled on the atomic scale. Thus, epitaxial growth enabled the fabrication of quantum devices [2D] consisting of nanoscale thin layers, i.e., two-dimensional quantum structures such as quantum wells, tunnel-barriers, or a two-dimensional electron gas. A number of proposals for quantum devices [0D,1D] with novel or enhanced functions, however, rely on quantum effects, which are specific for one- and zero-dimensional structures, such as quantum wires and quantum dots.

A versatile approach for the *fabrication of low-dimensional quantum structures* is lateral structuring of epitaxial layers (see Chap. 3). Most frequently, lateral structuring is

[A] The observation made in 1965 by Gordon Moore, co-founder of Intel, that the number of transistors per square inch on integrated circuits had doubled every year since the integrated circuit was invented. Moore predicted that this trend would continue for the foreseeable future. In subsequent years, the pace slowed down a bit, but data density has doubled approximately every 18 months, and this is the current definition of Moore's Law.

done by photolithography or electron-beam lithography followed by wet or dry etching. Alternative lithography techniques rely on the thermal inter-diffusion of epitaxial quantum-wells or the *in situ* pattern definition using focussed-ion beam, electron-beam, or atomic-force microscopy. Another approach especially useful in the fabrication of many quantum structures in a single process is based on self-assembly during epitaxial growth. Both methods have their own advantages and disadvantages: lithography techniques offer good lateral control and high reproducibility of the nanostructures, but they create exposed surfaces and thus introduce surface states, or they produce impurities and defects, which degrade the quality of the structures. In contrast, self-assembled nanostructures, which can be easily overgrown, are usually of good spectroscopic and structural quality, but their spatial arrangement, size, and concentration are not well controlled, which makes the latter approach less suitable for applications in, e.g., quantum transport devices or single-photon emitters. In order to obtain spatial control, selected area epitaxy (SAE) techniques have been developed, which exploit patterning of the substrate or a mask overlayer. Although, patterned SAE has several limitations, it has so far proved to be a promising approach for the fabrication of compound semiconductor nanostructures at predefined places.

In this work, it is demonstrated that a new variant of the SAE process called the *shadow mask assisted molecular beam epitaxy* (SMMBE), where the growth area is defined by molecular beams impinging on selected areas of the substrate, can be an attractive alternative for patterned SAE. In SMMBE, the size and spatial arrangement of MBE grown quantum structures are controlled by the incidence angles of the molecular beams and the geometry of a stationary shadow mask. This approach allows the fabrication of quantum structures of high spectroscopic and structural quality and can also achieve an equally high spatial precision as patterned SAE. Moreover, it is demonstrated that shadow masked SAE is more flexible than patterned SAE in the geometries of the nanostructures, which can be produced. Thus, SMMBE has the potential for the nanofabrication of defect-free complex quantum structures with the composition and doping profiles controlled with precision in all three dimensions.

This work is sectioned as follows: The first chapter, introduces the specific material properties of III-V and II-VI *compound semiconductors* and the quantum physics of *semiconductor nanostructures*. Subsequently, the principle of *molecular beam epitaxy* is explained (in Chap. 2) and a brief overview of the different *nanofabrication methods*, which can be used for the production of low-dimensional quantum structures, is given (in Chap. 3).

In Chap. 4, the *technological aspects* of shadow mask assisted SAE are discussed. In particular, technological advancements are presented, which enhance the precision and flexibility of the control of SMMBE.

Chapter 5 introduces a consistent *model for shadow effects* in molecular beam epitaxy of compound materials and discusses the roles of secondary fluxes below shadow masks, reactions between the constituent species, and surface diffusion.

Results from the investigations on SMMBE of II-VI and III-V compounds are presented in Chap. 6. In both cases, the predictions of the model regarding the growth regime below the shadow mask are tested. It is shown that surface diffusion and secondary fluxes govern the SAE growth of III-V and II-VI compounds, respectively. Corresponding to the different surface kinetics, different approaches have been developed to enable selected area growth of both II-VI and III-V nanostructures (see Chap. 7).

Finally, Chapter 8 discusses in general, the potential and limitations of SMMBE. It shows that the main potential of the technique lies in the fabrication of complex quantum devices with electronic, optical, and spintronic functions.

Chapter 1

Fundamentals of Semiconductor Nanostructures

In this work, novel methods for the fabrication of compound semiconductor nanostructures are presented. This chapter gives a brief introduction to (1) the specific material properties of II-VI and III-V compound semiconductors and (2) the properties and possible applications of nanostructures, based on these materials.

1.1 Compound semiconductors

I. Crystal structure The crystal structures of the common semiconductors are based on the face-centered cubic (FCC) structure, with two FCC sub-lattices displaced with respect to each other by |(¼, ¼, ¼)*a*|. Elemental semiconductors such as Si (group IV) crystallize in the diamond structure and, *compound semiconductors* (III-V and II-VI), in the *zinc-blende* structure [see Fig. 1.1(a)]. In the latter, the two FCC lattices are occupied by elements from different groups of the periodic system, i.e., group III and group V elements in the case of III-V semiconductors and group II and group VI elements in the case of II-VI semiconductors.

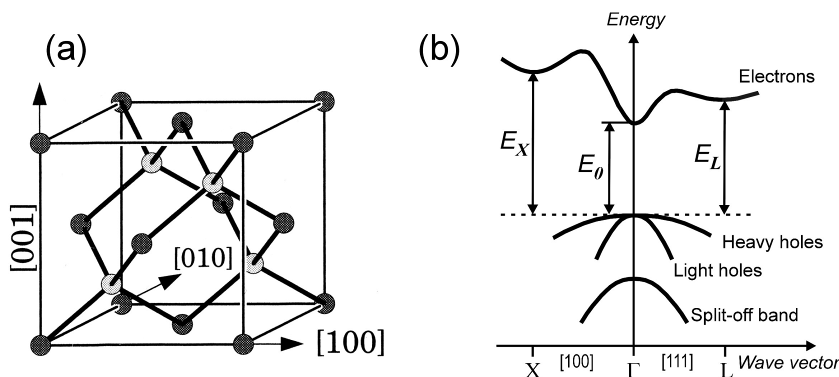

FIG. 1.1 – Schematic drawings of *(a) the crystal structure and (b) the band structure of zinc blende compound semiconductors.*

As shown in Fig. 1.1(a), the species alternate, i.e., each atom has four nearest neighbor atoms from the other elemental group. *Mixed crystals* (i.e. alloys) are formed by substituting atoms of one of the constituent elements partly with atoms from the same group (e.g. $Cd_xZn_{(1-x)}Se$ is formed by substituting a fraction x of Zn atoms in ZnSe with Cd atoms). Compounds with 2, 3, and 4 constituent atomic species are termed *binary* (ZnSe), *ternary* ($ZnS_xSe_{(1-x)}$), and *quaternary* ($Mg_xZn_{(1-x)}S_ySe_{(1-y)}$ or $Be_xMg_yZn_{(1-x-y)}Se$), respectively.[A]

II. Band gap One of the main advantages of using compound semiconductors in comparison to elemental semiconductors (e.g., Si) is their *direct band gap* (although not for all compounds), i.e., the top of the valence band and the bottom of the conduction band are the same point in K-space [see Γ in Fig. 1.1(b)], which is favorable for applications in opto-electronic devices (e.g., light emitting diodes, lasers, photo diodes).

A second important feature is the wide range of band gaps, which render these from half-metallic to semiconducting to insulating, and band gaps in the spectral range from infrared to visible to ultraviolet. Figure 1.2 shows the energy gap of a few common compound (and elemental) semiconductors versus their lattice constant a_0. The solid curves connecting selected binary compounds (ZnS and ZnSe) represent the complete range of their ternary alloy compositions (ZnSSe). This makes possible the adjustment of the band gap of the resultant composition by suitable proportioning of the end members. By this means, opto-electronic devices can be optimized for a spectral range. Moreover, the valence band and conduction band energy levels (*work functions*) can be controlled almost independently by substituting anion and cation species, respectively. This enables the fabrication of *band-engineered heterostructures*, which can increase the efficiency of devices with electronic and optical functions.

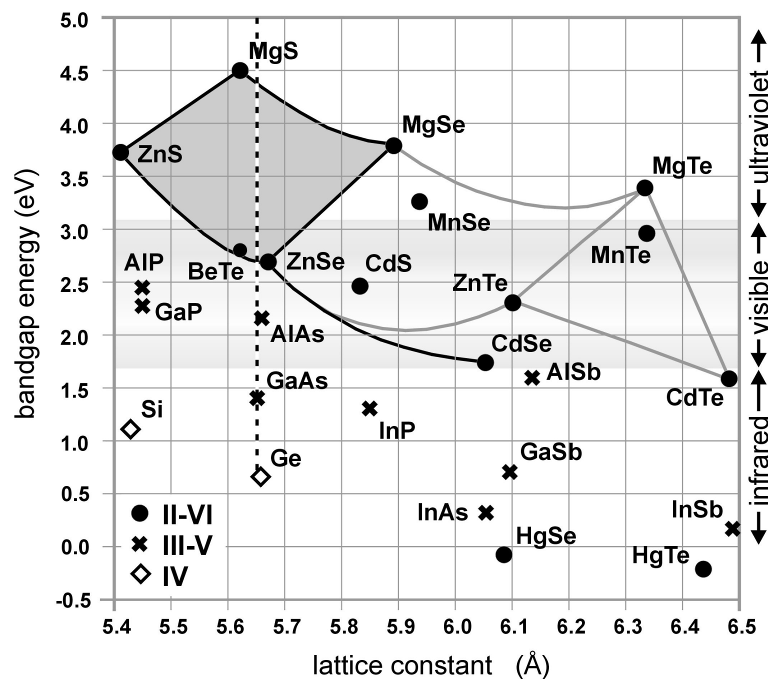

FIG. 1.2 – *Band gap energy versus lattice constant for group-IV, II-VI, and III-V semiconductors. The solid curves connecting selected binary compounds represent the complete range of the possible ternary alloy compositions (after [Faschinger99]).*

[A] For simplicity, one can write MgZnSSe (BeMgZnSe) instead of $Mg_xZn_{(1-x)}S_ySe_{(1-y)}$ ($Be_xMg_yZn_{(1-x-y)}Se$). The subscripts are used only to indicate the composition of a specific alloy, e.g., $Mg_{0.2}Zn_{0.8}S_{0.3}Se_{0.7}$.

III. Heterostructure Heterostructures consist of single crystalline regions (layers) with different chemical compositions (and, most of these, different lattice constants). A heterostructure composed of regions with a small mismatch of the lattice constants (a_0) is attributed *pseudomorphic* if by elastic deformation the inplane lattice constants ($a_{\|}$) of the two regions match at the heterointerface. During epitaxial growth on planar substrates, a growing layer is initially pseudomorphic to the substrate lattice. However due to strain accumulation, the elastic deformation energy increases with the layer thickness and above a critical thickness the strain relaxes via the incorporation of misfit dislocations.[Matthews74] This can be avoided by growing *lattice-matched* heterostructures [To within a critical layer thickness (1 µm), a residual misfit between the bulk lattice constants can be accommodated (<0.1%)]. Thus, for the fabrication of defect-free single crystal *heterostructures*, it is crucial to control of the lattice constant and the band gap independently, which can be accomplished with quaternary alloys. For example, the range of compositions (and band gap energies) where MgZnSSe is lattice-matched to GaAs substrate is given by the overlap of the dashed line and the shaded region in Fig. 1.2.

IV. Investigated materials In this study, compound semiconductor heterostructures consisting of AlGaAs, InGaAs, MgZnSSe, and CdZnSe alloys, have been fabricated on single crystal GaAs substrates, oriented in the (001) crystal direction (±0.2°). The GaAs substrates are usually cheaper than other zinc-blende substrates (GaP, InP, InAs) and of good quality.
The energy gap and the lattice constant of GaAs are E_{GaAs} = 1.42 eV at 300 K (1.52 eV at 4K) and a_0 = 5.65 Å, respectively. Substitution of Ga by Al (In) increases (decreases) the energy gap of the resulting alloy AlGaAs (InGaAs). Because of the small lattice mismatch between AlAs and GaAs (0.14% at 300 K), AlGaAs - GaAs heterostructures can routinely be fabricated without strain relaxation. In contrast, the mismatch between InAs (a_0=6.05 Å) and GaAs is large (= 7%) and, hence, the critical layer thickness of $In_{0.2}Ga_{0.8}As$ is very small (~ 10 nm). Moreover, $In_xGa_{(1-x)}As$ layers with $x > 0.5$ can decrease their strain energy by forming three-dimensional clusters, which has been used for the fabrication of self-assembled quantum dots (see Sect. 3.2.3).

In the II-VI system, binary ZnSe (lattice constant of 5.67 Å) is almost lattice-matched to GaAs (0.3%) and the critical thickness of pseudomorphic layers is about 200 nm. MgZnSSe alloys can be grown perfectly lattice-matched on GaAs substrates (see Fig. 1.2). Substituting Zn and Se with Mg and S increases the energy gap, $E_{MgZnSSe}$, relative to E_{ZnSe} = 2.71 eV at 300 K (2.82 eV at 4 K). In contrast, substituting Zn with Cd decreases the energy gap E_{CdZnSe}. Analogous to InGaAs, the large mismatch (= 7%) between CdSe (a_0 = 6.05 Å) and GaAs limits the thickness of pseudomorphic CdZnSe layers. In addition, self-assembly of nanoscale clusters may occur if the Cd fraction is large.

A problem in the fabrication of single crystal heterostructures consisting of both II-VI and III-V materials is in the fact that group-III and group-VI elements can react stable compounds (e.g., Ga_2Se_3). Such reactions degrade the II-VI / III-V heterointerface and need to be avoided.

V. Electronic doping Doping of a semiconductor crystal with donor (acceptor) impurity atoms generates free electrons (*holes*) in the conduction band (valence band). Thereby, the donor (acceptor) impurity substitutes a crystal atom, which has one valence electron less (more).[A] Free electrons and holes, being carriers of opposite charges may interact by Coulomb interaction resulting in a hydrogen-like neutral complex, namely the *exciton*, which can diffuse freely through the semiconductor bulk. The effective Bohr

[A] In III-V compounds, Si and Te are donors; Be and C are acceptors. In II-VI compounds, Al and Cl are donors; Li and N are acceptors.

radius $a_X \approx a_B m_0 \varepsilon_r / \mu$ of an exciton is, however, much larger than that of a free hydrogen atom a_B = 0.529 Å [$\mu = m_e^* m_h^* /(m_e^* + m_h^*)$ is the reduced excitonic mass (calculated from the effective electron m_e^* and hole m_h^* masses) and ε_r the (static) dielectric constant (corresponding to the screening of the Coulomb interaction)]. Due to different effective values (ε_r, m_e^*, m_h^*), excitons have a smaller Bohr radius a_D and a higher binding energy R_X in ZnSe (a_D = 4.5 nm; R_X = 20 meV) than in GaAs (a_D = 14 nm; R_X = 4.2 meV). The binding energy of the excitons reduces the minimum energy required for inter-band optical transitions E_0 - R_X (ZnSe: 2.80 eV at 4 K).

VI. Magnetic doping Recently, magnetic impurity containing compound semiconductor materials exhibiting magnetic properties have attracted much attention for the prospective application in semiconductor spin electronics (spintronics). Diluted magnetic semiconductors (DMS) can be fabricated by doping compound semiconductors with transition metal atoms (V, Cr, Mn, Fe, Co, and Ni). In the case of II-VI compounds, the dopants act as isoelectronic impurities and hence magnetic and electronic doping can be controlled independently. Ferromagnetic behavior up to the room temperature has been predicted for certain III-V compounds, where the magnetic dopants (Mn) act also as acceptors.

1.2 Mesoscopic structures

The physics of the macroscopic world can be described by classical physical laws and that of the microscopic world of atoms and molecules by quantum mechanics. In between (Greek: “meso”) lies the world of *mesoscopic structures*, which have in common with macroscopic structures a large number of atoms, and with microscopic structures, the size quantization effects.

I. Size quantization Quantum effects govern the properties of heterostructures when the structure dimensions are comparable to the de Broglie wavelength $\lambda = h/p = \hbar(2m^* E)^{-1/2}$ of carriers, in at least one dimension [m^* is the effective mass (m_e^*, m_h^*) and, *E*, the kinetic energy of the carriers]. At low temperatures *T (< 10 K)*, size quantization (< 1 meV) can be observed for structure sizes exceeding 100 nm. In order to distinguish quantized states at room temperature, however, the size of mesoscopic structures has to be of the order of *nanometers* (~ 10 nm). In opto-electronic devices, excitonic complexes play an important role. Strong confinement of an exciton is achieved when the size of a mesoscopic structure is of the order of the exciton Bohr radius (~ 10 nm).

For example, Figure 1.4(a) shows size quantization effects in a narrow potential well (in one dimension). Due to its boundary conditions, the Schrödinger equation has only discrete solutions for the wave functions and energy levels of carriers, which are localized in the potential well. Moreover, the carriers have a zero-point energy even in the ground state. Despite this finite kinetic energy, the wave functions (effective migration) of the carrier are stationary.

The opposite of a potential-well is a potential-barrier (tunnelling barrier). Carriers can pass through a thin barrier with higher potential than the bulk by *tunnelling*. Two

tunnelling barriers separated by a thin spacer (potential-well), result in quantized states in the well. Tunnelling transport through such a structure takes place resonantly when the quantized states, tuned by an electric field, are at the same level with carriers in the bulk. This is the basic concept of resonant tunnelling diodes.

A *short-period superlattice* is a periodic structure consisting of potential-barriers and potential-wells, whose periodic potential results in the formation of minibands. Short-period superlattices allow for the creation of artificial bulk materials with inherent asymmetries and whose properties can be tuned by varying the composition and the thickness of the layers.

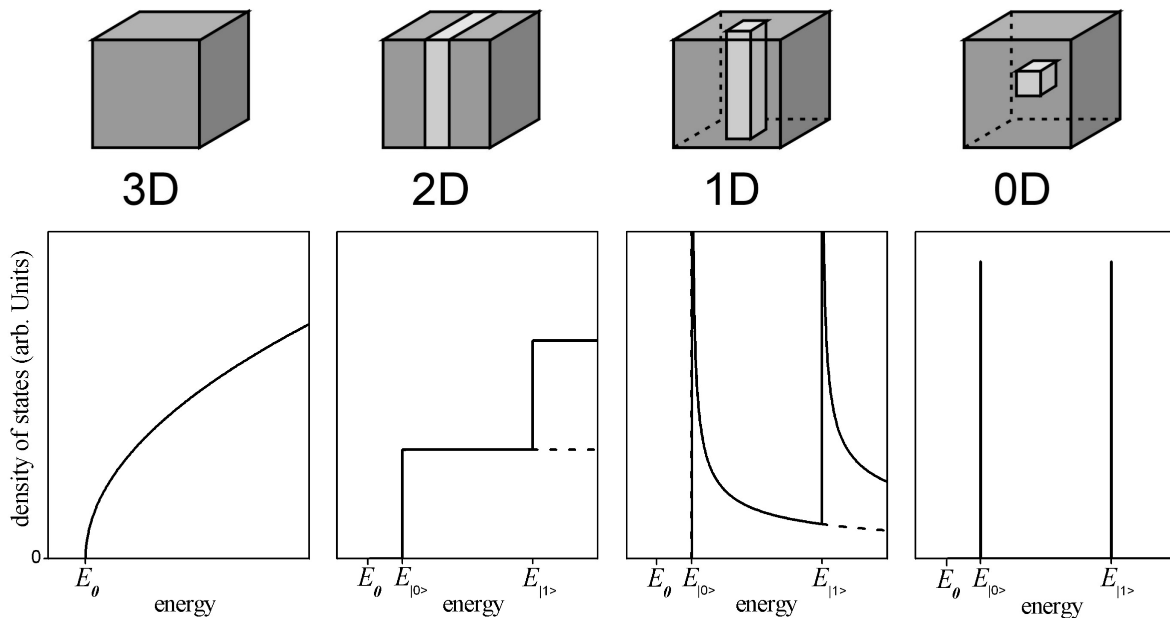

FIG. 1.3 –*Density of electronic states in bulk material (3D), quantum wells (2D), quantum wires (1D) , and quantum dots (0D).*

II. Low dimensional structures In a bulk semiconductor crystal, carriers can migrate in three dimensions (3D). This results in a continuous dispersion of energy states as a function of momentum. A thin layer (~ 10 nm) with a lower potential than the bulk material, namely a *quantum well* (QW), can be used to localize carriers in two dimensions (2D). Analogously to a square potential well [see Fig. 1.4(a)], for the direction in which the structure dimension is reduced, only discrete solutions exist for the wave functions, resulting in quantized states. However, the carriers can still move freely in the remaining two unconfined directions resulting in a continuous dispersion of the “discrete” energy states as a function of momentum. The same accounts for *quantum wires* (QWRs) in which the migration of the carriers is limited to one dimension (1D). Hence, mesoscopic structures are also known as *low-dimensional structures*. A low-dimensional electron gas can be achieved by modulation doping of a QW, QWR, or a heterointerface. The mobility of such a structure can be many orders of magnitude larger than that of doped bulk material. This has been exploited, e.g., for the fabrication of high electron mobility transistors (HEMT), which are the fastest transistors available.

III. Energy distribution Figure 1.3 shows the density of energy levels for the ground state of carriers, which can freely move in 3D, 2D, and 1D, respectively. As can be seen, reducing the dimensionality of the structure increases the density of electronic states

at the ground level and thus narrows the energy distribution of the carriers. Finally, in the zero-dimensional (0D) case of a *quantum dot* (QD), the continuous dispersion of energy states disappears completely and only the discrete levels of the ground and excited states remain.

The narrow energy distribution of confined carriers is important for quantum devices, which rely on resonant transitions, e.g., resonant tunneling structures and laser devices. Although, reducing the dimensionality of the quantum structures can in principle improve the performance of such devices, the realization of a narrow energy distribution is challenging. This results from the limits of nanofabrication and the fact that fluctuations of the nanoscale structure dimensions change the energies of the quantized states.

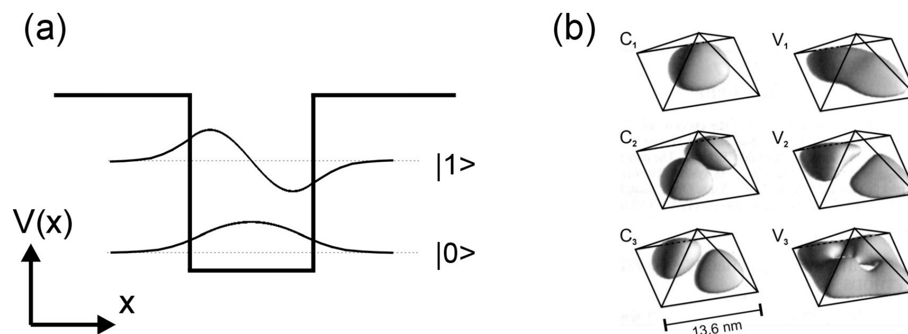

FIG. 1.4 – Wave functions of quantized electronic states. *(a) Ground and first excited state of a finite square potential well (in one dimension). (b) First conduction (C_1-C_3) and valence (V_1-V_3) band states of an InAs/GaAs quantum dot (after [Bimberg99]).*

IV. Artificial atoms Because of a variety of analogies with single atoms, semiconductor QDs are often referred to as *artificial atoms*.[Kastner93, Ashoori96, Alivisatos96, Fafard96] Such analogies imply for example discrete energy levels for confined electrons and holes, which results in sharp-line luminescence when electrons and holes forming excitonic complexes (exciton and multiexciton states) recombine.[Bockelmann90, Brunner94] Due to geometrical symmetries [e.g., InAs/GaAs QD in Fig. 1.4(b)] the energy levels may be degenerate and therefore form atomic-like electronic shells (s, p,…), which are populated with carriers according to the Pauli exclusion principle.[Banin99, Hawrylak00]

An important characteristic of the photon emissions from artificial atoms are temporal correlations, i.e., photon bunching and antibunching.[Michler00a, Regelman01, Becher01] The latter effect is the working principle of the single-photon emitter, which produces no more than one photon at a time.[Micheler00b, Santori01] Such a single-photon device would be useful in the field of quantum cryptography, which exploits fundamental principles of quantum mechanics to provide unrestricted security for communication.

The single-electron transistor (SET) is an example of the application of QDs in quantum transport devices. The SET is based on the Coulomb blockade effect, i.e., an extra electron can only be added to the dot if enough energy is provided to overcome the Coulomb repulsion between the electrons.[Likharev87, Tarucha96] The advantages of the SET include smaller dimensions (high-density integration), lower power consumption, and higher cut-off frequencies in comparison to the usual field-effect transistor.

Another prospective application of artificial atoms is in the field of quantum computation.[Cundiff94, Bennett00] Solid-state quantum computers consisting of quantum gates and wires could speed up certain computations, because the quantum algorithm requires far fewer steps. Examples for such problems imply the factorisation of large integers,[Shor94, Ekert96] database search and optimisation problems,[Grover97] and the simulation of many-

particle quantum systems.[Abrams97] Various proposals for solid-state quantum computers rely on intra-QD (artificial atom) or inter-QD (artificial molecule) coherent interactions due to electron spin effects,[Loss98] electronic charge effects,[Barenco95] and exciton-based quantum entanglement.[Quiroga99, Chen00, Bayer01] Long-range interaction between distant quantum dots spins has also been realized by the vacuum field of a microcavity.[Imamoglu99]

V. Technical requirements for the fabrication of quantum nanostructures

The technical requirements for the fabrication of solid state quantum devices are an excellent precision in defining the position and dimensions of the consisting quantum structures (QWs, QWRs, QDs, etc.) and a high reproducibility of the process. This is crucial in controlling the energy and resonance levels of the quantum structures, since fluctuations in the dimensions of the nanoscale structures would change the eigenenergies. In addition, a defect and contamination free process is also important as individual defects may cause perturbations and thus severely affect the functionality of a quantum device. These stringent requirements can not always be met by the standard nanofabrication methods (in particular for the fabrication of compound semiconductor nanostructures; see Chap. 3).

Chapter 2

Epitaxial Growth

This chapter gives a brief introduction to the basic principles of crystal growth by molecular beam epitaxy and in situ surface characterization using reflection high-energy electron diffraction. The various aspects of the techniques have been discussed here in brief but several comprehensive reviews of the subject are available in standard text books.[A]

2.1 Molecular beam epitaxy

Molecular beam epitaxy (MBE) is an ultra-high vacuum (UHV) technique for the crystal growth of thin epitaxial structures, such as semiconductors, isolators and metals. Effusion cells are used to sublimate source material, which produce a material flux of molecules and atoms in the UHV growth chamber (see Fig. 2.1). The molecules,[B] which impinge on a heated substrate placed in the chamber, are adsorbed and contribute to the epitaxial growth via reactions with the outermost atomic layers of the substrate surface. Mechanical shutters in front of the effusion cells are used to temporarily interrupt the material flow of the constituent elements of a growing film and of the doping materials. This enables the ordered growth of high-quality crystalline layers and complex heterostructures with precise control of the composition, doping concentration, and hetero-interfaces, which can be abrupt on the atomic scale.

Electronic and optical applications of epitaxial structures require extreme efforts to ensure the purity of the crystal because small densities of unintentional impurities strongly affect the material properties. For this reason, source material with a purity of 99.9999% is used. In addition, MBE growth is carried out in UHV. Under this condition the rate of residual

---

[A] (see Refs. [Herman89, Tsao93, Farrow95, Braun99])

[B] For simplicity, below we will refer to both molecular and atomic species as "molecular", and use "atomic" only where it is required to discriminate between them.

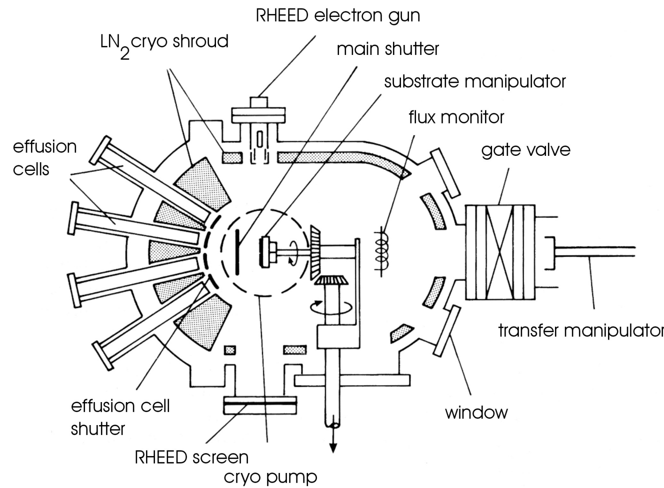

FIG. 2.1 - *Schematic illustration of a MBE growth chamber (RIBER 32 geometry).*

gas molecules impinging on the substrate is at least five orders of magnitude smaller than the beam flux.

Figure 2.1 shows the sketch of a growth chamber in the RIBER 32 geometry, which was employed for the experiments of this study. The position of the effusion cells, their mechanical shutters, the RHEED system, and the sample manipulator are shown. A He cryopump and liquid nitrogen (LN_2) cryogenic traps, surrounding the inner walls of the UHV chamber, keep the system base pressure low (< 10^{-10} torr). Substrates mounted on a substrate holder (molybdenum-block) are handled *in situ* with the substrate manipulator of the growth chamber. The substrate is radiation-heated from the backside and its temperature can be measured using a thermocouple, which is in thermal contact with the block and shielded from the radiation of the heater; additionally, one can use an infrared pyrometer for the calibration. Molecular fluxes can be monitored with an ion gauge, positioned on the backside of the manipulator, which is turned into the flux (position) by pivoting the sample manipulator.

Today, the MBE technique is used for the epitaxial growth of a wide range of different materials and heterostructures with interesting physical properties and applications in modern devices. However, when MBE growth is used for the fabrication of heterostructures consisting of different material systems, one has to consider that constituent elements of one material might be impurities for another. In order to achieve the highest possible quality of both material systems, the respective layers are grown in different growth chambers.

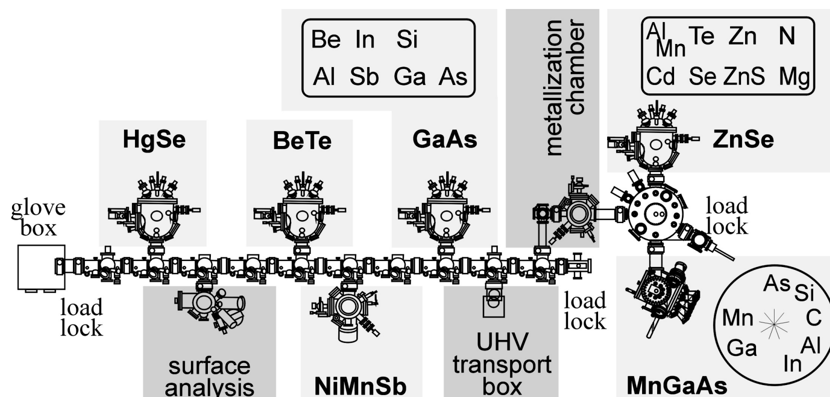

FIG. 2.2 - *Schematic illustration of the UHV cluster at the Physical Institute, EP III, of Würzburg University*

Figure 2.2 shows a sketch of the UHV system at Experimental Physics III, Würzburg University. In total, six MBE growth chambers (four RIBER 32 type) and an *in situ* metallization chamber are interconnected via tunnel modules, which enable sample transfer under UHV. These are complimented by load-lock and heating stations, storage facilities, a low-energy electron diffraction set-up, a surface analysis chamber, and a homemade portable UHV chamber. The pumping system is a combination of turbo, ion getter, and Ti sublimation pumps.

2.2 Reflection high-energy electron diffraction

An advantage of the UHV environment is that MBE growth can be controlled *in situ* by surface sensitive diagnostic methods such as reflection high-energy electron diffraction (RHEED), low-energy electron diffraction, and scanning tunnelling microscopy. This has led to a good understanding of the microscopic surface processes during epitaxial growth and resulted in a tremendous improvement of the process control.

RHEED is the standard technique used for monitoring MBE growth on a surface in real time. A RHEED measurement consists of the electron beam from an electron gun (see Fig. 2.1), which is directed towards a substrate surface at a glancing angle typically ranging from 0.5° to 3° to enable forward scattering of the beam. A fluorescence RHEED screen is used to visualize the diffracted electrons.

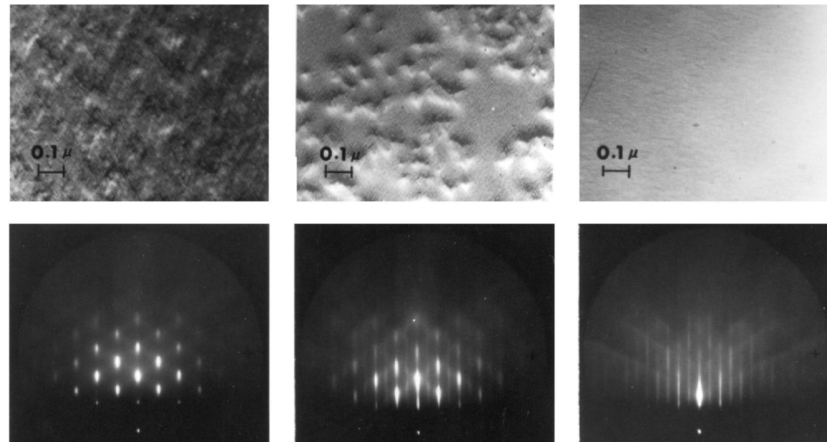

FIG. 2.3 – *The correlation between the RHEED pattern and the morphology of the GaAs (001) surface as a function of growth time (from left to right). The initial 3D surface giving rise to a spotty pattern due to electron transmission through 3D features. The more 2D surface giving rise to the commonly observed RHEED streaks (after [Cho71]).*

I. Surface morphology The diffracted beam visualized on the RHEED screen shows patterns which are characteristic for the surface morphology: As can be seen in Fig. 2.3, an atomically smooth interface (2D) corresponds to a streaky RHEED pattern, while three-dimensional islands or a rough surface morphology (3D) cause spotty features in RHEED images. The shape, symmetry, intensity, and width of superimposed streaky and spotty features give additional information on the nature of the surface morphology.

A key observation by Cho [Cho71] is the change of surface morphologies from initially 3D to quasi 2D during the growth of a GaAs buffer on a GaAs substrate (timescale from left to right in Fig. 2.3). This demonstrates that the lateral growth rate of islands on a

substrate can exceed the vertical, leading to a smoothing of the surface. In contrast to this, growth of certain heterostructures, e.g., InAs on GaAs substrates, induces a change of the morphology from 2D to 3D. This behaviour will be explained in Chap. 3.2 based on a thermodynamic model. However, kinetic limitations (growth at low substrate temperature) may also induce roughening of the surface and enhance 3D features in RHEED.

II. Surface reconstruction Another important piece of information gathered from RHEED images is the surface reconstruction, which depends on the growth conditions, i.e., the flux ratio and the substrate temperature (see Fig. 2.4). The lateral periodicity of the surface reconstruction is often one, two, or four unit-cells wide, and thus causes RHEED patterns with zero, one, and three minor diffraction rods, respectively. The right-hand RHEED image in Fig. 2.3 shows the characteristic pattern of the (2x4) reconstructed GaAs (001) surface, observed in the $(1\bar{1}0)$ azimuth. The surface reconstruction can be uniquely identified from the patterns of the $(1\bar{1}0)$, (110), and (100) azimuths.

Figure 2.4 shows (a) the surface phase diagram of the ZnSe(001) surface [Wolfframm00] and (b) the density of stacking faults in a ZnSe crystal grown at 280°C, as a function of the beam equivalent pressure (BEP) ratio.[Kuo96] Since BEP values can depend on factors such as the geometry and the measuring time, the BEP ratio is usually not the same in different growth chambers. However, the observed phase-transition of the surface reconstruction can be used to calibrate the BEP ratio (based on the surface phase diagram). Hence, the optimum Se:Zn atomic flux ratio is ~0.85, i.e., slightly Zn-rich. Although, this growth condition is often referred to as “Se-rich” because of the observed “Se-rich” (2x1) reconstruction.[Kuo96]

The geometric configuration of a reconstructed surface can be determined by combining surface analytical experiments (low-energy electron diffraction, photo electron spectroscopy, X-ray diffraction) with *ab initio* theory.[A] The geometric configuration determines growth processes on the molecular scale. Molecular processes on reconstructed surfaces are beginning to be understood, but there are still many open questions.

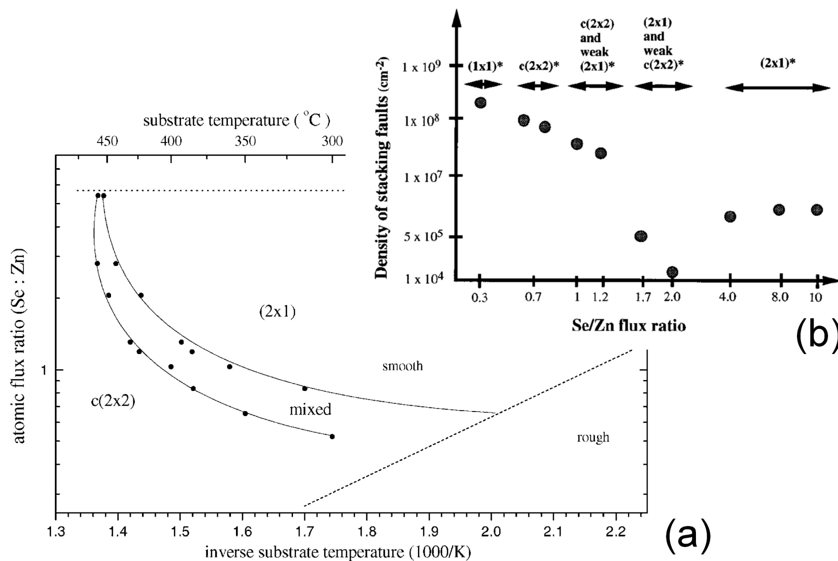

FIG. 2.4 – *(a) Surface phase diagram of the ZnSe(001) surface showing the surface reconstruction as a function of the substrate temperature and the atomic flux ratio (after [Wolfframm00]). (b) Density of stacking faults as a function of the Se:Zn BEP ratio (after [Gaines91]).*

[A] For example, recent investigations on samples grown by the author have identified the geometric configuration (Zn-vacancy model) of the c(2x2) surface reconstruction of the ZnSe(001) surface out of 3 different geometric models discussed in the literature. [Weigand03]

III. RHEED oscillations Yet another important piece of information gathered from RHEED is the intensity of the specular beam, which exhibits oscillatory behaviour [see Fig. 2.5(a)]. RHEED oscillations are observed in layer-by-layer growth. When 1 ML high islands nucleate on an atomically smooth surface [see Fig. 2.5(b)], the specular intensity first decreases because of the increasing disorder of the surface. When 1 ML high islands cover about half of the surface area, the specular intensity starts to recover because the islands coalescence and vacant areas between them are filled until the growth of 1 ML is completed. Thus, a smooth interface is recovered and new islands can start to nucleate, hence the period of RHEED oscillations is indicative for the growth rate. In a conventional MBE process, RHEED oscillations are always damped [see Fig. 2.5(a)], which shows that new islands nucleate before one full ML is completed, i.e., the surface roughness increases and can be up to several MLs.

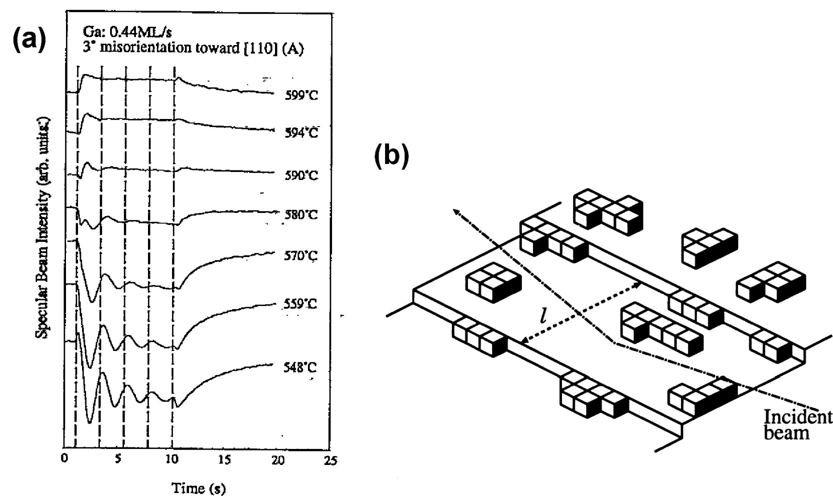

FIG. 2.5 – *(a) Specular beam intensity during GaAs MBE on 3° misoriented (001) substrate as a function of the time, at various substrate temperatures, showing RHEED oscillations at low substrate temperatures. (b) Schematic illustration of growth on a vicinal substrate. Adatoms are preferentially incorporated at the step edges. However, 1ML high islands nucleate on a terrace when the diffusion length is limited at low substrate temperature, thus contributing to the oscillatory modulation of the intensity of the specular beam.*

IV. Step-flow regime No RHEED oscillations are observed when, e.g., GaAs is grown on a vicinal substrate at a high substrate temperature, i.e., in the *step-flow regime* [see Fig. 2.5(a)]. On a vicinal substrate the mean terrace width $l = a \tan(\theta)$ is given by the misorientation angle (θ) and the step height a (usually 1 ML). At high substrate temperatures, the migration length of group-III adatoms is relative large, so that they can reach the terrace edges where they are preferentially incorporated into the growing crystal. This reduces the adatom density on a terrace and thus the probability for the nucleation of new islands, hence no RHEED oscillations are observed. This effect can be used to estimate the diffusion length l_D of adatoms, and gives values typically of the order of 10 nm for the MBE growth of GaAs (misoriented (001) substrates; at a substrate temperature of 600°C) [Neave85, Shitara92, Ohta88]. In ZnSe MBE, however, RHEED oscillations do not disappear even at high substrate temperatures and 4° misorientation of the (001) substrate, hence it has been concluded that $l_D < 4.0$ nm.[Gaines91]

V. Microprobe-RHEED A different method for determining the migration length of adatoms is the microprobe-RHEED technique. Spatially resolved specular RHEED measurements are carried out in an MBE growth chamber with a combined SEM /

RHEED system. An effect, which is known as *inter-surface diffusion* (see Chap. 3.3.1) causes a measurable change of the RHEED-oscillation period (growth rate) near the edges of a crystal plane. As can be seen in Fig. 2.6(a), the effect on the growth rate decays exponentially with the distance from the edge, where the exponential slope represents the *diffusion length of incorporation* l_{inc} of the adatoms. Hata *et al.*[Hata91] found that l_{inc} is of the order of one micrometer in the case of Ga adatoms during GaAs growth, i.e., it is much larger than the migration length l_D determined with the previously described method. In addition, it was found that the incorporation diffusion length l_{inc} of group-III adatoms depends on the group-V flux [see Fig. 2.6(b)]. When the group-V flux is high, the migration length of group-III adatoms is limited, however this does not explain the observed discrepancy between l_{inc} and l_D. The discussion concerning l_{inc} and l_D is far from over even today (e.g., Ref. [Verschuren99, DeLuca99, LaBella00, Kangawa02]).[A]

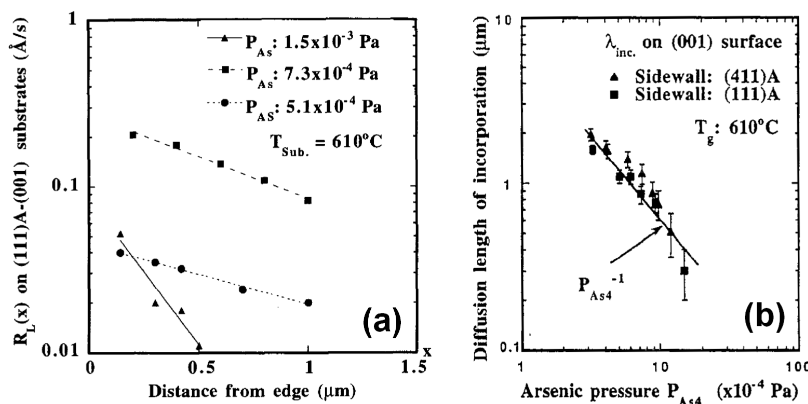

FIG. 2.6 – *Inter-facet diffusion of Ga adatoms during GaAs growth, studied by microprobe-RHEED. (a) Change of the growth rate on the (001) surface as a function of the distance from the facet edge (after [Shen94]). (b) The dependency of the diffusion incorporation length on the arsenic pressure (after [Nishinaga96]).*

VI. ALE and MEE techniques New growth strategies such as *atomic layer epitaxy* (ALE) and *migration-enhanced epitaxy* (MEE) have been developed in order to overcome the kinetic limitations of the MBE process[B] and to maintain an atomically smooth surface during the entire growth. ALE is based on the repeated adsorption saturation of constituent elements, which impinge separately in repeated pulses. This guarantees complete 1 ML (or half ML) coverage during the deposition of certain II-VI materials. However, for III-V compounds no adsorption saturation of group-III elements can be achieved because of their low vapour pressures at reasonable substrate temperatures. In this case, a MEE growth process is used, which consists of repeating 1 ML deposition of group-III atoms followed by the deposition of group-V elements. Without group-V flux, the migration length of group-III adatoms is enhanced [see Fig. 2.6(b)]. They spread on the surface and make one complete ML. Thus, by the subsequent deposition of group-V elements a flat epitaxial surface can be conserved. As a result, RHEED specular beam intensity variations in ALE and MEE processes can indicate flat growth surfaces even after the growth of thousands of monolayers.

[A] Large diffusion lengths of the order of one micrometer (contradicting the results by Ref. [Gaines91]) have also been reported for II-VI MBE [Luo98, Nishikawa96, Schumacher00]. In this work, the discussion on surface diffusion kinetics during II-VI and III-V MBE plays an important role in Sects. 5.1, 5.3.4, 6.1, and 7.1.

[B] For example, pure layer-by-layer growth is not possible with a finite diffusion length of adatoms in MBE. Because of this RHEED oscillations are always damped and the surface is not atomically smooth.

Chapter 3

Fabrication of Quantum Structures

A number of techniques have been used for the fabrication of QDs and QWRs. In this chapter, a brief overview of the different nanofabrication methods is given (For more details, please refer to the review [Bimberg99].) The discussion is sectioned in (1) lithography techniques (ex situ and in situ), (2) self-assembly techniques using planar substrates, and (3) selected area epitaxy, which combines the advantages of spatial control and in situ fabrication of high quality quantum structures. In the case of the MBE techniques, (2) and (3), the principle growth concepts are explained, as well.

3.1 Lithography techniques

I. *Ex situ* lithography Most frequently, lateral structuring is done by photolithography or electron-beam lithography followed by wet or dry etching. *Lithography and etching* offer good lateral control and high reproducibility of the nanostructures,[Temkin87] but they create *exposed surfaces* and thus introduce surface states, which cause side-wall depletion and also degrade the optical quality of the structures. Physical etching techniques such as Ar-ion sputtering introduces additional defects in the grown crystal. *Thermal treatment* in order to anneal or clean exposed surfaces is usually not very efficient and, in turn, can destroy the nanostructures (by surface diffusion) or introduce additional defects in the crystal. Hence, capping of *ex situ* fabricated quantum structures in a second MBE process does hardly improve the quality of exposed quantum structures.

II. Inter-diffusion techniques Another *ex situ* method relies on the *thermal inter-diffusion* of epitaxial quantum wells (QWs), which changes the composition and thus the energy gap of the QW.[Mackowski98, Bacher99] Spatial control of the inter-diffusion process has been demonstrated by focussed ion beam (FIB) implantation and by using an overlayer

mask (e.g. SiO_2). The advantage of the inter-diffusion approach is that lateral confinement can achieve without creating exposed surfaces. However, the local enhancement of the inter-diffusion processes relies on vacant lattice sites (= defects), which are incorporated in the crystal. Hence, quantum-structures produced by this method are embedded in an imperfect crystal. Also, the spatial control of this method is limited to “quantum dots” with a diameter $D > 100$ nm. Despite such large dimensions, the structures show behaviour characteristic of QDs, which can be explained by the composition profile of the structures.

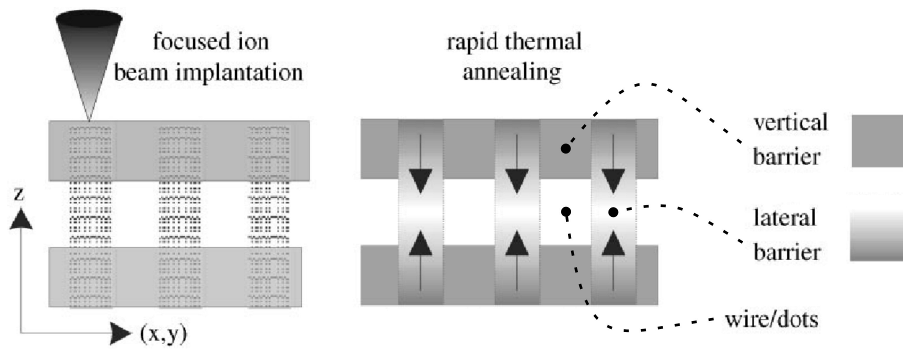

FIG. 3.1 – *Principle of the thermal inter-diffusion technique (after [Kümmell00]). FIB implants vacancies in the crystal, which locally enhances inter-diffusion between the QW and the matrix material.*

III. *In situ* lithography Alternative approaches for the fabrication of reduced dimensional epitaxial structures are based on *in situ* lithography using FIB [Seliger74], *scanning tunneling microscopy* (STM),[Kasu97] *atomic force microscopy* (AFM),[Hyon00] or *electron beam* (EB) [Sugimoto90] writing techniques. *In situ* FIB writing can be used to precisely control the doping concentration of epitaxial structures in three dimensions and has also been applied to control deposition and etching of material in selected areas. *In situ* STM, EB and AFM lithography have been used, e.g., to define sub-micron sized holes on a GaAs substrate. *In situ* overgrowth of this pattern resulted in the selective formation of self-assembled InAs QDs within the holes.[Kohmoto99, Ishikawa00, Hyon00] On one hand, this method is very flexible and allows for the growth of regular arrays of single QDs, with a spatial accuracy of ~100 nm. On the other hand, FIB, AFM, and electron-beam writing techniques are time consuming and, hence not suited for the fabrication of many quantum structures in one process. Even for the fabrication of a few quantum structures, one requires extended growth interruptions, which increase the impurity concentration at the interface. In addition, FIB writing techniques are known to cause irradiation damage.[Furuya96] Because of this, fabrication of quantum structures using *in situ* lithography processes does not always result in a better quality of the quantum structures.

3.2 Self-assembly techniques

In the early 1990s, self-organization concepts were for the first time successfully employed in the MBE process in order to fabricate self-assembled nanostructures.[Eaglesham90, Leonard94] Unlike lithographically defined quantum structures, self-assembled QDs and QWRs are usually of good structural and spectroscopic quality because of their *in situ* formation and subsequent overgrowth without growth interruption. In addition, self-assembly occurs on planar substrates and results in the formation of many nanostructures in a single process [see Figs. 3.3 (a) and (b)]. Because of these advantages over lithography techniques, self-organization techniques have become standard MBE processes, widely used to fabricate quantum-structures for light-emitting devices as well as for fundamental investigations of quantum effects. However, it is difficult to obtain sufficiently low densities and proper control of the exact locations of self-assembled nanostructures, which makes the approach less suitable for the fabrication of, e.g., quantum transport devices or single photon emitters.

The following sections give a brief introduction to a few critical aspects associated with self-organization in particular, and crystal growth in general, based on thermodynamic models. Although MBE is performed under non-equilibrium conditions and is therefore kinetically controlled, thermodynamics can explain under what conditions, the corrugation of an initially planar growth surface is favourable. The main self-assembly features, namely *step-bunching* (see Sect. 3.2.2) and the *Stranski-Krastanov* (see Sect. 3.2.3) growth, which can be used for the self-organized growth of QWRs and QDs, are due to the thermal instability of vicinal surfaces [A] and the misfit strain of heteroepitaxial systems, respectively. The shape of the resultant 3D features corresponds to the problem of equilibrium crystal shape (ECS; see Sect. 3.2.1).

3.2.1 Crystal shape

The phenomenon of step-bunching, as well as the shapes of self-assembled nanostructures are closely related to the problem of the equilibrium crystal shape (ECS). According to thermodynamic theory, a crystal (of fixed volume ω) takes the shape that minimizes the surface free energy $F_{surf} = \oint_{\partial\omega} \gamma(\hat{\mathbf{n}};T)\,dA$. Here, $\gamma(\hat{\mathbf{n}};T)$ is the surface free energy per unit area dependent of the orientation $\hat{\mathbf{n}}$ of the surface element dA relative to the crystal axes. $\gamma(\hat{\mathbf{n}};T)$ has minima in symmetry directions (with a low crystal index), which is associated with the energy contribution from steps on a vicinal surface (no symmetry direction). Consequently, at low temperatures, the ECS consists only of facets with low crystal index, e.g., (110), (100), (111) and $(\bar{1}\,\bar{1}\,\bar{1})$ surfaces in the case of zinc-blende GaAs.[Moll96] At higher temperature, the step contribution decreases and the corresponding low-index planes shrink. Above a critical temperature T_R, they disappear and the crystal becomes smoothly rounded. It has been observed, that the same qualitative behaviour characterizes the shapes of MBE grown nanostructures, although grown under non-equilibrium conditions.

[A] The orientation of vicinal surfaces does not correspond to a symmetry direction (with a low crystal index) of the crystal.

3.2.2 Step-bunching

Step-bunching corresponds to the rearrangement of atoms into hills and valleys on an initially planar substrate.[A] In this second ECS problem, the surface free energy is given by the surface integral over the corrugated substrate surface $F_{surf} = \int \gamma(\hat{\mathbf{n}};T)/(\hat{\mathbf{n}}\cdot\hat{\mathbf{m}})dA$, where $\hat{\mathbf{n}}$ is the surface normal at each point and, $\hat{\mathbf{m}}$, the unit normal of the initially planar surface. Out of all possible morphologies of the substrate surface (with fixed edges), the planar surface ($\hat{\mathbf{n}} \equiv \hat{\mathbf{m}}$) has the smallest surface free energy (it is stable), if γ has a minimum at $\hat{\mathbf{m}}$. On the other hand, vicinal surfaces are stable only if corrugated, i.e., an initially planar surface rearranges into a system with alternating tilted facets [$\hat{\mathbf{n}}_1, \hat{\mathbf{n}}_2$ with $\gamma(\hat{\mathbf{n}}) < \gamma(\hat{\mathbf{m}})$]. In the case of a vicinal substrate with a small miscut angle φ, the faceted structures are known as s*tep bunches* [*see* Fig. 3.2(a)].

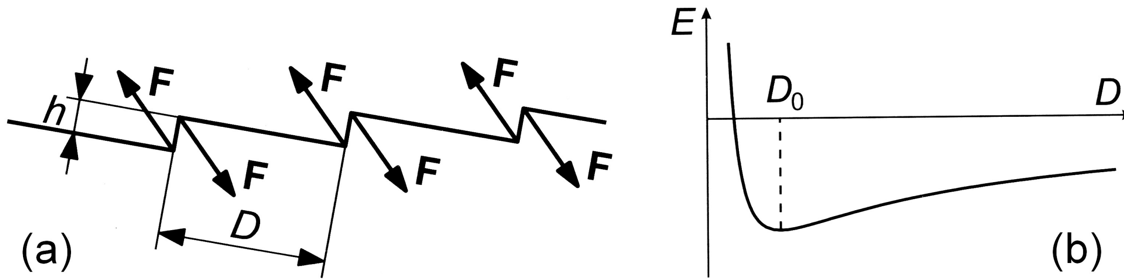

FIG. 3.2 – *(a) Periodically facetted structures, step bunches, resulting from faceting of a vicinal surface. Effective forces of alternating sign are applied to neighbouring edges.. (b) Total energy versus the period D. There always exists an optimum period of faceting D_{opt} due to the logarithmic dependence of the elastic relaxation energy on the period D. (after [Bimberg99])*

Moreover, the step bunches form a quasi-periodic array because of *intrinsic surface stress*, i.e., the local variation of the surface configuration and bond lengths causing force monopoles at crystal edges [*see* Fig. 3.2(a)]. These act on the elastic bulk of the crystal, resulting in a strain field. One can predict the period D of periodically faceted structures, such as the 1D saw-tooth profile illustrated in Fig. 3.2(a), by minimizing the total free energy per unit projected area with the contributions from surface free energy, F_{surf}, of the tilted facets (independent of D), the energy contribution of the stressed surface layer, E_{edges}, and the elastic relaxation energy, $\Delta E_{elastic}$, caused by the strain field (elastic deformation of the bulk). The total energy F (per unit projected area) as a function of the step height ($h \approx D\varphi$) is of the form $F = C_1 + C_2\varphi + \varphi[C_3 h^{-1} - C_4 h^{-1}\ln(h/a)]$.[Bimberg99] Due to the logarithmic term, there always exists an optimum equilibrium height and equilibrium period of step bunches [see Fig. 3.2(b)].

3.2.3 Self-assembly of 3D islands in heteroepitaxial growth

In heteroepitaxy, three well-known growth modes take place, depending on the interfacial energies and on the lattice mismatches of the substrates and the overgrown layers. Franck-van der Merwe (FvdM) growth implies layer-by-layer deposition, while 3D islands form in the Volmer-Weber (VW) growth mode. The Stranski-Krastanov

[A] The boundary conditions for the rearrangement are the fixed edges of the substrate surface.

(SK) growth mode is a sequence of initial layer-by-layer growth followed by 3D island growth.

In lattice-matched systems, the growth mode is solely governed by the interface γ_{int} and the surface energies γ_{sub}, γ_{lay} (per unit area) of the substrate and the epilayer, respectively. FvdM growth takes place when $\gamma_{lay} + \gamma_{int} < \gamma_{sub}$, i.e., when the deposited material wets the substrate. In contrast, non-wetting material ($\gamma_{lay} + \gamma_{int} > \gamma_{sub}$) forms 3D islands in the VW growth mode.

In heteroepitaxy of lattice mis-matched materials the elastic strain makes an important contribution to the total energy. The elastic energy is proportional to the thickness of a pseudomorphic layer ($E_{elastic} \propto t$). When $\gamma_{lay} + \gamma_{int} < \gamma_{sub}$, material deposits initially layer-by-layer. However, above a critical thickness, the island formation becomes energetically favourable, because the 3D islands can reduce the elastic energy by elastic relaxation in the free lateral direction.

Recently, there has been increasing interest in *self-assembly* of III-V and II-VI islands using the SK growth mode, because quasi zero-dimensional nanostructures can be fabricated and overgrown without incorporating defects or impurities in the crystal. Self-assembled QDs are important for applications in light-emitting devices. However, their random distribution makes it difficult for these structures to be exploited in structures like quantum transport devices or single photon emitters.

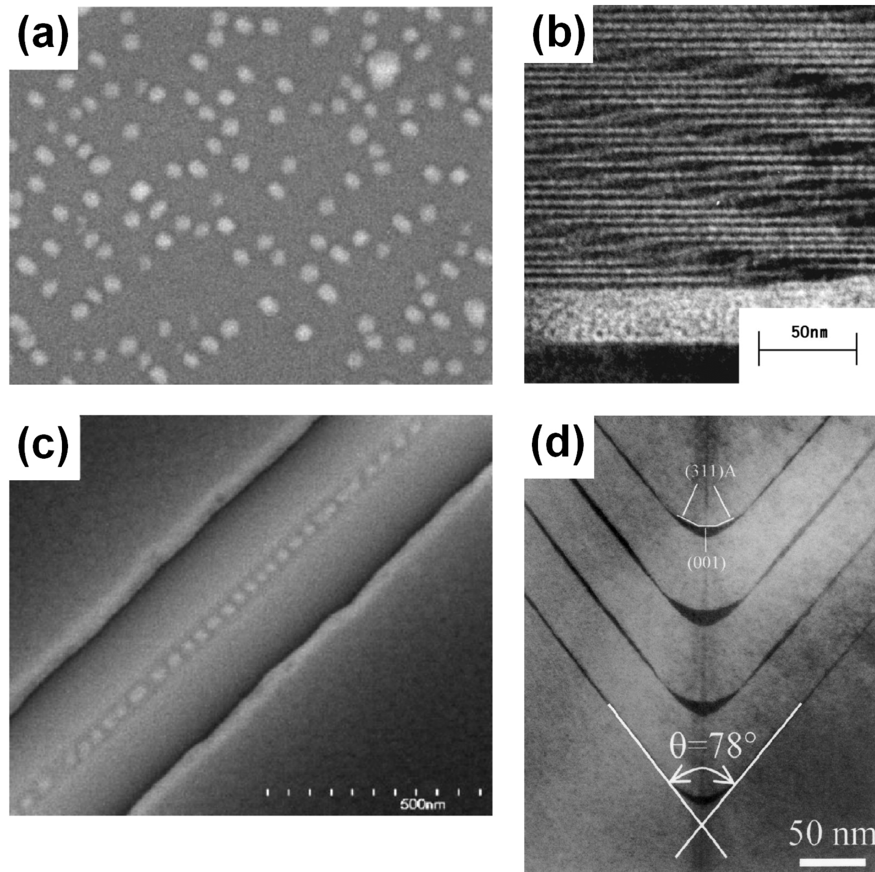

FIG. 3.3 – *(a,c) Plan view scanning electron micrographs of self-assembled InAs QDs on InP substrate (after [Lefebvre00]): (a) QDs formed on a planar substrate. (c) QDs selectively formed on a ridge patterned substrate. (b,d) Cross-sectional transmission electron microscopy images of GaAs QWRs. In the image, GaAs layers appear dark and AlGaAs appears bright. (b) Stacked GaAs QWRs formed on vicinal substrates (after [Kato98]). (d) QWRs formed in a V-groove patterned substrate (after [Wang00]).*

3.3 Selected area epitaxy

Selected area epitaxy (SAE) techniques have been developed in order to increase the flexibility of the conventional MBE process. Cho and Ballamy [Cho75] proposed growth over patterned substrates (*patterned SAE*) as an useful technique, which is well established nowadays for the *in situ* fabrication of high-quality QWRs and QDs at predefined places. Another variant of the SAE technique uses shadow masks for the patterning of thin films *(shadow masked SAE).* Several studies have demonstrated the potential of this method to overcome certain technological drawbacks and thus to fabricate novel devices, which are not feasible by alternative techniques. Although more flexible, shadow masked SAE has never gained the importance of patterned SAE. The reasons for this will be discussed below.

3.3.1 Growth on patterned substrates

In patterned SAE, conventional lithography is used for patterning either a mask overlayer (SiO_2 or Ga_2O_3) or the substrate itself (see Fig. 3.4). These patterns are then used to modulate the growth rate by making use of (1) *self-organization* concepts, (2) *orientation-dependent* growth rates, and (3) the *migration enhancement* from areas with the mask overlayer towards the unmasked growth area.
Although, an excellent spatial control can be achieved by patterned SAE, the method has several limitations. Critical issues are (1) the limited versatility of SAE with a single pre-defined pattern, (2) the fact that growth is orientation-dependent,[A] and (3) the requirement of *ex situ* processing to remove the mask overlayer before capping of SAE grown quantum structures can be performed.[Lee01, Mei02] Furthermore, thick buffer layers are often incompatible with patterned SAE because they affect the original pattern.[Ishikawa00, Lee01, Mei02]

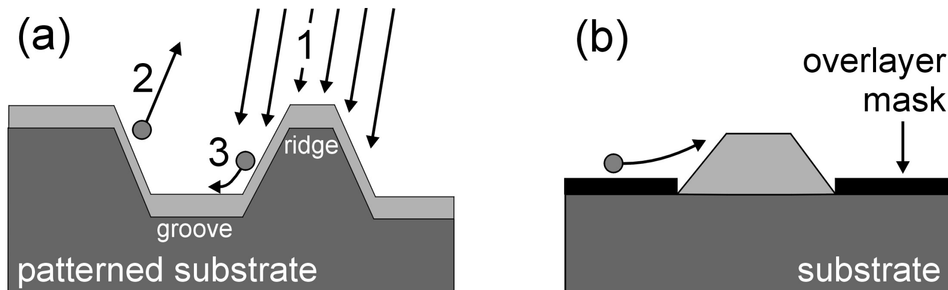

FIG. 3.4 – *Principle of patterned SAE. Growth is governed by (1) incident flux, (2) desorption, and (3) surface diffusion of adatoms. (a) Patterned substrate. (b) Overlayer mask.*

Thus, patterned SAE growth does not always result in improved quality of self-aligned quantum structures. Nevertheless, patterned SAE is the most prominent method for the fabrication of high-quality nanostructures at predefined places.

Below, the most important self-organization concepts of patterned SAE are introduced, based on thermodynamic models. This discussion neglects all kinetic growth effects, which result from the non-equilibrium growth conditions under which MBE is performed. Later, kinetic models are used to discuss the effects of orientation-dependent

---

[A] [Kapon87, Tsui97, Konkar98, Leifer00, Lee01]

growth kinetics, neglecting, however, the additional self-assembly effects caused by intrinsic surface stress and misfit strain.

I. Self-organization on patterned substrates[A] This paragraph discusses how a corrugated surface modifies the FvdM, VW, and SK growth modes in SAE and how the curvature of patterned substrates can be used to control the positions of self-assembled islands. In all three cases, it is assumed that the orientation-dependence of the surface energies γ (per unit area) is negligible and that the intrinsic surface stress is tensile.

In the VW growth mode, the deposited material ($\gamma_{lay} + \gamma_{int} > \gamma_{sub}$) forms 3D islands on a planar substrate, because this reduces the free surface energy F_{lay} by reducing the surface area of the non-wetting material. However, an island of the same volume can further reduce its surface area if the surface is convex. Therefore, VW islands form preferentially at the convex edges of a substrate pattern.

In the case of wetting materials ($\gamma_{lay} + \gamma_{int} < \gamma_{sub}$), similar effects are expected. In a modified FvdM growth, a film deposited on patterned substrates can reduce its surface area by the formation of clusters in the convex regions of the surface patterns. Unlike the previous case, a thin wetting layer, which is not involved in the cluster formation, has to remain and cover the entire substrate, so that only γ_{lay} is reduced, while γ_{int} and γ_{sub} are unchanged.

In the SK growth mode, 3D islands are formed on a planar substrate because 3D structures with a high aspect ratio can reduce their elastic energy by elastic relaxation. Analogously, concave edges regions (3D) of a patterned substrate are more flexible than planar regions (2D). Thus, SK islands which form at concave edges can reduce their elastic energy more efficiently, which can be used to control the nucleation of SK grown islands. A different approach to control SK growth is to use stressor in the substrate pattern.[Lee00]

The site-control is not the only advantage of self-organization on patterned substrates. Moreover, the narrowing of QD size distribution is also expected to be achieved by site control, as has been suggested by theoretical modeling.[Lee98]

II. SAE of III-V materials Under the non-equilibrium growth conditions of MBE, orientation-dependent growth dynamics are due to the orientation dependences of (1) the incident flux, (2) the sticking coefficients, and (3) the surface diffusion length [see Fig. 3.4(a); The impingement rate of the adatoms depends on the orientation of the surface relative to the beam direction. The sticking coefficient, the diffusion constant, and the incorporation lifetime of adatoms depend on factors such as the surface reconstruction, the step density, and the surface concentrations of the other constituent species.]. In the case of III-V MBE, the growth kinetics can be understood by surface migration of adatoms, which is driven by the orientation-dependence of the diffusion constant D_S of adatoms and by gradients of their surface concentration, N_a. The former is the intrinsic reason for *inter-surface diffusion* as it is observed, e.g., in microprobe-RHEED experiments (see Fig. 2.6). The second driving force for inter-surface diffusion is a local variation of the surface concentration of adatoms. According to the diffusion model, the surface concentration $N_a = G\tau$ depends on the generation and the recombination rates of mobile adatoms. The generation (rate G) of surface atoms corresponds to the incidence of the group III flux (f_{III}) and the recombination of surface adatoms means desorption of adatoms from the surface (desorption lifetime τ_{des})[B] as well

[A] Heteroepitaxial growth modes on corrugated substrates have also been discussed in Ref. [Bimberg99], but with different conclusions.

[B] In III-V MBE, desorption of adatoms is often negligible because of the low vapor pressure of group III elements.

as incorporation of adatoms into the solid phase (incorporation lifetime τ_{inc}). Hence the lifetime of the adatoms on the substrate surface is $\tau = (\tau_{des}^{-1} + \tau_{inc}^{-1})^{-1}$.

The inter-surface diffusion of the adatoms can then be described by the diffusion equation:

$$G - N_a/\tau - \nabla_S \cdot \boldsymbol{J}_S = 0, \tag{3.1}$$

where the three terms on the left hand side correspond to the generation, recombination, and surface diffusion of adatoms, respectively. Here, ∇_S is the surface gradient operator and $\boldsymbol{J}_S = -D_S \nabla_S N_a$ the surface diffusion current of adatoms. Figure 3.5(a) shows a schematic illustration of inter-facet diffusion of Ga adatoms from GaAs (111)B surface to (001), which is driven by the higher surface concentration N_a on the (111)B side-facet.

The observations from microprobe-RHEED experiments (see Fig. 2.6), that the incorporation diffusion length l_{inc} varies with the change of the arsenic pressure f_V, can be understood as follows: Group III surface atoms encounter As molecules more often when the group V flux f_V is high. Hence the incorporation lifetime τ_{inc} of group III adatoms is short. As a result, the incorporation diffusion length of the adatoms, given by $l_{inc} = \sqrt{D_S \tau_{inc}}$, is also limited. In the reverse case, when the flux of the group V species is low, the lifetime of group III adatoms is long. Thus, their surface concentration N_a becomes relatively high and they can move far away from the region of their incidence. Moreover, it has also been shown that $\tau_{inc} \propto f_V^{-\gamma}$ $(\gamma > 0)$, where γ is the order of the incorporation reaction.[Nishinaga96] For example, As_4 molecules are incorporated in the growing crystal following a second order process. Hence $l_{inc} \propto f_V^{-1}$, as is indicated by the solid line in Fig. 2.6(b).

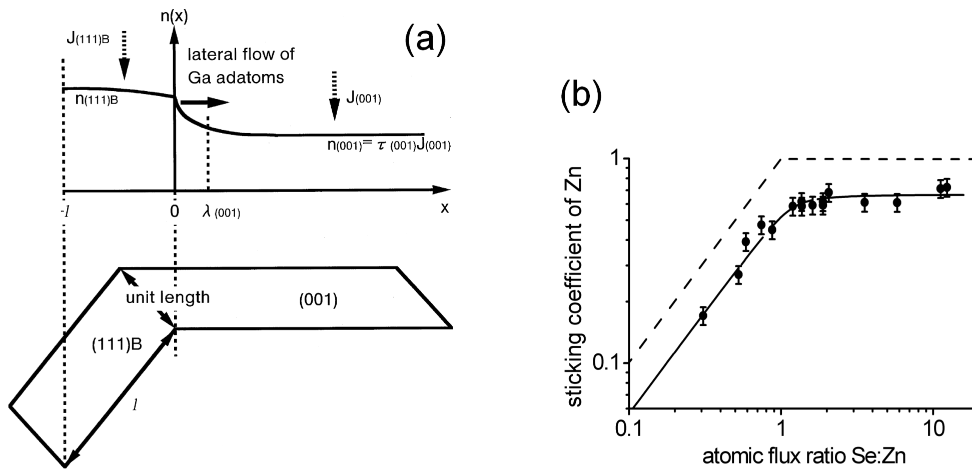

FIG. 3.5 – *(a) Schematic illustration of inter-facet diffusion of Ga adatoms from GaAs (111)B surface to (001) (after [Kishimoto00]). The upper diagram shows the surface concentration, according to the diffusion equation, as a function of the distance from the facet edge. (b) Sticking coefficient of Zn adatoms on the ZnSe (001) surface as a function of the Se:Zn flux ratio. (data points after [Riley96]; solid curve after [Ruppert94] and multiplied by the correction factor 0.68)*

III. SAE of II-VI materials Orientation-dependent growth on patterned substrates has also been used for the formation of II-VI nanostructures. In the case of II-VI materials, SAE is governed by the orientation-dependence of the sticking coefficients rather than the surface diffusion of adatoms, which is important in the case of III-V materials.

In II-VI MBE, the sticking coefficient s of one molecular species depends on the flux f of the other constituent elements of a compound material. For a binary semiconductor AB, the atomic incorporation rate, S, is given by $S = sf$, and it is equal for both A and B since the stoichiometry of the compound is restored. As a result of this, the sticking coefficients s_A and s_B depend on the fluxes f_A and f_B, as[A]

$$S = s_A f_A = s_B f_B . \tag{3.2}$$

The dotted line in Fig. 3.5(b) shows the sticking coefficient of Zn, s_{Zn}, for the case where it is assumed that all molecules of the minority species get incorporated ($s_{minority} = 1$). However, in reality a considerable fraction of the minority species molecules does not stick to the surface, i.e., it re-desorbs. This is revealed in the experimental data in Fig. 3.5(b), which shows the sticking coefficients of Zn on the ZnSe(001) surface, at a substrate temperature of 300°C, as a function of the atomic flux ratio (after [Riley96]). Similar data on the sticking probability of Zn on ZnSe surfaces have, to the best of our knowledge, not been published for different surface orientations [e.g. (111)]. Without this data, modeling of SAE of ZnSe on patterned substrates is hardly possible.

3.3.2 Growth through shadow masks

Another variant of the SAE technique uses shadow masks for the patterning of thin films *(shadow masked SAE)*. Several studies have demonstrated the potential of this method to overcome certain technological drawbacks[B] and thus to fabricate novel devices, which are not feasible by alternative techniques. Although more flexible, shadow masked SAE has never gained the importance of patterned SAE. The reasons for this will be discussed, here.

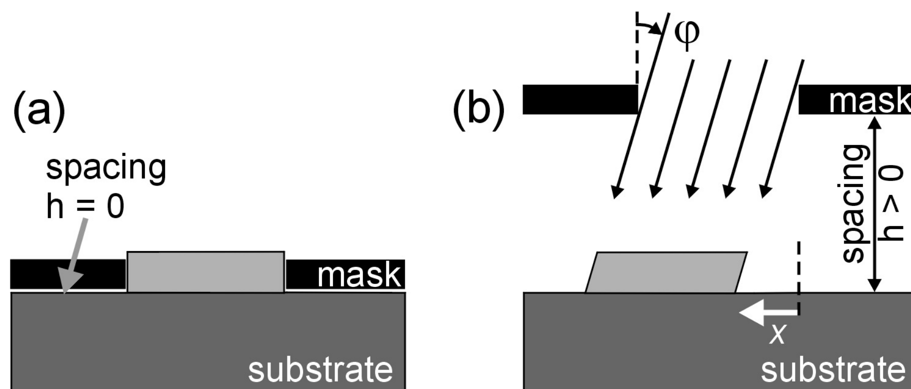

FIG. 3.6 – *Principle of shadow mask assisted MBE in two different configurations. (a) Removable mask in contact with the substrate (h = 0). (b) Mask spaced from the substrate (h > 0). Lateral growth can be controlled by the angle of incidence φ of the beams.*

[A] The application of Eq. (3.2) is not always allowed. For example, molecular beams might consist of different molecular species of an element, which obey different surface kinetics (see Sect. 5.2.4). In this case, the interaction of the different molecular species has to be considered, which makes the problem more complex.

[B] Shadow masked SAE has been used (1) to integrate optical elements and quantum structures laterally [Tsang77b, Saito95, Peake99, Luo00a] and (2) to produce selective contacts to embedded structures such as doping-superlattices and 2DEGs [Döhler86, Lorke95].

There are two different concepts of employing shadow masks in MBE, which are illustrated in Fig 3.6. In configuration (a), a mechanical mask is placed directly onto the substrate, and in configuration (b), it is positioned above the substrate, such that a non-zero spacing distance ($h_S > 0$) exists between them. For technical reasons, which are explained below, different mask types are used in the two configurations.

I. Removable mask When the shadow mask is in contact with the substrate ($h = 0$), the growth area is determined by

(1) the *geometry of the mask apertures* and

(2) the *position of the mask on the substrate*.

The growth area can thus be selected in a flexible way by using masks with different aperture patterns and/or by moving the mask to different positions on the substrate. However, this requires a technique for handling the masks under the extreme conditions of the MBE process (UHV[A], temperature variation[B]). Although Tsang and Ilegems [Tsang77b] have demonstrated that mechanical masks enable the growth of III-V structures with feature sizes as small as 1 μm and >5 μm with *in situ* handled shadow mask [see Fig. 3.7(a)]. The reason for this may be that *in situ* handling requires more robust masks, which are thicker and less flexible, which would imply a non-zero distance h_S between the shadow mask edge and the substrate.[C] Even worse is the fact that the precision of mechanical alignment of a mask is not reproducible on the scale of 10 μm with present mask holders [see, e.g., Fig. 3.7(b)]. Hence, shadow masked SAE based on removable masks is currently not suited for the fabrication of micro-scale (or nanoscale) heterostructures.

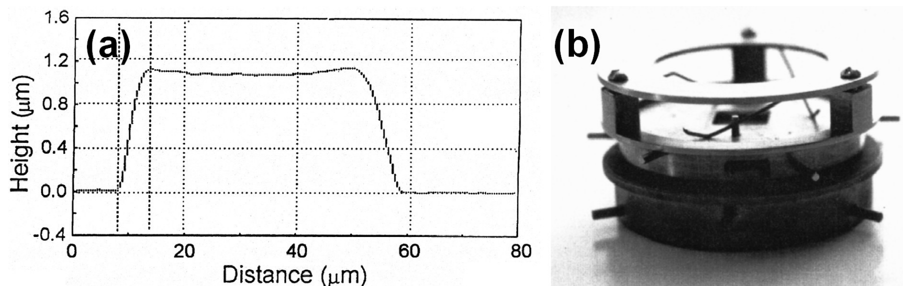

FIG. 3.7 – SAE using removable masks (after [Luo98]). *(a) Surface profile of CdTe deposited through an in situ handled shadow mask. The width of the edge regions is ~5 μm. (b) Assembly of substrate holder and mask holder, which can be used in situ to place and remove a shadow mask.*

II. Stationary mask Despite its outstanding designation, the "beam" character [D] is almost irrelevant in most "molecular beam epitaxy" techniques. This is different for shadow masked SAE in configuration (b) where the shadow mask is separated by a non-zero distance from the substrate (shown in Fig. 3.6). Molecules in a beam passing through an aperture of the shadow mask impinge on a limited area of the substrate, which is a projection of the aperture. The lateral position [$x = h_S \cdot \tan(\varphi)$] of this incidence depends

[A] In order to avoid the contamination of the UHV chamber with impurities, one is restricted in the materials used for the mask, the mask holder, and the mechanical parts of the substrate or mask manipulator. Lubricant-free mechanics are usually not very precise.

[B] The mask and the substrate have to withstand temperature changes of 300-600 degrees. Thermal expansion of the shadow mask and the substrate make precise alignment difficult or even impossible.

[C] (h_S) is the spacing between the shadow mask edge and the substrate, which may be larger than h if the shadow mask has a non-zero thickness (see Sect. 4.21).

[D] Under UHV, molecules propagate from their source on a linear path.

on the beam direction, i.e., the angle of incidence (φ) with respect to the normal of the shadow mask. Thus, the deposition of material can be controlled by

(1) the *geometry of the mask apertures*,
(2) the *position of the mask on the substrate*, and
(3) the *incidence direction of the molecular beams*.

The second and third degrees of freedom are almost equivalent, since both enable shifting of the incidence regions. Moreover, (2) seems to be more flexible than (3) because, in addition to shifting on the substrate, the mask can also be rotated around its surface normal. On the other hand, controlling the incidence angles has also distinct advantages over the second degree of freedom:

One benefits from independent control of the lateral positions of the incidence regions of different component beams on the substrate. For example, Döhler *et al.* [Döhler86] have demonstrated that by manipulating the incidence directions of the doping materials, one can control the doping concentration in selected areas, which is not possible in patterned SAE or shadow masked SAE, when the shadow mask is in contact with the substrate (s = 0). They used this degree of freedom to realize selective contacts to n-i-p-i doping superlattices using the flash doping technique sketched in Fig. 3.8(a).

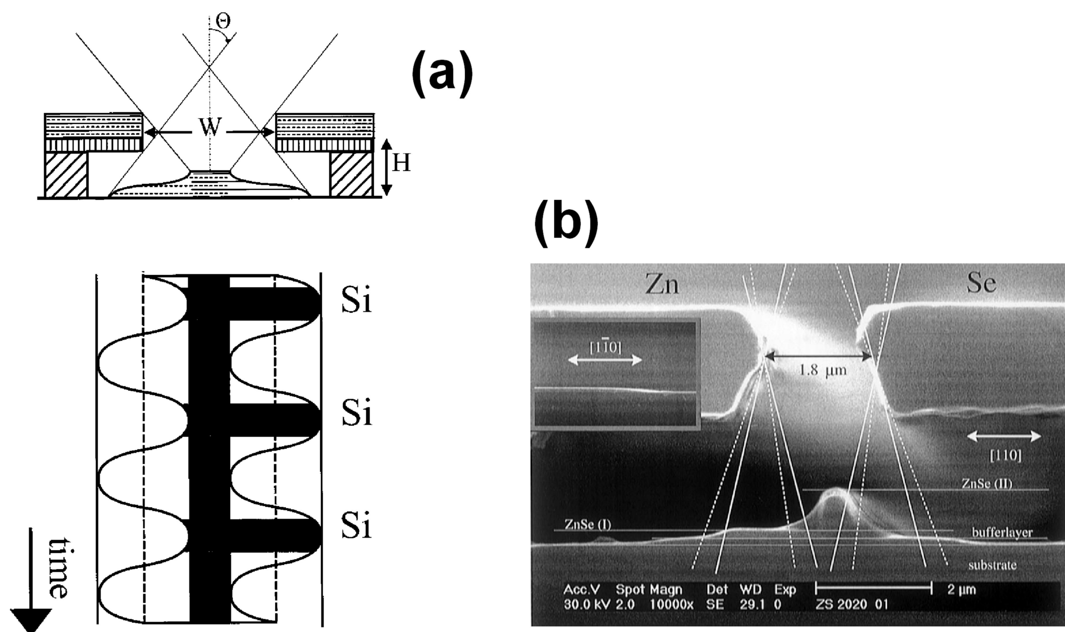

FIG. 3.8 – SAE using epitaxial shadow masks. (a) Principle of the growth of n-i-p-i-SL with selective contacts using a flash doping technique (after [Malzer96]). During the growth, the sample is continuously rotated and the respective shutters of the dopants effusion cells are opened for the time of appropriate alignment to the shadow mask. (b) Cross-sectional micrograph of a shadow mask (after [Schumacher00]). A ZnSe wire was grown through the mask with different incidence directions for Zn and Se beams. The width of the ZnSe structure is smaller than the width of the mask-aperture.

The second advantage is that controlling shadow masked SAE by the beam directions can be much more accurate than the mechanical alignment of a removable shadow mask on the substrate. This is because the lateral position of the incidence [$x = h_S \cdot \tan(\varphi)$] depends on the angle of incidence φ and also the spacing h_S between the shadow mask edge and the substrate. In a conventional MBE chamber, φ can be controlled with an accuracy of about 1° (see section 4.2) [which corresponds to a spatial precision of ~1 μm when h_S = 50 μm]. When the spacing between the mask and the substrate is only h_S = 1 μm, the lateral position of the incidence can be controlled with a precision of ~20 nm.

III. Epitaxial shadow mask Such low-lying shadow masks (h_S < 10 µm), however, can hardly be realized by mechanical means.[Tomita95] Tsang and Cho [Tsang77a] used anisotropic etching of the substrate to form micrometer-sized channels with undercut edges, which served as a shadow mask. In this case, the spacing h_S between the shadow edges and the substrate is given by the depth of the holes (of the order of one micrometer). However, this early mask concept was restricted in its geometry (only mask-channels oriented along the (110) direction of a GaAs(001) substrate) and it was not possible to remove the mask after the growth, which made access to SMMBE grown structures difficult.

Gulden *et al.* [Gulden93] subsequently developed an improved mask concept, which is based on epitaxial layers grown on a GaAs substrate. The epitaxial shadow mask consists of a AlGaAs spacer layer and a GaAs cap layer on top of it (see Sect. 4.1). Conventional lithography was used to open apertures in the cap, which act as the shadow mask. Selective etching removes the AlGaAs material below the apertures and forms a cavity. Thus, the spacing h_S between the stationary mask edge and the substrate is defined by the thicknesses of the spacer layer h and the cap layer g. Gulden and Döhler demonstrated that SAE can be controlled with spatial precision in the micrometer range by modulating the incidence angles of the beams [see Fig. 3.8(a)]. The new growth method based on the usage of epitaxial shadow masks was named “Shadow mask molecular beam epitaxial regrowth technique” (SMMBE).

At Würzburg University, Schumacher investigated the epitaxial growth of II-VI compound semiconductors through epitaxial shadow masks and developed novel growth techniques, which are also based on the control of the incidence angles of the beams. This has enabled the fabrication of II-VI structures with smaller lateral dimensions (sub-µm) than the width of the mask apertures [see Fig. 3.8(b)].[Schumacher99, Schumacher00].

Chapter 4

Technological Aspects

This chapter discusses the technological aspects of SMMBE. The main topics are the fabrication of the shadow masks and the control of the incidence angles of molecular beams in a conventional MBE growth chamber. In particular, developments discussed here, have enabled (1) the regrowth on shadow mask samples with a low defect-density, (2) the fabrication of shadow masks of nanoscale dimensions with high precision, (3) control of the incidence angles of the molecular beams with a precision of 1°, and (4) the reduction of the width of the partial shadow of the beams to ~20 nm.

4.1 Shadow mask technology

Epitaxial shadow masks are fabricated from MBE grown epitaxial layers, e.g., AlGaAs/GaAs epitaxial layers on a (001) GaAs substrate. The layers are patterned by photo or electron-beam lithography, followed by dry and wet etching processes. The advantage of using epitaxial masks is in the fact that the mask can be removed after the growth, without destroying the as-grown structures.

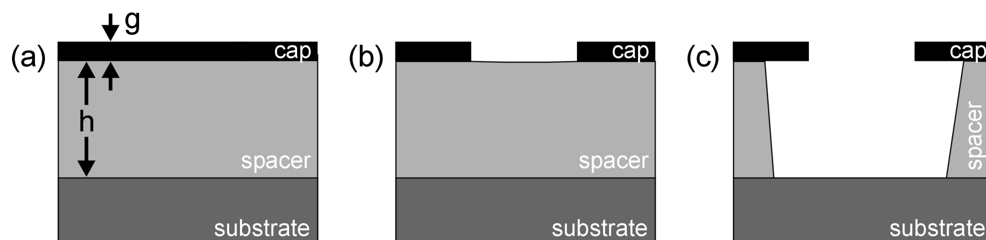

FIG. 4.1 – *Fabrication of epitaxial shadow masks. (a) GaAs cap and AlGaAs spacer layers are grown by MBE on GaAs substrate. (b) Apertures are etched through the cap and the lithography resist is removed, again. (c) The spacer is removed by selective etching. Finally, the surface of the shadow mask sample is passivated.*

4.1.1 Epitaxial shadow mask layers

Figure 4.1(a) shows the basic layer structure of an MBE grown, epitaxial shadow mask, grown in a III-V MBE chamber. First, a 2-inch, epi-ready GaAs(001) substrate, mounted on an indium-free sample holder, is introduced in the III-V growth chamber and heated to 400°C. Subsequently, with an arsenic beam equivalent pressure (BEP) of $\sim 5 \times 10^{-6}$ torr, the substrate temperature is further increased until a spotty (2x4) surface reconstruction in RHEED, which is indicative for the desorption of the amorphous oxide layer, is observed. This event is used for the calibration of the substrate temperature (T_{des} = 570°). After thermal cleaning of the substrate for five minutes at 620°C, typically, a 500 nm thick GaAs buffer layer is grown at 600°C. MEE technique is employed in order to achieve a smooth surface of the buffer. After the buffer growth, a streaky (2x4) pattern is observed in RHEED. Subsequently, an $Al_xGa_{1-x}As$ *spacer* layer (x = 0.6, h = 0.5 - 5 µm) and a GaAs *cap* layer (g = 0.1 – 1 µm) are grown at 570°C and 600°C, respectively. The ratio of the layer thicknesses *(h : g)* is typically in the range 4 - 10.

4.1.2 Preparation of the shadow masks

Shadow masks are fabricated from the epitaxial layers in three steps (see Fig. 4.1): Firstly, lithography and etching are employed to open windows in the GaAs cap. Secondly, a cavity is opened below these apertures using an etching process, which selectively etches the AlGaAs spacer layer. Finally, the mask is prepared for the second epitaxial growth. As is discussed below, additional steps have been introduced in the fabrication process, in order to avoid contamination of the samples.

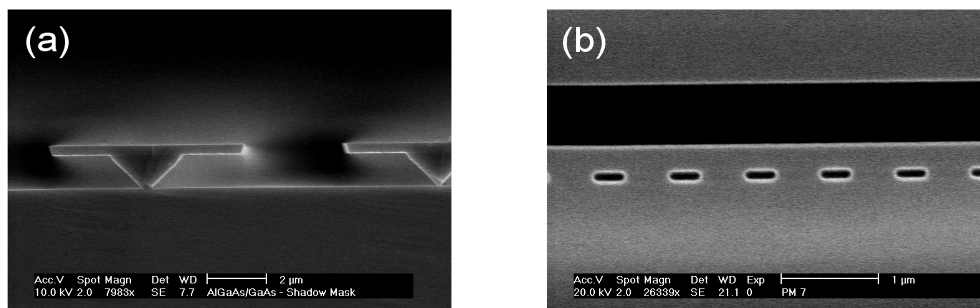

FIG. 4.2 – *Scanning electron micrographs of shadow masks samples. (a) Micrograph of the cross-section of an epitaxial shadow mask with stripe-shaped apertures. (b) Plan view micrograph of an epitaxial shadow mask with nanoscale precise pattern of aperture holes (dark).*

I. Lithography and etching of the cap A standard photolithography process usually defines a resist mask for the patterning of the cap layer. Optical masks are used to open 5-10 µm wide and 10 mm long windows (lateral period 60 µm) in a 2 µm thick photo-resist. Subsequently, this pattern is transferred to the epitaxial shadow mask by wet chemical etching of the GaAs cap layer using an aqueous solution of ammonia and peroxide [$NH_3 : H_2O_2 : H_2O$ (1:10:10)]. This is done with the optical mask aligned parallel to one of the cleaved edges of the epitaxial sample, so that the aperture stripes are aligned parallel to the [110] and $[1\bar{1}0]$ crystal directions, respectively.

An improved lithography process has been developed to fabricate shadow masks with aperture dimensions of ~1 µm, which is not possible with the standard process. First,

the shadow mask sample is dipped in HMDS (for 15 sec). Secondly, a 600 nm thick resist layer (Allresist ARU4060 photo-resist) is spin coated on the sample and baked at 90°C for 15 min. The resist, masked by an optical mask, is then exposed to UV light (for 8 sec), and developed with AR300-26 developer (2:1) for 8 seconds. Using this process, shadow masks with homogeneous apertures of widths as small as 1 µm can be fabricated. For this, two optical masks have been fabricated as templates. The first mask can be used to define a pattern of stripe apertures, 3 µm wide and 200 µm long, with a lateral period of 10 µm. The second optical mask can be used to define stripe apertures, 1 – 10 µm wide (width increases in steps of 0.2 µm) and 200 µm long, with a lateral spacing of 7 µm.

A process consisting of electron-beam lithography and chemical assisted ion beam etching has been developed for the fabrication of epitaxial shadow masks with aperture dimensions of nanoscale precision. First, a 180 nm thick polymethylmethacrylate layer is spin coated on the sample[A] and baked at 105°C for 1 h. Next, the polymethylmethacrylate is exposed to electrons with an energy of 10 keV and a dose of $D=400\ \mu C/cm^2$ (the double dose is used for holes with diameter <0.5 µm). The resist is developed with MIBK:IPA (1:5) for 1 min, and, finally, holes with precisely defined edges are opened in the cap by a chemical assisted ion beam etching process using an Ar-ion beam and BCl_3 for etching. Images of the sub-µm apertures in the GaAs cap layer are shown in Figs. 4.2(b) and 4.3(a).

II. Selective etching of the spacer After defining the apertures of the epitaxial mask, the lithography resist (on the cap) and the AlGaAs spacer (below the cap) have to be removed. It is crucial that the resist layer is removed first. This ensures that, the AlGaAs spacer acts like a protecting layer against the contamination of the substrate surface.

While the photoresists can be dissolved in acetone (5 min), polymethylmethacrylate resist is hardly soluble after electron-beam lithography and it is best removed by oxygen-plasma treatment (5 min). The plasma treatment, can also be used to clean the mask surface after the removal of a photoresist layer using acetone.

All subsequent preparations have to be carried out with special care in order to avoid any contamination of the sample. For this reason, bottles with organic solvents were removed from the working desk and the samples were rinsed in fresh deionized water ($>10^7\Omega$) after each preparation step. In addition, different dishes were used before and after the removal of the resist layer. In particular, one clean set of dishes were not used for other processes except the following preparation steps.

The spacer layer below the apertures of the mask-cap is removed with concentrated hydrofluoric acid, which selectively etches the AlGaAs material and does not affect GaAs structures, i.e., the cap and the substrate. However, hydrofluoric acid etching of the spacer produces particles (of unknown composition) on the substrate and the cap. It has been observed that it is advantageous to etch without interruptions, with a flow of hydrofluoric acid along the stripe apertures (by moving the sample), and to rinse the sample directly after hydrofluoric acid etching with deionized water flowing along the aperture stripes. Subsequently, the sample is dipped in peroxide for 15 sec. The latter treatment removes most of the particles when it is carried out immediately afterwards.

III. Passivation of the substrate The peroxide treatment has a second effect because it forms a protective oxide layer (Ga_2O_3) on the entire surface of the sample. Such an oxide passivates the interface, and thus avoids contamination of the sample, which is particularly important for the duration when the sample is exposed to the air.

In literature, different studies have demonstrated the importance of the surface passivation for the subsequent epitaxial growth. Depending on the procedure, Ga_2O_3 or

---

[A] Polymethylmethacrylate (3 % solution in ethyllactate); 3 sec at 2000 rps; 40 sec at 4000 rps

As_2O_3 layers are formed on GaAs substrates, which can subsequently be desorbed at 580°C and 450°C, respectively. During this work, various passivation treatments using aqueous solutions of peroxide, H_2SO_4, and NH_3, have been tested and compared with the standard process with concentrated peroxide. None of the tested alternatives resulted in a reproducible improvement of SMMBE growth start.

4.1.3 Loading of the samples

In order to minimize exposure to the ambitient, the shadow mask samples are loaded in the UHV system quickly after the passivation of their surface. For this, they are mounted on a molybdenum block (sample holder) using molten indium as glue. Usually two samples with (110) and $(1\bar{1}0)$ oriented stripe apertures were mounted with the stripe patterns aligned parallel. For the calibration of the incidence angles, however, the stripe patterns of the samples were aligned perpendicular. In addition to the shadow mask samples, an epiready substrate (unpatterned) was added as a 2D reference. It should be noted that the incidence angles of the molecular beams on the samples depend on their position on the molybdenum block (see Sec. 4.2.2).

Next, the molybdenum blocks with the samples are loaded in the UHV system and demoistened on a heating station (for 10 min at 300°C) before being stored under UHV until they are used for the second epitaxial growth.

4.1.4 New mask concept

Molecules of a beam traversing through an epitaxial shadow mask impinge within a limited area on the substrate, which is the projection of the apertures of the mask. While the shape of the *incidence region* (growth region) is defined by the shape of the apertures only, its lateral position depends additionally on the beam direction. In SMMBE using epitaxial shadow masks, the beam direction is the only *in situ* adjustable parameter. However, the control of the beam directions is limited in a conventional growth chamber (see Sect. 4.2). Therefore, the geometry of shadow mask, which has to be planned in advance of a growth experiment, plays an important role to overcome this limitation. During this work a new mask concept has been developed: Epitaxial shadow masks with multiple apertures in the mask-cap [see Fig. 4.2(b)], as discussed in Sect. 4.1.2. Unlike the standard procedure, selective etching of the AlGaAs spacer was continued until it was completely removed from the region between the apertures [e.g., see Fig. 4.4(a)]. Thus, the resulting masks consist not of one but of a number of apertures per mask-cavity.

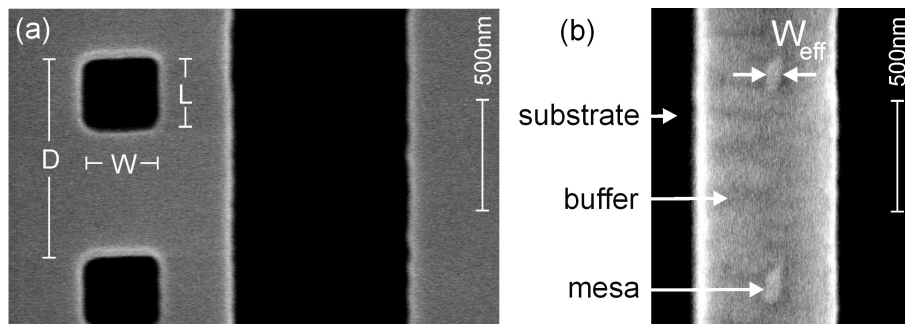

FIG. 4.3 - *(a) Scanning electron micrograph of a shadow mask with a stripe aperture and two W×L rectangular apertures. (b) Scanning electron micrograph of a ZnSe buffer stripe with two ZnSe mesas on top. The effective island width W_{eff} is 100 nm.*

By employing different incidence directions of the molecular beams, one can now use the variety of the aperture shapes for the SAE growth of different structures in one process as is illustrated by Fig. 4.3. The micrograph in Fig. 4.3(a) shows an epitaxial mask with a stripe aperture and two W×L rectangular apertures, before the growth of epitaxial ZnSe structures through the mask. First, Zn and Se were deposited through the stripe-shaped aperture resulting in the growth of a ZnSe stripe, which is clearly visible on the *scanning electron microscopy* (SEM) image (Philips XL30 SEM system) shown in Fig. 4.3(b). After growth, the substrate manipulator was tilted and rotated to a different configuration where the small rectangular apertures of the masks were used to deposit nanoscale ZnSe islands on selected areas on the mesa stripe. (A detailed discussion of the growth of compound materials through such a mask is given in Sect. 6.2 and Sect. 7.3).

4.1.5 Lift-off of the mask

I. Etching based lift-off An advantage of the epitaxial mask compared to anisotropically etched channels with undercut edges (see Sec. 3.3.2) is that it can be completely removed after the SMMBE process. Unless hydrofluoric acid threatens the SMMBE grown structures, it can be used to selectively etch the AlGaAs spacer to lift-off the shadow mask. However, etching with pure hydrofluoric acid is often not very effective because of the strength and elasticity of the GaAs cap. When the spacer is removed, the cap can buckle down to the substrate and stick to it without breaking. This can be avoided by ultra-sound agitation assisted hydrofluoric acid etching. The ultra-sound treatment mechanically breaks the fragile freestanding parts of the cap (where the spacer is removed) and prevents adhesion to the substrate. However, ultra-sound treatment is not effective after hydrofluoric acid etching, because it does not remove parts of the cap once they stick to the substrate.

Materials which are not threatened by hydrofluoric acid etching are, ZnSe and its alloys and GaAs. However, hydrofluoric acid etches III-V alloys with In and Al as constituents and also certain metals, e.g., Al. Obviously, it is not reasonable to use the hydrofluoric acid based lift-off process if a SMMBE grown structure consists of any of these materials.

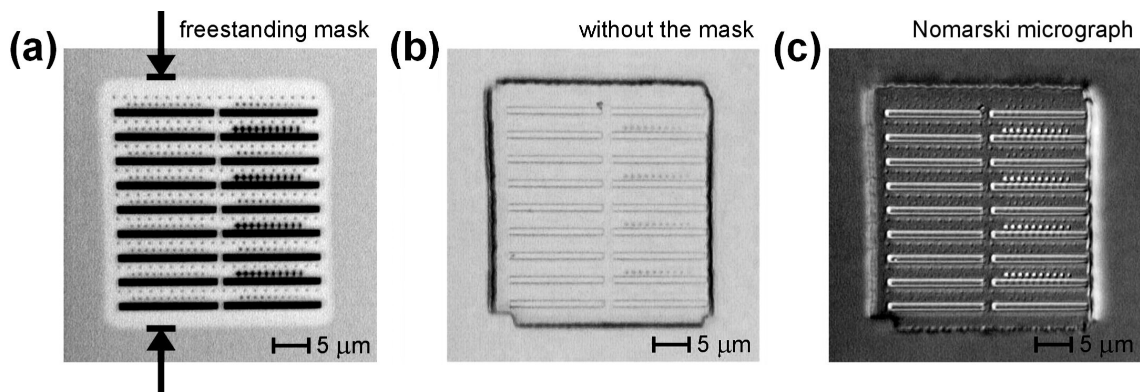

FIG. 4.4 – *Micrographs of a shadow mask sample after SMMBE of GaAs. (a) The image shows the aperture pattern (dark). The mask-cap is freestanding in the region (bright rectangular) indicated by the arrows. (b) Image of the sample after the mask had been removed by ultra-sound agitation, without etching. (c) Nomarski micrograph of the same region showing the details of the GaAs deposits on the substrate.*

II. Mechanical lift-off This problem has been solved through the development of shadow masks, which can be removed by ultra-sound agitation in deionized water, i.e., without etching. An example of this is shown in Fig. 4.4. Image (a) shows a plan view micrograph of a shadow mask. The dark stripes (1 µm wide) and dots (diameter <1 µm) are apertures in the 100 nm thick GaAs cap. In the image one can distinguish a 35x35 μm^2 field (appearing relatively bright) from the rest of the mask (appearing relatively dark). The different color of the field is caused by Fabry-Perot interference and indicates that the 1 µm thick AlGaAs spacer below the cap has been removed in the entire area before the second epitaxial growth. Nomarsky micrographs of the same area do not show a curvature of the cap. Thus, the 1 µm spacing between the cap and the substrate is almost constant, although the 100 nm thick cap is freestanding in the 35x35 μm^2 field.

Figure 4.4 shows the sample after SMMBE of 100 nm GaAs through the shadow mask (and on top of the cap). On the cap [see image (a)], the surface is mirror-like and there are no indications of defects, e.g., pits in the GaAs layer, which would result from an improper preparation of the sample before the second epitaxial growth. Image (b) shows the sample after ultra-sound agitation for 20 sec, which has removed the freestanding cap. In the 35x35 μm^2 field, the SMMBE grown structures on the substrate are easily accessible. Image (c) shows a Nomarsky image of the same area, which reveals more details of the nanoscale structures which were deposited through the shadow mask. There are no indications for defects, which demonstrates that the preparation of the sample for the second epitaxial growth was successful. After the ultra-sound agitation, one can find only two particles of the mechanically destroyed cap, which stick to the substrate.

4.2. Growth control

SMMBE through stationary shadow masks is controlled by (1) the geometry of the mask and (2) the angle of incidence of the molecular beams on the sample, which is the only *in situ* adjustable parameter. Henceforth, it is assumed that the beam directions can be controlled with precision and independently. However, this is not trivial in a conventional growth chamber where the beam directions are controlled by adjusting the position of the shadow mask sample relative to the stationary beam sources. The following sections discuss how the chamber geometry limits the control of the beam directions and what measures can be taken to overcome these limitations.

4.2.1 Control of the incidence angles

In a conventional MBE chamber the only *in situ* adjustable parameter, which enables a control of the beam directions is the sample position relative to the stationary sources. In the RIBER 32 MBE system, the sample position can be adjusted by pivoting and rotating the substrate manipulator (see Fig. 2.1 and Fig. 4.8). Thus, the position is determined by two coordinates, the tilt angle ϕ and the rotation angle θ of the sample manipulator. While the tilt angle ϕ defines the angle of incidence (ψ) of a beam with respect to the surface normal $\boldsymbol{n}_s$, the rotation angle θ determines the in-plane direction (angle ω) of the beam [see Fig. 4.5(a)]. It is important that the incidence directions of the molecular beams are uniquely determined by the sample position (ϕ,θ). Thus, *it is not possible to control the directions of two (or more) beams independently*. This limitation of conventional growth chambers is crucial for SMMBE, especially, when compound materials are grown for which one has to control the incidence directions of at least two molecular beams.

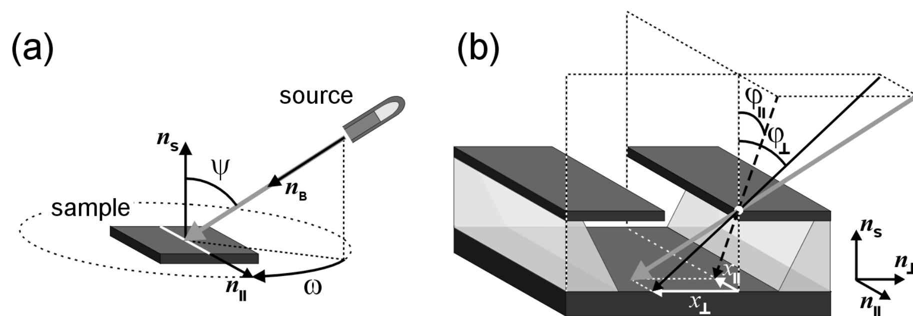

FIG. 4.5 – *Schematic illustration of incidence angles of a molecular beam. The beam direction is indicated by the gray arrow. (a) Incidence angle ψ with respect to the normal* **n** *of the sample. (b) Incidence angles ($\varphi_{\perp}$; $\varphi_{||}$) of the beam in the incidence planes perpendicular and parallel to the aperture stripe of an epitaxial shadow mask.*

I. Stripe aperture A method to overcome this limitation is to reduce the dimensionality of the shadow mask. Figure 4.5(b) shows the sketch of a shadow mask with a 1D stripe-shaped aperture. The black arrow indicates the incidence direction of a molecular beam, which can be described by the incidence angles ($\varphi_{\perp}$,$\varphi_{||}$) of the beam in the incidence planes perpendicular and parallel to the stripe direction.

The offset of the incidence region is, hence given by

$$x_{\perp} = h_S \cdot \tan\varphi_{\perp}, \quad \text{and} \quad x_{\parallel} = h_S \cdot \tan\varphi_{\parallel},$$

where the offset $x_{\parallel}$ (parallel to the stripe) can usually be ignored.[A] The incidence of a beam is thus defined by a single coordinate ($\varphi_{\perp}$) and, consequently *the directions of two molecular beams can be controlled independently* by adjusting the two sample position coordinates (ϕ,θ). However, this is still far from the ideal assumption that the beam directions can be controlled independently.

II. Arrangement of the sources For SMMBE of n-type, p-type, or mixed crystals of compound semiconductors, three, four, or even more molecular beams have to be used. Since it is not possible to control more than two beam directions independently, it is crucial that the alignment of the sample enables certain configurations where the beams impinge in a way such that it is suited for certain growth geometries. Such configurations are defined by the arrangement of the sources in the growth chamber and the geometry of the growth chamber itself. In a conventional growth chamber the arrangement of the sources can usually not be changed during a growth period (several months).

The arrangement of the sources depends on the design of the growth chamber. Two arrangements are commonly used. In one design, the sources are arranged on a circle, e.g., the MnGaAs chamber in Würzburg (see Fig. 2.2). The disadvantage of this arrangement is that more than two molecular beams never have the same $\varphi_{\perp}$ ($x_{\perp}$), which makes it relatively difficult to grow structures with more than two components. In the second design, the sources are arranged on a grid (see "GaAs" and "ZnSe" chambers in Fig. 2.2). For example, the RIBER 32 chamber consists of two horizontal rows where four effusion cells are arranged on each row (see Fig. 4.8). When the stripe shaped aperture of a shadow mask is aligned horizontal in the chamber, the beams originating from the "*parallel*" aligned sources (on a single row) impinge parallel to the aperture stripe of the mask. Thus, $\varphi_{\perp}$ is equal for all parallel aligned sources (while $\varphi_{\parallel} \in \{\pm 11, \pm 33°\}$ in this configuration), and hence up to four beams can impinge with the same lateral offset $x_{\perp}$. Thus, the grid arrangement is favorable for the growth of mixed crystals with up to four constituents and/or optional doping (when a mask with strip-shaped aperture is used).

III. Arrangement of the materials In addition to the arrangement of the sources, the distribution of the source materials over the effusion cells also determines the structures that can be grown. Fig. 2.2 shows the distribution of the source materials in the "GaAs" and the "ZnSe" growth chambers of the UHV system in Würzburg, which were used for the experiments of this work. III-V heterostructures have been fabricated in the "GaAs" chamber, while the "ZnSe" chamber has been used for SMMBE of II-VI heterostructures.

In the II-VI chamber, Cd, Mg, Zn (group II), S and Se (group VI) sources are arranged on the same row. This enables the growth of mixed II-VI materials with a wide range of compositions. In order to integrate all the five materials in the same row, compound ZnS was used a the source of both Zn and S. An additional elemental Zn source was placed in the upper row, on the opposite side of the manipulator axis with respect to the Se cell (see Fig. 2.2). This arrangement enabled a flexible control of the incidence

[A] (h_S) is the spacing between the shadow mask edge and the substrate. In the case of an epitaxial shadow mask, the values of (h_S) are different at the two opposite edges of an aperture ($h_S = h$ and $h_S = h + g + g_L$, where (g_L) is the thickness of material deposited on the mask-cap).

angles ($\varphi_{\perp}$) of Zn and Se beams for the growth of ZnSe. The beam directions could be adjusted independently in a wide parameter range by adjusting the sample position [see Fig. 4.9(c,d)]. Additional sources in this chamber enabled n-type doping (with Al or $ZnCl_2$), p-type doping (with a radio-frequency nitrogen-plasma source), and Mn-substitution for the fabrication of diluted magnetic semiconductors (DMS).

In the III-V chamber, Al, Ga, (group III), As and Sb (group V) sources are arranged on the same row. This enabled the SMMBE of mixed III-V materials with a wide range of compositions. On the other hand, In (group III) is not positioned in the same row, hence SMMBE of InGaAs alloy proved to be relatively difficult. Additional sources in this chamber enabled n-type doping (with Si) and p-type doping (with Be).

4.2.2 *Limitations of the beam control*

In the growth chamber the beam direction is given by the positions of the source and the sample, which are usually idealized as points. However, the aperture of an effusion cell, as well as the shadow mask sample, has finite dimensions which limits the angular accuracy of the beam directions in SMMBE. In addition, one has to consider mechanical limitations due to a conventional growth chamber which has not been optimized for the specific requirements of SMMBE.

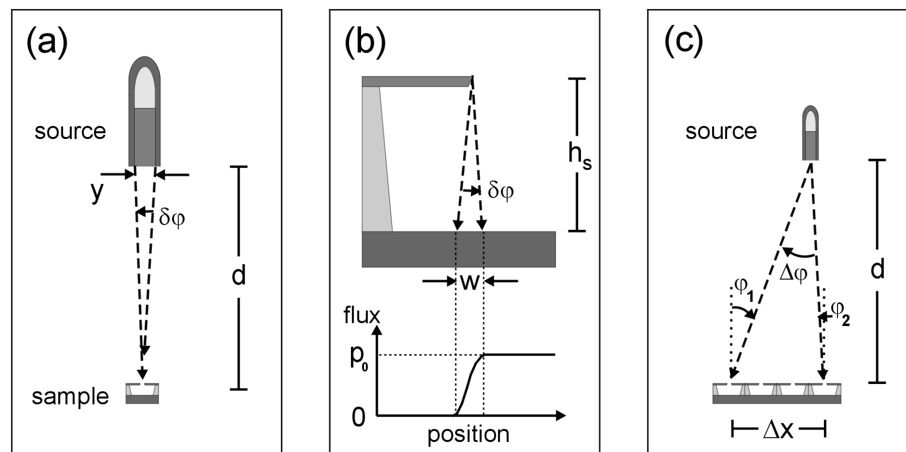

FIG. 4.6 – *Limitations of the angular accuracy of the beam directions. (a) The finite width y of the orifice of an effusion cell causes a dispersion $\delta\varphi$ of the beam directions. (b) The dispersion $\delta\varphi$ causes partial shadow effects below the mask-edge. (c) The incidence angle φ depends on the position on a sample of finite size Δx.*

I. Partial shadow effects The finite diameter (y) of the aperture of an effusion cell causes a dispersion $\delta\varphi \approx \arctan(y / d)$ of the beam directions, where, d, is the distance between the sample and the source [see Fig. 4.6(a)]. Below the shadow mask, the dispersion of the molecular beam causes partial shadow effects, i.e., the limits of the incidence region are not abrupt, but the fluxes increase gradually in a partial shadow region of width $w \approx s \cdot \tan \delta\varphi \approx sy / d$, as is illustrated in Fig. 4.6(b). Based on the assumptions that the aperture of the beam source is circular and that the outgoing flux from this extended source area is homogeneous, the beam flux as a function of the lateral position can be easily calculated. Figure 4.7(b) shows the flux distributions below stripe-shaped apertures of different widths W_A. As can be seen, the flux in the center of the incidence region becomes smaller when the aperture width W_A is reduced below w. In addition, the total width of the flux incidence region on the substrate is equal to W_A+w and cannot be

reduced below w by reducing the aperture width W_A. Obviously, the partial shadow limits the spatial resolution of SMMBE and thus has to be minimized.

This can be done by (1) reducing the spacing s between the shadow mask edge and the substrate, or (2) increasing the distance d between the sample and the source, or (3) reducing the diameter y of the aperture of the source. Since, s limits not only the width of the partial shadow ($w \propto s$), but also the spatial range in which one can adjust the lateral position of the incidence regions ($x_\perp \propto s$), use of shadow masks with s < 1 μm for SMMBE is often not reasonable. Also, reduction of w by increasing the distance d between the sample and the source is restricted by the finite dimensions of a conventional growth chamber. Thus, the best approach to minimize partial shadow effects is by reducing the diameter y of the orifice of the effusion cells.

In the RIBER 32 growth chambers, d ≥ 123 mm, and the diameter of the flux sources (pBN125 crucibles) y = 22 mm. Hence, $\delta\varphi \leq 10°$ and the width of the partial shadow region is $w \approx 180nm$ when a shadow mask with s = 1 μm is used. In order to reduce partial shadowing of the beam, the growth conditions in the “ZnSe” chamber were slightly modified: The aperture of the effusion cells was limited with pyrolytic boron nitride disks, with 2 mm holes in the center [see Fig. 4.7(a)]. The incorporation of such pinholes reduces the width of partial shadows to $w \approx 16nm$ ($\delta\varphi < 1°$) when a shadow mask with s = 1 μm was used.

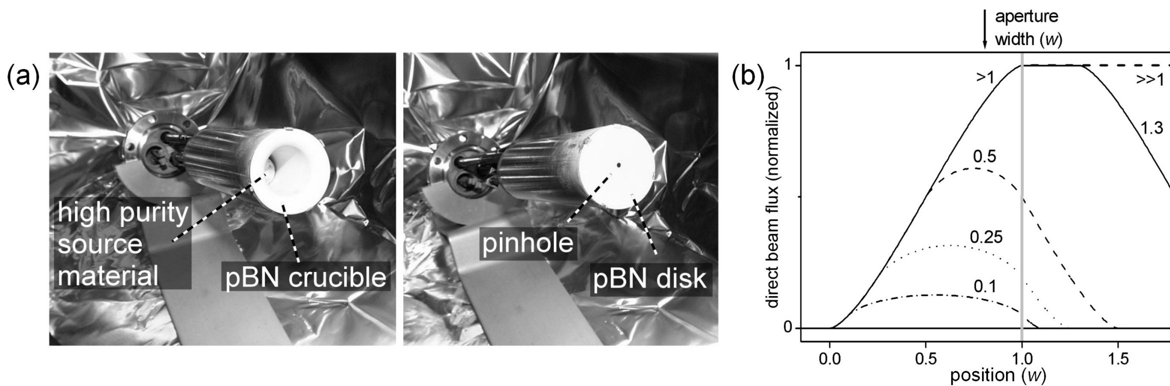

FIG. 4.7 – *(a) Photographs of solid source effusion cells. (left image) Standard configuration with wide orifice. (right image) A pyrolytic boron nitride disk, with 2 mm hole in the center, limits the aperture of the cell. (b) Direct beam flux versus the lateral position (in units of the partial shadow width w) below a stripe-shaped aperture calculated for different aperture widths, 0.1×w, 0.25×w, 0.5×w, 1.3×w, and ∞w (single shadow edge).*

II. Effect of sample dimensions Also the finite width of a shadow mask sample affects the control of the incidence angles. As is sketched in Fig. 4.6(c), the incidence angle φ depends on the position x on the sample. For example in the RIBER 32 geometry, the variation of the incidence angle $\Delta\varphi \approx \arctan(\Delta x / d)$ on a sample with Δx = 20 nm can be as large as $\Delta\varphi \approx 10°$. The variation would be less in a large growth chamber with large d. However conventional growth chambers are designed for other requirements than that of SMMBE, and hence d is relatively small. Without changing d, a precise control of the incidence angles implies that only small samples be used, which can be placed with precision of ±1 mm in the center of the molybdenum sample holder. Thus, the error due to the spatial variation of the incidence angles can be reduced below 1°.

III. Mechanical imprecision For the experiments of this study, $\delta\varphi$ and $\Delta\varphi$ have been reduced to ~1°. Smaller values are not reasonable because of the mechanical imprecision of the growth chamber. The reason for this is that the mechanical parts of an MBE system have to be durable and non-contaminating, i.e., lubricant free. In order to control abrasion of the mechanic parts, hard and soft materials have to be skillfully combined. Such an oil-free mechanical system has often a non-zero clearance, causing an inaccuracy of the angular positions. In standard MBE, this inaccuracy is not a limitation and in conventional MBE systems, such as the RIBER 32 apparatus, the mechanical reproducibility of the angular positions ($\phi;\theta$) is limited to about ± 1°.

4.2.3 Calibration of the incidence angles

I. Calibration of the sample position Prior to the initiation of the growth experiments, the angular scale of the manipulator tilt angle ϕ was calibrated visually. The vertical position of the manipulator is taken as the zero-angle, i.e., $\phi = 0$ (see Fig. 4.8).

Contrary to the tilt angle ϕ, the rotation angle θ had to be calibrated for each sample. In principle, this can be done visually. However, the small window on the backside of the RIBER 32 MBE allows only a very limited visual access: The sample holder (lower edge) is seen only when the tilt angle ϕ is smaller than about 40°. Hence visual calibration was not possible at the standard growth position $\phi = 60°$ of the sample holder. In this position, RHEED can be used to align a sample parallel to the electron beam, which is accurate to within ~1°. The direction of the electron beam itself can be assumed to be constant when the position of the direct beam on the RHEED screen is reproduced. In the RIBER 32 geometry, the alignment of a shadow mask with stripe aperture parallel to the electron beam ($\theta = 0°$) implies that the beams from the horizontally arranged sources impinge parallel to each other, i.e., at the same incidence angle $\varphi_{\perp}$. It is suitable to set this as the zero-angle $\theta = 0°$ and define that θ increases when the sample is rotated clockwise relative to this position.

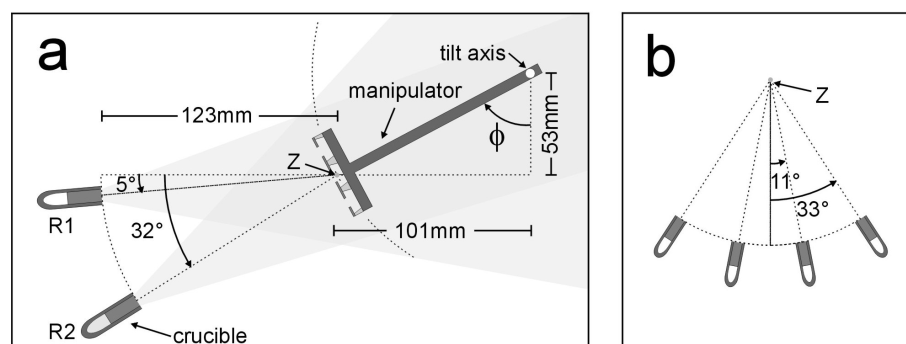

FIG. 4.8 – *Schematic illustration of the geometry of the RIBER 32 growth chamber. (a) Side-view, with the substrate manipulator in the standard growth position ($\phi = 60°$). The sources are arranged in two angles below the horizontal plane. (b) Top-view: The horizontal separation of the sources is 22°.*

II. Calibration of the incidence angles Figure 4.8 shows a schematic illustration of the geometry of the RIBER 32 growth chamber after the manufacturers data. This can be used to calculate the incidence angles as a function of the substrate positions as is shown in Fig. 4.9. However, in order to control the absolute incidence angles with

precision of ~1°, the incidence angles have to be calibrated (at the beginning of a growth period). This can be done by deposition of compound or elemental materials through the shadow mask samples. The incidence angles are subsequently obtained from cross-sectional SEM images.

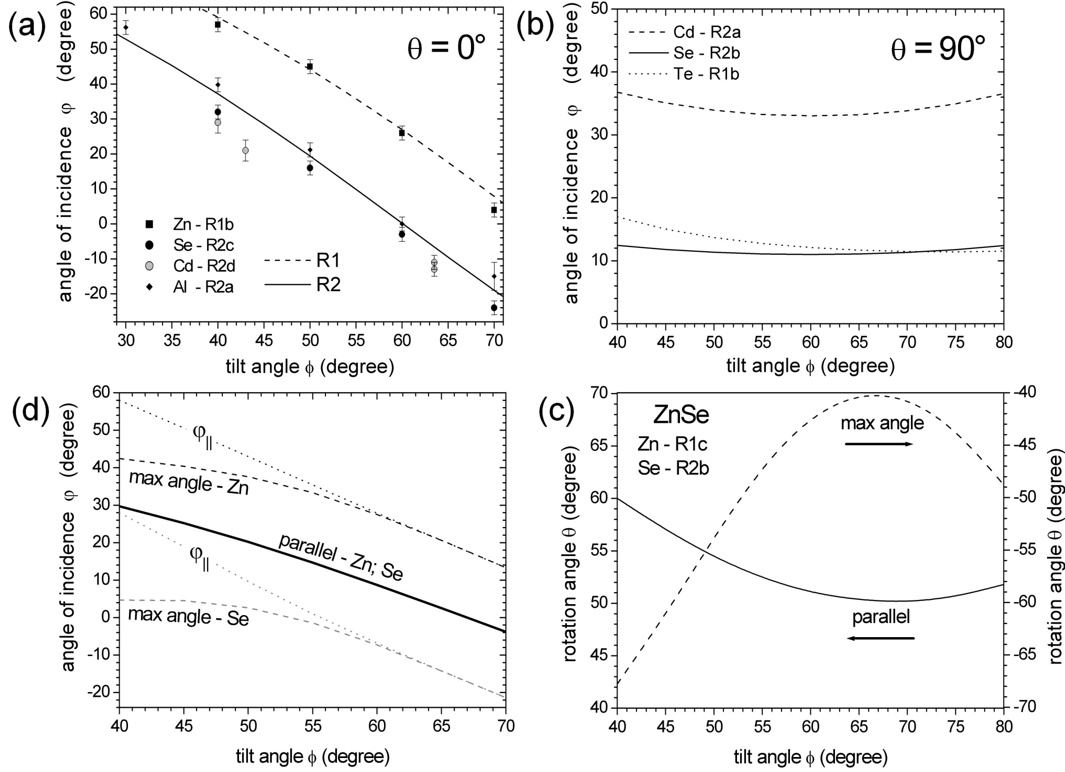

FIG. 4.9 – *Angle of incidence as a function of manipulator tilt ϕ. (a) θ = 0°. (b) θ = 90°. (c) "parallel" ($\varphi_{\perp,Zn} = \varphi_{\perp,Se}$) and "max angle" (max $|\varphi_{\perp,Zn} - \varphi_{\perp,Se}|$) positions for the growth of ZnSe. (d) Angle of incidence for the respective alignments as a function of manipulator tilt ϕ.*

Figure 4.9 presents calculated incidence angles and experimental data-points obtained from calibration experiments in the "GaAs" and the "ZnSe" growth chamber. Fig. 4.9(a) shows the dependence of the incidence angle $\varphi_{\perp}$ on the tilt angle (ϕ), when the aperture-stripe is aligned horizontally (θ = 0°). R1 (dashed line) and R2 (solid line) correspond to effusion cells in the upper and the lower row, respectively. Fig. 4.9(b) presents the incidence angle $\varphi_{\perp}$ versus the tilt angle ϕ at a rotation angle of θ = 90°. This is equivalent to the incidence angle $\varphi_{\parallel}$ (in the incidence plane parallel to the stripe direction) as a function of the tilt angle ϕ, when the aperture-stripe is aligned horizontally (θ = 0°). The incidence angles, whose values correspond to the horizontal position of the sources, are nearly constant when pivoting the sample manipulator [see Fig. 4.9(b)].

When compound material such as ZnSe is grown with two sources (Zn, Se) , both incidence angles $\varphi_{\perp,Zn}$, $\varphi_{\perp,Se}$ are important. The solid curve in Fig. 4.9(c) shows the sample position (ϕ,θ) at which the shadow mask is aligned "*parallel*" to the Zn and Se source, i.e., $\varphi_{\perp} = \varphi_{\perp,Zn} = \varphi_{\perp,Se}$. Fig. 4.9(d) shows the corresponding incidence angles $\varphi_{\perp}$ (solid curve), and $\varphi_{\parallel,Zn}$, $\varphi_{\parallel,Se}$ (dotted curves) as function of the tilt angle for the parallel

aligned mask. The difference between the incidence angles $|\varphi_{\parallel,Zn} - \varphi_{\parallel,Se}|$ in the incidence plane parallel to the stripe direction is near the maximum difference between the incidence angles $|\varphi_{\perp,Zn} - \varphi_{\perp,Se}|$ (in the incidence plane perpendicular to the stripe direction) which is taken in the *"max angle"* alignment of the sample. Fig. 4.9(d) shows the corresponding sample positions (ϕ,θ) and Fig. 4.9(c) the incidence angles $\varphi_{\perp,Zn}$, $\varphi_{\perp,Se}$ as function of (ϕ).

4.2.4 Variation of the fluxes

Usually MBE is done at a standard growth position (ϕ = 60°) for which the fluxes from the sources are calibrated. In contrast, in SMMBE the growth positions have to be adjusted in order to vary the beam directions. Pivoting of the sample manipulator changes the axial position and the orientation of the sample relative to the source. The former affects the local beam pressure (P_S), which is distributed with a specific angular distribution relative to the source. In addition, the orientation of the surface normal (**n**) relative to the beam direction (**n₀**) affects the effective flux (p_0) impinging on the sample surface according to

$$p_0 = P_S\,|\,\mathbf{n}\cdot\mathbf{n}_0\,|,$$

where the scalar product of the unit vectors corresponds to the cosine of the angle of incidence (ψ) of a beam. The data-points in Fig. 4.10(a) show the effect of the tilt angle (ϕ) variation on the growth rate of AlGaAs. Because Al, Ga, and As sources are arranged on R1, the incidence angle is minimum and hence the effective fluxes maximum for these materials at the standard growth position (ϕ = 60°). For sources positioned on R2, the effective fluxes are however maximum at (ϕ = 76°). Hence, the flux ratio between R1 and R2 sources changes with the tilt angle. This is important because it does not only change the growth rates [e.g. ZnSe growth rates in Fig. 4.10(b)], but it may also affect the quality of the epitaxially grown crystals, or change the composition of mixed crystals. A disadvantage of the RIBER 32 geometry is that usage of RHEED for the calibration of the fluxes is limited to the range ϕ = [50° , 65°].

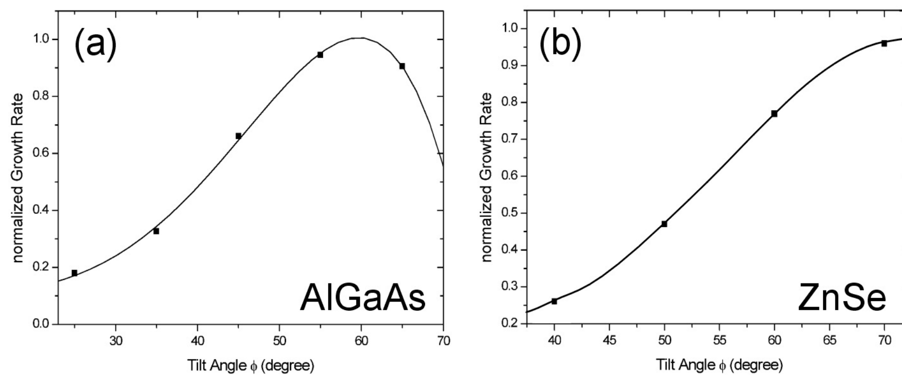

FIG. 4.10 – *Normalized growth rates as a function of the manipulator tilt. (a) AlGaAs (b) ZnSe*

Summary of Chapter 4

A number of novel technical improvements of shadow mask assisted molecular beam epitaxy (SMMBE) have been made. For example, the width of partial shadows has been reduced by a factor of 10 by narrowing the apertures of the effusion cells of the growth chamber, thus, enabling lateral growth control with nanoscale precision (~20 nm). In addition, electron-beam lithography and dry etching processes have improved the precision of the geometry of stationary shadow masks fabricated from epitaxial layers. Nanoscale apertures of the masks have enabled the direct definition of nanoscale growth areas (incidence regions).

Moreover, a new type of epitaxial shadow mask, the freestanding shadow mask, has been developed, which has not one but a number of apertures per mask-cavity. This has crucially enhanced the versatility of SMMBE: By adjusting the angle of the incident molecular beams with respect to such a mask one can grow structures of different shape and size, and at different locations. This method is equivalent to employing different mechanical masks, but is much more accurate since the precision of mechanical alignment is limited.

Chapter 5

Theory of SMMBE Growth

This chapter presents a consistent model for growth dynamics in molecular beam epitaxy of compound materials through shadow masks. The redistribution of molecular fluxes under shadow masks plays a crucial role in controlling growth rates on selected areas. Based on the model, it is shown that reactions between the constituent species determine the flux distribution within the mask cavity, and that this in tandem with the growth conditions, affects the deposition of compound material. In addition, the effects of surface diffusion and the interaction of the diffusing species with the molecular flux of the other constituent are discussed.

5.1 Previous studies

There are a few reports on the various aspects of the growth compound semiconductors through shadow masks. Examples of such effects are (1) variations of the growth rate, (2) the self-formation of low-index facets, and (3) partial shadow effects.

Tomita *et al.* [Tomita95] investigated the shadow mask assisted MBE of GaAs. Self-formation of low-index facets takes place at the edge of the grown GaAs structures, which is limited by the incidence of Ga on the substrate [x>0 in Fig. 5.1(a)]. Diffusion of Ga adatoms out of the incidence region is caused by the lateral gradient of the surface concentration of adsorbed Ga adatoms and the self-formation of low-index facets can be understood (and modelled) by the fact that the diffusion constant of adatoms depends on the surface orientation.

Nishikawa *et al.* [Nishikawa96] investigated shadow-masked MBE of ZnSe with compound source and observed that ZnSe grows also on the undercut side of the mask [see Fig. 5.1(b)]. This was attributed to surface diffusion and a diffusion length of 0.5 μm was extracted from the experiments. Schumacher *et al.* [Schumacher00] has investigated MBE growth of ZnSe with non-parallel incidence of Zn and Se beams, and observed the

formation of a shoulder structure in the incidence region of Se. The ZnSe shoulder (I) can be seen on the left-hand side of the main ZnSe deposit (II) in Fig. 3.8(b). This was explained by the diffusion of Zn into the region where only Se (no Zn) impinges on the substrate. Surface diffusion was also cited by Luo *et al.* [Luo98] as the reason for the finite edge-width of the CdTe deposits shown in Fig. 3.7(a).

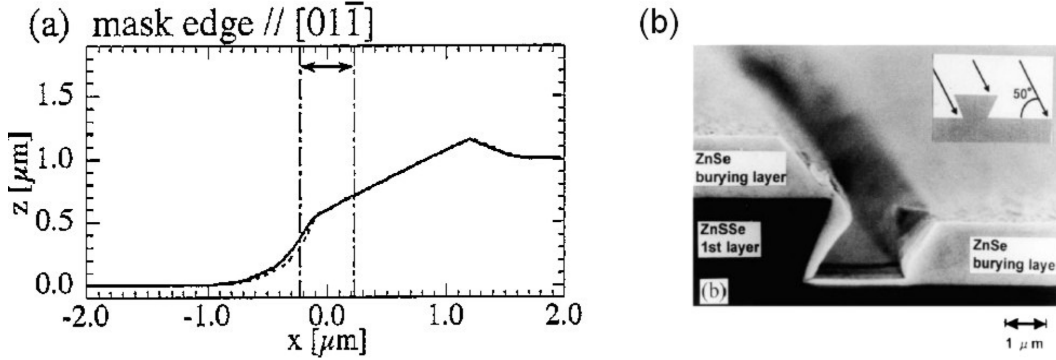

FIG. 5.1 – *(a) Growth of GaAs through a shadow mask (after [Tomita95]). The curves represent the calculated cross-section of a GaAs deposit. Surface diffusion causes facet formation at the edge of the incidence region of Ga (x>0) on the substrate. (b) Growth of ZnSe through a shadow mask (after [Nishikawa96]). The micrograph shows that ZnSe (bright) deposits also on the undercut side of the ZnSSe mesa (dark). The inset shows the incidence direction of Zn and Se.*

In this work, it is proposed that contrary to the previous results of II-VI MBE, shadow mask assisted growth of ZnSe can be understood to occur without surface diffusion of adatoms. The experimental observations can be explained by the unique growth regime within the cavity of the mask, where molecules can desorbed and be adsorbed many times without leaving the cavity. By modelling this repetitive redistribution process, one calculates the effective flux distribution in the steady state. The results accurately describe the effects, observed in the experiments with ZnSe growth, presented in Sect. 6.1. Results of additional experiments, demonstrate that the model is also valid for of other II-VI materials, e.g., CdSe.

In this work, the effects of surface diffusion in shadow mask assisted growth of compound materials are also modelled. In principle, the diffusion model used by Tomita *et al.* [Tomita95] is not specific for compound materials, because it does not consider the effects of the group-V flux. However, Hata *et al.* [Hata91] has demonstrated that the surface diffusion length of group-III adatoms strongly depends on the anion flux (see Sect. 3.3.1). This effect is included in the model and the important consequences on the SAE of III-V compounds are discussed.

5.2 SMMBE growth model

Below, the model is described starting from the growth of single-component and two-component materials, where it is assumed that the fluxes of the constituents are independent, i.e., the species do not react with each other. Subsequently, the model is expanded to compound materials where the interaction between the constituent species plays a crucial role. Because the constituents react with each other on the surface, their flux distributions depend on each other. In addition to the interaction between the fluxes of the constituents, the interaction between the redistribute of the fluxes via multiple desorption on the one hand and surface diffusion on the other hand are include in the model.

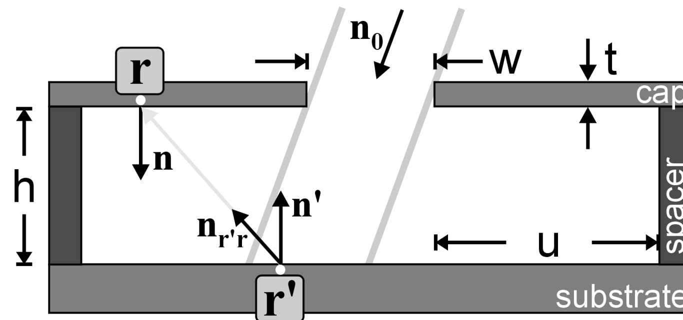

FIG. 5.2 – *Sketch of an epitaxial shadow mask. The dimensions and vectors were used in modeling the growth regime within the cavity of the mask.*

5.2.1 Single component material

Before analyzing the SAE growth of compound semiconductors, a simplified case is discussed wherein only the flux of a single species, p_0, is considered. After passing through an aperture of the mask, the impinging particles, as shown in Fig. 5.2, are adsorbed on a restricted area I_M on the substrate, which is the projection of the aperture cross section. (The lateral position of this incidence region is determined by the angle of incidence of the beam.) Adsorbed species have a finite lifetime τ on the substrate surface after which the material either gets incorporated into the growing crystal or desorbs and goes elsewhere. The probability of incorporation of the constituent elements is given by the sticking coefficient s, which is a constant parameter, in absence of any interaction between different species and local variations of temperature.

Non-sticking molecules (1-s) are subsequently reemitted from the surface with an angular distribution, which is given by the cosine law of effusion. This redistribution process contributes to secondary fluxes F_i (of the order $i > 1$) because the re-desorbed molecules, which do not leave the cavity through an aperture, impinge on other surface of the cavity. This process is iterative: The redistribution of these non-sticking, n^{th}-order molecules $(1\text{-}s)F_i$ gives an $(i+1)^{\text{th}}$-order flux F_{i+1}, where F_0 is defined as the direct flux, i.e., the primary flux from the source. F_0 is equivalent to p_0 for positions, $\mathbf{r}$, within the incidence region I_M and it is zero outside.

Thus, the total flux f is given by

$$f(\mathbf{r},t)=\sum_{i=0}^{\infty}F_i(\mathbf{r},t), \tag{5.1}$$

where the time-dependence (t) corresponds to the finite surface lifetime τ of adsorbed molecules, i.e., the iteration of the redistribution process is equivalent with time. Accordingly, the redistribution of non-sticking molecules after each collision is given by the implicit equation [A]

$$F_{i+1}(\mathbf{r},t+\tau)=\int_{A_M}(1-s(\mathbf{r}',t))F_i(\mathbf{r}',t)Z(\mathbf{r},\mathbf{r}')\frac{(\mathbf{n}_{\mathbf{r}'\mathbf{r}}\cdot\mathbf{n}')(\mathbf{n}_{\mathbf{r}\mathbf{r}'}\cdot\mathbf{n})}{(\mathbf{r}-\mathbf{r}')^2\pi}dA', \tag{5.2}$$

where $\mathbf{n}'$ ($\mathbf{n}$) is the unit normal to the surface element at $\mathbf{r}'$ ($\mathbf{r}$) and $\mathbf{n}_{\mathbf{r}'\mathbf{r}}$ ($=-\mathbf{n}_{\mathbf{r}\mathbf{r}'}$) is a unit vector pointing to $\mathbf{r}$ from $\mathbf{r}'$. A_M is the surface area of the mask-cavity and $Z(\mathbf{r},\mathbf{r}')$ is equal to 1 as long as there is line of sight between the surface elements at $\mathbf{r}'$ to $\mathbf{r}$, or if $(\hat{\mathbf{n}}_{r'r}\cdot\hat{\mathbf{n}}')$ is negative. In the latter case, Z is zero. The scalar products of the unit vectors in Eq. (5.2) are the cosines of the effusion and incidence angles.

When the primary flux from the source $F_0(\mathbf{r})$ is time-independent, the total flux $f(\mathbf{r},t)$ approaches a steady state distribution, $f_\infty(\mathbf{r})$. In the case of non-interacting species, where the sticking coefficient s is constant, f_∞ is easily calculated using Eq. (5.1) and (5.2).

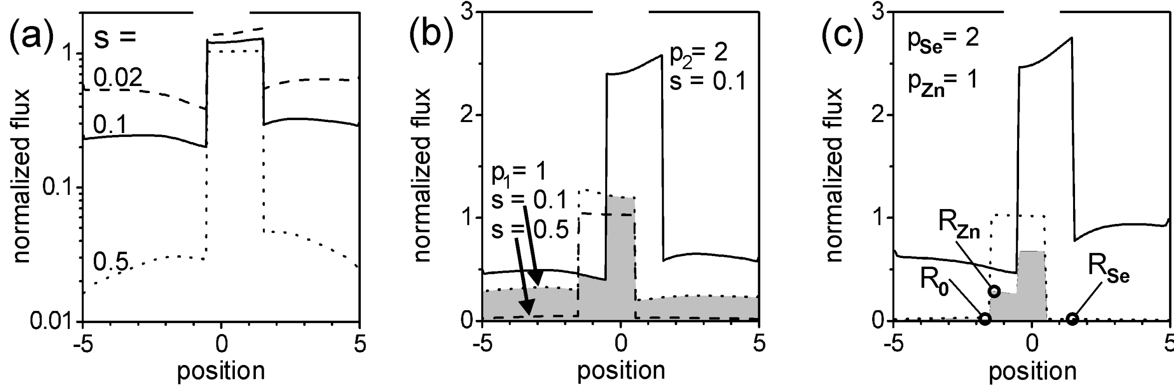

FIG. 5.3 – *Modeling of the total flux as a function of the lateral position below a shadow mask. (a) Total flux of a single molecule beam (p=1) with constant sticking coefficient s = 0.5, 0.1, and 0.02. (b) Total flux of two molecule beams (dotted line: $p_A = 1$; $s_A = 0.1$; solid line: $p_B = 2$, $s_B = 0.1$) without considering the interaction of the fluxes. The gray shaded area is an estimate of the growth rates when growth is limited by the smaller flux. The dashed line represents a higher sticking coefficient $s_A = 0.5$. (c) Total flux of interacting Zn flux (dotted line: $p_{Zn} = 1$) and Se flux (solid line: $p_{Se} = 2$). The gray shaded area is the modeled ZnSe growth rate as a function of the lateral position below the shadow mask. From the growth profile, the normalized growth rates R_{Se} (Se-shoulder), R_{Zn} (Zn-shoulder), and R_0 (without direct beam) were extracted for the data presented in Fig. 5.4.*

[A] See Sect. A.1 for the derivation of Eq. 5.2. Equation (5.2) can also be found in a similar form in Ref. [Drotar00]. Drotar *et al.* have modeled roughening of the growth interface, which takes place during sputtering deposition and etching processes as a result of shadowing and desorption of molecules. In this case, the surface was almost planar and consequently only F_0 and F_1 had to be considered. In contrast, for the shadow effects discussed here, higher order fluxes up to orders i exceeding 100 may contribute significantly to the total flux in the mask cavity and can therefore not be omitted.

Fig. 5.3(a) shows a typical result. f_∞ has been calculated for an ideal mask with dimensions (w,h,g,u) = (2,2,0,4) and considering a single direct beam (flux p_0 = 1) impinging through the aperture of the mask at an angle of φ = -14.0° [see Fig. 5.2]. The incidence region of the beam is, therefore shifted (by Δx = +0.5) relative to the aperture of the mask. (No absolute dimensions are required because of the angular redistribution process (scalability of the mask).) The three curves in Fig. 5.3(a) show the steady state flux distributions, $f_\infty(\mathbf{r})$, for molecules with sticking coefficients, s = 0.02, 0.1, and 0.5. The horizontal axis is the lateral position, x, on the substrate surface. As can be seen, f_∞ is non-zero outside the incidence region of the direct beam. This is due to the repetitive adsorption and reemission process, where higher order impingements ($i \geq 1$) contribute to the *secondary flux* $F_\infty = (f_\infty - F_0)$, within the mask-cavity. This contribution is large for a small sticking coefficient, i.e., when the probability of the molecules being desorbed multiple times is high. However, F_∞ is limited by (1) the impingement rate of molecules, i.e., the beam pressure p_0, and (2) the escape rate of molecules through the aperture of the mask. The latter causes a disruption of the secondary fluxes near the aperture [see Fig. 5.3(a)]. On the other hand, $F_\infty \approx p_0$ [$f_\infty \approx 2\, p_0$] when the sticking coefficient is negligibly small ($s \approx 0$) and only few molecules escape through the aperture, i.e., for a mask with small w and large h or near the end walls of the mask cavity.

5.2.2 Two component material

Next, the steady state flux distribution of two fluxes (p_A=1.0 and p_B=2.0) with the beams impinging at different angles (φ_A=+14.0° and φ_B=-14.0°) is calculated. Below, the two species are named *minority* and *majority* with respect to the different impingement rates p_A and p_B, respectively. Again, it is assumed that the molecules do not interact. The dotted and solid lines in Fig. 5.3(b) show the total flux $f_{A,B}$, for a constant sticking coefficient $s_{A,B}$ = 0.1. In this case, the flux of the majority species is dominant ($f_B > f_A$) within the cavity of the mask, except in the incidence region of the minority species ($f_B < f_A$), i.e., in the part where the direct beam of the majority species does not impinge. This local inversion of the flux ratio is important when compound semiconductors are grown because the growth rate is limited by the smaller of the two component fluxes.

This constraint can be used as a first order approximation of the growth rate, as is illustrated by the shaded area in Fig. 5.3(b). In the steady state, the growth rate is maximum in the overlap region. Outside this area, the growth rate is non-zero because of the coexistence of the secondary fluxes of both the species. The deposition rate, in general, is limited by the secondary flux of the minority species. In the domain of the minority species, however, due to reversal of the flux ratio $f_B : f_A$, it is limited by the secondary flux of the majority species. This results in the formation of a shoulder structure in the domain of the minority flux.

Schumacher *et al.*,[Schumacher00] however, has reported a similar structure in the Se-domain, under Se-rich growth conditions. Additionally, they observed a complete suppression of the effect with a [110] orientation of the mask. These apparent contradictions with the model can be explained considering the specific details of the growth experiments (Refer to Sect. 6.1).

5.2.3 Two interacting fluxes

This section introduces the interaction between the species in the model. The assumption of the sticking coefficient being constant does not enable a quantitative prediction of the growth rates. In particular, the estimated growth rate without a direct beam [for $s = 0.1$; see Fig. 5.3(b)] is an order of magnitude larger than that observed in the experiments (see, e.g., Fig. 6.3). A better agreement with the experiment is obtained only if the sticking coefficient of the minority species is assumed large compared to that of the majority species [e.g.: $s_A = 0.5$; see dashed line in Fig. 5.3(b)]. This behavior cannot be attributed to the difference in the material properties of the two species, but rather can be understood by considering the interaction of the fluxes, as explained below.

An interaction between the fluxes, f, implies that the sticking coefficients, s, depend on the fluxes, f, of both species. An example of such an interaction is revealed in Fig. 3.5(b), which shows the variation of s_{Zn} as a function of the Se:Zn flux ratio during ZnSe MBE at a substrate temperature of 300°C (see comments in appendix A.3). Equation 3.2 can be used to uniquely determine the corresponding Se sticking coefficients, s_{Se}. This shows that the interaction between the species is governed by a function $S(f_A,f_B)$.

Within the mask-cavity, the sticking coefficient $s(\boldsymbol{r},t)$ (of an individual species) is a function of both time and position, because it depends on the distribution of the fluxes $f(\boldsymbol{r},t)$ of the interacting species. Thus, Eq. (5.1), (5.2), and (3.2), describe a non-linear problem, which can be solved using a time-dependent ansatz. One finds the equation

$$f(\mathbf{r},t+\tau) = F_0(\mathbf{r}) + \int_{A_M} (1-s(\mathbf{r}',t))f(\mathbf{r}',t)Z(\mathbf{r},\mathbf{r}')\frac{(\mathbf{n}_{r'r}\cdot\mathbf{n}')(\mathbf{n}_{rr'}\cdot\mathbf{n})}{(\mathbf{r}-\mathbf{r}')^2\pi}dA', \qquad (5.3)$$

by applying Eq. (5.2) on Eq. (5.1), interchanging the summation with the integral, and applying Eq. (5.1) within the integral. Eq. (5.3) describes the evolution of the total flux $f(\mathbf{r},t)$, in response of a change of the direct beam flux $F_0(\mathbf{r})$ (e.g. start of the mass-flow). The steady state flux distribution is obtained in the limit $t\to\infty$, i.e., by the iterative application of Eq. (3.2) and (5.3) on the time-dependent flux-distribution $f(\mathbf{r},t)$ [see Sect. A.2 for comments on the mass-conservation]. Without the time-dependency, Eq. (5.3) becomes a continuity equation for the steady state. According to this continuity equation, the secondary flux $F_\infty = f_\infty - F_0$ is maintained in the steady state by the redistribution of the total flux f_∞ (integral term).

5.2.4 Surface diffusion and effective flux

Section 3.3.1 has introduced the basic attributes of surface diffusion in patterned SAE. It has been shown, that the diffusion of surface atoms can be described by a diffusion equation such as Eq. (3.1). It is also known that in patterned SAE of compound materials, the diffusion kinetics of one constituent species (group-III) depends on the flux of the other component (group-V). Hence, Eq. (3.1) describes the planar redistribution of the surface atoms, which is governed by the flux distribution within the mask-cavity [according to Eq. (5.3)]. In turn, the flux distribution depends on the sticking coefficient which is modulated by the planar redistribution of the surface concentration. In order to consider all interactions between the species under a shadow mask, one has to find a solution to a system consisting of four redistribution processes [desorption (Eq. (5.3)] and surface diffusion [Eq. (3.1)] of both constituent elements). This becomes even more complex, when two molecular species of one constituent element obey different surface kinetics, e.g., As_2 and As_4 molecules in III-V MBE [Foxon75]. In this case, one has to consider the

individual molecular species and their interactions, which have been studied only in certain cases (e.g. As_x [Brennan92]; not in the case of Se_x).

However, usually one can neglect certain redistribution processes. For example, as is shown in Sect. 6.1, the growth of II-VI compounds through shadow masks can be explained, without surface diffusion, by the recurring desorption of the fluxes of the constituents and the interaction between the species, i.e., two dependent redistribution processes. In contrast, in III-V MBE the diffusion of group-III adatoms affects the local growth rates and, thus can not be neglected. However, according to Eq. (5.3), secondary group-III fluxes can often be neglected because of the large sticking coefficient of group-III atoms ($s_{III} \approx 1$). On the other hand, since the desorption lifetime of group-V molecules is relatively short ($\tau_{des,V} \approx 0$), one can neglect the surface diffusion of group-V molecules, following Eq. (3.1) [see also Sect. A 1.5].

Thus, III-V MBE through shadow masks is governed by the redistribution of the group-V fluxes [Eq. (5.3)] and the surface migration of group-III adatoms [Eq. (3.1)], i.e., two dependent redistribution processes, when the group-V flux consists of a single molecular species. Analogous to Eq. (3.2), the equation for the conservation of stoichiometry of the compound can be written as

$$S = s_V f_V = N_{a,III} / \tau_{inc,III} \ . \qquad (5.4)$$

Eq. (5.4) connects Eq. (3.1) and Eq. (5.3) so that there exists a unique solution in the steady state.

5.3 Predictions from the model

This section discusses the implications of the interaction between the constituent species of compound materials, in the case of II-VI and III-V MBE through shadow masks. First, the effects of the surface reactions on the flux distribution (example ZnSe MBE) are discussed. Then, it is investigated how the growth conditions, i.e., the flux ratio and the growth geometry, affect the growth. The final subsection discusses the effects from the interaction between surface diffusion of one component and the fluxes distribution of the other component (example GaAs MBE).

For simplicity, the evolution of the growth interface is not modeled and the discussion of MBE of compound materials is restricted to the initial growth geometry. Thus, it is not considered that material deposits may affect the redistribution of secondary fluxes and diffusion currents in the mask-cavity. Consequently, the model does also not consider the evolution of the edges of the deposits, e.g., the self-formation of low-index facets.

5.3.1 Interacting fluxes

Fig. 5.3(c) shows a result of modelling the steady state flux distribution of coupled Zn (p_{Zn} = 1.0) and Se (p_{Se} = 2.0) fluxes in the previous growth geometry [as Fig. 5.3(b)]. The grey shaded curve represents the ZnSe growth rate dependent on the lateral position on the substrate.

The results for the total flux of interacting Zn and Se [see Fig. 5.3(c)] are similar to the dashed and solid lines in Fig. 5.3(b), i.e., non-interacting molecules with sticking coefficients of 0.5 and 0.1 for the minority and majority species, respectively. This "effective sticking coefficient" of the corresponding curves is a result of the interaction between the molecules: The majority species accumulates within the cavity of the mask. The increasing secondary fluxes of the majority species increases the sticking probability of the relative smaller number of minority species molecules. This reduces the total flux of the minority species in the steady state, which in turn means that the sticking coefficient of the majority species is relative low (as a result of the interaction).

Next, a far-etched mask-cavity ($u \gg h$) is considered. Mainly secondary fluxes F_n contribute to the total flux f in regions far underneath the mask. Because of the relatively high sticking coefficient, the secondary flux of the minority species fades within a short distance from the aperture [as in Fig. 5.3(c)]. In turn, this reduces the sticking coefficient of the majority species, which becomes negligible small ($s \approx 0$) far from the aperture. Consequently, the secondary flux F_∞ of the majority species (in the steady state) is constant in the deeply underneath region. In contrast to the non-interacting case (s = const. > 0), it does not fade with the distance from the aperture.

5.3.2 Change of the flux ratio

Next, the influence of a change of the growth conditions is discussed. By varying a single parameter of the standard growth conditions [$(w,h,g,u) = (2,2,0,4)$; $\varphi = \pm 14.0°$; p_{Zn} = 1.00, p_{Se} = 1.26)], one extracts the predicted growth rates in the Se-domain (R_{Se}), the Zn-domain (R_{Zn}) and beneath the Zn-domain (R_0), i.e., without a direct beam [see Fig. 5.3(c)]. Fig. 5.4 shows the extracted curves, which are normalized to the growth rate without a shadow mask. The first plot in Fig. 5.4(a) shows the effect of a variation of the atomic flux ratio ($p_{Se}:p_{Zn}$) with the direct flux of the minority species being fixed at p_{minority}

= 1. From left to right, there is an increase of R_{Zn} [solid line in Fig. 5.4(a)] with increasing Se flux. Without a sufficient Se overpressure [log(p_{Se}:p_{Zn}) < +0.07], the growth rates R_{Zn} and R_0 are about equal because on this side of the aperture of the mask growth is limited by the secondary flux of Se. A Zn shoulder structure ($R_{Zn} > R_0$) is selectively formed when the secondary flux of Se becomes larger than the secondary flux of Zn on both sides of the aperture of the mask [log(p_{Se}:p_{Zn}) > +0.07]. When the Se overpressure is further increased [p_{Se}:$p_{Zn} \gg 1$], the secondary flux of Se finally exceeds the total Zn flux in the incidence region of Zn. ZnSe grows in the entire incidence region of Zn with homogeneous growth rate, i.e., $R_{Zn} \approx 1$. While R_{Zn} increases with the Se flux, the deposition rate R_0 (growth without a direct flux) is decreased [see dashed line in Fig. 5.4(a)]. This is a result of the interaction between Zn

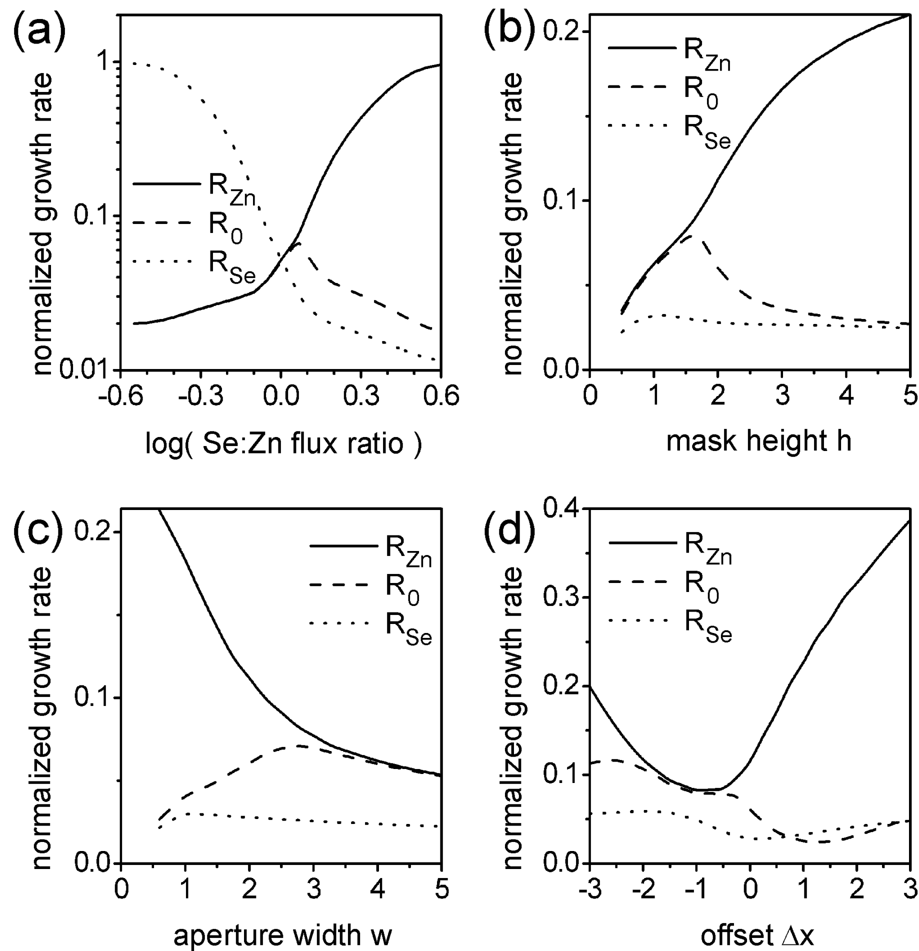

FIG. 5.4 – *Dependency of ZnSe growth rates in the Se-domain (R_{Se}), the Zn-domain (R_{Zn}), and without a direct beam (R_0) as a function of the growth conditions: (a) Change of the Se:Zn flux ratio. (b) Change of the mask height h. (c) Change of the aperture width w. (d) Change of the lateral position of the incidence regions of Zn and Se below the mask.*

and Se, i.e., the suppression of the secondary flux of Zn (minority species) when excess Se (majority species) is accumulated within the cavity of the mask. The symmetry between the curves R_{Se} and R_{Zn} in Fig. 5.4(a) with respect to an inversion of the flux ratio demonstrates that the interaction between the fluxes is a principal effect, i.e., the material properties of Zn and Se are of lesser importance.

5.3.3 Change of the growth geometry

Figures. 5.4(b) and (d) demonstrate the importance of the mask geometry. As can be seen, the accumulation of the majority species is strongly increased by increasing the height h of the shadow mask or by reducing the aperture width w. Both changes of the mask geometry principally reduce the escape of molecules out of the cavity of the mask. This increases the interaction between the fluxes, which is usually diminished by the escape of molecules, i.e., a weak coupling of the fluxes on both sides of the aperture of the mask. In the extreme cases, $w \to 0$ and $h \to \infty$, the probability of the escape of molecules of the minority flux is negligible small. Because of the pairwise extinction of molecules, the secondary flux of the majority species approaches ($p_{majority}$ - $p_{minority}$) in the steady state.

A different way to change the escape of molecules is by shifting the position of the incidence region on the substrate [changes both the solid angle of the aperture and the effusion angle]. Fig. 5.4(c) shows the effect of a synchronic shift Δx of the incidence regions of Zn ($\Delta x_{Zn} = -0.5 + \Delta x$) and Se ($\Delta x_{Se} = +0.5 + \Delta x$) relative to the aperture of the mask. For positive offsets ($\Delta x > 0$), the escape of Se is decreased, i.e., the secondary flux of Se is increased. On the other hand, shifts in the opposite direction ($\Delta x < 0$), reduce the escape of Zn while increasing the escape of the majority species Se. This changes the ratio of the secondary flux in a way that at $\Delta x = -1$ no Zn-shoulder is formed ($R_{Zn} \approx R_0$) in spite of the Se-rich growth conditions [see Fig. 5.4(d)]. This demonstrates that the growth geometry is crucial for the growth regime below the mask. When the incidence regions are shifted deep underneath the mask ($\Delta x \to +\infty$ or $\Delta x \to -\infty$), the escape of both species is minimized. Therefore, the problem is equivalent to $w \to 0$, $h \to \infty$, and the secondary flux of the majority species approaches a constant value ($p_{majority}$ - $p_{minority}$) near the end walls of the mask-cavity in the steady state.

5.3.4 Effects of surface diffusion

This section discusses the influence of surface diffusion on the growth of compound materials through a shadow mask. The redistribution of material under a shadow mask is a complex process. In order to delineate the basic diffusion effects, we, however, assume that only one species (group-V) is redistributed in the mask cavity by desorption, while the other component (group-III) redistributes via surface diffusion. This corresponds to MBE of III-V materials with $\tau_{des,V} \approx 0$ and $s_{III} \approx 1$. In addition, it is assumed that the V:III flux ratio is large. In this case, the group-III flux is relatively low and does not significantly affect the distribution of group-V flux in the cavity. The sticking coefficient of the group-V species is almost zero in almost the entire area of the mask cavity and one can calculate the distribution of group-V flux using Eq. (5.3) and assuming $s_V \equiv 0$ [see for example Figs. 6.8(a) and 7.15(b)]. However, in this section, a simplified flux distribution f_V is used, which is shown in Fig. 5.5(a): The direct beam (flux p_0) impinges in the region $0 < x < w_0$, and the secondary flux is defined to be equal to p_1 for $x < 0$ and p_2, for $x > w_0$, with a steady, linear intersection in the region between $x = 0$ and $x = w_0$. In the case of the diffusing group-III species, mobile surface atoms are generated selectively in the incidence region of the direct beam ($G = p_{III}$) and no group-III adatoms impinge outside the incidence region ($G = 0$). The incorporation diffusion length of group-III adatoms depends on the total group-V flux f_V, according to $l_{inc} = c_1 f_V^{-1}$ (c_1 is a constant). It is suitable to define a characteristic diffusion length $L_0 = l_{inc}(p_0)$, which depends on the direct group-V flux p_0.

In shadow mask experiments the incidence of both group-V and group-III species is limited by the apertures of the mask. Despite this, one can find certain geometries where either group-V or group-III species can be assumed position-independent and constant (e.g., when the incidence regions have different sizes). In the following subsections, these two special cases are discussed first and, subsequently, the case where both species impinge in limited incidence regions.

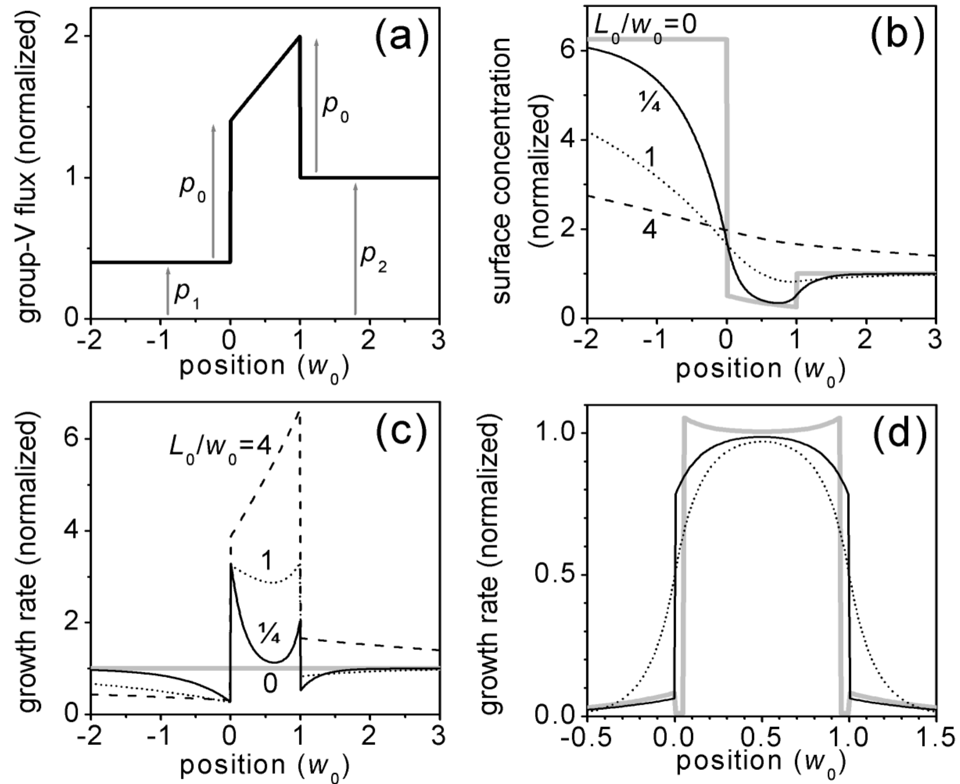

FIG. 5.5 – *Schematic illustrations of surface diffusion of group-III adatoms dependent on the distribution of the group-V flux. (a) Simplified distribution of the group-V flux. The direct beam impinges in the region* $0<x<w_0$. *(b-c) The incidence of group-III species is non-local. (d) The incidence of group-III species is local in the range* $0<x<w_0$. *(b) Surface concentration and (c) growth profiles obtained for characteristic diffusion lengths* $L_0 = 0, 0.25\times w_0, w_0,$ *and* $4\times w_0$. *(c) Growth profiles in the case of local (solid lines) and non-local (dotted line) group-V flux, for* $l_{inc}=0.143\times w_0$ *in the range* $0<x<w_0$, *and* $p_1 = p_2 = 0.4\times p_0$. *The grey line shows the growth rates, when* $0.05\times w_0$ *wide facets with 100 times higher diffusion constant* D_S *terminate the edges of the growth region.*

I. Constant group-III flux

In the first example, it is assumed that the generation of adatoms ($G = f_{III} \equiv p_{III}$) is position-independent and use the distribution of the group-V flux shown in Fig. 5.5(a), with $p_2 = p_0$ and $p_1 = 0.4\, p_0$ [analogous to the data shown in Fig. 6.8(a)]. According to Ref. [Nishinaga96], the incorporation lifetime $\tau_{inc,III} \propto f_V^{-2}$ (see Fig. 2.6) of group-III adatoms is long when the group-V flux is low and short when f_V is high. Using Eq. (3.1), one calculates the surface concentration N_a of group-III adatoms. The grey curve in Fig. 5.5(b) shows the surface concentration N_a, when the diffusion term, $\nabla_S \cdot \boldsymbol{J}_S$, is neglected in Eq. (3.1). As can be seen, N_a is low in the incidence region of As (low τ_{inc}) and is relatively high where the As flux is low (large τ_{inc}). If D_S>0, this surface concentration gradient

results in surface diffusion currents $\boldsymbol{J}_S$, from regions with high N_a (low group-V flux) to regions with low N_a (high group-V flux). The resultant redistribution of N_a is illustrated by the black curves in Fig. 5.5(b). The solid, dotted, and dashed lines correspond to characteristic diffusion lengths $L_0 = 0.25\times w_0$, w_0, and $4\times w_0$, respectively. It is obvious that a deviation of the surface concentration from the grey curve implies a change of the incorporation rate $S = N_a / \tau_{inc}$. Fig 5.5(c) shows the growth rates for $L_0 = 0$, $0.25\times w_0$, w_0, and $4\times w_0$. As can be seen, surface diffusion reduces the growth rate S in regions with low group-V flux, which act as a source for the effective migration of adatoms towards regions with higher group-V flux. Consequently, the growth rate is increased in the incidence region of the direct group-V beam.

However, the migration of the adatoms is limited by the incorporation diffusion length $l_{inc} = \sqrt{D_S \tau_{inc}}$. Hence, the migration induced growth rate coincide with the edges of the step in the group-V flux distribution curve, and [according to Eq. (3.1)] it decreases exponentially, on the scale of the surface diffusion length l_{inc}. Because of this, surface diffusion does not change the growth rate in areas distant from the step edges, i.e., the black curves in Figs. 5.5(b) and 5.5(c) approach the grey curve when $|x| \to \infty$. In the case, where $L_0 \ll w_0$, the migration induced growth rate is also negligible in the middle of the incidence region [see $L_0 = 0.25\times w_0$ (black solid curve) in Fig. 5.5(c)] and it takes a maximum value directly at the step edges of the group-V flux, which is particularly high when the ratio of the group-V fluxes is large, i.e., at $x = 0$.

A different behaviour is expected when the migration length of group-III adatoms is long, i.e., $L_0 \gg w_0$. Increasing the diffusion length L_0, reduces the gradients of the surface concentration N_a [see Fig. 5.5(b)], so that in a limited region (width $\ll L_0$), N_a is approximately constant. In this case, the growth rate [see $L_0 = 4\times w_0$ in Fig. 5.5(c)] is roughly proportional to the square of the group-V flux ($S \propto f_V^{\,2}$).

II. Constant group-V flux

In the second example, the group-V flux is non-local ($f_V \equiv p_0$) and group-III adatoms (flux p_{III}) impinge selectively in the range $0 < x < w_0$. When $l_{inc}(p_0) \ll w_0$, the redistribution of adatoms is negligible and, hence, the growth rate is proportional to the group-III flux ($S \propto f_{III}$).

However, with a finite diffusion length l_{inc}, surface diffusion reduces the gradients of the surface concentration of adatoms at the edge of their incidence region. Because N_a is maximum in the incidence region, the direction of surface diffusion currents at the edge of the group-III incidence region is opposite to that at the edge of the group-V beam. Adatoms effectively migrate out of the incidence region, hence increasing the width of the deposit and decreasing the growth rate at the centre. The dashed curve in Fig. 5.5(d) shows the resulting growth profile for l_{inc} ■ $0.143\times w_0$. In the limit $w_0 \ll l_{inc}$, the growth profile has a gaussian shape and the width is proportional to the diffusion length l_{inc}.

III. Common incidence region

In the third example, it is assumed that the common incidence region of group-III and group-V species is in the range $0 < x < w_0$. The group-V flux distribution is defined by $p_1 = p_2 = 0.4\times p_0$ [see Fig. 5.5(a)] and $L_0 = 0.2\times w_0$, so that $l_{\rm inc} = 0.143\times w_0$ in the incidence region (as in the previous example). Apparently, it could be expect that the increased diffusion length ($l_{\rm inc} = 0.5\times w_0$) in the region without direct group-V beam would enhance the diffusion of group-III adatoms out of the common incidence region. However, as is

shown by the solid black curve in Fig. 5.5(d), the step-edge of the group-V flux causes an opposite effect and reduces the out-diffusion of the group-III adatoms as in the first example.

In the limit $w_0 \ll L_0$, the gradient of the redistributed surface concentration is small, again; hence, N_a can be assumed constant in a limited region (width $\ll L_0$), and the local growth rates proportional to the square group-V flux ($S \propto f_V^{\,2}$).

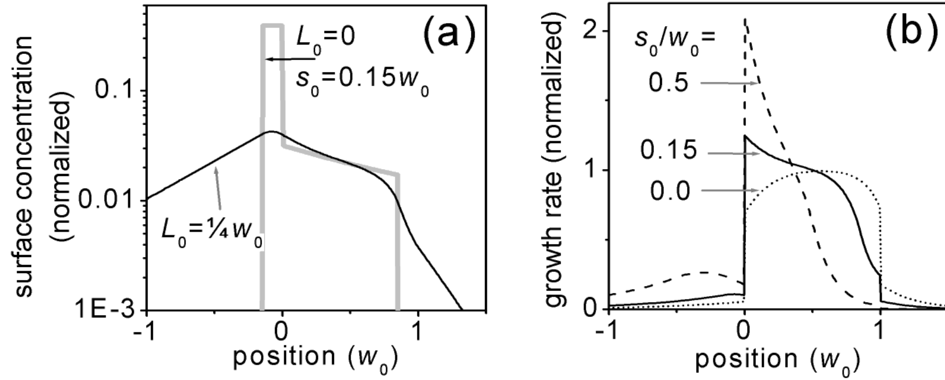

FIG. 5.6 – *Schematic illustrations of surface diffusion of group-III adatoms when the incidence regions of group-III (*$-s_0 < x < w_0 - s_0$*) and group-V species (*$0 < x < w_0$*) are displaced by* s_0*. (a) Surface concentration for* $L_0 = 0$ *and* $0.25\times w_0$*, and* $s_0 = 0.15\times w_0$*. (b) Growth rates for* $L_0 = 0.25\times w_0$ *and* $s_0 = 0$*,* $0.15\times w_0$*, and* $0.5\times w_0$*.*

IV. Displaced incidence regions

The fourth example assumes that the group-III incidence region (range $-s_0 < x < w_0 - s_0$) is displaced relative to that of the group-V species (range $0 < x < w_0$). We use the group-V flux distribution of the first example with $p_2 = p_0$ and $p_1 = 0.4\times p_0$ and set $L_0 = 0.25\times w_0$. Figure 5.6(a) shows the surface concentration corresponding to $s_0 = 0.15\times w_0$, with (black curve) and without (grey curve) considering surface diffusion. As can be seen, the largest change of N_a takes place in the domain of the group-III species and it is caused by the effective diffusion of adatoms out of this region. Figure 5.6(b) shows the growth profiles for $s_0 = 0$, $0.15\times w_0$, and $0.5\times w_0$. As can be seen, the offset of the incidence regions causes asymmetry in the growth profiles. The maximum growth rates are limited to the group-V incidence region. The displacement increases the growth rates on the side adjacent to the domain of the group-III species, because the latter is the source of adatoms, which increase the growth rates at $x = 0$.

In the case $w_0 \ll L_0$, the surface concentration is locally homogeneous and, hence, $S \propto f_V^{\,2}$. The corresponding growth profile is similar to the dashed curve in Fig. 5.5(c) and is almost independent of the displacement s_0.

V. Side facets

Finally, the effect of facet formation is briefly discussed. Tomita *et al.* [Tomita95] have investigated the evolution of the growth profile, when GaAs is deposited through a shadow mask. The self-formation of low-index facets was modeled (*without considering the interdependence between group-V flux and surface diffusion of group-III adatoms*) by assuming that the lifetime τ of adatoms depends on the surface orientation, and without considering the fact that the diffusion constant, D_S, may cause faceting. However, Nishinaga *et al.* [Nishinaga96] has observed that on patterned GaAs substrates, D_S for Ga

adatoms, is more than 100 times larger on (111)B surfaces than on (001), i.e., the diffusion on (111)B is much faster than on the (001) surface. This suggests that the orientation-dependence of D_S is a stronger factor than τ in inducing self-faceting.

The fourth example demonstrates the importance of the orientation-dependence of D_S in shadow-masked growth (*with considering the interdependence between group-V flux and surface diffusion of group-III adatoms*). For this, we return to the third example (common incidence region of group-III and group-V flux in the range $0 < x < w_0$; $p_1 = p_2 = 0.4 \times p_0$; $L_0 = 0.2 \times w_0$). The black curve in Fig. 5.5(d) shows the growth rates when the surface is planar. However, after some time a mesa is deposited in the common incidence region and the surface is not planar any more. One can assume that (111)B facets were formed at the edge of the incidence region and that the rest of the corrugated surface consists of vicinal (001) planes (in agreement with the experiments; see Sect. 6.2). The width of the (111)B planes in the example is set $0.05 \times w_0$ and they extend in the range $0 < x < 0.05 \times w_0$ and $0.95 \times w_0 < x < w_0$. Because of a 100 times larger diffusion constant, the incorporation diffusion length ($l_{inc} = 1.43 \times w_0$) is 10 times larger than in the rest of the incidence region. The grey curve in Fig. 5.5(d) shows the resulting growth rates. As can be seen, in the incidence region the growth profile changes from an initial concave (black curve; without (111)B facet) to a convex shape (grey curve; with (111)B facet). This is because, adatoms impinging on the (111)B facet are hardly incorporated there. Instead they migrate to the top (001) surface.

Summary of Chapter 5

A consistent model has been developed for growth dynamics in molecular beam epitaxy of compound materials through shadow masks. The redistribution of molecular fluxes under shadow masks plays a crucial role in controlling growth rates on selected areas. Based on the model, it has been demonstrated that reactions between the constituent species determine the flux distribution within the mask cavity, and that this in tandem with the growth conditions, affects the deposition of compound material. In addition, the effects of surface diffusion and the interaction of the diffusing species with the molecular fluxes of the other constituent have been discussed.

Chapter 6

SMMBE of II-VI and III-V Compounds

This chapter describes an investigation of the basic growth dynamics during molecular beam epitaxy of compound materials through epitaxial shadow masks. Sections (6.1) and (6.2) present the results from growth experiments with II-VI and III-V compounds, respectively. In both cases, the predictions from the model presented in Chap. 5, regarding the growth regime below the shadow mask are verified. Basic experiments prove that the model can predict growth rates as a function of the growth conditions for both II-VI and III-V compounds. Moreover, it is shown, that SMMBE of II-VI and III-V compounds is governed by different surface kinetics, namely secondary fluxes and surface diffusion, respectively.

In addition to the basic surface kinetic processes described by the model, the role of partial shadow, facet formation, crystal orientation, and material deposition on the mask (closure of apertures) are discussed.

6.1 Growth of II-VI compounds through shadow masks

This section, descibes an investigation of molecular beam epitaxy of II-VI materials through GaAs/AlGaAs epitaxial shadow masks on GaAs(001) substrate. The experiments are based on the model ZnSe system. *Scanning electron microscopy* (SEM) on a Philips XL30 SEM system is employed to investigate the role of material deposition on the mask (closure of apertures), partial shadow, facet formation, and surface diffusion for the SAE growth of II-VI compounds using epitaxial shadow masks. In addition, the validity of the predictions of the model presented in Chap. 5 regarding MBE growth mechanisms in the mask cavity have been investigated.

6.1.1 Partial shadow

I. Experiments ZnSSe layers were deposited through shadow masks at standard growth conditions, typically used for the growth of high quality two-dimensional layers (T_{sub} = 280°C). This was done with the mask aligned parallel to the effusion cells, so that the molecular beams impinged *parallel*,[A] i.e., at the same angle of $\varphi_\perp \approx 10°$. No pinholes were employed in the experiments; hence, the angular dispersion of the molecular beams is $\delta\varphi \approx 10°$. In the first experiment, a Si-mask with stripe-shaped apertures (with V-shaped cross-sections) was placed on a GaAs(001) substrate so that the height h_S of the shadow edge above the substrate is given by the wafer thickness (250 µm). Thereafter, a 17 µm thick layer of ZnSe was grown through the mask. In the second experiment, a 1.1 µm thick layer of $ZnS_xSe_{(1-x)}$ (x = 0.05) was grown through an epitaxial shadow mask with the dimensions of h = 3.3 µm and g = 0.6 µm.

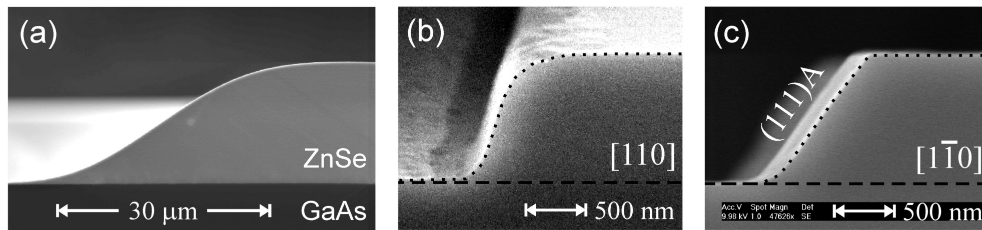

FIG. 6.1 - *Cross-sectional SEM images of the edges of ZnSSe structures grown on a GaAs(001) substrate. (a) Deposition through a 250 µm thick Si-mask. (b,c) Deposition through an epitaxial shadow mask. (b)* [110] *orientation (c)* $[1\bar{1}0]$ *orientation.*

II. Discussion Figure 6.1 shows SEM images of the samples, which were cleaved after the growth in order to determine the profile of the ZnSSe deposits near the shadow edge. Fig. 6.1(a) shows an edge of the ZnSe layer grown through the Si-mask. As can be seen, the edge of the layer is not abrupt and extends over a width as large as 30 µm. A similar rounded edge was formed when ZnSSe was grown through a [110] oriented epitaxial shadow mask [see Fig. 6.2(b)]. However, the width of the edge is much smaller ($w \approx$ 500 nm). These observations can be attributed to the formation of the partial shadow, which originate from the finite aperture diameter y = 22 mm of the effusion cells [see Fig. 4.6(a)]. A finite flux gradient exists in this partial shadow region, the width of which is proportional to the spacing between the shadow mask edge and the substrate. This results in the observed rounded profile of the edges. Based on the results, one determines the effective dispersion of the beam directions to be $\delta\varphi \approx 7°$ [see Fig. 4.6(b)].

Figure 6.1(c) shows the edge of a ZnSSe layer when the substrate is oriented along the $[1\bar{1}0]$ direction. As can be seen, the shape of the edge corresponds to the self-formation of a (111)A surface. Obviously, in this orientation, the formation of facets is a stronger effect than the partial shadow effect.

6.1.2 Facet formation

I. Experiments ZnSe layers were deposited through epitaxial shadow masks at standard growth conditions, typically used for the growth of high quality two-

[A] See Sect. 4.2.1 for details of the geometry.

dimensional layers (at T_{sub} = 280°C; see Fig. 2.4). The angular dispersion of Zn and Se molecular beams is $\delta\varphi \approx 1°$ and the dimensions of the shadow masks, *h* and *g,* range between 1-3 µm and 100-300 nm, respectively. Hence, the width of the partial shadow region in these experiments is some tens of nanometers.

II. Discussion Figure 6.2(a) shows the SEM image of the cross-section of a shadow mask (left hand side) and a ZnSe layer grown through the aperture of the mask (right hand side). The white arrow indicates the incidence direction of Zn and Se beams during overgrowth of the mask. A 490 nm thick ZnSe layer was deposited on the mask and through the aperture on the substrate (growth rate: $R_{(001)}$). In the micrograph, the ZnSe layer appears brighter than III-V features (substrate and shadow mask) due to a material contrast (This contrast would also identify structures from elemental Zn or Se, which, however, are not expected due to the high vapor pressure of the elements at growth temperature.) As can be seen, the left edge of the ZnSe mesa is a smooth crystal plane (black dashed line) with steep inclination angle α = 70°, which evidently does not correspond to a low index crystal plane. Typically, the edges of ZnSe structures grown through a [110] oriented channel mask grown round shaped because of the flux gradient in the partial shadow of the beams. However, for the experiments related to this report, beam plates have been employed and, thus, minimized the width of the partial shadow region (here $\delta x \approx$ 20-30 nm). The formation of an edge with smooth side plane [see Fig. 6.2(a)], is understood from the geometry of growth. As can be seen in Fig. 6.2(a), ZnSe is deposited on top (growth rate: $R_{(001)}$) and edge (lateral growth rate: $R_{(110)}$) surfaces of the mask. The resultant lateral growth of the mask continuously shrinks the aperture, which is indicated by the white dashed lines. As can be seen in the micrographs the beam edges at the beginning and end of growth, coincide with the edges of the side plane of the ZnSe deposit. Thus, the continuous propagation of the shadow edges causes the linear increase of the layer thickness in the edge region, where the inclination angle is α = 70°, given by the ratio of the growth rates: $\tan(\alpha) = R_{(001)} / R_{(110)}$. (This equation is valid only in case of near vertical incidence of the beams.) When the beams impinge at acute angles (slanting incidence), the growth rate $R_{(110)}$ is increased for the mask edges facing the beams. Hence, the slope of the edge of a ZnSe deposit on this side of the aperture is relative small. In contrast, on the other side of the mask, $R_{(110)}$ is small and, thus, the edge of a deposit on this side is relatively steep. Also, the value of $R_{(001)}$ on the cap is less near the edge of the mask (not shown). For this reason, the edges of the structures grown by SAE using epitaxial shadow masks are not limited to slopes of 90° only, as is the case with constant $R_{(001)}$.

This is demonstrated by Fig. 6.2(b), which shows the overhanging edge of a ZnSe deposit (α = 122°; the white arrow indicates shallow incidence of the molecular beam). The formation of such structures clearly demonstrate the non-equilibrium character of SAE growth of II-VI materials. Surface diffusion does not significantly affect the shape of the edges (the round shape of the edges is due to the finite width of the partial shadow). This is remarkable for the growth of nanostructures and is different from the shadow mask assisted growth of III-V materials, where surface diffusion affects the shape of the edges of GaAs deposits, on the micrometer scale (see Sect. 6.2).

Figure 6.2(c) shows the edge of a ZnSe layer, which represents the growth through a $[1\bar{1}0]$ oriented channel mask. As in case of the [110] oriented channel [see Fig. 6.2(a)], ZnSe grown on top of the cap layer partly closes the aperture (indicated by white dashed lines) and results in the formation of a steep side plane (inclination angle: 65°) of higher index. In addition, a (111)A facet is formed on the upper tail of the steep edge. Additional experiments show that the (111)A facets are not formed when the Se:Zn flux ratio is smaller.

Faceting of the edges is also enhanced at higher substrate temperatures as shown in Fig. 6.2(d). The image shows a ZnSe layer grown at 380°C. In this case, only (111)A facets (no steep low-index facets) were formed at the edge of the deposits. The black lines in Fig. 6.2(d) show a geometric construction of the structure's cross-section (due to closing of the mask, indicated by white lines), without faceting of the edges. As is clearly seen, less ZnSe is deposited within the growth area when a (111)A facet is formed. Obviously, facet formation is driven by smaller sticking coefficients for adatoms at the (111)A surface. This is different from the growth of III-V compounds where faceting of the edges is due the orientation dependency of surface diffusion coefficients of adatoms, while the sticking coefficients are close to unity independent of the crystal orientation (see Sect. 5.1). Thus, diffusion dynamics and the formation of facets increases the width of III-V deposits over the area where adatoms impinge on the substrate. In contrast, facet formation decreases the amount of II-VI material deposited within the incidence regions and, thus, effectively decreases the width of II-VI structures.

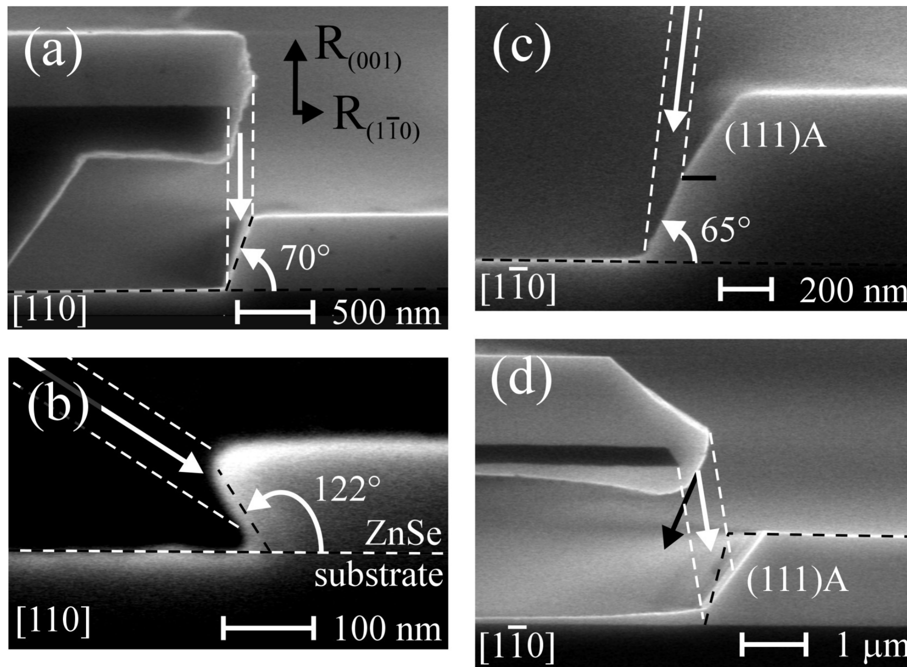

FIG. 6.2 - *Cross-sectional SEM images of ZnSe structures grown through epitaxial shadow masks. The directions of the molecular beams are indicated by the arrows. White dashed lines indicate the edges of the beam at the beginning and end of ZnSe growth. The propagation of the edge is due to deposited on the mask. (a) (b)* [110] *orientation. (c) (d)* $[1\bar{1}0]$ *orientation.*

6.1.3 Formation of a shoulder structure

I. Experiments In order to test the predictions of the model, they are compared with the observations from experiments, wherein ZnSe was grown through a shadow mask with different incidence angles for Zn and Se, and using different growth parameters.

MBE growth of the ZnSe layers was carried out at a substrate temperature of 280°C and a beam equivalent pressure (BEP) of 5×10^{-7} torr for Zn, while the Se-flux was varied. A flux ratio, BEP_{Zn}/BEP_{Se}, of 0.45 corresponds to the standard growth conditions, typically used for the growth of high quality two-dimensional layers. For experiments #1 - #4, the flux ratio was set to 0.28, 0.75, 2.5, and 0.19, respectively. [The growth conditions for the

second sample were chosen to obtain a mixed, c(2x2) and (2x1) surface reconstruction, in RHEED. Consequently, a "Zn-rich" c(2x2) reconstruction was observed during the growth of sample #3 and a "Se-rich" (2x1) reconstruction, when samples #1 and #4 were grown.] By this means, one can verify the predictions of the model regarding the flux ratio.

In the first three samples, the angular dispersion of the Zn and Se molecular beams is $\delta\varphi \approx 1°$ and the dimensions of the epitaxial shadow masks are h = 1.27 μm, g = 400 nm, u = 2-4 μm, and w = 3-6 μm. Hence, the width of the partial shadow region in these experiments is ~20 nm. The last sample (#4), was grown without using pinholes to limit the width of the apertures of the effusion cells. Therefore, partial shadow effects are observed in this case. The dimensions of the shadow mask are h = 2.77 μm, g = 280 nm, and u = 1 μm, while the width w of the apertures was varied from 1 to 6 μm for different stripes. By this means, the predictions of the model regarding the mask geometry can be verified.

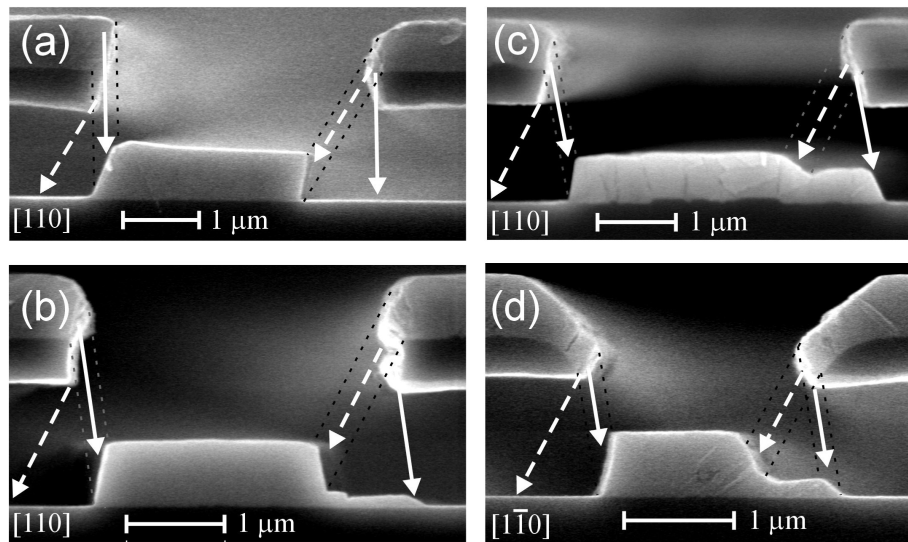

FIG. 6.3 – *Electron micrographs of the cleaved edge of an epitaxial shadow mask (dark material), which was overgrown with ZnSe (bright material). The incidence directions of Se (solid lines) and Zn (dashed lines) are indicated by the arrows. The three micrographs (a),(b), and (c) represent ZnSe growth with increasing Zn:Se flux ratio for the* [110] *orientation . Micrograph (d) represents the* $[1\bar{1}0]$ *orientation of the mask for the same flux ratio as in (b).*

II. Flux ratio Fig. 6.3 shows cross-sectional SEM images of the cleaved edge of samples #1,#2, and #3. As can be seen, ZnSe was grown both on the mask and through its apertures. In the case of sample #1 [Fig. 6.3(a)], the ZnSe deposit on the substrate is limited to the overlap of the incidence regions of the component beams (*overlap region*). The beam directions are indicated by the dashed (Zn) and solid (Se) arrows. Because of the different angles of incidence (+26° and –2°), the width of the growth area is smaller than the aperture of the mask.

When the Se:Zn flux ratio is decreased (see Fig. 6.3(b,d) [sample #2]), ZnSe grows at a lower growth rate also in the region where only Se beam impinges on the substrate (*Se-domain*). The shoulder structure is formed independent of the crystal orientation as is shown by Figs. 6.3(b) and 6.3(d) representing shadow masks with [110] and $[1\bar{1}0]$ oriented apertures, respectively. The growth rate of this shoulder structure increases when the Se:Zn flux ratio is further decreased (see Fig. 6.3(c) [sample #3]) and its thickness becomes similar to the main structure in the overlap region. On the other hand, with a high

Se overpressure [sample #4] ZnSe grows in the entire incidence region of Zn, i.e., a shoulder is formed in the *Zn-domain*.

These results agree well with the prediction of the model [see Fig. 5.4(a)] that a shoulder formed in the domain of the minority species, i.e., Se or Zn, depending on the ratio of the beam pressures, which determine the growth rates. The flux ratio at which R_{Zn} matches the experimental growth rate of the shoulder structure has been determined by employing the dimensions of the shadow mask and the incidence angles of Zn and Se of each experiment in the model. The determined logarithmic flux ratio log($p_{Se}:p_{Zn}$) is +0.32, +0.05, -0.30, and -0.60 for samples #4, #1, #2, and #3, which is reasonable for the change of the flux ratio towards Zn-rich growth conditions. Finally, sample #1 demonstrates that no shoulder is formed when the atomic flux ratio is stoichiometric, as predicted by the model when one considers the interaction between the constituent species.

In addition to the formation of a shoulder structure, the growth rates in the main growth area also depend on the flux ratio. As can be seen in Fig. 6.3(a), the growth rate is larger (factor: 1.14) on the left hand side of the deposit in the overlap region. In contrast, a flat plateau is obtained in the overlap region of samples #2, #3, and #4 [see Fig. 6.3(b,c)]. The increase of the growth rate in the case of sample #1 can be explained by the secondary flux of Zn (minority species), which increases the growth rate limiting Zn-flux. In good agreement with the experiment, the model predicts an increase of the growth rate (factor: 1.09) near the Zn-domain, where Zn is still the majority species on the lower side of the mask. However, a substantial increase of the growth rate by the secondary flux of the minority species is obtained only when the flux ratio is near stoichiometry. For higher flux ratios (samples #2,#3,#4), the interaction between the fluxes suppresses the secondary flux of the minority species and a flat plateau is obtained.

III. Growth geometry Sample #4 was fabricated in order to control the predictions of the model regarding a variation of the mask geometry: In one growth experiment the aperture width *w* was varied. Fig. 6.4 shows the experimental data of the growth rates R_{Zn} and R_0 (normalized to the growth rate without shadow mask) as a function of the aperture width *w*. The horizontal error bars correspond to the closing of the aperture during overgrowth, i.e., a systematic error. The theoretical values of R_{Zn} and R_0 have been extracted from modelling the growth regime based on the geometry of the experiment (i.e., incidence angles and mask dimensions). The only fitting parameter is the atomic flux ratio, which was set to $p_{Se}:p_{Zn} = 10^{+0.32}$. As is shown by the solid lines in Fig. 6.4, the model gives an excellent fit of the experimental data for both the growth rate of the Zn shoulder structure R_{Zn} , which decreases when the aperture width is decreased. This is understood by the weaker coupling between the cavities on both sides of the aperture for large *w* (see Sect. 5.3.3).

Because of the coexistence of a partial Zn and Se pressure within the cavity of the mask, ZnSe grows on the entire surface of the mask-cavity. From the model, the growth rate without a direct beam R_0 (on the substrate) is in the range of 2-8% of the growth rate without shadow mask. However, it is larger (can exceed 10%) on the bottom side of the mask-cap, where the secondary flux has a maximum (near the edge of the aperture). This is in good agreement with the experiment (see Fig. 6.3 and 6.4). In contrast to R_{Zn}, R_0 increases with the aperture width from left to right in Fig 6.4, in agreement with the model (lower solid line). This is explained by the weaker coupling between the cavities on both sides of the aperture for large *w*, i.e., the secondary flux of the minority species, which limits the growth rate R_0, is less effectively reduced by the interaction with the majority species.

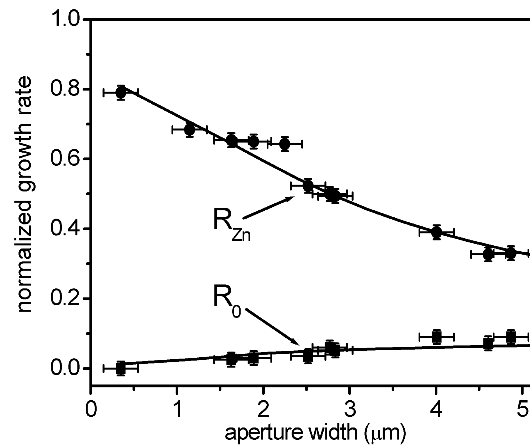

FIG. 6.4 – *Normalized ZnSe growth rates in the Zn-domain (R_{Zn}) and outside the Zn-domain (R_0) versus the aperture width w. The solid lines show growth rates extracted from the model for an atomic flux ratio given by $\log(p_{Se}:p_{Zn})$ = +0.32. The corresponding experimental data were obtained from sample #4.*

IV. Temperature Fig. 6.2(d) shows a shadow mask sample, with ZnSe deposits grown at an unusually high substrate temperature (T_{sub} = 380°C). It is clearly observed that the ZnSe growth rate without a direct beam, R_0, is significantly larger than that of samples grown at T_{sub} = 280°C. In particular, on the lower side of the mask-cap, R_0 exceeds 20% of the growth rate without a shadow mask. This can be explained by the decreased sticking probability of Zn and Se at a higher substrate temperature,[Riley96] which increases secondary fluxes (The reflection of impinging molecules from the tilted side facet and different sticking probabilities on a (111)A facet may also increase the secondary fluxes.) In particular, the minority species is less effectively reduced by the majority species, thus R_0 is increased.

Nishikawa *et al.*[Nishikawa96] reported previously, that ZnSe deposits on the lower side of a shadow mask with high growth rates when ZnSe itself, instead of the elemental materials, is used as a source [see Fig. 5.1(b)]. The growth of ZnSe on the lower side of the mask was explained by inter-surface diffusion, analogous to patterned SAE growth of III-V materials (see Sect. 3.3.1). The higher deposition rates, using a compound source instead of elemental sources, have been attributed to the higher vaporization temperature of the former, resulting in higher thermal energies and hence an increased surface diffusion length of the adatoms. However, this interpretation assumes the unrealistic condition that adatoms can diffuse long distances on a substrate surface without relaxing their thermal energy to equilibrate with the lower substrate temperature. On the other hand, a high thermal energy of an impinging molecule plays a significant role only at its first encounter with the substrate surface, i.e., when it has not yet equilibrated with the substrate temperature. It has been observed, that the high thermal energy of the incoming adatoms increases their reflection probability and hence decreases their sticking coefficient.[Okuyama97] The resultant increase in the secondary fluxes, rather than an increased surface diffusion length, causes the observed deposition of ZnSe on the lower side of a shadow mask, in accord with the model [see Eq. (5.3)].

6.2 Growth of III-V compounds through shadow masks

In this section, experimental results on the growth of III-V materials through GaAs/AlGaAs epitaxial shadow masks on GaAs(001) substrate are presented. The experiments are based on the GaAs system. Section 6.2.4 presents additional results on SMMBE of InAs. Scanning electron microscopy is employed to investigate the role of material deposition on the mask (closure of apertures), partial shadow, facet formation, and surface diffusion for the SAE growth of III-V compounds using epitaxial shadow masks. In addition, the predictions of the model presented in Chap. 5 regarding the growth regime in the mask cavity are tested.

6.2.1 Facet formation

Here, the role of facet formation in SMMBE of III-V compounds is investigated. GaAs layers were deposited through shadow masks at standard growth conditions, typically used for the growth of high quality two-dimensional layers at the respective growth temperatures. This was done with the mask aligned parallel to the row of effusion cells. Since, no pinholes were employed in the experiments, the angular dispersion of the molecular beams was $\delta\varphi \approx 5°$ for Ga and As ($\delta\varphi \approx 10°$ for the other sources in the III-V chamber).

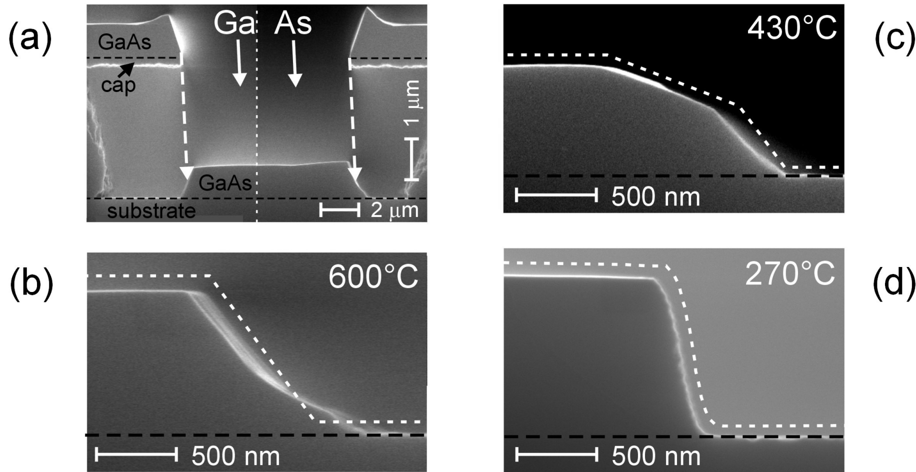

FIG. 6.5 – (a) *Micrographs of GaAs structures grown at 600°C through an epitaxial shadow mask oriented parallel to [110]. The black lines indicate the original surface of the substrate and the mask; white arrows indicate the incidence direction of Ga and As. (b-c) Right edge of GaAs deposits grown with the same growth geometry, at different substrate temperatures: (b) 600°C, (c) 430°C, and (d) 270°C.*

I. Temperature First, the role of the substrate temperature on SMMBE of GaAs is studied. Figure 6.5(a) represents the growth geometry of experiments in which GaAs (~ 1 μm thick) was grown through a [110] oriented mask with dimensions of g=100 nm and h= 3.2 μm, at different growth temperatures. The white arrows indicate the direction of the parallel Ga and As beams, which impinged at $\varphi_{\perp}$=6° through the aperture of the epitaxial mask. The black lines show the original surface of the mask and the substrate. Figures 6.5(b), (c), and (d) represent the right-hand edge of GaAs deposits, which were grown at temperatures of 600, 430, and 270 °C, respectively. As can be seen, the steepest edge formed when GaAs was grown at low temperature of 270 °C. The shape

of the edge corresponds to the gradient of the Ga flux in the partial shadow region, whose width is ~300 nm in this experiment.

In contrast to SMMBE at 270 °C, low-index facets formed at the edges of the deposits when GaAs was grown at 430 and 600 °C. (111)B facets are observed in Figs. 6.5 (c) and (d), while additional (114)B facet formed selectively at 430 °C. In the latter, the edge width is 1.2 μm, i.e., much larger than the width of the partial shadow.

II. Crystal orientation In addition to the growth temperature, the formation of facets depends also on the crystal orientation. Figures 6.6 (a) and (b) show epitaxial shadow masks with stripe apertures oriented parallel to the $[1\bar{1}0]$ and [110] directions, respectively. The profile of the edges of the deposits is very different (see Fig. 6.6), even though GaAs has been deposited on the samples with identical growth geometry and growth conditions at 600 °C.

Smooth (111) facets evolved at the edges of the deposited GaAs layers. A second large facet is observed only on the $[1\bar{1}0]$ profile of a 0.9 μm thick GaAs layer [see Fig. 6.6(a)]. From 28 structures grown in different experiments (not presented), the inclination angle of this second facet had a mean value of $\varphi = 20.8° \pm 2.2°$. Hence, it can be identified as a (114)A facet ($\varphi_{(114)} = 19.5°$ and $\varphi_{(113)} = 25.2°$). As can be seen in Fig. 6.6(a), the GaAs growth rate is significantly increased at the upper edge of the facet region. Behind the edge, the surface is curved and approaches the GaAs (001) surface (regular growth rate) asymptotically. Hence, the total width of the edge region of GaAs deposited through the $[1\bar{1}0]$ oriented mask exceeds 2 μm.

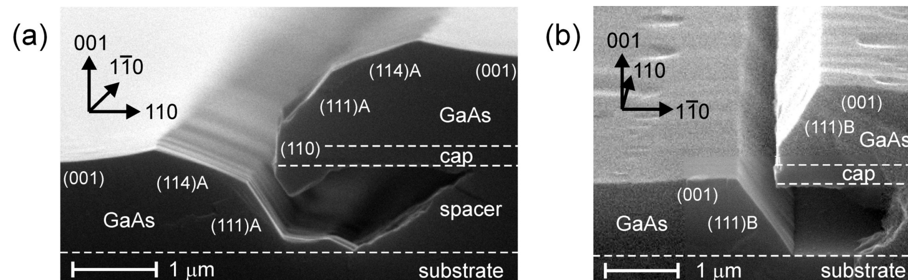

FIG. 6.6 – *Micrographs of GaAs structures grown through epitaxial shadow masks. The orientation of the mask and the facets are indicated.*

III. Discussion Section 6.1 has shown that low-index facets formed also at the edges of II-VI deposits, which was explained by the orientation-dependence of the sticking coefficients. In contrast, in III-V MBE, the vapor pressure of group-III elements is low at reasonable growth temperatures. The corresponding sticking coefficients are approximately unity ($s_{III} \approx 1$) and do not depend on the surface orientation, hence these effects do not shape the edges of III-V deposits.

Thus, facet formation at the edges of III-V deposits correspond to a different process, which is introduced by the migration of group-III surface atoms. Tomita *et al.*[Tomita95] have demonstrated that the profiles of GaAs deposits can be reproduced with a diffusion model. Although, the limitations of the diffusion model (see Sect. 5.1), which does not consider microscopic growth dynamics such as the preferential incorporation of adatoms at step-edges, it can reproduce the macroscopic facet formation, which is driven by the orientation-dependence of the diffusion constant (and the incorporation lifetime of adatoms). It is obvious from the width of the edge region [see Fig. 6.6(a)] that adatoms

migrate over distances larger than 1 μm before they are incorporated in the growing crystal, hence the diffusion length of Ga atoms is of the order of 1 μm for the samples grown at 430 and 600 °C.

The thermal activation of the surface diffusion is low at low substrate temperatures, such as 270 °C. As a result of limited diffusion lengths ($l_D \ll$ 100 nm), the width of the edge of the GaAs deposit in Fig. 6.5(d) is not broadened by surface diffusion, and the shape does not indicate that low-index facets have formed.

IV. GaAs as a buffer These observations also have practical consequences for SMMBE of II-VI semiconductors, where GaAs is important for the growth of a buffer layer. The main demand on this type of structure is that it provides a planar heterointerface. This is not fulfilled in the relative wide edge region of a thick GaAs buffer layer deposited through $[1\bar{1}0]$ oriented stripe apertures. On the other hand, for shadow masks with stripes oriented in the [110] direction, smooth buffers can be realized. For this reason, shadow masks with [110] oriented aperture stripes have been employed in the growth of II-VI materials.

A different and probably better strategy, which has not been tried, would be to grow a GaAs buffer at a low temperature (~270 °C) so that surface diffusion does not enlarge the width of the edge region. However, the surface morphology of GaAs layers grown under these conditions is microscopically rough as a result of the kinetic limitation. Therefore, a second buffer grown by MEE is required to smooth the surface. The thickness can be very thin (~10 nm), so that facet formation hardly increases the edge width of such a structure.

6.2.2 Surface diffusion induced by the arsenic beam

In order to investigate the effects of the group-V flux on the surface diffusion of group-III adatoms, a sample was fabricated by a thermal process, which does not employ group-III fluxes. Similar to the previous experiments, a shadow mask sample consisting of a GaAs/AlGaAs epitaxial shadow mask [h = 1.16 μm; g = 140 nm] on a GaAs (001) substrate was loaded in the growth chamber and the native oxide layer was desorbed at 580 °C. Subsequently, the sample was tempered at 630°C for 10 minutes, and, finally cooled to 300°C. During the entire process, the arsenic beam (BEP: 1.2×10^{-5} torr) was so adjusted that it impinged on the GaAs substrate through the apertures of the mask at an angle of $\varphi_{\perp} = 11°$.

Figure 6.7 shows cross-sectional SEM images of the cleaved $[1\bar{1}0]$ edge of the GaAs sample. The image is magnified in the growth direction in order to exhibit the details of the shallow structures, which were formed during the thermal treatment. The white lines in Fig. 6.7 indicate the incidence direction of the arsenic beam, while the black lines indicate the original surface of the GaAs substrate, before the thermal treatment. Obviously, tempering of the sample with arsenic flux modifies the GaAs interface. In the incidence region of the arsenic beam, GaAs deposited, while grooves were formed on either side [see Fig. 6.7(a)]. Almost the same effects are observed for the growth assisted by shadow masks with the [110] orientation of the stripe aperture [see Fig. 6.7(c)]. Only, the edges of the GaAs deposits exhibit (111)B and (001) faceting instead of (114)A, which is observed in Figs. 6.7(a,b).

Since no external Ga fluxes were employed in the experiment, it can be unambiguously concluded that Ga atoms migrate from the outside to the inside of the incidence region of the arsenic beam on the substrate. The effect is restricted to the region near the step-edge of the arsenic flux, as is clearly seen in Figs. 6.7(b,c), where the width

of the aperture was 7 µm. Obviously, the incidence of the arsenic flux governs the surface diffusion of the Ga atoms, as is discussed below.

Interesting is the fact that the interface of the GaAs substrate is modulated without incidence of primary group-III species. According to Eq. (3.1), no surface diffusion should take place without a surface concentration (N_{III} >0) of group-III adatoms. Since f_{III} =0, a different generation process, which has not been considered in previous investigations of surface diffusion,[Hata91, Nishinaga96] causes the observed effects. This can be understood by considering a thermal generation process *g(T)*, which coincides with desorption of As_2 from the surface. Brennan *et al.*[Brennan92] investigated the onset of As_2 desorption by means of reflection mass spectroscopy. In the case of the GaAs(001) surface it was found that the outgoing As_2 flux exceeds the equivalent of 1 ML/s at temperatures above 600 °C. This probably generates weakly bound Ga surface atoms with a rate *g*, which is of the same order. Thus, the total generation rate of adatoms is $G(\boldsymbol{r},T) = g_0(T) + f_{\mathrm{III}}(\boldsymbol{r})$, where g_0 is assumed position independent (on a planar substrate). Hence, the thermal process causes an intrinsic surface concentration of adatoms $N_i = g_0\tau$, which does not increase the growth rate, which is then given by the net incorporation rate $S = N_{III}/\tau_{inc} - g_0$.

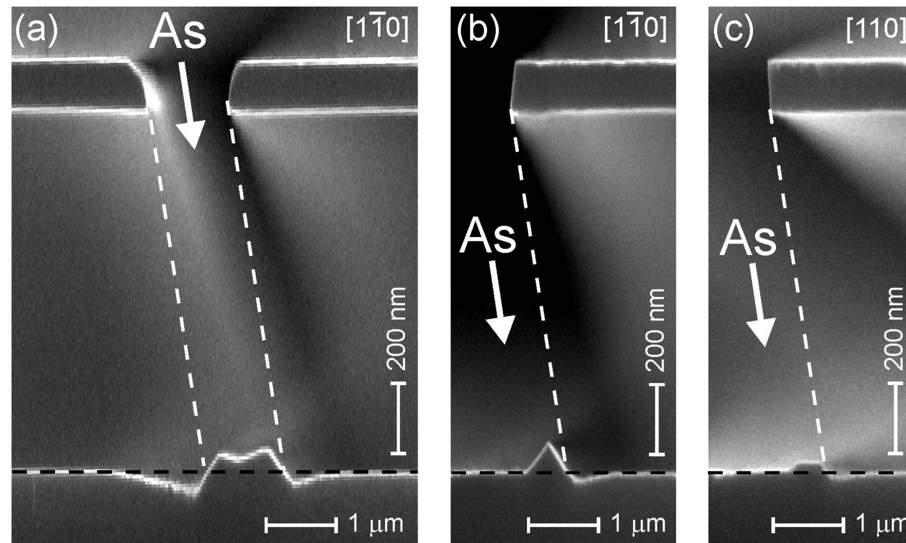

FIG. 6.7 – *Electron micrographs of the cleaved edge of an epitaxial shadow mask, with different aperture widths of (a) 1.2 µm and (b,c) 7.0 µm, and different orientations: (a,b) parallel [1$\bar{1}$0] and (c) parallel [110]. Surface diffusion, which causes the modulation of the substrate surface, was activated thermally. The lateral modulation coincides with the incidence of As through the aperture of the mask, as indicated by the white lines. The black line indicates the interface of the GaAs substrate before the thermal process.*

During the thermal treatment of the GaAs sample, a beam of (mainly) As_4 molecules impinged through the mask aperture (see white lines in Fig. 6.7). Because no additional group-III flux was employed in the experiment, one can assume that the affect of the group-III surface concentration on the redistribution of the group-V flux is limited. In particular, the sticking coefficient of group-V species is about zero in most areas of the cavity of the mask [Only in the incidence region of the direct beam a small fraction (<10%) of the arsenic is incorporated in the growing structure, while areas with negative growth rate act as an arsenic source.] Therefore, Eq. (5.3) gives a reasonable approximation of the distribution of arsenic fluxes when a constant sticking coefficient *s*=0 of arsenic molecules

is assumed. Figure 6.8(a) shows the flux distribution normalized for the primary arsenic flux p_{As} = 1.2×10^{-5} torr.

According to Nishinaga *et al.*[Nishinaga96] the incorporation lifetime of group-III adatoms depends on the arsenic (As_4) pressure f_V as $\tau_{inc} \propto f_V^{-2}$, i.e., $\lambda_{inc} = cf_V^{-1}$ [see Fig. 2.6(b)] where (c) is a constant. Fig. 6.8(b) shows the surface concentration of group-III adatoms obtained by solving Eq. (5.3) for the flux distribution shown in Fig. 6.8(a). The dashed line represents the surface concentration $N_{III} = g_0 \tau_{inc}$ when one neglects surface diffusion of adatoms (D=0). Surface diffusion (D>0) reduces the gradients of this curve via planar redistribution of the surface atoms. The solid curve shows the surface concentration when the incorporation diffusion length at f_{As} = 1.2×10^{-5} torr is chosen to correspond to λ_{inc}= 1.2 μm, a value, which is consistent with the results from microprobe-RHEED experiments, for a substrate temperature of 630°C.[Nishinaga96] As can be seen, the effect of the surface diffusion is pronounced in the regions where the concentration gradient is large, i.e., $\boldsymbol{J}_S = -D\nabla_S N_a$ is large, and when/where the arsenic flux is low, i.e., λ_{inc} is large (> 2 μm).

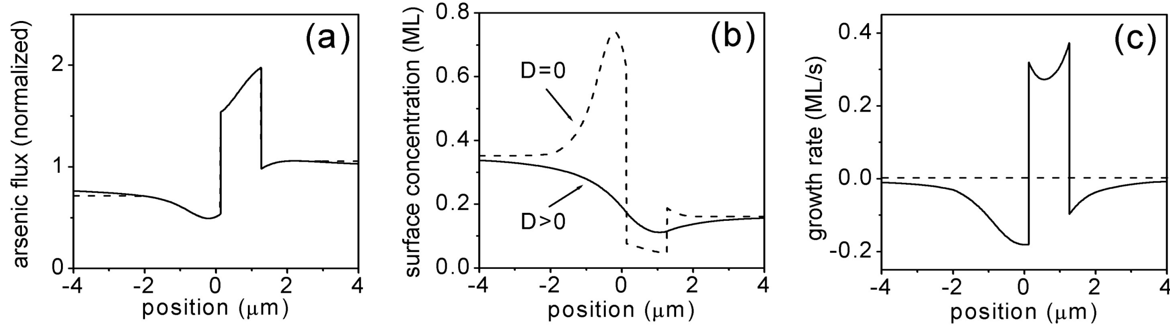

FIG. 6.8 – *Modeling of the surface diffusion of group-III adatoms dependent on the arsenic pressure. (a) Normalized arsenic flux in the case of the GaAs sample [see Fig. 6.7(a)]. (b) Intrinsic surface concentration of Ga adatoms with (solid curve) and without (dashed curve) surface diffusion. (c) Calculated growth rates caused by the surface diffusion, which is controlled by the arsenic flux.*

The resulting growth rates $S = N_{III}/\tau_{inc} - g_0$ are presented in Fig. 6.8(c). As can be seen the shape of the curve is in good qualitative agreement with the experiment [see Fig. 6.7(a)]. (Although, the model does not consider the evolution of the growth interface, which affects the shape of the structure via the self-formation of low-index facets.) Due to the model (and demonstrated by the experiment), positive growth rates are expected in the incidence region of the arsenic beam and the effect is maximum near the edges. On the outside of the incidence region, the growth rates are negative, and again the maximum negative growth rate is near the edges. This can be explained by the spatial distribution of the arsenic flux. A gradient of the group-V surface concentration, causes an inverse gradient of the surface concentration of group-III adatoms as shown in Fig. 6.8(b). Diffusion currents $\boldsymbol{J}_S$ from regions with low group-V pressure towards regions with high group-V pressure reduce the gradient $\nabla_S N_a$. As a result of the planar redistribution, compound material grows in the incidence region of arsenic on the substrate, while the growth rate is negative in regions with low group-V pressure, which act as a source of group-III atoms.

The gradient of the As flux also explains why deeper grooves are formed on the left-hand side of the structure shown in Fig. 6.7(a), while the maximum positive growth

rate is observed at the right-hand side of the incidence region of arsenic. In the incidence region of arsenic, the total flux [see Fig. 6.8(a)] increases from left to right and hence causes a net diffusion current in the same direction. However, the diffusion currents at the edges of the incidence region are larger than inside the incidence region. Hence, there is a local maximum of the growth rate at the left limit, and an absolute maximum at the right limit of the incidence region.

According to Eq. (3.1), surface kinetics, such as the limited mobility of surface atoms (D) and their finite lifetime (τ), limit the surface diffusion. Hence, diffusion currents decay exponentially with the distance from the source, on the scale of the incorporation diffusion length $\lambda_{inc} = \sqrt{D\tau_{inc}}$. This is analogous to inter-facet diffusion during MBE on patterned substrates.

Since the growth rates *S* in Fig. 6.8(c) scale with *g*, the (position independent) scaling factor can be determined by comparison with the experiment. In this experiment the intrinsic generation rate was as high as $g_0 \approx 0.25$ ML/s. Hence, the thermal process generates surface adatoms with a rate, which is comparable to typical impingement rates of group-III atoms in III-V MBE. Hence, this effect should be considered also in experiments with an external flux of group-III atoms.

6.2.3 Surface diffusion as a function of Ga and As beams

Next, an investigation of the effect of surface diffusion when Ga and As species impinge in different regions of the substrate is described. GaAs layers were grown at 600 °C, in a configuration where Ga (BEP: 0.5x10^{-6} Torr) and As (BEP: 2.4x10^{-6} torr) beams impinge at $\varphi_{\perp,Ga}$=11°, and $\varphi_{\perp,As}$=33°, respectively. The angular dispersion of the molecular beams is $\delta\varphi \approx 5°$.

Fig. 6.9 shows cross-sectional SEM images of the epitaxial shadow mask and the GaAs structures grown at different incidence angles for Ga and As; the directions of Ga and As are indicated by white arrows and the original surface of the substrate by the black lines. The image is magnified in the growth direction in order to exhibit the details of the structures, which were grown through the aperture of the shadow mask.

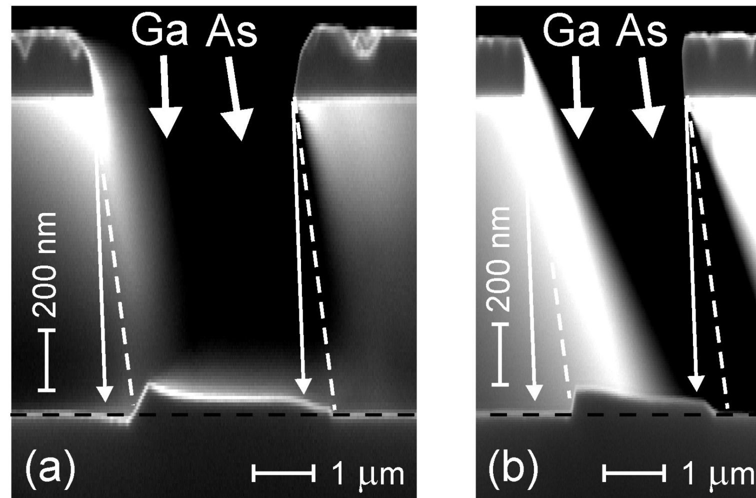

FIG. 6.9 – *Micrographs of GaAs structures grown at 600°C through an epitaxial shadow mask. The black lines indicate the original surface of the substrate; white arrows indicate the incidence direction of Ga (solid arrows) and As (dashed lines). (a)* $[1\bar{1}0]$ *orientation. (b) [110] orientation.*

Independent of the mask orientation, the growth area of GaAs on the substrate is restricted to the incidence region of As, while the offset of the incidence region of Ga relative to the growth region coincides with a modulation of the growth rates: The growth rate has a maximum near the edge of the Ga-domain and it decrease in the As domain with distance from the common incidence region of Ga and As.

This can be explained by surface diffusion, which is governed by the arsenic flux. Analogous to the previous experiment, Ga adatoms are effectively “attracted” by the higher arsenic flux in the incidence region of As. Hence, Ga atoms impinging in the Ga-domain migrate into the incidence region of As, where they locally increase the growth rate near the step-edge. In contrast, diffusion near the As-domain is governed by the gradient of the surface concentration of Ga adatoms, which is a direct result of the local Ga flux. Surface diffusion of Ga results in a steady decrease of the surface concentration in the As domain, which explains the modulation of the growth rates as observed in Fig. 6.9(a).

However, with the [110] oriented mask, the GaAs deposit formed an abrupt edge, positioned in the center of the As-domain, which cannot be understood by the macroscopic diffusion model. A similar effect is that the increased growth rates near the left edge of the growth area forms plateau [see Figs. 6.9(b) and 6.7(c)] instead of a peak as predicted by the diffusion model. Only when the mask is oriented parallel to $[1\bar{1}0]$, a peak is formed [see Figs. 6.9(a) and 6.7(a,b)]. These observations can be explained by the different characteristics between A- and B-type steps. According to theoretical investigations of adsorption behavior on GaAs(001) surfaces by Ito and Shiraishi,[Ito96] the B-type steps, unlike A-type steps, provide active sites for Ga adsorption. Consequently the B-surface propagates as a macro-step, which is not considered by the diffusion model.

Different from the previous experiments, the surface of the substrate is almost flat (see black dashed lines), i.e., no deep groves were formed near the edges of the incidence region of As. This can be explained by the lower substrate temperature (600 °C), which results in a lower intrinsic generation rate g_0 (see Sect. 6.2.2). In particular, g_0 is much smaller than the generation of adatoms by impinging group-III atoms. However, a shallow groove (ca. 20 nm deep; rate: 0.12 ML/s) can still be observed at the left edge of the GaAs deposit for the $[1\bar{1}0]$ oriented mask [see Fig. 6.9(a)].

6.2.4 Surface diffusion dependent on In and As beams

A second sample was grown with similar geometry and growth conditions as before. However, In atoms impinged through the mask aperture instead of Ga. This was done in a configuration where In (BEP: 1.2×10^{-6} Torr) and As (BEP: 8.0×10^{-6} Torr) beams impinged at $\varphi_{\perp,In}$=-11°, and $\varphi_{\perp,As}$=33°; and the corresponding angular dispersion $\delta\varphi$ was 10° and 5°, respectively. During the 30 min deposition of InAs, the substrate temperature was maintained at 580 °C, which is higher than the temperatures usually employed in the growth of InAs.

Figure 6.10 shows micrographs of the cross-section of the epitaxial shadow mask with InAs deposits. The black lines indicate the original surface of the substrate and the white arrows in Fig. 6.10(a), indicate the beam directions of In (solid arrows) and As (dashed lines). As can be seen, the morphology of the mask-cap was affected by the growth of a InAs layer (~200 nm thick), while the planar morphology of the surface of the substrate was almost maintained. However, an InAs deposit (~200 nm thick) can be observed on the substrate, and its boundaries coincide with the incidence of the As beam (between the white dashed lines). In addition, one can see that grooves formed in the GaAs substrate, on both sides of the InAs deposit.

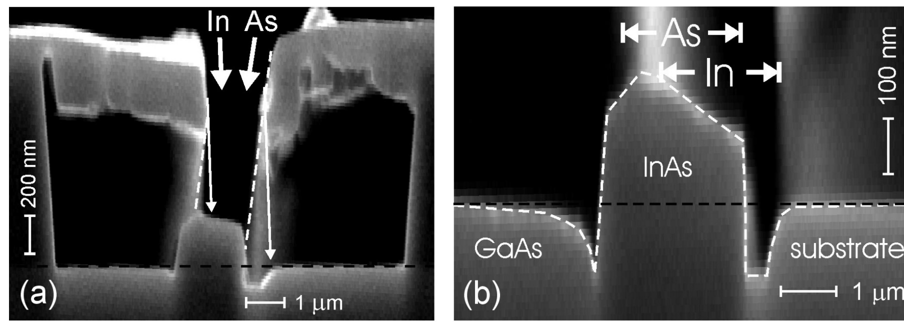

FIG. 6.10 – *Micrographs of InAs structures grown at 580°C through an epitaxial shadow mask. The black lines indicate the original surface of the substrate. (a) White arrows indicate the incidence direction of In (solid arrows) and As (dashed lines). (b) Dashed line indicates the surface of substrate with InAs deposits.*

Figure 6.10(b) shows the profile of the structures at higher magnification. The black line indicates the original surface of the substrate and the white curve indicates the modulated surface of the substrate with InAs deposits, after the growth. As can be seen, the shapes of the grooves on both sides of the InAs deposit are unequal. The left-hand groove is narrower, with a maximum negative growth rate at the edge of the InAs deposit, i.e., the step-edge of the arsenic beam. Up to this point, the observations are similar to the previous GaAs experiments, and thus can be explained analogously, i.e., by the generation of group-III adatoms and their effective migration from regions with a low arsenic flux towards higher pressure regions.

However, the wider groove on the right-hand side of the deposit is almost planar at the bottom, and its area coincides with the As domain. In addition, the depth of the groove is 130 nm, which corresponds to an etch rate of ~0.26 ML/s of the GaAs substrate. This value is significantly higher than that obtained in the previous GaAs experiment, which also implies that the intrinsic generation rate of Ga adatoms is higher in the present experiment although the substrate temperature is 20°C lower. This suggests that the intrinsic generation of Ga adatoms is enhanced by the additional surface concentration of In adatoms.

Summary of Chapter 6

The growth model presented in Chapter 5 has been tested by growth experiments with II-VI and III-V materials [on GaAs(001) substrates] under different growth conditions. Scanning electron microscopy has been used for the investigation of the SMMBE grown structures. The experimental results agree well with the model and demonstrate that the model enables a quantitative prediction of the fluxes and the growth rates. Moreover, the results demonstrate that SMMBE of II-VI and III-V materials is governed by different surface kinetic processes.

One of the problems in the understanding of epitaxial growth processes is the discrepancy between the reported values for the surface diffusion length of adatoms. The results from different types of experiments are often contradictory and differ by as much as two orders of magnitude for both II-VI [A] *and III-V* [B] *compounds. In this work, it has been demonstrated that surface diffusion features can be reliably identified in SMMBE growth experiments and that the model allows the estimation of the surface diffusion length of adatoms:*

In the case of II-VI MBE, the results show that surface migration is very limited at standard growth conditions ($\lesssim$ 10 nm) and does not affect the shapes of II-VI deposits. The growth experiments also demonstrate that II-VI SMMBE is governed by coexisting secondary fluxes of both constituent species. The latter also explains previous observations,[C] *which had been misinterpreted as surface diffusion effects.*

In contrast, this study also proves that group-III adatoms are very mobile. Their diffusion length is of the order of 1 μm at standard MBE growth conditions and increases with decreasing group-V flux. Hence, the group-V flux controls the migration and incorporation of the group-III adatoms. Experiments have also shown that surface diffusion takes place even without incidence of group-III flux. This has been explained by the thermally activated generation of mobile adatoms via the decomposition of the compound, resulting in negative growth rates in regions with low group-V flux. Moreover, in the case of GaAs, it has also been shown that this etching rate can be locally increased by the incidence of indium flux.

[A] Due to [Gaines91], $l_D < 4$ nm. Due to [Nishikawa96, Luo98 Schumacher00], $l_D \gtrsim 500$ nm.
[B] Due to [Neave85, Ohta88, Shitara92, Verschuren99], $l_D \lesssim 10$ nm. Due to [Hata91, Nishinaga96], $l_D \approx 1000$ nm.
[C] [Nishikawa96, Luo98 Schumacher00]

Chapter 7

SMMBE of Quantum Structures

This chapter demonstrates the potential of SMMBE for the fabrication of compound semiconductor nanostructures and optically efficient quantum structures. Corresponding to the different surface kinetics, different approaches have been developed to enable selected area growth of both II-VI (Sects. 7.1 and 7.2) and III-V (Sects. 7.3 and 7.4) nanostructures.

Section (7.1) demonstrates a versatile method for in situ lateral growth control of optically efficient quantum structures, which are defined by SAE of a lateral barrier structure. This has the advantage that the quantum-confined area can be adjusted independent of the mask aperture. This method has been used for the fabrication of ZnSe QWRs with excellent optical quality. In addition, it is shown how the same growth concept enables one to control the nucleation of self-assembled CdSe quantum dots within selected areas.

In Sect. (7.2), a method, which increases the versatility of molecular beam epitaxy through multiple application of a stationary shadow mask with manifold apertures is presented. By adjusting the incidence angle of the molecular beams, one can grow structures through apertures of different shape and size and thus control the growth area on the substrate. This method is equivalent to employing different mechanical masks, but is much more accurate since mechanical alignment is limited. Important modifications of this technique are also discussed. Based on different growth configurations and growth modes, they allow an unprecedented control of SAE of II-VI nanostructures.

Section (7.3) demonstrates how shadow mask assisted SAE can be applied for in-situ controlling of self-organized growth of III-V nanostructures. In particular, the method has been applied to self-organized growth of nanoscale InAs quantum wires at the step-edge of the arsenic beam. The high quality of in situ fabricated nanostructures is confirmed by bright cathodoluminescence of InAs quantum wires embedded in GaAs barriers. In addition, it is demonstrated that based on the multiple application of a stationary shadow mask with manifold apertures, one can control self-assembly of nanoscale GaAs dots at predefined places on a planar mesa structure.

7.1 Fabrication of quantum structures by SAE of a lateral barrier

Here, a versatile method for *in situ* lateral growth control of optically efficient quantum structures is demonstrated. The method is based on MBE through an epitaxial shadow mask. The quantum structures are defined by selected area growth of a lateral barrier structure. This has the advantage that the quantum-confined area can be adjusted independent of the mask aperture. This method has been used for the fabrication of ZnSe QWRs with excellent optical quality by overgrowing a single, photolithographically defined, shadow edge. In addition, it is shown how the same growth concept enables one to control the nucleation of self-assembled CdSe quantum dots within selected areas.

7.1.1 Experiments

The experiments presented in this section were carried out before the modification of the effusion cells in the II-VI growth chamber, i.e., the angular dispersion of the molecular beams was $\delta\varphi \approx 10°$. In order to minimize the width of the partial shadow of the beams, extremely thin and low lying epitaxial shadow masks of h = 460 nm and g = 100 nm were used, thus the width of the partial shadow is ~100 nm. The stripe apertures of the mask (width w = 3-6 μm) were defined by photolithography.

Lateral *in situ* growth control was achieved by adjusting the angles of incidence $\varphi_\perp$ of the molecular beams, as shown in the inset of Fig. 7.1. For the structures described in this section, molecular beams that impinged at three different $\varphi_\perp$ angles $\varphi_\perp$=(α, β, and γ) with respect to the mask surface were used. Changing $\varphi_\perp$, which causes lateral shifting of the deposited layers, was achieved by pivoting and rotating the substrate manipulator relative to stationary positions of the effusion cells.[A] First, a 40 nm thin GaAs buffer layer was grown in the III-V chamber at $\varphi_\perp = \alpha$. Subsequently, the sample was transferred into a II-VI chamber and a 10 nm thick ZnSe buffer ($\varphi_\perp = \alpha$) was grown at low substrate temperature (210 °C). Neither the GaAs nor this ZnSe buffer is shown in Fig. 7.1. On top of the initial ZnSe buffer, a 100 nm thick higher quality buffer layer was deposited with optimised growth conditions at substrate temperature of 280 °C ($\varphi_\perp = \alpha$). In the next step, a *short period superlattice* (SPSL), i.e., a sequence of thin QWs and thin barriers, was deposited, as discussed further below. The SPSL was grown at different angles of incidence, i.e., $\varphi_\perp = \beta$ for QWs and $\varphi_\perp = \gamma$ for barriers (see the inset in Fig. 7.1). By changing $\varphi_\perp$, lateral offset of the deposition areas was obtained, and in a narrow region only the QW material was deposited. Finally, this structure was covered by a 50 nm thick cap layer (deposited at $\varphi_\perp = \alpha$) made of the same material as the barriers and the higher quality buffer. Below, these layers are referred to as the matrix material, in which quantum structures and the SPSL are embedded.

This method has been applied to lattice-matched (see Sect. 6.1.2) as well as to strained (see Sect. 6.1.3) materials, which favor self-assembly of quantum dots. In the first case a MgZnSSe embedded ZnSe QWR formed. The excellent optical quality was proved by bright cathodoluminescence at room temperature. In the second case, this method enabled one to control self-assembly of the quantum dots, and limit it to a 100 nm wide region. The spontaneous nucleation of self-assembled QDs was essentially prevented by the ZnSe barriers, even though the total thickness of the three CdSe layers exceeded the critical thickness.

[A] See Chap. 4 for details of the geometry.

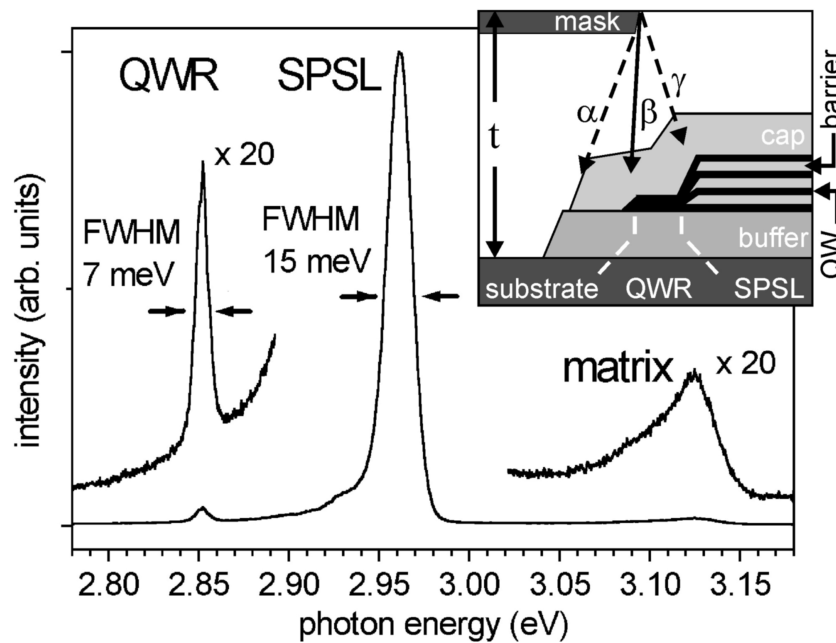

FIG. 7.1 - *PL (at 2 K) of a sample containing ZnSe QWRs embedded in a lattice-matched MgZnSSe matrix. The QWRs were defined by growth of a short period superlattice over the shadow mask edge, with molecular beams impinging at different angles of incidence (α, β, and γ). The principle of growth is sketched in the inset, which shows a cross section of the shadow mask.*

7.1.2 Lattice matched system – ZnSe QWR

As the first example, this growth procedure has been applied to the lattice-matched MgZnSSe/ZnSe system. $Mg_xZn_{1-x}S_ySe_{1-y}$ (x=0.2, y=0.25) was used as the matrix material and ZnSe for the QWs. The SPSL consists of 10 repetitions of two monolayer (ML) thick ZnSe QWs and four ML thick MgZnSSe barriers. This results in the formation of a ZnSe QWR in the region where a 5.6 nm thick ZnSe layer is deposited. Lateral confinement of the QWR is caused by the higher gap in energy of the SPSL.

I. Photoluminescence After liftoff of the epitaxial shadow mask, the sample was characterized by cathodoluminescence and *photoluminescence* (PL). Figure 7.1 shows PL (at 4 K) of the first sample (with QWRs). The three luminescence lines at 2.85, 2.96, and 3.13 eV can be attributed to excitonic recombination in the ZnSe QWR, the SPSL, and the MgZnSSe matrix, respectively. A reference sample, grown on an unpatterned GaAs substrate, did not show any PL signal at 2.85 eV, as expected. The fact that the PL spectrum is dominated by the 2.96 eV line associated with the SPSL can be explained by the huge difference in area between SPSL (5.7 mm wide) and QWR regions (100 nm wide).

II. Cathodoluminescence The *cathodoluminescence* (CL) results observed for the same sample at room temperature (JEOL JSM 840 system; see Ref. [Christen91]) are shown in Fig. 7.2. In contrast to the PL measurements in Fig. 7.1, where the laser excitation spot was large compared to the structure investigated, the CL excitation was much more localized. The light excited by the electron beam originates in a region about 400 nm in diameter, thereby enabling scanning over the sample surface. A spectrally resolved CL scan across the ZnSe QWR and the SPSL is shown in Fig. 7.2. The horizontal axis represents the spatial position of the exciting electron beam, the vertical axis the emission wavelength, and the CL intensity is indicated by the brightness of the image. Two

dashed lines indicate the edges of the MgZnSSe matrix stripe according to a SEM images (not shown here). Intense CL is observed at energies of 2.75 and 2.87 eV (λ = 450 and 432 nm). These signals can be assigned to the ZnSe QWR and the ZnSe/MgZnSSe SPSL regions. Compared to these CL signals the contribution of the thick MgZnSSe buffer layer is very weak - the buffer signal can barely be detected at 3.03 eV (λ = 408 nm). Both the intensity and emission energy are constant across the SPSL, indicating that the composition and thickness of the quaternary $Mg_xZn_{1-x}S_ySe_{1-y}$ matrix are homogeneous over the width of the structure. The intensity of the SPSL signal decays only in the region near the edge of the buffer mesa (dashed line on the right in Fig. 7.2). This effect is most likely due to diffusion and nonradiative recombination of excited electron-hole pairs on the exposed side of the mesa stripe. In contrast, a bright CL spot is located 250 nm from the left edge of the stripe, where the ZnSe QWR is expected. This emission at wavelength of 450 nm can be directly assigned to the ZnSe QWR. At room temperature, the CL signal of the ZnSe QWR is four times more intense than the CL from the SPSL region. Both CL and PL results clearly indicate that the excellent optical quality of the QWR was not degraded by the growth interruptions required for deposition of the barrier layers. The higher quantum efficiency of the QWR (compared to that of the SPSL) in the CL experiment is most likely due to its lateral barriers: Excitons in the QWR are confined by the SPSL, which acts as a 110 meV high barrier on one side, and by the 200 meV matrix barrier on the other sides, which prevent carrier diffusion in the CL.

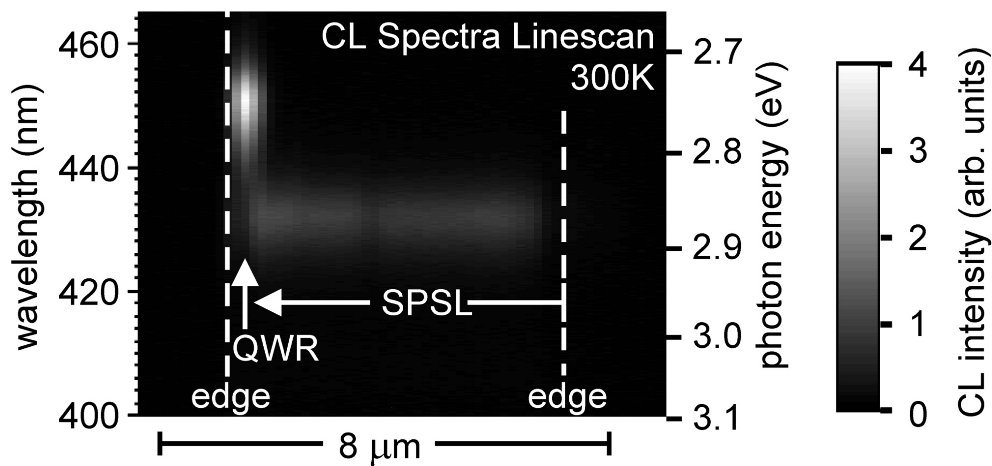

FIG. 7.2 - *Room temperature CL (at 300 K) of a ZnSe QWR in a MgZnSSe matrix stripe. The line scan of the CL spectra shows the signals of the QWR and the SPSL. The dashed lines indicate the edges of the stripe. The scale on the right indicates the intensity of the CL signal.*

7.1.3 Lattice unmatched system – CdSe QDs

In the second example, the versatility of this technique to control self-assembly of QDs within selected areas of the substrate surface is demonstrated. In this case, ZnSe is used as the matrix material and CdSe for the strained QWs. The SPSL consists of three single MLs of CdSe separated by two six ML thick ZnSe barriers. Self-formation of CdSe QDs occurs if the layer thickness exceeds a critical thickness of about 2 ML. Therefore QDs are expected to nucleate within the narrow stripe (100 nm wide) where only CdSe was deposited.

I. RHEED Growth of this sample was monitored by RHEED, which is representative of the growth in the CdSe/ZnSe SPSL region (below the mask). Streaky (2x1) Se-rich reconstruction was observed throughout growth. Since the formation of QDs below the shadow mask cannot be monitored by RHEED, a reference sample (without a shadow mask) was grown by the identical procedure, with the exception that growth was interrupted when a ZnSe barrier was grown on the shadow mask sample. RHEED showed streaky (2x1) Se reconstruction during deposition of the first two CdSe MLs. This pattern was superimposed on sharply defined spots after the third pulse of CdSe, which is indicative of the onset of the formation of quantum dots. The difference in RHEED pattern behavior for both samples indicates that spontaneous nucleation of self-assembled QDs can be effectively prevented by ZnSe barriers, as is the case in the CdSe/ZnSe SPSL region. This is true even when the total thickness of the three CdSe layers exceeds the critical thickness.

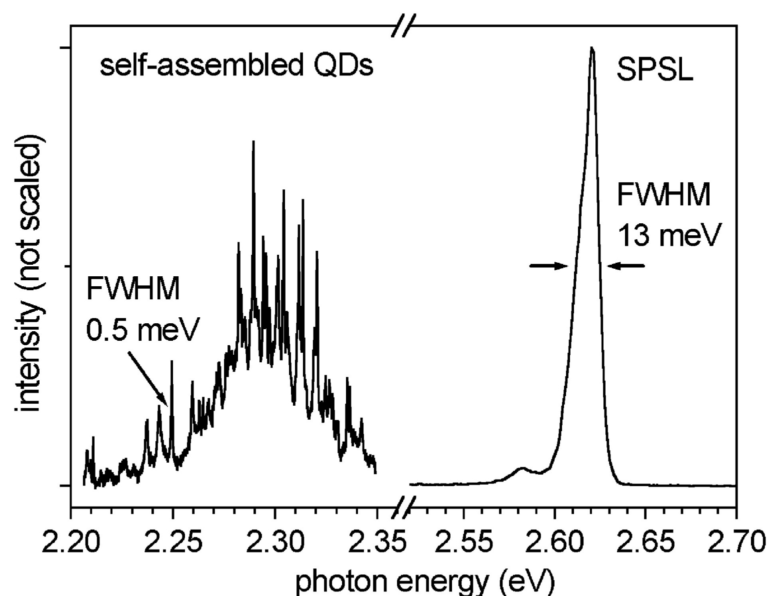

FIG. 7.3 - *CL (at 6 K) of a sample containing self-assembled CdSe QDs in ZnSe barriers. This sample demonstrates the growth concept sketched in the inset of Fig. 7.1 to unmatched lattice systems. The CL spectra were acquired from one position in the SPSL region and from one in the region where only CdSe was deposited during growth of the SPSL.*

II. Cathodoluminescence Although the formation of QDs in the second shadow mask experiment was not detected by RHEED, their presence is clearly demonstrated by CL investigations. Figure 7.1 shows CL spectra of the second sample which were taken at positions in the SPSL region (spectrum on the right) and in the region where only CdSe was deposited (spectrum on the left). The CL was excited with a focused electron beam at 6 K (JEOL JSM 840 SEM & CL system [Christen91]). The SPSL spectrum is dominated by an emission line at 2.62 eV. The spectrum on the left shows very different characteristics. Extremely sharp luminescence lines [the full width at half maximum (FWHM) is given by the spectral resolution of the setup] are characteristic of excitonic emission in individual QDs. This shows that a rather small number of self-assembled QDs was selectively grown in this narrow region.

7.2 SMMBE exploiting multiple, nanoscale apertures

Here, a method is presented which increases the versatility of molecular beam epitaxy through multiple application of a stationary shadow mask. The method is based on epitaxial shadow masks with multiple, nanoscale apertures, which are fabricated using electron-beam lithography and chemical assisted ion beam etching. The AlGaAs spacer is removed from the entire region between different apertures, so that by adjusting the incidence angle of the molecular beams, one can grow structures through apertures of different shape and size and thus control the growth area on the substrate. This method is equivalent to employing different mechanical masks, but is much more accurate since the precision of mechanical alignment is limited.

The principle of shadow-masked growth is sketched in Fig. 7.4. The apertures of the mask consist of stripes, which are accompanied by a row of rectangular holes, aligned parallel to the stripe. First, the stripe aperture is used for the growth of a high-quality buffer, i.e., a stripe shaped mesa with flat surface. Next, the small holes are used for the deposition of island structures on top of the mesa. The size and shape of an island is defined by the size and shape of the small aperture. Finally, a cap layer is grown in the initial configuration, thus, embedding the islands.

I. Growth modes The technique has been applied to lattice matched and unmatched systems. In the first case, the embedded deposit is a nanoscale island with 2D surface morphology. Section 7.2.2 describes an investigation of such nanoscale deposits using atomic force microscopy and Sect. 7.2.4 demonstrates the application of this growth mode to the growth of nanoscale ZnCdSe QW islands. In Sect. 7.2.3, the technique is employed for the local growth of CdSe, which forms self-assembled QDs when the layer thickness exceeds the critical thickness. Cathodoluminescence shows that such nanoscale CdSe deposits consist only of a small number of self-assembled QDs, and that the number of QDs on an island can be controlled by the size of the growth area.

II. Growth configurations In addition to employing different growth modes, there are three important modifications of the technique, which are based on different configurations of the incidence of different species as will be explained in the following section.

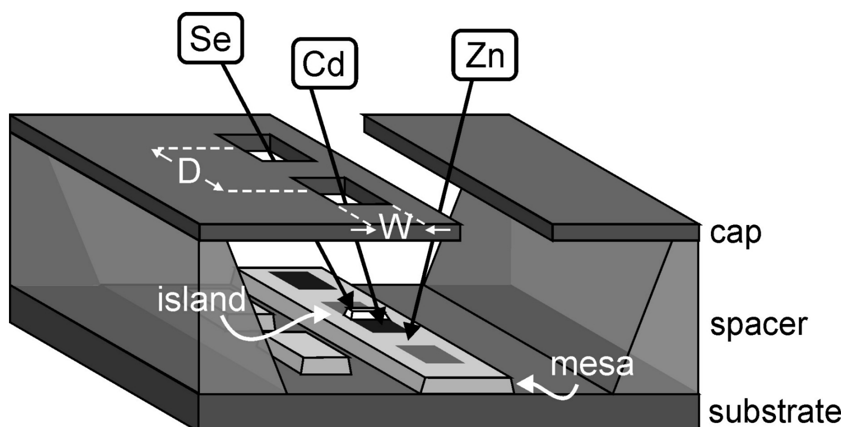

FIG. 7.4 – *Sketch of the principle of SMMBE employing apertures of different shapes and sizes. An epitaxial shadow mask is under etched between neighboring apertures. The incidence region of the impinging molecules is a projection of the aperture pattern. For parallel beams the common incidence region defines the growth area of a mesa structure. The arrows indicate the incidence configuration during the growth of CdZnSe islands on top of the mesa (see Sect. 7.2.3). Islands grow selectively in the region where both Cd and Se are impinging.*

7.2.1 Experiments

The shadow masks are fabricated from GaAs/AlGaAs epitaxial layers grown on a GaAs(001) substrate, consisting of a 1.7 µm thick $Al_{0.6}Ga_{0.4}As$ spacer and a 200 nm thick GaAs cap. Electron beam lithography and reactive ion etching are employed to open apertures in the GaAs cap layer. The set of apertures consist of a stripe (70 µm long; 800 nm wide), which is accompanied by a row of rectangular holes, aligned parallel to the stripe (see Figs. 4.3 and 7.4). The AlGaAs spacer below these apertures is removed by selective etching in hydrofluoric acid. The etching is continued until the GaAs substrate surface is reached, and the patterned cap layer then is under etched over a distance of 2 µm. Figure 7.4 shows a sketch of the mask with a long stripe aperture and the two small rectangular apertures in the cap layer. In the experiment, either the width of the rectangular holes W (from 120 nm up to 320 nm in steps of 20 nm) or the distance between the holes D (from 900 nm up to 1080 nm in steps of 20 nm) have been varied. The length of the holes L was fixed at 320 nm.

SMMBE is carried out using two different MBE chambers, which are interconnected via an ultra high vacuum transfer system. Pyrolytic boron nitride disks disks with a 2 mm pinhole were used to limit the aperture of the effusion cells of the II-VI growth chamber in order to reduce partial shadow effects. The patterned sample was first placed in the III-V chamber and the native oxide was desorbed under As flux, which impinged at an angle $\varphi_{\perp} = 11°$. Optionally, a 100 nm thick GaAs buffer layer was grown in a configuration with parallel molecular beams ($\varphi_{\perp} = 11°$), resulting in the formation of a mesa structure (as sketched in Fig. 7.4). Subsequently, the sample was transferred into the II-VI chamber, and a 10 nm thick ZnSe buffer was grown with similar growth geometry ($\varphi_{\perp} = 11°$) at low substrate temperature (210 °C). On top of the initial GaAs and ZnSe buffers, a 100-150 nm thick higher quality buffer layer was deposited with optimised growth conditions at substrate temperature of 300 °C ($\varphi_{\perp} = 11°$).

The arrows in Fig. 7.4 represent the incidence directions of the molecular beams for another growth configuration which has been used for the growth of nanoscale II-VI islands (ZnSe, CdSe, or ternary CdZnSe) on top of the mesa stripe. In this configuration, the Zn flux ($\varphi_{\perp} = 11°$) covers the entire surface of the mesa while for Cd and Se ($\varphi_{\perp} = -13°$), only molecules passing through the small apertures hit the mesa stripe. Due to the different *parallel* incidence angles of Cd ($\varphi_{\parallel} = 11°$) and Se ($\varphi_{\parallel} = 33°$), the respective incidence regions are offset along the stripe. Therefore, Cd and Se beams passing through different holes fall on the same area when the center to center distance D of the apertures is about 850 nm. For different values of D, the incidence regions are offset from each other and the beams overlap partially or not at all. The idea of this growth geometry is to control the island dimensions independently by the aperture dimensions ($W \times L$) and by the distance D of the apertures, i.e., the width of the overlap region (see Figs. 4.3 and 7.4).

Finally, the sample is returned to its initial position ($\varphi_{\perp} = 11°$) and the mesa stripe is overgrown *in situ* with a 50 nm thick ZnSe cap layer. After the growth, removal of the shadow masks is performed by lift-off in hydrofluoric acid. The latter selectively dissolves the AlGaAs spacer and does not affect the II-VI materials.

I. Reference sample A sample with nanoscale ZnSe and CdSe deposits was fabricated as a reference for the growth geometry. The sample was grown without a GaAs buffer and without the ZnSe cap. Initially, a 10 min deposition of Zn and Se through the stripe-shaped aperture resulted in the growth of the 150 nm thick ZnSe stripe, which is

clearly visible on the scanning electron micrograph shown in Fig. 7.5(b). After growth, the substrate manipulator was tilted and rotated to the configuration sketched in Fig. 7.4. First, 25 nm thick ZnSe islands were grown in the incidence regions of the Se beam, which is transmitted through the small rectangular apertures and, thus reaches the ZnSe stripe, where it overlaps with the Zn flux. Subsequently, growth was continued with the deposition of 17 nm of CdSe in the same sample position, so that Cd and Se beams passing through different $W \times L$ holes overlap on the mesa stripe dependent on the center-to-center distance D of the apertures. MBE growth of the II-VI layers was carried out at a substrate temperature of 300 °C and beam equivalent pressures of 0.5, 0.5, and 1.0×10^{-6} Torr for zinc, cadmium, and selenium, respectively.

II. CdSe QDs sample A sample containing nanoscale CdSe deposits was grown in order to investigate self-assembly of QDs in such restricted templates. The sample was fabricated without a GaAs buffer. First a 100 nm thick ZnSe stripe mesa was grown as described above. Next, CdSe is deposited in the second configuration (see Fig. 7.4), in which only the projections of the small apertures for Cd and Se fall on the ZnSe mesa. Nominally 3 MLs of CdSe were deposited as follows: The Cd flux consisted of three pulses, each 3 s long. In order to enhance surface kinetics after every pulse, the Cd flux was interrupted for 20 s while the sample was exposed to the Se flux. After the deposition of CdSe in this geometry, the sample was returned to its initial position and the ZnSe stripe covered with nanoscale CdSe deposits was overgrown with a 50 nm thick ZnSe cap layer. MBE growth of the II-VI layers was carried out at a substrate temperature of 300 °C and beam equivalent pressures of 0.5, 0.5, and 1.0×10^{-6} Torr for zinc, cadmium, and selenium, respectively.

III. CdZnSe QW sample The third sample, demonstrates the growth of nanoscale QW islands with ternary CdZnSe composition. First, a 100 nm thick GaAs buffer layer is grown in a III-V chamber. Subsequently, the sample is transferred into a II-VI chamber, and 150 nm ZnSe is grown on top of the GaAs mesa stripe. Next, 10 nm thick CdZnSe QW islands are grown in the configuration described above, i.e., with the Cd, Zn, and Se beams passing through neighboring apertures (see Fig. 7.4). Finally, the sample is returned to its initial position and the mesa stripe is overgrown *in situ* with a 50 nm thick ZnSe cap layer. MBE growth of the ZnSe and CdZnSe layers was carried out at a substrate temperature of 300 °C and beam equivalent pressures of 0.5, 0.1, and 0.7×10^{-6} Torr for zinc, cadmium, and selenium, respectively.

7.2.2 SEM and AFM on the reference sample

This section presents SEM and atomic force microscopy (AFM) results on the reference sample.[A] Figure 7.5(a) is a planar view of the SEM image of the mask-cap after it was overgrown with 200 nm ZnSe. As indicated by the dashed line, the initial shape of the small openings is rectangular (dimensions $W \times L$; see Fig. 4.3), but after overgrowth the holes are partially closed. In particular, the formation of a fast growing facet in the upper right edge changes the shape of the holes. The fast growth rate of this facet is due to the relative direction of the beams during the deposition of ZnSe. As indicated in Fig. 7.5(a), (111)A facets are formed on the lower and upper edge of the holes.

Figure 7.5(b) shows an AFM image of a ZnSe mesa stripe (grey stripe) with nanoscale ZnSe and CdSe deposits (white) on top of the mesa stripe. One can identify

[A] RASTERSCOPE 4000 AFM (Danish Micro Engineering). For an introduction to the AFM technique, see Ref. [Binnig86].

ZnSe and CdSe deposits by their material contrast, which is observed in additional SEM images (not shown). AFM and SEM show that ZnSe and CdSe deposits form independent of the distance D between the small apertures. In particular, CdSe deposits are observed for D=1100 nm, i.e., when the incidence regions of Cd and Se do not overlap. Thus, CdSe was deposited in the entire incidence region of Cd on the mesa stripe, independent of the incidence of the Se beam (which impinged on the nanoscale ZnSe deposits). This can be understood by secondary Se fluxes in the mask-cavity, as discussed in Chap. 5. Thus, CdSe deposition is due to the Cd from the direct beam and the secondary flux of Se below the shadow mask. Hence, ZnSe and CdSe deposits represent the incidence regions of Se and Cd beams, respectively. This also explains why ZnSe and CdSe islands overlap for D = 900 nm, and are grown in separate regions for the D = 1100 nm spacing between the apertures.

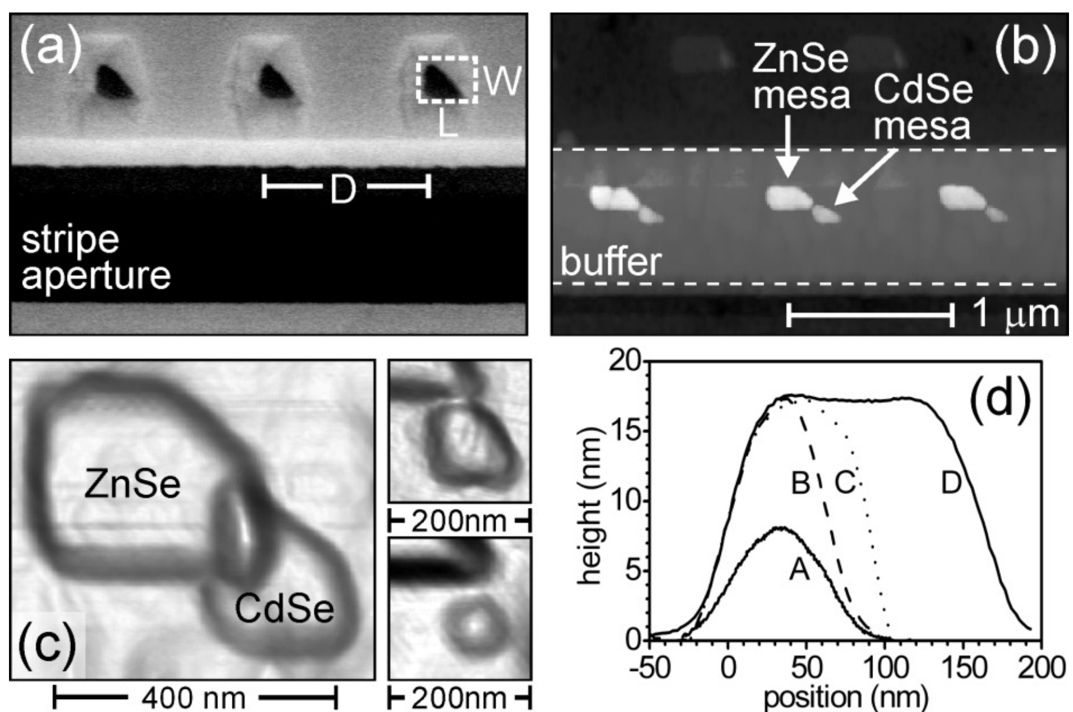

FIG. 7.5 - *(a) SEM image of a shadow mask with a stripe aperture and three W×L rectangular apertures (dashed line). The image shows the mask after it was overgrown with 200 nm ZnSe. (b, c) AFM images of a ZnSe mesa (dashed lines indicate the edges of the stripe) with ZnSe and CdSe deposits on top. (b) The brightness of the image indicates the surface height. (c) The brightness of the images indicates the surface gradient. Planar regions appear bright, sloped regions dark. (d) AFM height-profiles of SAE grown CdSe deposits obtained for different aperture widths W.*

The AFM images in Fig. 7.5(c) show a section with a ZnSe island (left top) and a smaller CdSe island (right bottom). Dark regions in Fig. 7.5(c) correspond to a gradient of the surface (sloped island edge), while bright regions represent planar regions. Despite using apertures of equal dimensions *W*×*L*, the CdSe deposit is much smaller than its ZnSe counterpart (see large AFM image). This is due to the aspect ratio of the three-dimensional openings and shallower incidence angles of the Cd beam (in comparison to Se in case of ZnSe). Therefore, the effective aperture width for the passage of Cd (projection of the three-dimensional aperture) is relatively small, and hence a CdSe deposit is smaller than a ZnSe deposit. As can be seen, the SAE grown islands are planar and their shapes are almost rectangular with exception of the missing right upper corner. The latter can be

attributed to the modification of the aperture shape by the fast growing ZnSe facet. As can be seen, the edges of the islands are not totally abrupt. Their edge radius of about 30 nm (at half structure height) corresponds to (1) the edge radius of the aperture of 5-20 nm [see Fig. 7.5(a)] and (2) the partial shadow of the beam, which increases the radius by another 25 nm.

As is clearly seen in the large AFM image [Fig. 7.5(c)] that the CdSe deposits and the ZnSe deposits overlap on a small region. Within this nanoscale region, CdSe is deposited on top of the ZnSe island, which increases the total thickness. Small AFM images in Fig. 7.5(c) demonstrate the accurate control of the relative position and size of the ZnSe islands (in left upper corner) and the CdSe islands (in center) that can be achieved by adjusting *D* and *W*. In case of the upper right image the nanostructures grown through the 1000 nm distant apertures are deposited precisely side by side. The lower right AFM image shows a CdSe deposit ("A") grown through an aperture with smaller width *W*. In contrast to the CdSe deposits corresponding to larger aperture widths *W*, the shape of island "A" is circular. Fig. 7.5(d) shows AFM height profiles of CdSe islands grown through openings of different widths, *W*. For islands "D" to "B" the structure width decreases with the width of the aperture W, while the height remains unchanged (17 nm). In contrast, for aperture widths smaller than that used in case "B", the thickness of the deposit ("A") decreases, while the width of the deposit does not shrink any further. For all CdSe deposits, the width of the edge is about 30 nm at half structure height [see left edges in Fig. 7.5(d)], which is obviously limited by the width of the partial shadow of the Cd flux (width at half maximum, $\delta x \approx 25$ nm). Thus, the dimensions and shape of CdSe deposit "A" can be attributed to the partial shadow of the Cd flux that passes through an opening whose effective width is smaller than the width of the partial shadow.

7.2.3 Self-assembly of QDs in nanoscale CdSe deposits

Here, cathodoluminescence (CL) results on the CdSe QD sample are presented [The CL micrographs were taken at T = 6K with an electron current of 1 nA and an electron energy of 7 keV in a JEOL JSM 840 system (described in Ref. [Christen91])]. In particular, self-assembly of QDs has been investigated as a function of the dimensions of the CdSe deposits, i.e., the dependence on the width W of the mask-apertures. A scanning electron micrograph of three ZnSe stripes with embedded CdSe deposits is shown in Fig. 7.6(a). The image shows that the AlGaAs spacer and top GaAs layer, which were used to form the shadow mask, have been completely removed. The resulting ZnSe matrix stripes are flat and regular. CL measurements performed on the sample exhibited clear features, which can be unambiguously associated with the presence of CdSe inclusions embedded in the ZnSe matrix.

Figure 7.6(b) shows an CL image of the same area of the sample as shown in Fig. 7.6(a). The micrograph was taken at T = 6 K with an electron current of 1 nA and an electron energy of 7 keV. Under excitation, rows of regularly distributed bright luminescence spots become clearly visible. The spots emit light at wavelengths of 450–500 nm, i.e., well below the energy gap of ZnSe. The spots are located in the middle of the ZnSe matrix stripes. Compared to their bright luminescence, the CL signal originating from ZnSe, at a wavelength of 442 nm, is homogeneous along the stripes, and much less intense. The distance between the spots is equivalent to the period D of the apertures in the mask. These observations are strong evidence that the bright spots indeed originate from CdSe inclusions embedded in the ZnSe matrix stripes.

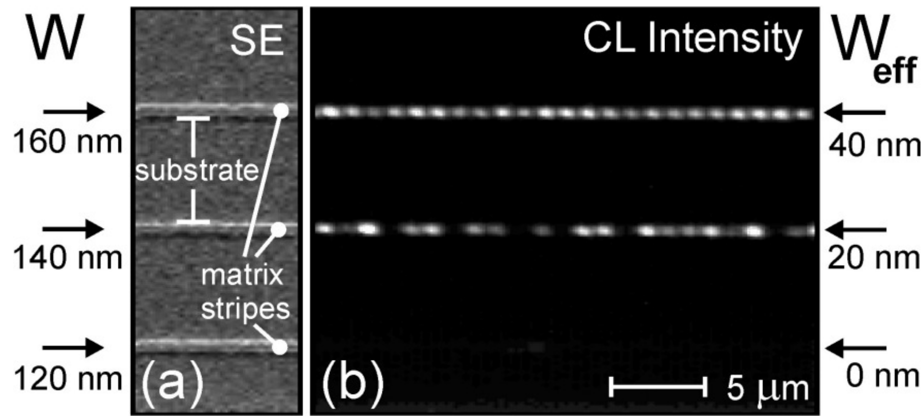

FIG. 7.6 - *(a) Scanning electron micrograph of three ZnSe matrix stripes. The shadow mask has been removed after growth. The original widths W of the rectangular apertures of the mask were 160, 140, and 120 nm. (b) Micrograph of the CL intensity of CdSe islands which are embedded in the matrix stripes. The effective width of the apertures, W_{eff}, which defines the CdSe growth areas, is 40, 20, and 0 nm, respectively.*

For the three stripe structures discussed herein, the Cd and Se beams were directed through rectangular apertures with widths given by W = 120, 140, and 160 nm, respectively. For the 120 nm aperture, not any CL was observed [Fig. 7.6(b)], suggesting that the aperture was effectively closed for CdSe deposition. This is due to the partial closing of the apertures. During the deposition of the first ZnSe layer, the width of the apertures shrinks by approximately 80 nm. At a reduced aperture width of 50 nm, the oblique incident beams are then totally blocked due to the aspect ratio of the three-dimensional holes. Therefore, it is convenient to define an effective aperture width given by W_{eff} = W - 120 nm. As shown in Fig. 7.6(b), for W_{eff}= 20 nm (W = 140 nm), the intensity of the luminescence spots strongly fluctuates (some of the spots are completely dark) indicating that the fluctuation of the effective aperture width is in the range of 20 nm. Starting from W_{eff}= 40 nm, the CdSe islands grow reproducibly and lead to a regular and homogeneous intensity pattern along the stripe.

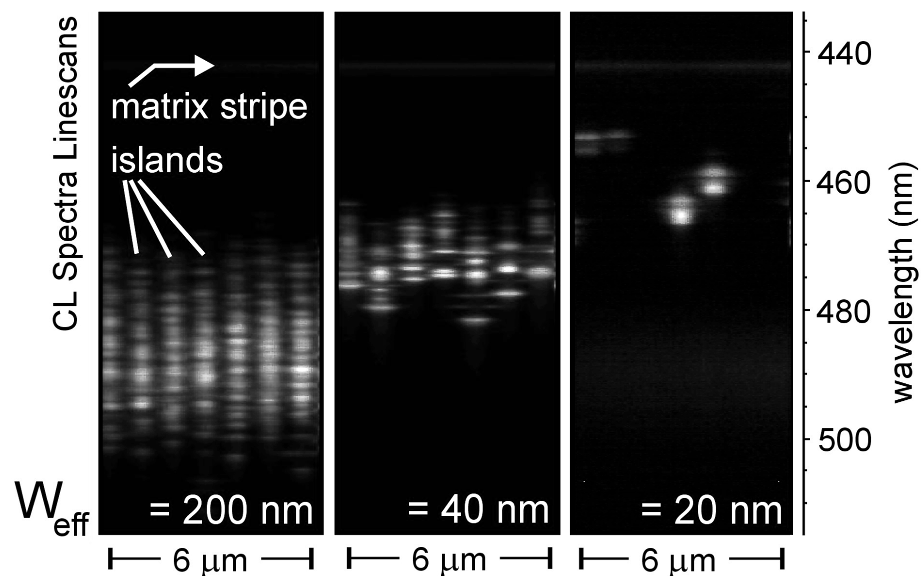

FIG. 7.7 - *CL spectra line scans along matrix stripes with CdSe islands of different widths. CL signals of the ZnSe matrix (λ=442 nm), and 7 CdSe islands (λ=500-450 nm) are observed.*

Figure 7.7 presents spectrally resolved CL from CdSe deposits grown with effective aperture widths of 20 nm, 40 nm, and 200 nm. In every case, only a fragment of the stripe, which contains seven neighboring CdSe islands, is shown. The vertical axis represents the wavelength of the emitted radiation, the horizontal axis represents the spatial position along the ZnSe stripes, while the brightness of the spots reflects the intensity of the CL signal. The spectra consist of a series of narrow lines. Apart from small differences in the intensity distribution between particular luminescence lines, spectra belonging to the same W_{eff} group exhibit significant similarities. In particular, the spectral range and the number of the emission lines are similar for spots grown with the same W_{eff} . With decreasing W_{eff} , the spectra shift to higher energy and the number of emission lines decreases. These effects are more clearly observed in Fig. 7.8, where typical CL spectra of CdSe islands grown at different W (W_{eff}) are plotted at a higher resolution. All spectra consist of a series of emission lines with half widths of <0.6 meV, which was the spectral resolution in the experiments. Such spectra are clear proof of the existence of individual QDs, indicating their formation during the deposition of the CdSe islands.

The blueshift in the spectra is most likely due to a change of the QD composition, size, or shape with the size of the CdSe islands. The reduction of the number of CL lines in the spectra is a direct result of the decrease in the number of dots on each CdSe islands, since the deposition area decreases. In the extreme case of W_{eff}=20 nm, spectra characteristic for a single QD have been observed (see Fig. 7.8). Such spectra are well known from CL investigations using optical near-field masks on self-assembled CdSe QDs in a ZnSe matrix.[Türck01] The CL spectra of single CdSe QDs in Ref. [Türck01] exhibit emission lines which are due to the recombination of excitons and additional multiparticle states. The spacing and number of lines, as observed in Ref. [Türck01], agree well with those in a spectrum for W_{eff}=20 nm (see Fig. 7.8). This suggests that the CdSe islands harbor only a single QD. The excellent quality of the QDs is indicated by intense room-temperature CL, as shown in the inset of Fig. 7.8.

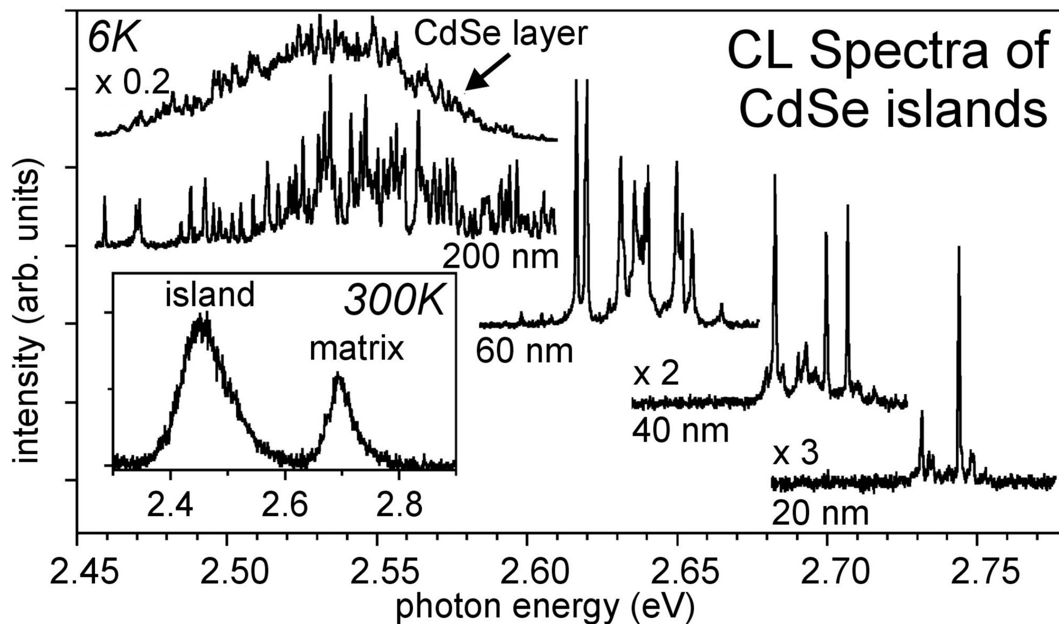

FIG. 7.8 - CL spectra of CdSe QDs grown with and without a mask. The effective aperture widths are given by W_{eff} =200, 60, 40, and 20 nm, respectively. The insert shows the CL spectrum of a CdSe island (W_{eff}=200 nm) at room temperature.

7.2.4 CdZnSe QW islands

Here, CL results on the CdZnSe QW sample are presented. In particular, the observed CL spectra are discussed as a function of the spacing D between the mask-apertures.

I. Selective growth and size-control of islands Figure 7.9 shows typical cathodoluminescence (CL) results obtained on the CdZnSe QW sample. The three CL micrographs were taken at T = 6 K with an electron current of 1 nA and electron energy of 7 keV. They present the spectrally integrated CL (2.63 – 2.84 eV) for a shadow mask with 320x320 nm^2 apertures, with D = 900, 960, and 980 nm, respectively. The effective width W_{eff} of the apertures is 80 nm (W_{eff} has been determined analogous to the previous section: W_{eff} = W – 240 nm. In this sample, the closing of the apertures is further propagated because of the GaAs buffer layer.) Under electron excitation, a row of regularly distributed bright luminescence spots becomes clearly visible for the D = 900 nm (left-hand image) and D = 960 nm (the image in the center of Fig. 7.9) apertures. The spots are located in the middle of a 800 nm wide ZnSe matrix stripe and emit light at a photon energy of 2.718 ± 0.006 eV and 2.747 ± 0.006 eV, respectively, i.e., well below the energy gap of ZnSe [CL spectra of individual spots are shown in Fig. 7.11(a)]. This clearly indicates the presence of CdZnSe inclusions embedded in the ZnSe matrix for D ≤ 960 nm. The CL originating from ZnSe, at a photon energy of 2.801 eV, is homogeneous along the stripes (see Fig. 7.10, left panel, for a D = 1060 nm structure), and less intense than that of the CdZnSe dots [see Fig. 7.11(a)]. For larger center to center distances of the apertures (D ≥ 980 nm) only the homogeneous CL of the ZnSe matrix is observed. These observations are strong evidence that the bright spots indeed originate from CdZnSe QW islands, which were selectively grown in the overlap region of the Se and Cd fluxes, as it is sketched in Fig. 7.4. For D ≥ 980 nm the incidence regions of the beams do not overlap and no CdZnSe islands are grown (see the right-hand image of Fig. 7.9). The increase of the spacing between the apertures by only 20 nm effectively prevents the formation of the islands. This implies that Cd and Se atoms, at our growth condition, diffuse over distances smaller than 20 nm.

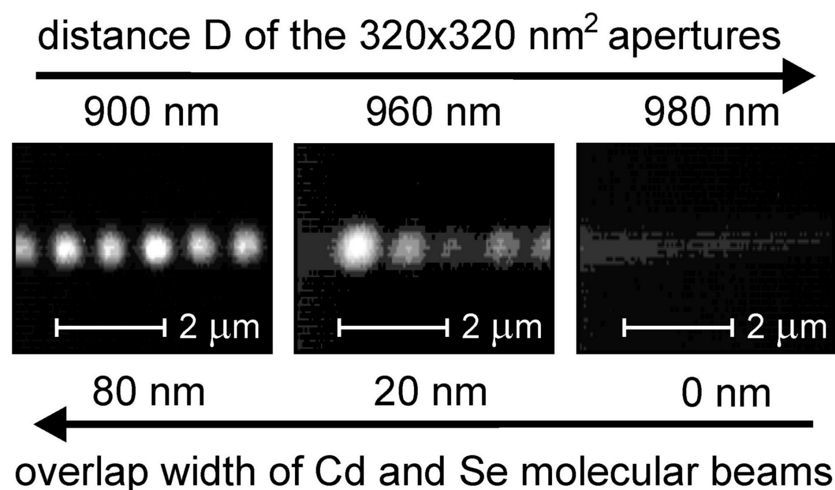

FIG. 7.9 – *Micrographs of the CL intensity (at 6 K) of a ZnSe matrix stripe with (and without) embedded CdZnSe quantum-well islands. The shadow mask has been removed after growth. The original distances D of the rectangular apertures (effective width: W_{eff} = 80 nm) of the mask were 900, 960, and 980 nm. The width of the overlap region where both Cd and Se are impinging is 80, 20, and 0 nm, respectively.*

II. Unintentional incorporation of Cd The case when Cd and Se beams do not overlap (D = 1060 nm) has been investigated more closely. During the growth, the Cd beam impinges for 90 s on the ZnSe mesa. Thus, a small amount of Cd ions is incorporated into the ZnSe matrix. Figure 7.10 shows CL micrographs of the structures, which are obtained for D = 1060 nm. The left-hand micrograph shows the CL at a photon energy of 2.801 eV, i.e., the excitonic emission of the ZnSe matrix. This homogeneous signal exhibits the maximum CL intensity because no CdZnSe islands are present. A different behavior is observed 5-6 meV below the ZnSe band gap: The right-hand micrograph shows the CL intensity at 2.795 eV, which is modulated along the ZnSe stripe. This indicates that even though no direct Se beam

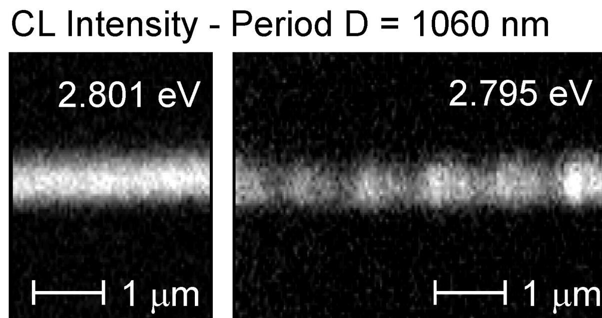

FIG. 7.10 – *Monochromatic micrographs of the CL intensity (at 6 K) of a ZnSe matrix stripe for an energy of 2.801 and 2.795 eV and for an aperture distance of 1060 nm. No CdZnSe islands are embedded in the matrix, but the CL intensity is modulated 5 meV below the ZnSe excitonic emission.*

was present, small amounts of Cd are locally adsorbed and incorporated into the ZnSe matrix. This decreases the band gap energy locally by about 5 meV.

In contrast to unintentional incorporation of Cd, ZnSe is deposited (with similar growth rate of CdZnSe) in the region where Se (no Cd) impinges on the substrate because Zn is present on the entire mesa. However, this local structure does not create additional CL features since ZnSe is the matrix material.

III. CL of nanoscale QW islands Figure 7.11(a) shows CL spectra taken at 6 K from QW islands (A,B) of different size and a reference CL spectrum taken from the unpatterned QW. The QW emits light at a photon energy of 2.692 eV. The full-width at half maximum (FWHM) of the peak is 9 meV broadened at the low-energy tail. It is obvious that the CdZnSe layer forms a QW and does not consist of self-assembled quantum dots. Islands A and B [CL spectra shown in Fig. 7.11(a)] were fabricated with the D = 900 nm and D = 960 nm spacing between the apertures, respectively. Thus, the overlap width of Cd and Se beams, which defines the length of an island is at maximum 80 and 20 nm, respectively (see Fig. 7.9). In addition to the length, the width of the islands varies since apertures of different width were employed. The effective width W_{eff} of the openings is 80 nm (island A) and 30 nm (island B). The spectra taken from QW islands show very different characteristics than the reference QW. The topmost spectrum of Fig. 7.11(a) [island A] is representative for a large QW island emitting light at two main luminescence lines, which are separated by 8.5 meV. The observed emission lines (FWHM $\approx$ 2 meV) are much sharper than the lines in the reference spectrum indicating that the excitons are stronger confined on a nanoscale island.

Doublet luminescence is characteristic for all islands, as demonstrated by Fig. 7.11(c), which shows a micrograph of the wavelength $\lambda_{\max}$ (indicated by the brightness) for

which maximum luminescence intensity is measured [The micrograph has been taken from the same section of the sample, as the left panel in Fig. 7.9 (D = 900 nm)]. The dashed lines indicate the edges of the ZnSe mesa with embedded A-type QW islands. As is clearly seen, each island is surrounded by an inner circular region and an outer ring with different λ_{max}, which correspond to the two main luminescence lines of A-type CL spectra [see Fig. 7.11(a)]. While the luminescence wavelength, varies for different islands, the separation between the doublet lines is 8.6 ± 1.0 meV for each island. Obviously, the relative intensity of the peaks depends on the excitation intensity, which decreases with the distance of the excitation spot from an island. At high excitation (near an island), the maximum CL intensity corresponds to the low-energy signal, while the high-energy signal dominates the spectrum when the excitation intensity is decreased.

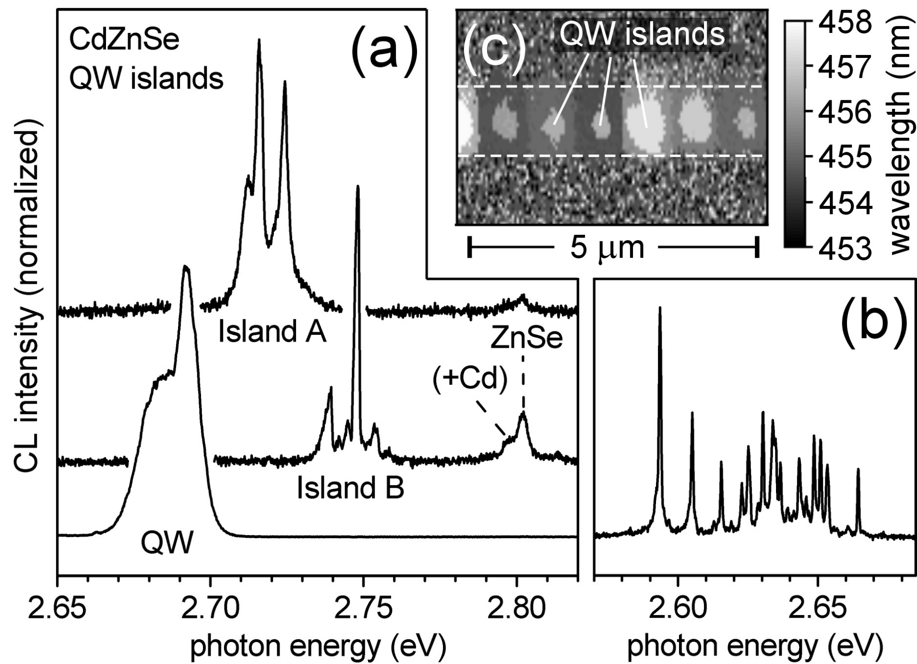

FIG. 7.11 – *(a) CL spectra (at 6 K) of CdZnSe quantum-well islands (A,B) in ZnSe barriers and a reference spectrum of the QW layer. Islands A (B) were grown through a mask with openings of effective width* W_{eff} = *80 nm (30 nm) and D = 900 nm (960 nm) spacing between the apertures. (b) CL spectrum (at 6 K) of a CdSe deposit in ZnSe barriers, which was grown through a mask (*W_{eff} *= 80 nm) with growth conditions favoring self-assembly of QDs. (c) Micrograph of the wavelength of the maximum CL intensity of A-type QW islands (D = 900 nm), which are embedded in a ZnSe matrix stripe.*

The relative intensity of the emission peaks depends also on the island dimensions. When the island size is reduced (by reducing the overlap width or W_{eff}), the peaks shift to higher energy, and the relative intensity of the low-energy peak is decreased. The middle spectrum of Fig. 7.11(a) [island B] shows the CL spectrum of a small QW island with an intense peak found at 2.747 eV (FWHM limited by the spectral resolution of the experiment) and, 8 meV below, the less intense signal of the low-energy peak (FWHM ≈ 3 meV). In addition to the doublet, luminescence lines of low intensity (at 2.745 and 2.754 eV) appear in the CL spectra. All these signals disappear when the incidence regions of Cd and Se are separated (D > 960 nm). Thus, one can conclude that the doublet and additional less intense CL lines originate from CdZnSe selectively grown in the overlap of the beams.

Apart from the edge region of the CdZnSe growth area, the thickness and composition of the QW are not spatially modulated by flux gradients caused by the

geometry of the experiment. On the other hand, fluctuations of the composition and thickness may result in localized states and thus explain why multiple CL lines are observed in the spectra of island A and B. In the previous section, nanoscale CdSe deposits embedded in ZnSe have been investigated, whose CL spectra are characteristic for localized states induced by spatial fluctuations of the composition, i.e., the CdSe deposits consist of self-assembled QDs. A CL spectrum acquired from a CdSe deposit of A-type island dimensions (effective aperture width W_{eff} = 80 nm) is shown in Fig. 7.11(b). The difference between the spectra of CdSe deposit and CdZnSe QW islands is striking. The spectrum of the CdSe deposit [see Fig. 7.11(b)] consists of many randomly distributed emission lines, which correspond to different luminescence centers (i.e., QDs) and the maximum intensity peak (maximum intensity micrograph not shown) is determined by the direction between island and excitation spot, not just by the distance. In contrast, CL spectra in this study [see Fig. 7.11(a)] are characterized by emission lines, which correlate in energy and intensity as is demonstrated by Fig. 7.11(c). Thus, one can exclude that multiple luminescence lines in the case of CdZnSe originate from different locations within a QW island.

In conclusion, the doublet and additional CL lines below 2.79 eV originate from ground and excited states within the confinement potential of a nanoscale QW island. Lateral confinement is due to the potential gradient near the island edge, where composition and thickness of CdZnSe change gradually because of diffusion effects and the flux gradient of the partial shadow. Although the diameters of islands A (~80 nm) and B (~20 nm) are relatively large, the extension of the exciton, i.e., wave function in the ground state is expected to be significantly smaller because the lateral barrier (edge region) extends 20-30 nm into the island. This explains the observation of a set of luminescence lines and the blueshift of the CL on decreasing island dimensions. This is analogous to the behavior observed in "quantum dots" created by selective thermal interdiffusion for the lateral modulation of the band-gap of a QW (using focused ion beam lithography or patterned SiO_2 masks).[Bacher99] However, the lateral control of our method is more precise (diameter 20 nm instead of 100 nm) and *in situ* fabricated "quantum dots" (nanoscale QW islands) do not suffer from defects induced by ion implantation and thermal annealing.[Bacher99]

7.2.5 Growth of CdSe without direct Se flux

Here, the CL spectra observed from the CdSe sample are discussed as a function of the spacing D between the mask-apertures. Fig. 7.12(a) shows spectra of the integral CL of 7 CdSe deposits (W_{eff} = 180 nm) and the ZnSe matrix in which they are embedded in. The corresponding distance D between the rectangular apertures is 900, 960, and 1060 nm, respectively. The dashed curves represent reference spectra of CdSe grown without a shadow mask, which were acquired near the corresponding CdSe deposits. Contrary to the sample containing CdZnSe QW islands, all CL spectra indicate the presence of CdSe inclusions in the ZnSe matrix by the bright CL observed below the energy gap of ZnSe. This signal shifts from 2.53 eV to 2.62 eV, when the spacing D between the small apertures is increased from 900 to 1060 nm (The reference spectra confirm that the energy shift is caused by the shadow mask. The energy shift caused gradients of the source flux is just 10 meV). Due to the growth geometry, the incidence regions of Cd and Se overlap for D = 900 nm, and are separated for D = 1060 nm. Since, neither Cd nor Se adatoms diffuse over distances larger than 20 nm, the CdSe deposits observed for D = 1060 nm are grown with secondary fluxes in the mask cavity. This can be understood in terms of the growth procedure: The CdSe was deposited in short pulses, interrupted by 20 s under Se flux.

During the pauses, Se does not stick on the (Se-saturated) surface, and thus produces a secondary flux in the mask-cavity, which is of the same order as the pressure of the direct Se beam [see Fig. 5.3(a)]. Hence, CdSe deposition rates with pulsed deposition are about the same in the domain of the Cd beam and in the overlap of the incidence regions of Cd and Se.

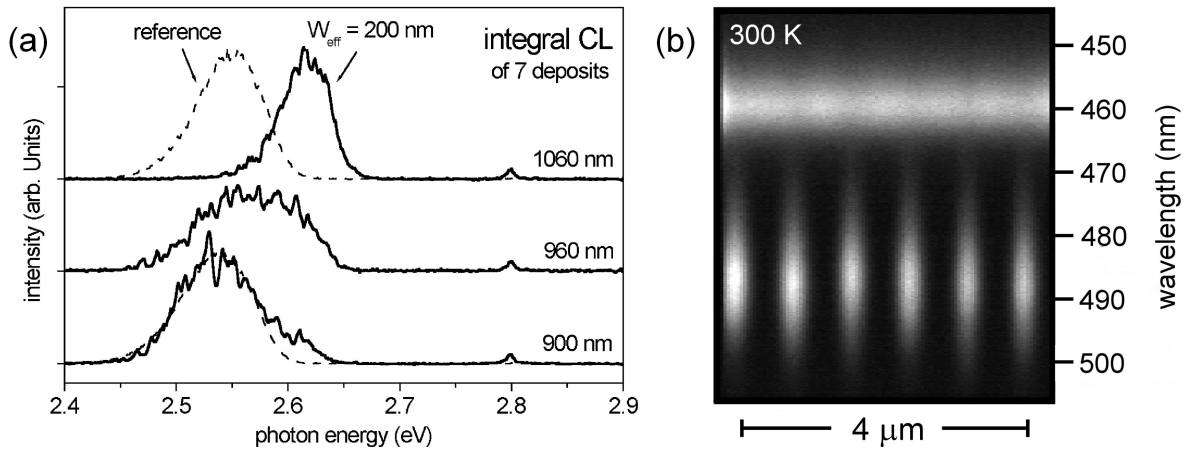

FIG. 7.12 – *(a) Spectra of the integral CL of a ZnSe matrix stripe with 7 CdSe inclusions (solid line) and of the reference CdSe layer (dashed line). The spacing D between the small apertures (W_{eff} = 180 nm) is 900, 960, and 1060 nm, respectively. (b) Room temperature CL spectra line scan along a ZnSe matrix stripe with 6 CdSe inclusions (W_{eff} = 180 nm).*

This also explains the energy shift of the CL signal by 90 meV. The CL signal at 2.62 eV corresponds to CdSe, which is grown by exploiting the Se secondary flux (D = 1060 nm). A higher growth rate is caused by the additional direct Se flux when the incidence regions of Se and Cd overlap. Hence, the corresponding CL is observed at a lower energy (E = 2.53 eV). The broad emission line width for D = 960 nm [see Fig. 7.12(a)], can thus be understood by the superposition of the two peaks, when the beams partially overlap. This also explains the high-energy tail of the D = 900 nm spectrum. Remarkable is that a high optical quality has been obtained for the growth with direct Se flux (CL at 2.53 eV) and without direct Se flux (CL at 2.62 eV).

Figure 7.12(b) represents CL measurements on a ZnSe matrix with CdSe inclusions at room temperature. The spectra line scan demonstrates that a bright CL signal originates from the CdSe inclusions, which were grown with the secondary Se flux (without direct Se flux).

7.3 Shadow mask assisted self-organized growth of nanostructures

At first glance, III-V shadow mask assisted SAE may appear much more difficult than its II-VI counterpart, where the growth area is spatially restricted (on the nanometer scale) to the incidence region of adatoms. This is because group-III adatoms on the surface of a growing III-V epilayer are very mobile. Their surface diffusion length exceeds 1 μm at normal growth conditions, which would appear to make *in-situ* nanofabrication by selective deposition through shadow masks impossible. However, based on the investigations of molecular beam epitaxy of III-V materials through epitaxial shadow masks (see Sect. 6.2) a novel approach has been developed, which can be used to control self-organized growth of III-V nanostructures. The method is based on the surface diffusion of group-III adatoms governed by the group-V surface concentration. Lateral control is achieved by the geometry of the mask and the incidence angles of the molecular beams. The method has been applied to self-organized growth of nanoscale InAs quantum wires at the step-edge of the arsenic beam. The high quality of *in situ* fabricated nanostructures is confirmed by bright cathodoluminescence of InAs quantum wire embedded in GaAs barriers. In addition, it is demonstrated that based on the new mask concept presented in Sect. 4.1.4, one can control self-assembly of nanoscale GaAs dots at predefined places on a planar mesa structure.

7.3.1 Experiments

The shadow masks used in the experiments consist of a 1.16 μm thick $Al_{0.6}Ga_{0.4}As$ spacer and a 140 nm thick GaAs cap. The stripe apertures of the mask, whose width ranges from 1 to 10 μm, were defined by photolithography. The arsenic source is a valved cracking cell, in which the thermal cracking zone is kept at 560°C. The angular dispersions $\delta\varphi$ of the In, Ga, and As molecular beams are 10°, 5°, and 5°, respectively. Thus, the width of the partial shadow is ~100 nm for Ga and As beams.

After defining the masks, the samples were loaded into the growth chamber and thermally cleaned for three minutes at a temperature of 610°C and a As beam equivalent pressure (BEP) of 5.0×10^{-7} torr, in a configuration where the As beam impinged at an incidence angle of $\varphi_\perp = +9°$. For the first sample, a 150 nm thick GaAs buffer was grown at a substrate temperature of 580°C with Ga and As BEPs of 1.0 and 3.0 $\times10^{-7}$ torr, respectively. The configuration was such that both the beams were set at $\varphi_\perp = +9°$ and hence a GaAs mesa grew in the region of common incidence of the beams [see black arrows in Fig. 7.13(a)]. Thereafter, the sample were cooled to 480°C and a 20 nm thick InAs layer was grown in a configuration such that In (BEP: 3.0 $\times10^{-7}$ torr) and As (BEP: 5.0 $\times10^{-7}$ torr) incidence angels were $\varphi_{\perp,In} = +11°$ and $\varphi_{\perp,As} = -33°$, respectively. Consequently, In impinged directly onto the area of the GaAs mesa [black arrows], while the incidence region of the As beam is offset by 1.0 μm relative to the mesa [white dashed arrows in Fig. 7.13(a)], or 0.7 μm relative to the aperture. Outside the incidence region of the As beam, the As flux should not be considered zero because of the As overpressure. Non-sticking As molecules reflected from the walls of the cavity, result in a finite secondary flux within the mask, which effectively prevents the segregation of elemental group-III material (droplets).

A second sample, optimized for optical characterization, was fabricated in a very similar way. However, instead of layer 20 nm thick, only 4 monolayers (= 1.2 nm) of InAs were deposited onto the GaAs mesa. Subsequently, the InAs deposit was covered by a 100

nm thick GaAs cap. The GaAs cap was grown at the initial configuration where both Ga and As impinged on the same area of the mesa. The shadow mask was lift-off before cathodoluminescence (CL) characterization. The CL experiment was carried out at 6 K with an electron current of 1 nA and an electron energy of 7 keV in a JEOL JSM 840 system (described in Ref. [Christen91]).

7.3.2 SEM investigations on the reference sample

Figure 7.13 show SEM images of the cleaved $[1\bar{1}0]$ edge of the first sample. The images are stretched in the growth direction in order to exhibit the details of the shallow structures, which were fabricated using the shadow mask. The GaAs mask with a 2.36 μm wide aperture can be observed at the top of Fig. 7.13(a). The dashed lines indicate the directions of incidence of the molecular beams during the growth of (1) the GaAs mesa (black lines for both Ga and As) and (2) the InAs deposit (black lines for In beam, and white lines for As beam). The 150 nm thick GaAs mesa extends between the black lines. A considerable amount of material deposition is also observed on the right-hand side of the mesa. These pyramidal structures can be associated with the deposition of InAs because their location coincides with the edge of the As flux (the right white line). A similar structure is visible on top of the GaAs mesa. Again, its position coincides with the (left) boundary of the As beam (see the left white line). Figure 7.13(b) shows a cross-section of this structure at a higher magnification. As can be seen, the base of the triangle is 200 nm wide and the side walls appear to be smooth crystal planes. Figure 7.15(a) shows that the structure is continuous along the mask aperture, which demonstrates the self-formation of a nanoscale InAs wire at the step-edge of the As beam.

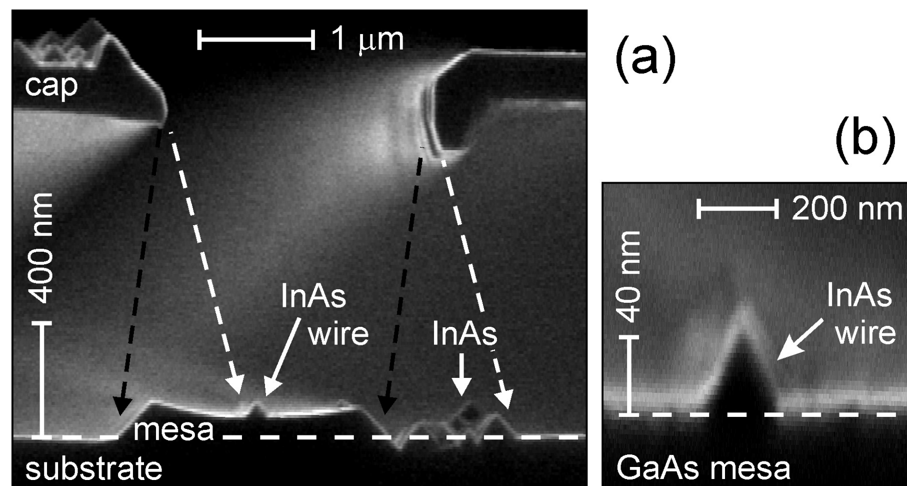

FIG. 7.13 – *(a) Scanning electron micrograph of the cross-section of a shadow mask after SAE growth of a GaAs mesa (between the black lines) and a nanoscale InAs wire at the left edge of the arsenic incidence region (white lines). During InAs deposition, In atoms impinged between the black lines. (b) Higher magnification of the triangular shaped InAs wire formed on top of the GaAs mesa.*

7.3.3 CL investigations on the InAs QWR sample

CL measurements on the second sample are shown in Fig. 7.14. In this case, the GaAs matrix stripe (dashed lines indicate the edges) is 6.5 μm wide and, as discussed,

InAs quantum structures are embedded in the matrix. The CL micrograph in Fig. 7.14(a) shows the CL intensity integrated over the spectral range 920-980 nm. At 1.30 eV, bright CL originates from a narrow stripe centered at 0.9 µm from the left edge of the mesa stripe, which coincides with the left-hand limit of the As flux during the deposition of InAs. As can be seen, the CL signal is continuous along the stripe while the narrow spatial width is limited by the resolution of the experiment. One can assume thus, that the InAs deposit forms a QWR with triangular cross-section similar to the one observed in the first sample in Fig. 7.13(b). The dimensions of the wire are, however, much smaller because much less InAs was deposited (only 5.6 % of the first sample). For narrower GaAs matrix stripes a blue-shift of the "QWR" signal (w = 4.3 µm: 1.35 eV) has been observed, which suggests that less InAs is deposited at the step edge of the As beam. In this case, the CL intensity is broken along the stripe, which indicates that self-organized growth of InAs QWRs initiate in spots (eventually forming QDs) distributed along the stripe.

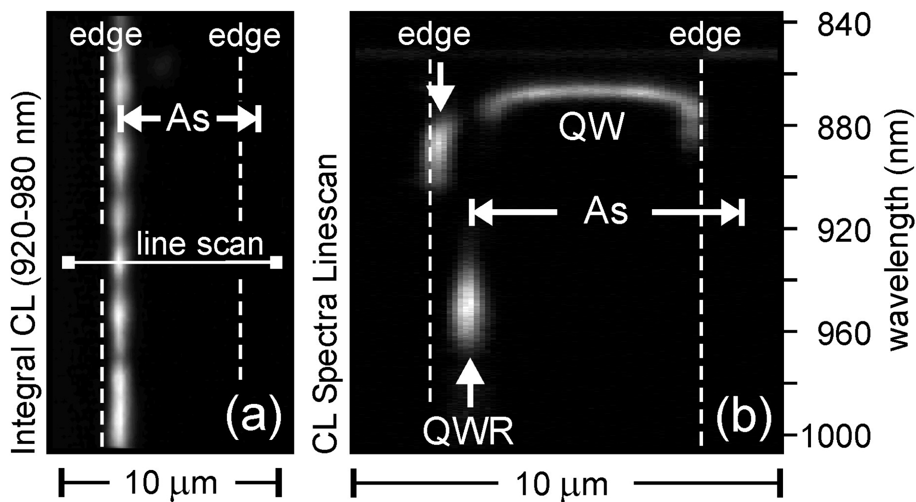

FIG. 7.14 – *CL (at 6 K) of InAs quantum structures in a GaAs matrix stripe. The CL intensity is indicated by the brightness of the image and dashed lines show the edges of the stripe. (a) Micrograph of the integrated CL intensity (λ = 920 – 980 nm) of a InAs QWR which was selectively grown at the edge of the As beam. (b) CL spectra line scan across the matrix stripe with embedded QWR, QW and additional InAs deposits near the edges.*

Figure 7.14(b) shows a spectrally resolved CL scan across the 6.5 µm wide GaAs matrix. The abscissa represents the location of the exciting electron beam and the ordinate, the emission wavelength (λ). The CL intensity is indicated by the brightness of the image. As can be seen, the QWR signal (at 950 nm) is accompanied by luminescence at 865 and 890 nm. The short wavelength signal at 865 nm corresponds to a very thin InAs quantum well (QW), a so-called wetting layer, homogeneously distributed in the incidence region of the As beam. Only near the right hand edge, the signal is red-shifted, which indicates the self-assembly of InAs QDs (or QWR) selectively at the edge of the matrix stripe. This can be attributed to the facet-dependent migration of In adatoms, which is known from previous studies.[Tsui97, Konkar98] The same effect also explains the origin of the CL signal at λ = 890 nm, which is observed at the left hand edge [see Fig. 7.14(b)]. Comparing the CL intensities of the InAs deposits (at λ = 865, 890, and 950 nm), one finds that the maximum CL intensity corresponds to the InAs QWR formed at the step-edge of the arsenic flux, suggesting that a good optical quality has been achieved. The intensity contrast is further enhanced (up to factor 4) for bright CL spots distributed along the step-edge in case of a narrow matrix stripe (w = 4.3 µm).

7.3.4 Discussion

The SAE growth of InAs nanowires observed here is caused by surface migration of the In adatoms, which is spatially controlled by the As flux. The corresponding flux distribution, as a function of the lateral position (on the substrate) is shown in Fig. 7.15 (see dashed line). Due to a gradient in the surface concentration, In adatoms effectively diffuse from regions not exposed to As flux to regions which are exposed to a high As flux, where they locally increase the growth rate of the layer. In the shadow mask experiment, InAs is preferentially grown near the edges of the incidence region of the As beam [see Fig. 7.13(a) and Fig. 7.14(a)] because the diffusion current is maximum at the step-edge of the As flux. The shape of the InAs wire in case of the first sample [see Fig. 7.13(b)] indicates that a mechanism other than surface diffusion is involved in the self-ordering process. Based on the diffusion model [see Eq. (3.1)], one expects an exponential reduction of the wire thickness with distance from the step edge (on the scale of the incorporation diffusion length). Faceting of the planes enclosing the InAs wire [Fig. 7.13(b)] is probably driven by elastic stress and the orientation dependency of the diffusion coefficient.

In conclusion, the driving force for the wire formation is obviously surface diffusion of In adatoms, caused by the nonuniform distribution of As flux, but the shape and the width of the nanoscale InAs wires (first sample: 200 nm) are not controlled entirely by this simple diffusion mechanism, which in principle would result in a much wider structure. In case of the first sample, the diffusion length of In adatoms is obviously much larger than 1 μm, because the largest fraction of InAs is deposited near the right-hand edge of the As beam [see Fig. 7.13(a)] where the As flux is maximum (because the secondary flux of As is maximum in the under etched region). That is, distant from the regions where In adatoms impinge on the substrate.

7.3.5 Growth on the mask-cap

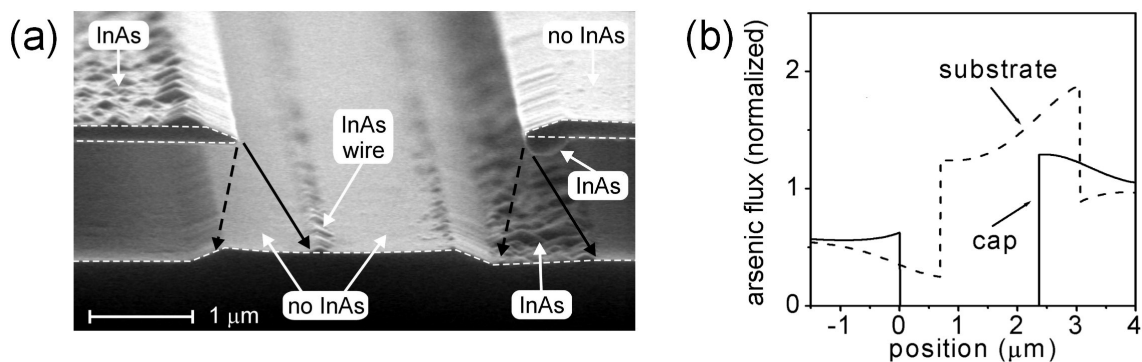

FIG. 7.15 – *(a) Electron micrograph of an epitaxial shadow mask with InAs deposits [see also Fig. 7.13(a)]. White dashed lines indicate the interface of the GaAs substrate and the mask. The black arrows indicate the incidence directions of In (dashed line) and As (solid line). (b) Normalized arsenic flux on the substrate and on the under-side of the mask.*

Based on the model, the observations on the mask-cap can also be explained. As can be seen in Figs. 7.13(a) and 7.15(a), InAs deposits are clearly visible on the left wing of the mask, whereas only a negligible amount of InAs is observed to have deposited onto the right wing. In contrast, some deposition can be seen on the bottom side of the right wing of the mask. These features can be understood by surface diffusion phenomena, resulting from the interactions between the constituent species of compound materials.

Such effects may also be important for the growth of III-V materials on patterned substrates. The solid curve in Fig. 7.15(b) shows the calculated flux distribution of arsenic on the under surface of the mask's cap layer. As can be seen, near the side-walls of the mask-cavity the arsenic flux (solid line) approaches the same value as that of the flux on the substrate (dashed line). As a result of the non-normal incidence of the arsenic beam, the incidence region on the substrate is offset to the right (relative to the aperture). The secondary As flux on the bottom side of the cap, therefore, increases on the right wing. In particular, it is maximum near the aperture ($f_{As} > 1.2$) and the calculated flux exceeds the primary flux of the direct beam, ($f_{As} = 1$) which impinges on the top-side of the cap. As a result of surface diffusion [Eq. (3.1)], In adatoms effectively diffuse from the top to the bottom side of the cap, which explains the observed InAs deposit on the under surface of the right wing of the mask. In a ~3 µm wide stripe on the mask, no InAs pyramids were formed, suggesting that the surface diffusion length of In adatoms exceeds this value in the experiment. In contrast, on the bottom side of the left wing of the mask, the secondary arsenic flux is slightly smaller ($f_{As} < 0.8$) than the direct beam flux. Because of this, there is no effective migration of In adatoms from the top side to the bottom side of the left wing.

7.3.6 III-V SMMBE exploiting multiple, nanoscale apertures

Finally, it is demonstrated that freestanding shadow masks with multiple, nanoscale apertures enable a more direct definition of the growth areas of III-V nanostructures than the approach presented in the previous section. The geometry of the shadow masks and the growth configurations are similar to those of the II-VI experiments presented in Sect. 7.2 (see Fig. 7.4). In this case, (a) the thicknesses of the spacer and the mask-cap, (b) the width of the stripe aperture, and (c) the center-to-center distance between the stripe aperture and the parallel row of rectangular holes are (a) h = 1.16 µm, g = 140 nm, (b) 1.0 µm, and (c) 1.1 µm, respectively. The separation between the rectangular holes is D = 1.0 µm (in the stripe direction). Unlike the masks used in Sect. 7.2, the width W varies for different ($W \times L$) holes of the same stripe (from 100 nm up to 280 nm in steps of 20 nm; L = 205 nm).

Since, no pinholes was employed in the experiments, the angular dispersion of the molecular beams was $\delta\varphi \approx 5°$ for Ga and As, which corresponds to a partial shadow width of ~110 nm. In the III-V growth chamber, a nominally 133 nm thick GaAs buffer layer was grown at a substrate temperature of 600°C and with Ga and As BEPs of 0.55 and 3.4 $\times 10^{-6}$ torr, respectively. This was done in a configuration with parallel molecular beams ($\varphi_{\perp} = +11°$), resulting in the formation of a mesa structure. Thereafter, the sample configuration was changed to one wherein only As molecules passing through the small rectangular holes ($\varphi_{\perp,As} = +33°$) and Ga atoms passing through the stripe aperture ($\varphi_{\perp,Ga} = +11°$) impinged on top of the mesa. Subsequently, a nominally 30 nm thick GaAs layer was grown at a substrate temperature of 610°C and with Ga and As BEPs of 0.55 and 8.0 $\times 10^{-6}$ torr, respectively. Directly after the growth, the substrate temperature was reduced to 300°C in the same configuration and in an As rich ambient.

Figure 7.16 shows a three-dimensional AFM height profile,[A] which has been recorded from a 2.9×2.9 µm² area of the sample after lift-off of the shadow mask. The total height range of the plot is 171 nm. In the middle of the scan area, one can clearly identify a stripe-shaped GaAs mesa, which deposited in the first growth configuration through a stripe aperture of the mask. The top surface of the mesa is planar, except for three nanoscale deposits in the center of the stripe. Obviously, the nanostructures have

[A] RASTERSCOPE 4000 AFM (Danish Micro Engineering). For an introduction to the AFM technique, see Ref. [Binnig86].

selectively formed (during the growth of GaAs in the second configuration) in the nanoscale incidence regions of the As beam (separated by 1 µm), as a result of the migration of Ga adatoms, governed by the As flux distribution.

Unlike previous experiments where the incorporation rate of the migrating group-III adatoms was maximum at the edge of the incidence region of the As beam (see Figs. 6.7 and 7.13), the GaAs deposits have a peak in the center of the nanoscale incidence region. The different heights and widths of the shown deposits correspond to the different widths of the mask-aperture. Only the larger structures have a planar top surface, which is tilted in the direction perpendicular to the stripe (see dotted curve in the right plot of Fig. 7.16). When the width *W* of the apertures is reduced, both the width and the height of the GaAs deposits become smaller. In contrast, the length of the GaAs deposits in the direction parallel to the stripe is constant (FWHM ≈ 140 nm; see curves A, B, C in the right plot of Fig. 7.16).

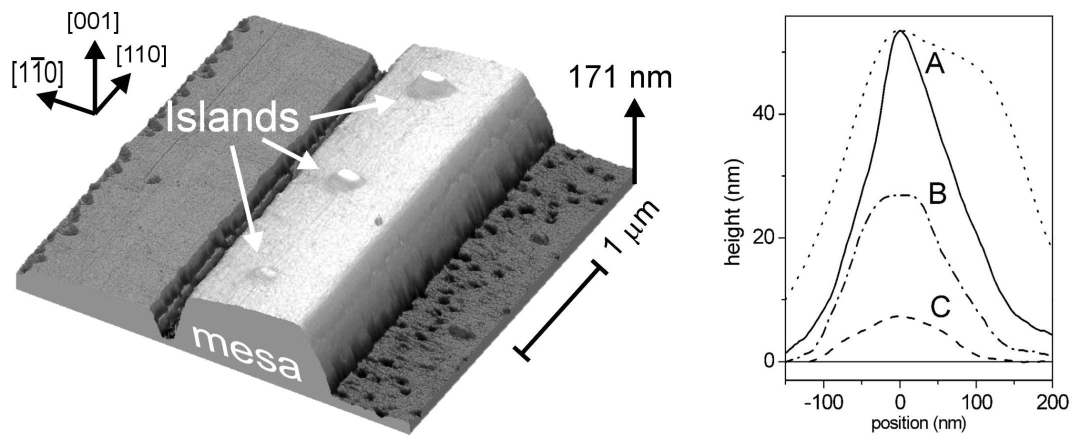

FIG. 7.16 – *(Left) Atomic force micrograph of a GaAs mesa stripe with nanoscale GaAs islands on the top of the mesa. The scan range is 2.9×2.9 µm², and the total range in growth direction is 171 nm. (Right)* [1$\bar{1}$0] *cross-sections of nanoscale deposits grown through apertures of different width W. The dotted curve shows the* [110] *cross-section of deposit A.*

These observations suggest that the shape of the deposits formed in the As incidence regions is governed by the flux distribution caused by the partial shadow of the As beam [see Fig. 4.7(b)]. Moreover, the incorporation dynamics correspond to the case of the model where the diffusion length L_0 of the group-III adatoms is large compared to the width of the group-V incidence region w_0 (see Fig. 5.5), which is a reasonable assumption for the nanoscale size of the As incidence regions. Eventually, SMMBE can control the shape of individual III-V nanostructures by tailoring the flux distribution of the group-V flux. In the experiment, the minimum structure size was limited by the partial shadow of the As beam. It can therefore be expected that reducing the dispersion of the molecular beams by employing pinholes [see Fig. 4.7(a)] would reduce the minimum size of SMMBE grown III-V nanostructures to ~10 nm.[A]

[A] The surface diffusion of As molecules is limited and does probably not limit the minimum structure size (see appendix A.4).

Summary of Chapter 7

Because SMMBE of II-VI and III-V materials is governed by different surface kinetic processes, a number of different approaches have been developed to enable the fabrication of the two classes of compound semiconductor nanostructures.

In the case of II-VI SMMBE, due to the limited surface migration, the growth rates within the (nanoscale) incidence regions of the molecular beams are constant, except for flux-gradients in the edge regions caused by the partial shadow. Thus, based on the technological progress regarding partial shadow effects and freestanding masks with mask apertures of different shapes and sizes, selected area growth of II-VI nanostructures and subsequent overgrowth has been achieved. Cathodoluminescence has shown that the resulting embedded quantum structures are of high structural and optical quality. The method has also been applied to epitaxy with three molecular beams, which enables the selected area growth of ternary QW islands with precisely defined lateral dimensions (smallest islands: ~20 nm), limited by partial shadow effects. Cathodoluminescence of nanoscale QW island exhibits features that suggest the observation of multiparticle states from within a zero-dimensional structure. The interpretation is that a single QD is obtained without entering the Stranski-Krastanov growth regime.

During the SMMBE process, the incidence angles of the molecular beams can be adjusted by controlling the sample position in the growth chamber. This real-time manipulation has been used to control both the position and size of the growth area and, therefore, the dimensions of the resulting nanostructures without changing the dimensions of the apertures. The latter has been demonstrated by selective growth on substrate regions where the incident molecular beams, impinging through different apertures of a freestanding mask, overlap.

A high secondary flux of one constituent species below the shadow mask can also be exploited for the SMMBE growth of nanostructures. Experiments have shown that a high secondary flux for one species can be achieved by a high flux ratio or, alternatively, by a pulsed deposition technique. Under these conditions, compound material deposits in the entire incidence region of the species with the lower flux, irrespective of the incidence angle of the species with the higher flux. Thus, only the incidence angle of one molecular beam has to be controlled with precision, which is important because the range over which the incidence configurations of two or more molecular beams can be adjusted is limited.

In II-VI SMMBE using freestanding masks, quantum structures can be defined directly by the nanoscale incidence regions of the molecular beams. A different approach is based on the selected area growth of short period superlattices, which act as a lateral potential barrier structure. This method has been used for the fabrication of ZnSe QWRs with high optical quality by overgrowing a single, photolithographically defined, shadow edge. In contrast to the cleaved edge overgrowth technique [Pfeiffer90] (which uses a similar concept) the confining potential barrier is high enough to confine excited carriers in the ZnSe QWR at room temperature.

II-VI SMMBE not only allows the fabrication of low dimensional quantum structures without entering the Stranski-Krastanov growth regime, but also makes possible the controlled self-assembly of nanoscale QDs in selected areas. Two approaches have been pursued. The first one is based on selected area growth of CdSe, resulting in the formation of QDs within nanoscale deposition areas. The

second method relies on the selected area growth of short period superlattices, consisting of ZnSe barriers and strained CdSe layers. The spontaneous nucleation of QDs was essentially prevented by the deposition of the ZnSe barriers (in selected areas), even though the total thickness of the CdSe layers exceeded the critical thickness.

In III-V SMMBE, the large diffusion length of group-III adatoms, apparently, makes in situ nanofabrication by selective deposition through shadow masks impossible. A novel approach has been developed to come round this limitation. The method relies on the shadow mask assisted control of the arsenic flux, thereby modulating the surface concentration of group-III adatoms laterally. Surface diffusion, which is induced by gradients of the surface concentration, transfers adatoms from regions with low As flux to regions with high As flux. The step edge of the As beam flux causes a sharp local increase of the growth rate, a fact which has been exploited for the self-formation of nanoscale InAs wires at the edge of the As incidence region. Moreover, it has been demonstrated that freestanding shadow masks with nanoscale apertures can directly control the growth areas of nanoscale GaAs islands on a planar surface. Previous attempts (e.g., [Tomita95, Songmuang01]) to employ shadow masks for the selected area growth of III–V nanostructures were unsuccessful because the role of the group-V flux for the surface diffusion of group-III adatoms was not considered.

Chapter 8

Potential and limitations of SMMBE

In this chapter, the potential and limitations of SMMBE are discussed.[A] *The experiments presented in Chaps. 6 and 7 have already demonstrated that SMMBE allows versatile and precise SAE growth of both II-VI and III-V nanostructures with a high structural and spectroscopic quality. In addition, in Chap. 4, the various technological aspects have been discussed and the technological innovations, required for the experiments, have been introduced.*

Sections 8.1 and 8.2 discuss the technological limitations which still remain and suggests various approaches to overcome them. In particular, advanced shadow mask technology has the potential to solve most of the limitations which are due to the chamber geometry.

Section 8.3 discusses the limitations of SMMBE, which are due to the redistribution of the species via repetitive desorption (causing secondary flux) and surface diffusion, which may affect the growth rate, the composition of alloys and the material quality.

In Sect. 8.4, it is shown that the versatility of SMMBE selected area growth can be enriched by pattered SAE techniques, non-local growth techniques, and shadow mask assisted etching in selected areas. Moreover, selected area growth can be combined with shadow mask assisted (electronic and magnetic) doping and in situ contact formation in selected areas. Hence, the main potential of the SMMBE technique is the fabrication of complex quantum devices with prospective electronic, optical, and spintronic functions.

[A] The discussions in this chapter are based on our understanding of the growth regime in the mask-cavity (Chap. 5), the experience from the innovations and experiments presented in Chaps. 4, 6 and 7, and on the literature. Unlike Chaps. 4, 6 and 7, only a few aspects are illustrated by additional experiments.

8.1 Limitations due to the geometry

SMMBE through stationary shadow masks is controlled by the geometry of the mask and the angle of incidence of the molecular beams on the sample. In Chap. 4, several limitations of the beam control are discussed and methods are presented, which have been used to overcome them. This section discusses which limitations remain and presents additional approaches to enhance the precision and the versatility of SMMBE, and discusses their applicability.

8.1.1 Dependent incidence angles of the molecular beams

In a conventional growth chamber, the incident beam directions are controlled by adjusting the position of the shadow mask sample relative to the stationary beam sources. In the RIBER 32 MBE system, which was used for the experiments of this study, two coordinates define the sample position. Hence, it is not possible to control the incidence directions of two (or more) beams independently.[A]

I. Modifications of the growth chamber The ideal solution to this problem is a *growth chamber with in situ, movable sources*, whose positions can be adjusted independently. However, the construction of such a UHV chamber would be a technical challenge, because it requires a complex UHV suited mechanical system, which has to work accurately and reliably and has to withstand material deposition. Less difficult is probably the construction of *sources with movable exits*. This could be realized, e.g., by means of a valved source with a double-kink shaped thermal zone. Rotating the thermal zone (which is the only technical challenge) allows one to move the exit of the source on a circle. A different approach to enhance the beam control is by *manipulating more than two coordinates of the sample position*. The maximum number of independent coordinates of the sample position is 6 (3 spatial plus 3 rotational coordinates). Hence, up to 3 beam directions could be controlled independently.[B] However, this is limited by the stationary array of the sources and the range in which the sample position can be adjusted. For example, in the RIBER 32 system, the tilt and rotation angles plus the three spatial coordinates (x,y,z) of the substrate manipulator could be manipulated. Because the range of the x,y,z coordinates is small (± 10 mm), the incidence angles can be adjusted only within a small range (±5°). Hence, in this study, only the tilt and rotation angles of the sample have been used to manipulate the incidence angles over a relatively wider range (see Sect. 4.2.3).

In Sect. 4.2.1, it has been shown that the distribution of the source materials over the array of effusion cells determines which incidence configurations of molecular beams on the shadow mask sample are possible and, hence, which structures can be grown. This limitation can be overcome by the use of *exchangeable sources*, which have been developed at the University of Würzburg. The effusion cells can be retracted from the growth chamber under UHV and replaced by another cell, which is filled with a different source material. Although exchanging the cells cannot be done during a growth procedure, this technique enhances the flexibility of SMMBE during one maintenance cycle of the UHV chamber.

II. Process modification Although the limitations on the beam control are caused by the growth chamber geometry, the most efficient approaches to overcome these

[A] Two beam directions can be controlled independently when a mask with strip-pattern is used (see Sect. 4.2.1).

[B] Up to six beam directions are independent when a mask with strip-pattern is used.

limitations are not based on changing the growth chamber. The standard approach is to use a *mask with strip-pattern* (reduced dimensionality), which increases the number of independent adjustable beam directions (see Sect. 4.2.1). The second approach is to *adapt the mask pattern to the limited parameter range of incidence configurations* (see Sect. 8.2.2). The third approach is to use *sequential deposition techniques*. For example, short-period superlattices (SPSL) consisting of binary (ternary) well and barrier layers can often replace quaternary materials as a digital alloy. In the case of the samples presented in Sect. 7.1, the individual layers of the SPSL had been grown sequentially using different growth configurations. In this way, only two (three) beam directions have to be adjusted at once (instead of four). Additional sequential growth techniques are based on atomic layer epitaxy and migration enhanced epitaxy techniques.

8.1.2 Finite diameter of source and sample

I. Partial shadow effects As has been shown in Sect. 4.2.2, reducing the diameter of the aperture of the sources reduces partial shadow effects. However, placing an aperture plate with a small pinhole on a conventional effusion cell is not the best solution because certain source materials (Zn, Cd, Te) diffuse to the cell-tip, which affects the thermal characteristic of the cell. This can be avoided with a two-zone effusion cell, e.g., by separately heating the material bulk and the cell-tip (aperture plate).

II. Effect of sample dimensions In Sect. 4.2.2, it has been shown that the finite source to sample distance d causes a variation of the incidence angles across a sample of finite width. To increase d, implies the volume of the UHV chamber must be increased, which makes this approach inefficient. When the SMMBE method is used for the fabrication of small test structures (as in this study), reducing the sample size is a possible solution. However, this is not reasonable for production purposes. The most efficient approach to overcome this problem is to adapt the mask pattern to the incidence angles of the beams as a function of the position on the sample. This implies that the SMMBE growth of the same structures in different regions of the sample is based on different dimensions of the aperture pattern. In addition to the incidence angles, also the molecular fluxes depend on the position in a conventional MBE apparatus. Usually the resulting flux gradients across a sample of finite width are reduced by rotating the sample in a specific position (tilt angle) of the sample manipulator. However, in SMMBE the manipulation of the incidence angles is used to control the incidence angles of the molecular beam. Hence, the variation of the fluxes can be reduced only by reducing the sample size and improving the geometry of the growth chamber.

8.1.3 Imprecision and limited spatial range

I. Mechanical imprecision In a MBE apparatus, the mechanical reproducibility of the angular positions ($\phi;\theta$) is limited to about $\pm 1°$. This limitation of the control of the beam directions can only be overcome with a technical improvement in the accuracy of the sample manipulator.

II. Range of incidence angles The range of incidence angles of the molecular beam, which is accessible in SMMBE, is limited in different ways. First, the range of the positions of the substrate manipulator is limited (e.g., in the RIBER 32 chamber, the tilt angle ϕ has an upper limit at 80° and the range of the x,y,z coordinates is

negligible). Second, the range of substrate positions where RHEED is visible is limited (e.g., 50° < ϕ < 65° and θ = 0°, 90°, 180°, 270° in the RIBER 32 geometry). This limits the *real time* growth control using RHEED, although, it does not imply that the positions without RHEED signal cannot be used for SMMBE. Third, the incident flux depends on the position of the substrate manipulator. Even though the fluxes can be calibrated (see Sect. 4.2.4), this does not make much sense when the effective flux becomes too small. For example, in the RIBER 32 chamber, the sample is turned out of the molecular flux at the lower limit of ϕ = 30-40°. A sample manipulator with the tilt axis going through the middle of the sample could improve this (in this case: $f \propto \cos\phi$). In addition, this geometry would also increase the tilt angle range with a visible RHEED signal. However, even in this geometry the source flux has to be adjusted for different growth positions. This implies that unless a valved cell is used, the temperature of the source material has to be changed during the growth.

III. Spatial range and precision The thickness h of the spacer of an epitaxial shadow mask affects the spatial control of the incidence regions of the molecular beams on the substrate in opposite ways. On the one hand, a thick spacer enhances effects, which are caused by the dispersion of the beam directions (partial shadow effect) and the variation of the incidence angles across a sample of finite size (see Sect. 8.1.2). Thus, controlling the positions of the incidence regions with precision becomes difficult, if the spacer thickness is large. On the other hand, the offset range of the incidence regions also is proportional to the spacer thickness. Thus, the position of the incidence regions of the beams can be controlled only over a very limited range when the spacer thickness is small and hence SAE using such a mask is severely restricted.

In this study, shadow masks with a spacer thickness h ranging from 200 nm to 5 µm were used. Below h = 500 nm, the growth of buffer layers becomes problematic, because the edge region of the buffer (corresponding to the diffusion of group-III adatoms) becomes larger than the spatial range of incidence regions. On the other hand, samples with a thick spacer relax and may therefore have a degraded quality. In order to increase the critical thickness, one has to decrease the Al-composition of the spacer. Furthermore, selective etching of the spacer layer is based on the different compositions of the substrate and spacer. Therefore, the minimum Al composition and thus the maximum spacer thickness are limited.

8.1.4 Limitations of the shapes of the mask apertures

In this study, electron-beam lithography processes have been developed, which allow defining the sizes and shapes of the mask apertures with nanoscale precision.

I. Stability of the mask-cap There are few basic limitations on the shapes of the aperture pattern except a stability requirement of the mask-cap, which has to withstand the removal of the underlying spacer layer. For this reason, e.g., full-ring-shaped apertures cannot be used.

II. Closure of the mask apertures Another limitation of the control of the shapes of the mask apertures is caused by the deposition of materials on the mask (see Sect. 6.1.2). This changes the size and shape of the mask-apertures and may also result in roughening of the edges. The first approach to overcome this is to adapt the initial shape of an aperture to the predictable change of its shape during the growth process. However, this approach can not produce all aperture shapes, e.g., the formation of circular apertures is

hardly possible with orientation-dependent growth dynamics resulting in incurved side facets. The second approach is to reduce the deposition of material on the mask. This can be realized with shadow masks produced from materials, which have a low bonding strength for the growing materials (e.g., III-V's on SiO_2). At a sufficiently high temperature, the weakly bound adatoms desorb from the mask-cap and material deposits only on the substrate below the mask. However, masks produced from a different material than the substrate have a different thermal expansion coefficient and are therefore limited in their geometry (e.g., freestanding masks may bend or crack due to thermally induced strain). This can be avoided by epitaxial shadow masks with a thin passivating overlayer. In addition to the desorption of adatoms from the mask, one can also exploit the enhanced migration of adatoms on a passive overlayer (analogously to patterned SAE) to avoid the deposition of material in the vicinity of an aperture. In contrast to the desorption approach, the diffusion method can be used at a lower substrate temperature, which may result in a better material quality. Figure 8.1(b) shows a possible realization of this approach. A shadow mask with nanoscale apertures is produced by (1) opening windows in a micrometer-sized areas with the mask-overlayer, (2) selective etching of the mask-cap (forms a secondary aperture with a larger diameter), and (3) selective etching of the spacer (forms a cavity below the mask). During epitaxial growth, adatoms impinging on the overlayer structure effectively migrate to the uncovered surface of the cap and deposit there. The latter is important because it avoids the uncontrolled formation of droplets, which would result from a low desorption rate and may affect the shapes of the mask-apertures.

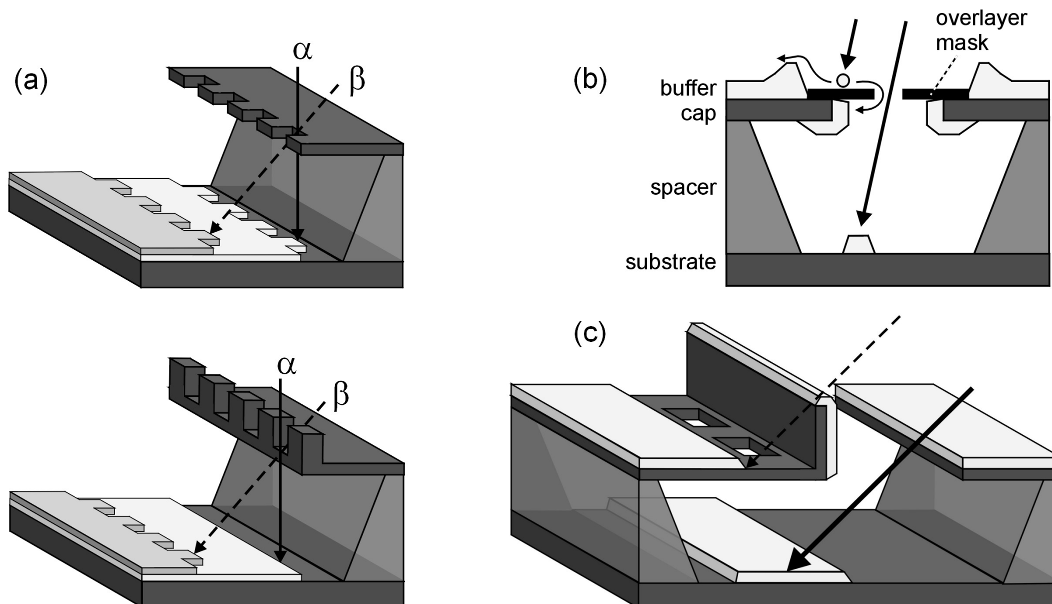

FIG. 8.1 - *(a) Schematic illustration of material deposition at different incidence angles α and β over three-dimensional mask edges of different shapes. (b,c) Schematic diagrams of self-protecting shadow masks. (b) No material deposits on the overlayer structure, which defines the aperture of the mask. (c) No material deposits in the shadow of the vertical wall on the mask-cap. Thus, closure of the small apertures can be avoided.*

Figure 8.1(c) shows a different approach to realize a self-protecting shadow mask, which may be particularly useful for II-VI SMMBE where the diffusion lengths of adatoms are short. A 3D mask consists of a “wall” and apertures of different size. Nanoscale apertures positioned in the shadow region of the wall do not change their shapes during the growth of initial structures, and can thus be used to deposit nanostructures in a different growth configuration where the wall does not block the molecular beams.

8.2 Potential of advanced mask geometry

The geometry of an epitaxial shadow mask plays a crucial role for SMMBE and can help to overcome the limitations, which are due to the growth chamber and the single stationary mask. During this work a new mask concept has been developed (see Sect. 4.1.4). The epitaxial shadow masks consist not of one but of a few apertures per mask-cavity, so that the various apertures of different size and shape can be employed together. In one sense, SMMBE through such a mask is equivalent to employing multiple removable shadow mask, but is much more precise, because the accuracy of mechanical alignment is limited.

8.2.1 Freestanding mask

In a standard SMMBE process, material is deposited only in a small selected area of the mask-cavity and a large fraction of the sample surface is occupied by the spacer. Because of these two reasons, the surface-filling factor of the shadow mask technique is usually small, which may be a drawback.[Schmidt96] In this work, however, a new mask concept has been developed, which is based on the removal of the spacer between different apertures, so that the mask-cap is freestanding in a wide region [see Fig. 4.4(a)]. With this mask concept, the surface occupied by the spacer can be reduced to small values (<10%).

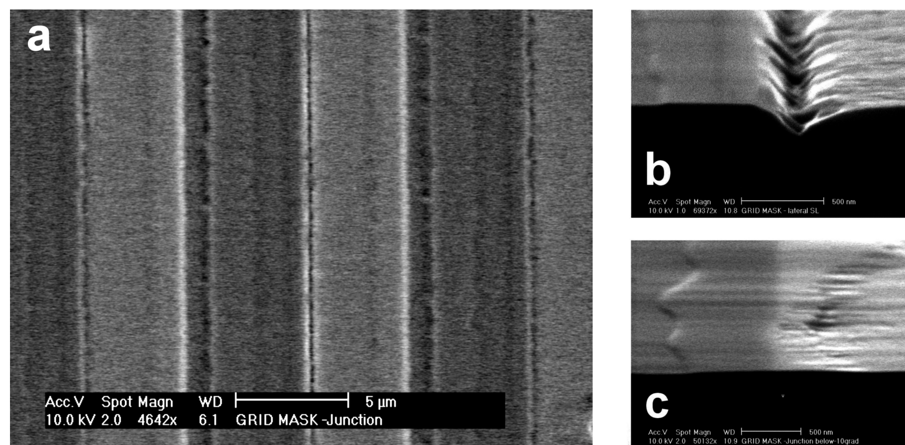

FIG. 8.2 - *(a) Scanning electron micrographs of AlGaAs and GaAs structures grown through a 10-µm-period grid mask with 4.6-mm-wide apertures. (b) A groove between the AlGaAs and the GaAs stripe. (c) No grooves remain when the aperture-width is increased. Coherent periodic semiconductor structures can be realized in this way.*

Nevertheless, in most of the experiments (Chaps. 6 and 7), the exploited substrate area was limited to the size of the apertures of the mask. In order to demonstrate that this is no principal limitation, an epitaxial shadow mask with a grid pattern has been used for the SAE of laterally aligned structures [see Fig. 8.2]. First, an array of aperture stripes with 10 µm lateral periodicity was opened in the 1-µm-thick GaAs cap layer of the epitaxial mask. The length of the apertures is 150 µm and their width ranges from 4.5 – 5.5 µm. The underlying AlGaAs spacer was completely removed in an area of 200×150 μm^2 by selective etching with hydrofluoric acid, thus leaving a freestanding grid mask. The sample was introduced in the III-V chamber, and AlGaAs and GaAs layers were grown through the apertures of the mask at different incidence angles so that the absolute offsets of the

growth regions are Δx = +2.5 µm and Δx = -2.5 µm for AlGaAs and GaAs, respectively. Consequently the growth areas are shifted half of the width of the mask stripes and meet both in the centers of the aperture stripes and of the mask stripes. Figure 8.2(a) shows, that the 4.5-µm-wide AlGaAs and GaAs stripes have been deposited side-by-side and cover most of the substrate surface. Whether the deposits are separated by grooves [see Fig. 8.2(b)] or form an interconnected structure [see Fig. 8.2(c)] is controlled by the width of the apertures. This demonstrates that freestanding shadow masks enable the growth of coherent, periodic semiconductor structures with a surface-filling factor of ~1.

Another advantage of freestanding masks is that mechanical agitation can remove the mask completely. This has been demonstrated by ultra-sound agitation in water (see Fig. 4.4). Potentially, the removal of the masks by mechanical agitation can also be performed *in situ*, using a vacuum suited process.

8.2.2 Advanced mask pattern

During this study, it has been demonstrated that SMMBE can be used for the *in situ* fabrication of nanostructures at predefined places. For the experiments where the shapes and sizes of the nanostructures are defined by the geometry of the mask apertures (see Sect. 7.2), electron-beam lithography has been used to define the apertures with precision. Alternatively, one can use *imprint lithography*, which is particularly interesting to fabricate mask-patterns on a large scale.

The flexible control of the mask pattern has the potential to overcome most of the limitations due to the chamber geometry by *adapting the mask pattern to the limited parameter range of incidence configurations*. That is, the individual incidence directions are not (*in situ*) adjusted relative to a mask pattern, but rather the relative positions of the mask apertures are (*ex situ*) adjusted relative to an (*in situ*) adjustable incidence configuration (of dependent beam directions). For example, this approach has been used in Sect. 7.2.4 to control the growth of nanoscale CdZnSe island by varying the spacing between the apertures of a shadow masks.

In this study, only 2D mask-patterns have been employed, however, 3D mask-patterns would further enhance the flexibility of the method, because the shape of the shadow (incidence) region of a 3D mask (aperture) depends on the beam direction. For example, Figure 8.1(a) shows two mask edges of different shapes. Although, at oblique incidence (β), both deposits have a meander shape, at vertical incidence (α), the upper mask produces a meander shaped edge and the lower one a linear edge. Thus, the mask pattern can be adapted in 3D to produce different shaped deposits in different incidence configurations. In one sense, this is equivalent to employing different 2D-patterned masks. On the other hand, the “2D”-patterned masks also have 3D character because of the finite thickness of the mask-cap (see Sect. 6.1.2). Hence, the shape of the incidence region of a beam always depends on its incidence direction.

8.3 Limitations due to surface kinetic processes

The model for the growth regime within the mask-cavity presented in Chap. 5 could successfully explain most of the kinetic growth effects, which are observed in SMMBE growth experiments (see Chaps 6). It has been shown that surface diffusion and secondary flux govern the SMMBE growth of II-VI and III-V compounds, respectively. Although, it has been shown that surface kinetic processes can be exploited advantageously in SMMBE (see Chap 7), in certain cases, they may as well limit for the growth control and quality of SMMBE grown nanostructures.

8.3.1 Secondary flux

According to the model presented in Chap. 5, the desorption of non-sticking molecules causes secondary fluxes in the mask cavity. The corresponding spatially varying total fluxes may result in position-dependent growth rate (see Sect. 6.1 and 6.2), composition, and material quality.

I. Material quality It is known that the quality of MBE grown materials crucially depends on the growth conditions, i.e., the substrate temperature and the flux ratio. Defects (e.g., vacancies) are incorporated in the crystal when the flux ratio differs from its optimum value [see Fig. 2.4(b)]. For example, in the case of ZnSe-based materials, this optimum flux ratio is nearly unity (see Sect. 2.2) and hence selective growth in the overlap region of two molecular beams is possible. SMMBE structures grown under these conditions are characterized by a highly intense luminescence signal in PL and CL (see Sect. 7.2.4 and also Sect. 7.1), indicating that good structural and spectroscopic quality can be achieved.

However, flux ratios, $p_{II}:p_{VI} \ll 1$ or $p_{II}:p_{VI} \gg 1$ are required to grow II-VI compounds with a homogeneous growth rate, selectively in the incidence region of the species with lower flux (see Sect. 6.1.3). This has been proposed as a useful SMMBE growth mode, which enhances the versatility of the method. Under these conditions, however, standard MBE growth results in a poor structural quality of the deposits [see Fig. 2.4(b)]. In Sect. 7.2.5, it has also been shown that during a *pulsed growth* mode, when the Cd flux is pulsed and only the Se flux impinges continuously, growth takes place selectively in the incidence region of the Cd beam. Instead of the fact that the flux ratio $p_{Cd}:p_{Se} \ll 1$, the growth interruption between the Cd pulses causes an accumulation of Se species in the mask-cavity, so that CdSe can be grown without the direct Se beam by exploiting the Se secondary flux. CdSe nanostructures grown by this method are characterized by a high intensity in CL investigations. Thus, pulsed SMMBE processes may be helpful in controlling secondary fluxes and avoid non-stoichiometric growth conditions.

II. Composition of II-VI alloys When II-VI alloys with three or more constituent species are grown, SMMBE growth becomes more complex because the flux distribution in the mask-cavity not only affects the growth rates but also the composition of the material, and thus its electronic and structural properties [An unintentional variation of the composition (lattice constant) may cause plastic relaxation of the deposits by incorporating defects]. In the simplest case, the constituents of a ternary alloy (e.g., $A_xB_{(1-x)}C$ or $CA_xB_{(1-x)}$) impinge at the same incidence angle and the common incidence region of the beams defines the growth area. If $p_A + p_B \ll p_C$, the majority species C reduces the contribution of the secondary fluxes of the alloying species A and B to the total flux

(analogous to Sect. 5.3.1). Hence the flux ratio takes on about the same value on top of the mask (p_A:p_B) and in the mask-cavity (f_A:f_B), and the composition of layers is hardly affected. In all other cases, the secondary fluxes of the alloying species cannot be neglected. Due to their different sticking coefficients ($s_A \neq s_B$), the rate and distribution of the secondary fluxes of the alloying species is diverse and hence the composition of deposited material may change, in particular the molar fraction of the species with the lower sticking probability is thereby increased. However, the circumstances may become more complex if the source and the substrate have different temperatures. In this case, primary and secondary fluxes of the same element have different thermal energies and molecular configurations, resulting in different sticking coefficients. For example, based on the data of Ref. [Okuyama97], for $Mg_yZn_{(1-y)}S_xSe_{(1-x)}$ grown at T_{sub} = 280°C with a hot sulphur source T_{source} = 800°C, the sulphur sticking probability of the secondary flux (which can be assumed to be in thermal equilibrium with the substrate) is a factor 2.5 higher than that of the sulphur species in the direct beam. On the other hand, using a lower temperature sulphur source, T_{source} = 120°C, the relative incorporation efficiency of the secondary sulphur species can be reduced by a factor 2.1. Therefore, it is advantageous to use a valved source with a variable temperature exit zone because this allows one to control the incorporation efficiency of the secondary flux relative to the primary flux.

II-VI alloys (e.g., $A_xB_{(1-x)}C$) can also be grown in configurations where the constituents impinge at different incidence angles. For example, species B and C can have a common incidence region (*growth area*), which overlaps partially with the incidence region of species A. The ternary alloy grows selectively in the overlap region and binary BC in the rest of the growth area. This can be used to modulate the composition laterally and thus increases the versatility of shadow mask assisted selected area growth. Depending on the width of the partial shadow region of flux A, the composition change can be abrupt or gradual over a wide region. On the other hand, the method has several limitations: Firstly, the modulation of the composition also modulates the lattice mismatch with the substrate and may result in relaxation of the SMMBE structures. Secondly, the ternary alloy grows faster than the binary compound resulting in a modulation of the structure height. Thirdly, the binary AC also grows in the region outside of the growth area with the growth rate determined by the secondary flux of species *C*. The resulting C rich growth is unfavorable if not intended. On the other hand, when *C* is the minority species, the compositions of the ternary and the binary compound are changed by secondary fluxes of A and B (as explained above). Finally, elemental material may also deposit if the vapor pressure of species A is low at the growth temperature (e.g., Be, Mg).

The composition of growing layers can be also modulated by growing QWs and barrier layers of a short period superlattice in selected areas (analogous to Sect. 7.1). On the one hand, this approach is more flexible, because of the sequential deposition of different materials at different growth configurations enabling digital alloying. On the other hand, homogeneous alloys can be grown with much less sample movements.

III. Composition of III-V alloys In III-V SMMBE, desorption (secondary flux) of group-III species can usually be neglected because of the low vapor pressure of the elements at usual growth temperature (Although, in certain growth conditions, this assumption may not be correct). Thus, only the secondary flux of group-V species affects the composition of III-V nanostructures. However, the interplay between surface diffusion of the group-III species and desorption of the group-V species may cause non-trivial effects. A comprehensive discussion is out of the scope of this work.

8.3.2 Surface diffusion

I. Composition of III-V alloys In Sect. 6.2 it has been shown that the redistribution of group-III adatoms in the cavity of an epitaxial shadow mask takes place via surface diffusion. A novel approach has been developed in this work, which allows the control of the surface diffusion of group-III adatoms by tailoring the distribution of the group-V flux in the mask cavity. This has enabled SMMBE growth of III-V nanostructures. Orientation, strain, and group-V-flux dependent diffusion dynamics may, however, make selected area growth of III-V alloys difficult. The main disadvantage is that group-III elements (Al, Ga, In) have different surface diffusion lengths ($l_{Al} < l_{Ga} < l_{In}$ at standard growth conditions). This may affect the composition of SMMBE grown III-V alloys with two ore more group-III elements in a non-trivial way. For example, a few basic diffusion effects resulting from alloys with a slow and a fast diffusing species have been discussed by Tersoff *et al.* [Tersoff03] (for patterned SAE).

Selected area growth of III-V alloys with two or more group-V elements is expected to be less difficult because of a short surface diffusion length of group-V species at standard growth conditions. However, even in this case, the interplay between surface diffusion and desorption (as a function of the growth conditions) may cause non-trivial effects.

II. SMMBE with reduced surface migration An approach to overcome the limitations caused by surface diffusion uses certain growth conditions to reduce the surface diffusion length ($l_{inc} \lll 1$ µm). In Sect. 6.2.1, III-V SMMBE growth has been investigated as a function of the growth temperature. Sharply defined edges of GaAs deposits grown at a low substrate temperature demonstrate that the migration of Ga adatoms is very limited. Alternatively, one can use high group-V fluxes to limit the diffusion length of the adatom. However, reducing the growth temperature as well as increasing the group-V flux is problematic and may affect the structural and spectroscopic quality of SMMBE grown nanostructures. The potential of this growth regime is the fabrication of diluted magnetic semiconductor nanostructures, which are usually grown under these migration limited conditions (see Sect. 8.2.5).

The surface diffusion length is also limited at very high substrate temperatures corresonding to the short desorption time. In this case, repetitive desorption would become the dominant redistribution process for group-III adatoms in the mask cavity and hence the surface concentrations of both group-III and group-V species have a maximum in the respective incidence regions. Therefore, both incidence regions could control selected area growth of III-V nanostructures (analogously to II-VI SMMBE).

III. Absence of surface diffusion during II-VI SMMBE In Sect. 6.1 it has been shown that surface diffusion does hardly affect the shape of II-VI deposits on a nanometer scale (~10 nm). On the one hand, this simplifies SMMBE growth of II-VI nanostructures in comparison to the fabrication of III-V nanostructures. On the other hand, the apparent absence of surface diffusion, combined with reduced partial shadow effects results in steep inclination angles and possibly overhanging edges of II-VI deposits. Directly at the edge of a deposit, the drastically changed flux ratio may produce defects during over growth.

8.4 Prospective shadow masks assisted processes

8.4.1 Strain and orientation dependent growth

In Sects. 7.1.3 and 7.2.2, it has been demonstrated that Stranski-Krastanow like growth mode can assist II-VI SMMBE in the area-controlled self-formation of nanostructures. Although the growth kinetics are very different in III-V SMMBE, strain and orientation dependent growth dynamics may also be exploited in this case. In selected area growth using patterned substrates, it has been demonstrated that the Stranski-Krastanow growth mode can be used to form regular arrays of quantum dots (molecules or chains) depending on the geometry of the growth area.[Lee00, Lefebvre00] Although there is no evidence to date, the same growth dynamics can probably be used for the formation of QD molecules or QD chains during III-V SMMBE.

SMMBE growth can also be assisted by orientation-dependent growth on *in situ* grown substrate patterns. In this case, substrate patterns (e.g., a wire-like mesa) are *in situ* fabricated by means of shadow masked SAE. Subsequently, orientation-dependent growth is exploited to control selected area growth (e.g., selective growth on the mesa), analogous to patterned SAE. This may be assisted by SMMBE, which would enhance the growth control (e.g., growth area is limited to the overlap of the incidence regions of the arsenic beam with the narrow upper mesa surface).

Whereas strain and orientation dependent growth dynamics can be exploited in SMMBE of III-V compounds, these additional dynamics also cause limitations of the growth control. For example, the self-formation of facets at the edges of III-V deposits makes selected area growth of buffer layers and, e.g., cylindrically shaped mesas difficult (see Sects. 6.2.1 and 8.2.3). In addition, growing homogeneous QWs and QWRs, e.g., in the InAs/GaAs system (see Sect. 7.3), is difficult because strain-dependent growth dynamics may induce self-assembly of dots in the Stranski-Krastanow growth mode.

8.4.2 Non-local growth

In this section it is discussed how, not only nanoscale heterostructures on selected areas, but homogeneous layers can as well be realized below the shadow mask. Such homogeneous layers are important for the fabrication of embedded quantum structures (sandwiched between buffer and cap layers). In addition, non-local growth would allow the the fabrication of bragg-mirrors and QWs (connecting the nanostructures).

I. Smooth flux distribution In SMMBE, the step-edge profile of the fluxes makes non-local growth of homogeneous layers difficult. This limitation can be overcome by exploiting (1) partial shadow, (2) growth with rotating substrate, or (3) eventually the MEE techniques. For example, the growth of III-V buffer layers is governed by the group-V flux, which is never homogeneous below a single mask-aperture [see Fig. 4.7(b)]. However, a homogeneous flux distribution and thus homogeneous buffer layers can be achieved by the usage of freestanding shadow masks with quasi-periodic aperture patterns. Figure 8.3(a) shows the flux distributions below stripe-shaped apertures with a lateral period P and an aperture width $W_A = P/3$, calculated with the assumptions that the aperture of the beam source is circular and that the emergent flux from this extended source area is homogeneous (see Sect. 4.2.2). The curves represent distributions obtained for the partial shadow widths $w = 0.5 \times P$, P, $1.22 \times P$, $1.4 \times P$, and $3 \times P$, respectively. The incidence regions of the individual apertures are separated if the spacing between the apertures, $P - W_A > w$, and overlap if $P - W_A < w$. Moreover, a homogeneous flux distribution can be achieved if the

partial shadow width w is much larger than the spacing between the apertures $P\text{-}W_A$ [see $w = 3\times P$]. Decreasing the period P, increasing the spacer thickness g, or increasing the dispersion of the molecular beam $\delta\varphi_0$ can produce this. However, in order to define nanostructures in a subsequent SMMBE process, the dispersion $\delta\varphi_1$ of the defining molecular beam has to be much smaller than that of the As-beam ($\delta\varphi_0$) during the growth of the buffer, i.e., $\delta\varphi_0:\delta\varphi_1 \gg 1$, which may be limited by the geometry of the growth chamber. Alternatively, one can exploit the almost homogeneous flux distribution at $w \approx 1.22\times P$, which requires a lower $\delta\varphi_0:\delta\varphi_1$ ratio.

Alternatively to partial shadow effects, one can also exploit the continuous shifting of the incidence regions (on a width w) when a shadow mask sample is rotated [see Fig. 3.8(a)]. This results in a time-integrated smooth flux distribution, which however depends on the surface kinetics and the rotation frequency of the sample. Eventually also MEE techniques can be exploited in SMMBE to achieve non-local growth by alternating deposition of group-III and group-V species. During the deposition of group-III species and the absence of the direct group-V flux, the growth regime in the mask-cavity is governed by the smoothly distributed secondary group-V fluxes. Thus, non-local growth can eventually be achieved if the time-constant of the decay of the secondary group-V flux, which depends on the geometry of the mask-cavity, is much longer than the incorporation time of group-III species.

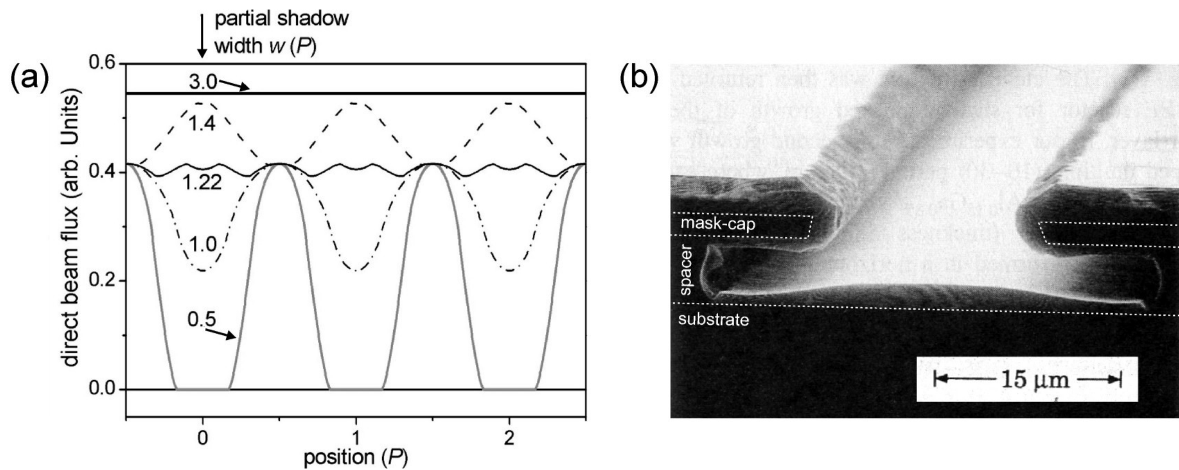

FIG. 8.3 – *(a) Direct beam flux versus the lateral position below a freestanding shadow mask with a periodic pattern of stripe-shaped apertures (period P, aperture width P/3) calculated for partial shadow widths w = 0.5×P, P, 1.22×P, 1.4×P, and 3×P. (b) Cross-sectional micrograph of AlGaAs/GaAs heterostructures grown by OMVPE through an epitaxial shadow mask (after [Armour95]).*

II. Gas-phase diffusion A different approach with the potential to enable non-local growth of homogeneous layers through epitaxial shadow masks is based on organometallic vapor-phase epitaxy (OMVPE). Armour *et al.*[Armour95] have investigated OMVPE growth of GaAs/AlGaAs heterostructures through epitaxial shadow masks. They have observed that OMVPE results in smoothly varying growth profiles [see Fig. 8.3(b)], devoid of the step-edged profile of similar structures grown by shadow mask assisted MBE. This has been explained by the accumulation of organic radicals, which governs the growth regime below the shadow mask. The recombination of the radicals with group-III surface atoms enhances the gas-phase diffusion in the mask-cavity, thus decreasing the gradients of the growth profiles. Hence, exploiting the enhanced gas-phase diffusion during OMVPE is a promising approach to realize homogeneous buffer layers (e.g., below

a freestanding shadow mask with a periodic pattern of apertures). When the required OMVPE sources are introduced in a MBE chamber, OMVPE and MBE growth regimes can be used to realize shadow masked growth of both homogeneous layers and nanostructures.

8.4.3 In situ etching in selected areas

In addition to selected area growth, epitaxial shadow masks may also be employed for controlled etching in selected areas. The possibility to accomplish both deposition and etching in the same process would enhance the versatility of the shadow mask technique for the fabrication of complex nanostructures and increase the flexibility in heterostructure design. For example, a structure consisting of two layers separated by a barrier layer with a single nanoscale hole in the middle, would be a possible way to realize a point contact. Shadow mask assisted selected area growth of such (ring-shaped) barrier structure however is hardly possible [see Subsect. 8.1.4.(I)]. In contrast, growth of the barrier and subsequent etching of the hole can realize this structure.

In situ etching on nanoscale areas can possibly be accomplished with a molecular beam consisting of a chemically reactive species, which passes through a nanoscale aperture of an epitaxial shadow mask. In the incidence region of the beam, the chemical species reacts with the crystal atoms and forms volatile products, which can be thermally desorbed from the surface, resulting in an effective etching rate. For example, GaAs can be etched at a low temperature of 180°C by molecular chlorine (Cl_2), which forms the volatile products $AsCl_3$ and $GaCl_3$.[Balooch86] However, the reaction probability is relatively low (~0.3 at 180°C)[Balooch86] and, hence, it can be supposed that a molecular beam of Cl_2 produces secondary fluxes of Cl_2 in the entire mask-cavity (The Cl_2 flux distribution can be calculated using Eq. 5.3). If the etching rate is limited by the incident Cl_2 flux, it is higher in the incidence region of the direct beam and thus selective etching is possible. However, the etching rate may be limited by the desorption rate of the volatile products,[Balooch86] which implies that the etching rate is hardly higher in the incidence region. In this case, one can activate the desorption by increasing the substrate temperature during the etching process. However, this may also activate surface diffusion, inter-diffusion, and the backward reaction of the products. Hence, the selective etching process may become rather complex.

As an alternative to such a chemical assisted thermal etching process, compound material can be removed ("etched") from selected areas by manipulation of the local surface free energy. This can be achieved by controlling the incidence of the molecular beams of the constituent species of the compound. In the case of III-V materials, this effect has been observed in Sects. 5.3.4 and 6.2. It has been shown, that at high substrate temperatures, III-V compounds dissociate in regions with a low group-V flux and the group-III surface atoms migrate to regions with a higher group-V flux. Based on this migration-induced etching of the III-V compounds, material can be removed from regions selected by a local minimum of the group-V flux. In addition, in Sect. 6.2.4 it has been shown that the GaAs etching rate is increased within the incidence area of an In molecular beam. Thus both group-V and group-III beams can be used to control selected area "etching" of III-V compounds. However, this method is limited because the etching rates vary with the distance from the edge of the respective incidence regions on the scale of the incorporation diffusion length of the group-III species (see Sect. 5.3.4). In addition, this process takes place at non-equilibrium conditions and it has not yet been investigated as to whether a low defect density can be preserved.

As an alternative to such thermal "etching" processes, standard dry etching processes relying on ion beams (e.g., Ar^+) can be used. However, a disadvantage of using ion beams is that it produces defects (In addition, the trajectories of charged species may be affected by coulomb effects).

8.4.4 Electronic doping in selected areas

The fabrication of complex heterostructures often requires a precise control of the doping concentrations in three dimensions. From recognized nanofabrication techniques, only focused ion-beam (FIB) assisted MBE (see Sect. 3.1) and shadow-mask assisted MBE can do this (see below). However, the FIB process causes extended growth interruptions (depending on the size of the implanted region), which increases the concentration of unintentional impurities. In addition, scattering of high-energy ions is known to cause damage in the implanted regions, which limits the applicability of this technique.

In contrast, SMMBE allows doping in selected areas without long-lasting growth interruptions and without scattering damage. Moreover, the recent progress in both the SMMBE technology (see Sect. 8.2) and the understanding of SMMBE growth (see Chaps. 5-7) can boost the versatility and spatial precision of the shadow mask assisted doping technique (see below), which were the main drawbacks compared to the FIB technique. Secondary flux and surface diffusion of the dopant adatoms limits the spatial precision of shadow mask assisted doping in nanoscale selected areas. Although, this implies incorporation of unwanted electronic impurities, which may severely affect the properties of the quantum structures, one can, however, choose from a number of possible dopant species, the one which is best suited to avoid redistribution processes. SMMBE can probably control the doping concentration with a higher spatial precision than the FIB technique.

8.4.5 In situ contact formation in selected areas

An important problem of semiconductor technology, especially in wide gap material systems, is the fabrication of (ohmic) contacts. For certain wide gap materials, there does not exist a suitable metal that has a large enough work function to overcome the transport barrier to p-type layers (e.g., 6.76 eV for p-type ZnSe).[Swank67] In addition, the maximum doping concentration is limited (e.g., p-type ZnSe: N_A-N_D < 2×10^{18} cm^{-3}) [Faschinger95] and hence the probability of tunneling through the resulting Schottky barrier is small. A contact grating structure, i.e., an alloy with a composition gradient (e.g., p-type $ZnSe_{(1-x)}Te_x$) can be used to increases the doping concentration at the interface.[Fan95] This can decrease the width of the Schottky barrier and, hence, the contact resistance. However, exposure of the interface prior to the MBE growth of the grating structure destroys this effect. In addition, Schüll [Schüll97] has investigated technological processes for the fabrication of contacts on ZnSe layers, and observed that *in situ* deposition of metal films resulted in a much smaller contact resistance compared to *ex situ* processes (for both n-type and p-type ZnSe). Hence it is advantageous to employ *in situ* processes for the fabrication of contacts to (certain) wide gap materials.

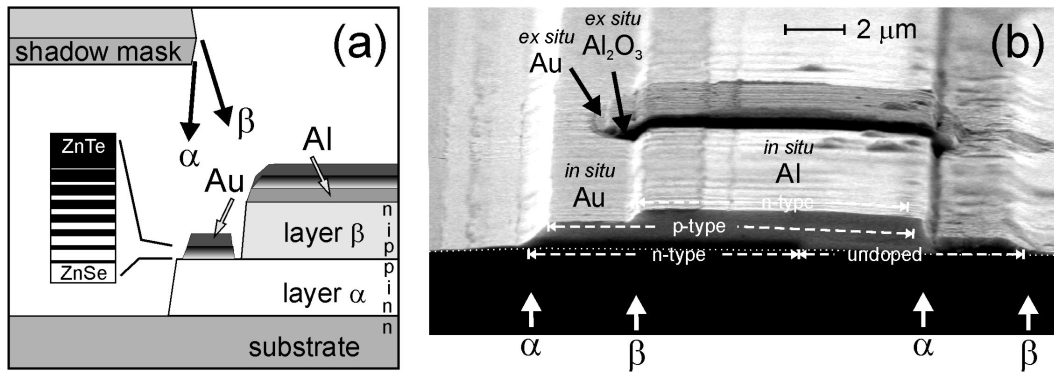

FIG. 8.4 - *(a) Sketch of the principle of producing in situ contacts to both a top n-type and a buried p-type MgZnSSe layer. After SMMBE growth (layers α and β), an Au film, a p-ZnSe/ZnTe contact grating, and an Al film are deposited in selected areas of the structure using the shadow mask. (b) Scanning electron micrograph of the cross-section of a test structure. The dotted line indicates the interface of the substrate. A material contrast clearly marks the selectively doped n-type region of the layer α (above the dotted line). An Au contact pad on isolating Al_2O_3, which selectively contacts the in situ Au contact, has been deposited in a selected area assited by the shadow mask edge and photoresist with a window.*

I. Contacts to embedded structures More difficult than the fabrication of contacts to surface layers is the fabrication of contacts to embedded layers, e.g., a doped layer with (undoped) cap layers on top of it. In the case of wide gap materials such as ZnSe, the above-mentioned difficulties make the fabrication of low resistance contacts by means of standard processes (deposition, implantation, diffusion, etching) almost impossible. In contrast, shadow mask assisted SAE provides two different approaches to solve this problem.

The first approach is analogous to the doping of the cap layer in a selected contact area by means of implantation (or diffusion). Assisted by a shadow mask, doping of the nominally undoped layer in a selected region can be accomplished without incorporating defects or impurities (see Sect. 8.2.5). In addition, a contact grating structure can be grown on this selectively doped area thus enabling ohmic contacts to the buried layer.

The second approach is based on the SMMBE growth of the cap layer on a selected area of the doped layer, thus leaving a part of the doped layer uncovered [see Fig. 8.4(a)]. After deposition of the cap, shadow mask assisted deposition of the contact structures in the uncovered regions of the doped layer can be accomplished *in situ*. This method allows fabricating direct contacts to “buried” layers without etching.

An example of a contact structure with two different *in situ* contacts is shown in Fig. 8.4. The heterostructure consists of two wide gap II-VI layers (MgZnSSe), which are grown through a shadow mask at two different angles, α and β, resulting in an offset between the layers. In addition, doping in selected areas of the layers controlled by manipulating the incidence angles of the dopants beams can produce a n-i-p-i-n doping profile as is indicated in the image.[A] After the SMMBE growth, the shadow mask can be used for the *in situ* deposition of a metal film (Al) selectively onto the surface of the topmost n-type layer. Thereafter, selected area growth of a contact grating structure (p-ZnSe/ZnTe) and *in situ* deposition of a metal film (Au) onto the uncovered offset region of the “buried” p-type layer (MgZnSSe) can be accomplished. This SMMBE method can probably produce ohmic contacts to both the top n-type and the buried p-type MgZnSSe layers.

[A] In the case of the bottom n-type layer, the selectively doped incidence region of the dopants beam (Al) can be distinguished from the undoped region because it appears dark in the SEM image [see Fig. 8.4(b)].

II. Shadow mask assisted post-processing In addition to the deposition of metal films in selected areas of a SMMBE structure, the shadow mask can also control the deposition area of insulating films, e.g., Al_2O_3. This can be accomplished *in situ* and *ex situ*. In the latter, standard lithography can assist the control of the deposition area. An example of this is shown in Fig. 8.4(b). After the fabrication of the *in situ* contacts, a contact pad was made, which selectively contacted the narrow *in situ* Au contact. This has been accomplished by the *ex situ* deposition of Al_2O_3 and Au at two different incidence angles so that the insulating Al_2O_3 separates the *ex situ* Au from the structure except for a narrow contact stripe on the *in situ* Au, because of a small offset between the deposition areas. The restriction of the contact pad in the direction of the mask-aperture has been achieved by photolithography. Before the deposition of the contact pad, photoresist was spin-coated on the shadow mask sample and a stripe-shaped window produced in the direction perpendicular to the mask-aperture. The area-restricted contact pad results from the lift-off of the photoresist with *ex situ* deposited films. In addition to the deposition of metal and insulator films in selected areas, the shadow mask can also assist in *ex situ* etching in selected areas (analogous Sect. 8.2.4). Hence, shadow mask assisted post-processing can reduce the number of lithography processes required for the fabrication of a device and thus can potentially reduce the production costs.

III. Selective contacts to embedded structures Other contact problems, which can often not be solved with the above-mentioned standard techniques, include structures in which selective contacts to different buried structures have to be formed. This is particularly difficult if the dimensions of the individual structures (QWs, QWRs, QDs, 2DEGs, δ-layer) and the distances between them are small.

The shadow mask technique is particularly useful to solve these problems, because selected area growth, doping in selected areas, and metallization in selected areas can be accomplished *in situ* with nanoscale precision. For example, Döhler *et al.* [Döhler86] used shadow mask assisted doping in selected areas to realize structures consisting of n-i-p-i superlattices with selective contacts to n-type and p-type layers [see Fig. 3.8(a)]. Lorke *et al.* [Lorke95] have also demonstrated that SMMBE can result in the growth of stacked, two-dimensional electron gases which can be selectively contacted without the use of complicated *in-situ* or post-growth patterning techniques. These results have been realized by means of nanoscale precision in the growth direction, although the lateral growth control was imprecise. In this work, it has been demonstrated that lateral growth control (deposition and doping) in SMMBE can also be done with nanoscale precision. It is obvious, that nanoscale growth control in three dimensions and the advanced freestanding masks with multiple apertures developed in this work will enable versatile SAE growth of complex heterostructures. They may even allow selective contacts to individual nanostructures.

8.4.6 Magnetic doping in selected areas

Semiconductor materials with magnetic properties have recently attracted much attention for the application of semiconductor spintronics. Diluted magnetic semiconductors in the III-V system can be fabricated by doping with the transition metal Mn, which acts also as an acceptor by substituting for a group-III atom. Because of the low solubility of Mn, III-V diluted magnetic semiconductors have to be grown at a low substrate temperature to avoid the formation of Mn-clusters. In the case of II-VI compounds, a variety of transition metals (V, Cr, Mn, Fe, Co, and Ni) can induce magnetic

properties. In this case, the dopants act as isoelectronic impurities, hence magnetic and electronic doping can be controlled independently.

Because of the low vapor pressure of the transition metals and the low growth temperatures of diluted magnetic semiconductors, surface diffusion and desorption of transition metals are limited. Hence, SMMBE can allow SAE of diluted magnetic semiconductors with very high spatial precision, which would be important for prospective applications in spintronic devices (In contrast, patterned SAE of diluted magnetic semiconductors is hardly possible and thermal annealing, required after implantation of transition metal atoms, may result in the formation of clusters).

8.4.7 Complex quantum devices

In this work, it has been demonstrated that SMMBE is one of very few methods enabling the fabrication of high-quality compound semiconductor nanostructures at predefined places with very high spatial precision (see Chap. 7). Although SMMBE has its own limitations (discussed in Sects. 8.1 and 8.3), the method has two important advantages over patterned SAE, which, so far, has been considered the most prospective alternative method.

Firstly, SMMBE allows selected area growth of nanostructures on a planar substrate, resulting in quantum structures embedded in a planar matrix. In contrast, patterned SAE growth is always non-planar and orientation-dependent. Moreover, *real-time* control of the growth area can be achieved during SMMBE by adjusting the incidence angles of the molecular beams with respect to the stationary shadow mask and one can exploit apertures of different shape and size (analogous to using different mechanical masks) and thus control the deposition (composition) in all three dimensions (3D). In contrast, patterned SAE growth is pre-defined by the substrate (overlayer) pattern and, hence, the method does not allow the manipulation of the growth areas during the growth, i.e., control of the deposition (composition) is limited (quasi-2D). Finally, the versatility of SMMBE selected area growth can be enriched by pattered SAE techniques (see Sect. 8.4.1), non-local growth techniques (see Sect. 8.4.2), and shadow mask assisted etching in selected areas (see Sect. 8.4.3). *In general, SMMBE is less restricted than patterned SAE in the geometries of the nanostructures, which can be produced.*

The second advantage of SMMBE over patterned SAE is in the fact that both growth and *doping* of quantum nanostructures can be achieved (see Sects. 8.4.4 and 8.4.6) and combined with *in situ* contact formation in predefined selected areas (see Sect. 8.4.5). Only FIB and shadow-mask assisted MBE can *control the doping concentrations in all three dimensions*. However, the FIB process is known to produce scattering-damage and unintentional impurities, which limits the applicability of this technique for the fabrication of complex quantum structures, which are degraded by such disturbances. Moreover, FIB, implantation, and diffusion processes require thermal annealing, which may cause additional problems (defects, degradation). In particular, nanostructures may be destroyed by thermal interdiffusion. In contrast, SMMBE allows doping in selected areas without long growth interruptions and without scattering damage.

In conclusion, SMMBE has the potential for the nanofabrication of defect-free complex quantum devices with the composition and doping profiles (donors, acceptors, and transition metals) controlled with very high precision in 3D.

Summary

Shadow Mask assisted Molecular Beam Epitaxy (SMMBE) is a technique enabling selected area epitaxy of semiconductor heterostructures through shadow masks. The objective of this work was the development of the SMMBE technique for the reliable fabrication of compound semiconductor nanostructures of high structural and optical quality. In order to accomplish this, technological processes have been developed and optimized. This, in combination with model calculations of the basic kinetic growth processes has enabled the fabrication of high quality quantum structures.

A high spatial precision and control of the incidence regions of the molecular beams during the SMMBE process are required for the fabrication of nanostructures. One of the technological developments to this effect, which has substantially enhanced the versatility of SMMBE, is the introduction of a new type of freestanding shadow masks: Growth through such a mask with different incidence angles of the molecular beams is equivalent to employing different mechanical masks, but is much more accurate since the precision of mechanical alignment is limited.

A consistent model has been developed, which successfully explains the growth dynamics of molecular beam epitaxy through shadow masks. The redistribution of molecular fluxes under shadow masks may affect the growth rates on selected areas of the substrate drastically. In the case of compound semiconductors, reactions between the constituent species play important roles in controlling the growth rates as a function of the growth parameters.

The predictions of the model regarding the growth of II-VI and III-V compounds have been tested experimentally and the dependence of the growth rates on the growth parameters has been verified. Moreover, it has been shown, that selected area epitaxy of II-VI and III-V compounds are governed by different surface kinetics. Coexisting secondary fluxes of both constituent species and the apparent non-existence of surface diffusion are characteristic for SMMBE of II-VI compounds. In contrast, III-V SMMBE is governed by the interplay between secondary group-V flux and the surface migration of group-III adatoms. In addition to the basic surface kinetic processes described by the model, the roles of orientation and strain-dependent growth dynamics, partial shadow, and material deposition on the mask (closure of apertures) have been discussed.

The resulting advanced understanding of the growth dynamics (model and basic experiments) in combination with the implementation of technical improvements has enabled the development and application of a number of different processes for the fabrication of both II-VI and III-V nanostructures. In addition to specific material properties, various other phenomena have been exploited, e.g., self-organization. It has been shown that, e.g., single quantum dots and quantum wires can be reliably grown. Investigations performed on the SMMBE nanostructures have demonstrated the high positional and dimensional precision of the SMMBE technique. Bright cathodoluminescence demonstrates that the resulting quantum structures are of high structural and optical quality.

In addition to these results, which demonstrate SMMBE as a prospective nanofabrication technique, the limitations of the method have also been discussed, and various approaches to overcome them have been suggested. Moreover, propositions for the fabrication of complex quantum devices by the multiple application of a stationary shadow mask have been put forward. In addition to selected area growth, the shadow masks can assist in etching, doping, and *in situ* contact definition in nanoscale selected areas.

Due to the high precision and control over the dimensions and positions of the grown structures, which at the same time are of excellent chemical, crystal, and optical quality, SMMBE provides an interesting perspective for the fabrication of complex quantum devices from II-VI and III-V semiconductors.

Zusammenfassung

Die *Schattenmasken-gestützte Molekularstrahlepitaxie* (SMMBE) ist eine neue Methode welche die ortsselektive Epitaxie von Halbleiterheterostrukturen mittels stationärer Schattenmasken ermöglicht. Ziel der vorliegenden Arbeit war die Entwicklung der SMMBE-Methode für die gezielte Herstellung von Nanostrukturen hoher Güte aus Verbindungshalbleiter. Dazu wurden technologische Prozesse entwickelt und optimiert, Modellrechnungen für die grundlegenden kinetischen Wachstumsprozesse in Schattenmasken entwickelt und darauf aufbauend Quantenstrukturen hergestellt und untersucht.

Eine hohe Ortsauflösung und flexible Kontrolle der Einfallsgebiete der Molekularstrahlen während des SMMBE-Wachstums sind notwendige Voraussetzungen für die Herstellung von Nanostrukturen. Einer der technologischen Fortschritte, der zu einer erheblich höheren Flexibilität der SMMBE-Methode führte, ist der Einsatz neuartiger, freistehender Schattenmasken: Die Epitaxie durch solche Masken unter verschiedenen Einfallswinkeln der Molekularstrahlen ist vergleichbar mit der Verwendung mehrerer mechanischer Masken, ermöglicht jedoch eine weit höhere Ortsauflösung und Präzision.

Im Rahmen der Arbeit wurde ein konsistentes Modell entwickelt, welches die grundlegenden kinetischen Wachstumsprozesse unter der Schattenmaske beschreibt. Adsorbierte Atome und Moleküle werden durch Diffusion und Desorption innerhalb der Maskenkavität umverteilt, wodurch sich die lokalen Wachstumsraten drastisch ändern können. Beim Wachstum von Verbindungshalbleiter spielen die Reaktionen zwischen den einzelnen Konstituenten eine entscheidende Rolle und beeinflussen die Wachstumsraten abhängig von den Wachstumsbedingungen.

Die Vorhersagen des Modells in Bezug auf das Wachstum von II-VI und III-V Verbindungshalbleiter wurden in grundlegenden Experimenten verifiziert und die Abhängigkeit der Wachstumsraten von den Wachstumsbedingungen bestätigt. Darüber hinaus konnte ein grundsätzlicher Unterschied in der Wachstumsdynamik der beiden Materialsysteme nachgewiesen werden. Charakteristisch für das SMMBE-Wachstum von II-VI Verbindungen ist die Koexistenz von Sekundärflüssen beider Konstituenten und eine vernachlässigbare Diffusionsdynamik. Hingegen ist die vom Gruppe-V-Gesamtfluss abhängige Oberflächendiffusion entscheidend für das Wachstum von III-V Strukturen. Über diese vom Modell beschriebenen grundlegenden Wachstumsprozesse hinaus wurde zusätzlich auch auf orientierungs- und verspannungsabhängige Prozesse, Halbschatteneffekte und das Zuwachsen der Maskenöffnungen eingegangen.

Basierend auf diesen Ergebnissen der Modellrechnungen, den Experimenten und den technologischen Fortschritten wurden verschiedene neuartige Methoden zur Herstellung von II-VI und III-V Nanostrukturen entwickelt. Diese ermöglichen zum Beispiel Quantendrähte und Einzelquantenpunkte gezielt mit Schattenmasken zu wachsen. Dabei werden verschiedene Verfahren angewandt, die neben der materialspezifischen Wachstumsdynamik auch z.B. Selbstorganisationseffekte ausnutzen. Untersuchungen an SMMBE-Nanostrukturen demonstrierten die sehr hohe Positions- und Dimensionspräzision der SMMBE-Methode und eine hohe strukturelle und optische Qualität der hergestellten Quantenstrukturen, die sich z.B. in intensiver Kathodolumineszenz widerspiegelt.

Diese Ergebnisse weisen SMMBE als vielversprechende Methode zur Herstellung von Nanostrukturen aus. Es werden aber auch die Grenzen des Verfahrens diskutiert und verschiedene Ansätze zu deren Überwindung vorgeschlagen. Darüber hinaus wurde das Potenzial der SMMBE-Technik dahingehend diskutiert, komplexe Quantenstrukturen durch mehrfache Anwendung einer stationären Schattenmaske herzustellen. Zusätzlich zum ortselektiven Wachstum kann die Schattenmaske auch zum lokalen Ätzen und Dotieren und zur *in-situ*-Kontaktierung ausgewählter Gebiete genutzt werden.

Mit der Vielfalt der in dieser Arbeit entwickelten und vorgeschlagenen SMMBE Methoden, der präzisen Kontrolle der Strukturdimensionen und –positionen und der hohen Güte der hergestellten Quantenstrukturen bietet SMMBE eine interessante Perspektive für die Herstellung von komplexen quantenelektronischen Bauelementen aus II-VI und III-V Halbleiter.

References

[Abrams97] D. S. Abrams and S. Lloyd, Phys. Rev. Lett. **79**, 2586 (1997).

[Alivisatos96] A. P. Alivisatos, **271**, 933 (1996).

[Armour95] E. A. Armour, S. Z. Sub, K. Zheng, and S. D. Hersee, J. Appl. Phys. **77**, 873 (1995).

[Ashoori96] R. C.Ashoori, Nature **379**, 413 (1996).

[Bacher99] G. Bacher, T. Kümmell, D. Eisert, A. Forchel, B. König, W. Ossau, C. R. Becker, and G. Landwehr, Appl. Phys. Lett. **75**, 956 (1999); M. K. Welsch, H. Schömig, M. Legge, G. Bacher, A. Forchel, B. König, C. R. Becker, W. Ossau, and L. W. Molenkamp, Appl. Phys. Lett. **78**, 2937 (2001).

[Balooch86] M. Balooch, D. R. Olander, and W. J. Siekhaus, J. Vac. Sci. Technol. B **4**, 794 (1986).

[Banin99] U. Banin, Y. Cao, D. Katz, and O. Millo, Nature **400**, 542 (1999).

[Barenco95] A. Barenco, D. Deutsch, A. Ekert, and R. Jozsa, Phys. Rev. Lett. **74**, 4083 (1995).

[Bayer01] M. Bayer, P. Hawrylak, K. Hinzer, S. Fafard, M. Korkusinski, Z. R. Wasilewski, O. Stern, and A. Forchel, Science **291**, 451 (2001).

[Becher01] C. Becher, A. Kiraz, P. Michler, A. Imamoglu, W. V. Schoenfeld, P. M. Petroff, Lidong Zhang, and E. Hu, Phys. Rev. B **63**, 121312(R) (2001)

[Bennett00] C. H. Bennett and D. P. DiVincenzo, Nature **404**, 247 (2000).

[Bimberg99] D. Bimberg, M. Grundmann, and N. N. Ledentsov, *„Quantum Dot Heterostructures"*; [ISBN 0 471 97388 2], Wiley Verlag, Chichester (1999).

[Binnig86] G. Binnig, C. F. Quate, and Ch. Gerber, Phys. Rev. Lett. **56**, 930 (1986).

[Bockelmann90] U. Bockelmann and G. Bastard, Phys. Rev. B **42**, 8947 (1990).

[Braun99] W. Braun, *„Applied RHEED"*; Springer-Verlag Berlin (1999).

[Brennan92] T. M. Brennan, J. Y. Tsao, and B. E. Hammons, J. Vac. Sci. Technol. A **10**, 33 (1992); S. Y. Karpov and M. A. Maiorov, Surf. Sci. **344**, 11 (1995).

[Brunner94] K. Brunner, G. Abstreiter, G. Böhm, G. Tränkle, and G. Weimann, Phys. Rev. Lett. **73**, 1138 (1994).

[Burton51] W. K. Burton, N. Cabrera, and F. C. Frank, Phil. Trans. Roy. Soc. (London) A **243**, 299 (1951).

[Chen00] G. Chen, N. H. Bonadeo, D. G. Steel, D. Gammon, D. S. Katzer, D. Park, L. J. Sham, Science **289**, 1906 (2000).

[Cho71] A. Y. Cho, J. Vac. Sci. Technol. **8**, S31 (1971).

[Cho75] A. Y. Cho and W. C. Ballamy, J. Appl. Phys. **46**, 783 (1975).

[Christen91] J. Christen, G. Grundmann, and D. Bimberg, J. Vac. Sci. Technol. B **9**, 2359 (1991).

[Cundiff94] S. T. Cundiff, A. Knorr, J. Feldmann, S. W. Koch, and E. O. Göbel, and H. Nickel, Phys. Rev. Lett. **73**, 1178 (1994).

[Davies98] J. H. Davies, *« The Physics of low-dimensional semiconductors »*; [ISBN 0 521 48491 X], Cambridge University Press (1998).

[DeLuca99] P. M. DeLuca, J. G. C. Labanda, and S. A. Barnett, Appl. Phys. Lett. **74**, 1719 (1999); P. M. DeLuca, and S. A. Barnett, Surface Science **426**, L407 (1999).

[Döhler86] G. H. Döhler, G. Hasnain, and J. N. Miller, Appl. Phys. Lett. **49**, 704 (1986).

[Drotar00] J. T. Drotar, Y.-P. Zhao, T.-M. Lu, and G.-C. Wang, Phys. Rev. B **61**, 3012 (2000); J. T. Drotar, Y.-P. Zhao, T.-M. Lu, and G.-C. Wang, Phys. Rev. B **62**, 2118 (2000).

[Eaglesham90] D. J. Eaglesham and M. Cerullo, Phys. Rev. Lett. **64**, 1943–1946 (1990).

[Ekert96] A. Ekert and R. Jozsa, Rev. Mod. Phys. **68**, 733 (1996).

[Fafard96] S. Fafard, K. Hinzer, S. Raymond, M. Dion, J. McCaffrey, Y. Feng, and S. Charbonneau, Science **274**, 1350 (1996).

[Fan95] Y. Fan, Appl. Phys. Lett. **67**, 1739 (1995).

[Farrow95] R. F. C. Farrow, "*Molecular Beam Epitaxy – Applications to Key Materials*"; Noyes Publications (1995).

[Faschinger95] W. Faschinger, J. Crystal Growth **146**, 80 (1995).

[Faschinger99] W. Faschinger, M. Ehinger, T. Schallenberg, and M. Korn, Appl. Phys. Lett. **74**, 3404 (1999).

[Fischer95] C. Fischer, *"Optische Charakterisierung von ZnSe-Schichten und Laserdioden"*; Diplomarbeit, Physikalisches Institut, EP III, Universität Würzburg (1995).

[Foxon75] C. T. Foxon and B. A. Joyce, Surface Science **50**, 434 (1975); C. T. Foxon and B. A. Joyce, Surface Science **64**, 293 (1977).

[Furuya96] K. Furuya and T. Saito, J. Appl. Phys. **80**, 1922 (1996).

[Gaines91] J. M. Gaines, J. Cryst. Growth **137**, 187 (1991).

[Grover97] L. K. Grover, Phys. Rev. Lett. **79**, 325 (1997).

[Gulden93] K. H. Gulden, X. Wu, J. S. Smith, P. Kiesel, A. Höfler, M. Kneissl, P. Riel, and G. H. Döhler, Appl. Phys. Lett. **62**, 3180 (1993).

[Hata91] M. Hata, A. Watanabe, and T. Isu, J. Cryst. Growth **111**, 83 (1991); M. Hata, T. Isu, A. Watanabe, and Y. Katayama, J. Vac. Sci. Technol. B **8**, 692 (1990).

[Hawrylak00] P. Hawrylak, G. A. Narvaez, M. Bayer, and A. Forchel, Phys. Rev. Lett. **85**, 389 (2000).

[Herman89] M. A. Herman and H. Sitter, „*Molecular Beam Epitaxy - Fundamentals and Current Status*“; Springer-Verlag Berlin (1989).

[Hyon00] C. K. Hyon , S. C. Choi, S.-H. Song, S. W. Hwang, M. H. Son, D. Ahn, Y. J. Park and E. K. Kim, Appl. Phys. Lett. **77**, 2607 (2000).

[Imamoglu99] A. Imamoglu, D. D. Awschalom, G. Burkard, D. P. DiVincenzo, D. Loss, M. Sherwin, and A. Small, Phys. Rev. Lett. **83**, 4204 (1999).

[Ishikawa00] T. Ishikawa, T. Nishimura, S. Kohmoto, and K. Asakawa, Appl. Phys. Lett. **76**, 167 (2000); T. Ishikawa, S. Kohmoto, S. Nishikawa, T. Nishimura, and K. Asakawa, J. Vac. Sci. Technol. B 18, 2635 (2000).

[Kangawa02] Y. Kangawa, T. Ito, A. Taguchi, K. Shiraishi, T. Irisawa, T. Ohachi, Appl. Surf. Sci. **190**, 517 (2002).

[Kapon87] E. Kapon, M. C. Tamargo, and D. M. Hwang, Appl. Phys. Lett. **50**, 347 (1987).

[Kastner93] M. Kastner, Phys. Today **46**, 24 (1993).

[Kasu97] M. Kasu, T. Makimoto, and N. Kobayashi, Appl. Phys. Lett. **70**, 1161 (1997).

[Kato98] T. Kato, T. Takeuchi, Y. Inoue, S. Hasegawa, K. Inoue, and H. Nakashima, Appl. Phys. Lett. **72**, 465 (1998).

[Kishimoto00] D. Kishimoto, T. Ogura, A. Yamashiki, T. Nishinaga, S. Naritsuka, and H. Sakaki, J. Cryst. Growth **216**, 1 (2000).

[Kohmoto99] S. Kohmoto, H. Nakamura, T. Ishikawa, and K. Asakawa, Appl. Phys. Lett. **75**, 3488 (1999).

[Konkar98] A. Konkar, A. Madhukar, and P. Chen, Appl. Phys. Lett. **72**, 220 (1998).

[Kümmell00] T. Kümmell, G. Bacher, M. K. Welsch, D. Eisert, A. Forchel, B. König, Ch. Becker, W. Ossau, and G. Landwehr, J. Crystal Growth **214/215**, 150 (2000).

[Kuo96] L. H. Kuo, K. Kimura, S. Miwa, T. Yasuda, and T. Yao, Appl. Phys. Lett. **69**, 1408 (1996).

[Kurtz96] E. Kurtz, *„P-Dotierung von ZnSe im Hinblick auf die Anwendung in blau-grünen Laserdioden.“*; Dissertation, Physikalisches Institut der Universität Würzburg (1996).

[LaBella00] V. P. LaBella, D. W. Bullock, Z. Ding, C. Emery, W. G. Harter, and P. M. Thibado, J. Vac. Sci. Technol. A **18**, 1526 (2000).

[Lee98] C. Lee and A.-L. Barabasi, Appl. Phys. Lett. **73**, 2653 (1998).

[Lee00] H. Lee, J. A. Johnson, M. Y. He, J. S. Speck, and P. M. Petroff, *et al.,* Appl. Phys. Lett. **78**, 105 (2000).

[Lee01] S. C. Lee, L. R. Dawson, K. J. Malloy, and S. R. J. Brueck, Appl. Phys. Lett. **79**, 2630 (2001).

[Lefebvre00] J. Lefebvre, P. J. Poole, G. C. Aers, D. Chithrani, and R. L. Williams, J. Vac. Sci. Technol. B **20**, 2173 (2002).

[Leifer00] K. Leifer, A. Hartmann, Y. Ducommun, and E. Kapon, Appl. Phys. Lett. **77**, 3923 (2000).

[Leonard94] D. Leonard, K. Pond, and P. M. Petroff, Phys. Rev. B **50**, 11687–11692 (1994).

[Likharev87] K. K. Likharev, IEEE Trans. Magn. **23**, 1142 (1987).

[Lorke95] A. Lorke, J. H. English, A. C. Gossard, and P. M. Petroff, J. Appl. Phys. **77**, 3578 (1995).

[Loss98] D. Loss and D. P. DiVincenzo, Phys. Rev. A 57, 120 (1998); G. Burkard, D. Loss and D. P. DiVincenzo, Phys. Rev. B **59**, 2070 (1999).

[Luo98] Y. Luo, A. Cavus, M. Tamargo, J. Wan, and F. H. Pollak, J. Vac. Sci. Technol. B **16**, 1312 (1998).

[Luo00a] Y. Luo, S. P. Guo, O. Maksimov, V. Asnin, F. H. Pollak, Y. C. Chen, and M. C. Tamargo, Appl. Phys. Lett. **77**, 4259 (2000).

[Mackowski98] S. Mackowski, N.T. Khoi, A. Golnik, P. Kossacki, J.A. Gaj,E. Kaminska, A. Piotrowska, G. Karczewski, T. Wojtowicz and J. Kossut, Solid State Com. **107**, 267 (1998).

[Malzer96] S. Malzer, M. Kneissl, and P. Kiesel, K. H. Gulden, X. X. Wu and J. S. Smith, and G. H. Döhler, J. Vac. Sci. Technol. B **14**, 2175 (1996).

[Matthews74] J. W. Matthews and A. E. Blakeslee, J. Crystal Growth **27**, 118 (1974).

[Mei02] X. Mei, D. Kim, Q. X. Guo, and H. E. Ruda, Appl. Phys. Lett. **81**, 361 (2002).

[Michler00a] P. Michler, A. Imamoglu, M. D. Mason, P. J. Carson, G. F. Strouse, and S. K.Buratto, Nature **406**, 968 (2000).

[Michler00b] P. Michler, A. Kiraz, C. Becher, W. V. Schoenfeld, P. M. Petroff, Lidong Zhang, E. Hu, and A. Imamoglu, Science **290**, 2282 (2000).

[Moll96] N. Moll, A. Kley, E. Pehlke, and M. Scheffler, Phys. Rev. B 54, 8844 (1996).

[Neave85] J. H. Neave, P. L. Dobson, B. A. Joyce, and J. Zhang, Appl. Phys. Lett. **47**, 100 (1985).

[Nishikawa96] T. Nishikawa, M. Kubo, and Y. Sasai, Appl. Phys. Lett. **68**, 3428 (1996).

[Nishinaga96] T. Nishinaga, X. Q. Shen, and D. Kishimoto, J. Crystal Growth **163**, 60 (1996); X. Q. Shen and T. Nishinaga, J. Crystal Growth **146**, 374 (1995); A. Yamashiki and T. Nishinaga, J. Crystal Growth **198/199**, 1125 (1999); T. Ogura and T. Nishinaga, J. Crystal Growth **211**, 416 (2000); D. Kishimoto, T. Ogura, A. Yamashiki, T. Nishinaga, S. Naritsuka, and H. Sakaki, J. Crystal Growth **216**, 1 (2000).

[Ohta88] K. Ohta, T. Kojima, and T. Nakagawa, J. Cryst. Growth **95**, 71 (1988).

[Okuyama97] H. Okuyama, T. Kawasumi, A. Ishibashi, M. Ikeda, J. Crystal Growth **175/l76**, 587 (1997).

[Peake99] G. M. Peake, L. Zhang, N. Y. Li, A. M. Sarangan, C. G. Willison, R. J. Shul, and S. D. Hersee, J. Vac. Sci. Technol. B **17**, 2070 (1999).

[Pfeiffer90] L. Pfeiffer, K. W. West, H. L. Störmer, J. P. Eisenstein, K. W. Baldwin, D. Gershoni, and J. Spector, Appl. Phys. Lett. **56**, 1697 (1990); A. R. Göni, L. Pfeiffer, K. W. West, A. Pinczuk, H. U. Baranger, and H. L. Stormer, Appl. Phys. Lett. **61**, 1956 (1992).

[Regelman01] D. V. Regelman, U. Mizrahi, D. Gershoni, E. Ehrenfreund, W. V. Schoenfeld, and P. M. Petroff, Phys. Rev. Lett. **87**, 257401 (2001).

[Riley96] J. Riley, D. Wolfframm, D. Westwood, and A. Evans, J. Crystal Growth **160**, 193 (1996).

[Ruppert94] P. Ruppert, D. Hommel, T. Behr, H. Heinke, A. Waag, and G. Landwehr, J. Crystal Growth **138**, 48 (1994).

[Saito95] H. Saito, I. Ogura, Y. Sugimoto, and K. Kasahara, Appl. Phys. Lett. **66**, 2466 (1995).

[Santori01] C. Santori, M. Pelton, G. Solomon, Y. Dale, and Y. Yamamoto, Phys. Rev. Lett. **86**, 1502 (2001).

[Schmidt96] G. Schmidt, *„Herstellung von Si/Si1-xGex-Nanostrukturen mittels selektiver Niederdruck-Gasphasenepitaxie: Wachstum und Charakterisierung“, Thesis;* [ISBN 3-8265-1971-X], Shaker Verlag (1996).

[Schüll97] K. Schüll, „Optimierung technologischer Prozesse zur Herstellung von ZnSe-basierten Halbleiterlaserdioden“; Dissertation, Physikalisches Institut der Universität Würzburg (1997).

[Schumacher99] C. Schumacher, W. Faschinger, V. Hock, H. R. Reß, J. Nürnberger, and M. Ehinger, J. Crystal Growth **201/202**, 599 (1999).

[Schumacher00] C. Schumacher and W. Faschinger, J. Crystal Growth **214/215**, 732 (2000).

[Seliger74] R. L. Seliger and W. P. Fleming, J. Appl. Phys. **45**, 1416 (1974).

[Shen94] X. Shen, D. Kishimoto, and T. Nishinaga, Jpn. J. Appl. Phys. **33**, 11 (1994).

[Shitara92] T. Shitara, J. Zhang, J. H. Neave, and B. A. Joyce, J. Appl. Phys. **71**, 4299 (1992).

[Shor94] P. W. Shor, Proceedings of the 35th Annual Symposium on the Foundations of Computer Science 124-133 (IEEE Computer Society Press, Los Alamos, California, 1994).

[Songmuang01] R. Songmuang, S. Kiravittaya, S. Thainoi, P. Changmuang, S. Sopitpan, S. Ratanathammaphan, M. Sawadsaringkarn, and S. Panyakeow, J. Cryst. Growth **227**,**228**, 1053 (2001).

[Sugimoto90] Y. Sugimoto, K. Akita, M. Taneya, and H. Hidaka, Appl. Phys. Lett. **57**, 1012 (1990).

[Swank67] R. K. Swank, Phys. Rev. **153**, 844 (1967).

[Tarucha96] S. Tarucha, D. G. Austing, T. Honda, R. J. van der Hage, and L. P. Kouwenhoven, Phys. Rev. Lett. **77**, 3613 (1996); M. Digler, R. J. Haug, K. Eberl, and K. von Klitzing, Semicond. Sci. Technol. **11**, 1493 (1996); H. Ishikuro and T. Hiramoto, Appl. Phys. Lett. **71**, 3691 (1997); L. Zhuang, L. Guo, and S. Y. Chou, Appl. Phys. Lett. **72**, 1205 (1998); J. Motohisa, F. Nakajima, and T. Fukui , W. G. van der Wiel, J. M. Elzerman, S. De Franceschi, and L. P. Kouwenhoven, Appl. Phys. Lett. **80**, 2797 (2002).

[Tatsuoka01] Y. Tatsuoka, M. Uemura, T. Kitada, S. Shimomura, and S. Hiyamizu, J. Crystal Growth **227**, 266 (2001); Yu Higuchi, M. Uemura, Y. Masui, T. Kitada, S. Shimomura, and S. Hiyamizu, J. Crystal Growth **251**, 80 (2003).

[Temkin87] H. Temkin, G. J. Dolan, M. B. Panish, and S. N. G. Chu, Appl. Phys. Lett. **50**, 413 (1987).

[Tersoff03] J. Tersoff, Appl. Phys. Lett. **83**, 353 (2003).

[Tok97] E. S. Tok, T. S. Jones, J. H. Neave, J. Zhang, and B. A. Joyce, Appl. Phys. Lett. **71**, 3278 (1997).

[Tomita95] N. Tomita, N. Yoshida, S. Shimomura, K. Murase, A. Adachi, and S. Hiyamizu, J. Crystal Growth **150**, 377 (1995).

[Tsang77a] W. T. Tsang and A. Y. Cho, Appl. Phys. Lett. **30**, 293 (1977).

[Tsang77b] W. T. Tsang and M. Ilegems, Appl. Phys. Lett. **31**, 301 (1977).

[Tsao93] J. Y. Tsao, "*Materials fundamentals of Molecular Beam Epitaxy*"; Academic Press (1993).

[Tsui97] R. Tsui, R. Zhang, K. Shiralagi, and H. Gorokin, Appl. Phys. Lett. **71**, 3254 (1997).

[Türck01] V. Türck, „*Elektronische Eigenschaften einzelner Halbleiterquantenpunkte*"; Thesis, TU Berlin, (2001); V. Türck, S. Rodt, R. Heitz, O. Stier, M. Strassburg, U. W. Pohl, and D. Bimberg, Phys. Status Solidi B **224**, 217 (2001).

[Quiroga99] L. Quiroga and N. F. Johnson, Phys. Rev. Lett. 83, 2270 (1999); J. H. Reina, L. Quiroga, and N. F. Johnson, Phys. Rev. A **62**, 12305 (2000).

[Verschuren99] C. A. Verschuren, M. R. Leys, H. Vonk, and J. H. Wolter, Appl. Phys. Lett. **74**, 2197 (1999); C. A. Verschuren, M. R. Leys, T. Marschner, H. Vonk, and J. H. Wolter, J. Crystal Growth **188**, 11 (1998).

[Wang00] X.-L. Wang and M Ogura, J. Crystal Growth **221**, 556 (2000).

[Weigand03] W. Weigand, A. Müller, L. Kilian, T. Schallenberg, P. Bach, G. Schmidt, L. W. Molenkamp, O. Bunk, R. L. Johnson, C. Kumpf, and E. Umbach, Phys. Rev. B **68**, 241314(R) (2003).

[Wolfframm00] D. Wolfframm, D.A. Evans, D.I. Westwood, and J. Riley, J. Crystal Growth **216**, 119 (2000).

Appendix

Modeling of epitaxial growth

A.1 Redistribution by desorption

The non-sticking part (1-s) of a flux F_i of particles after their ith "collision" with the surface desorbs again and contributes to the $(i+1)$th-order flux F_{i+1} at a different position. The angular distribution of the desorption of the molecules is given by the cosine law of effusion

$$d\Gamma_{\vartheta} = \Gamma_e \pi^{-1} \cos(\vartheta') d\omega', \qquad \text{(A.1)}$$

where Γ_e is the desorption rate from a surface element dA' at $\mathbf{r}'$ and $d\Gamma_{\vartheta}$ is the differential angular effusion rate in the direction of the polar effusion angle ϑ'.[Herman89] At a different position $\mathbf{r}$ on the surface of the mask-cavity (see Fig. 5.2), the incoming flux is proportional to the solid angle

$$d\omega' = (\mathbf{r} - \mathbf{r}')^{-2} \cos(\vartheta) dA', \qquad \text{(A.2)}$$

where, ϑ, is the polar incidence angle and, dA', the same differential size. Combining Eqs. (A.1) and (A.2) gives Eq. (5.2).

If a shadow mask consists only of (parallel) stripe-shaped apertures, the flux is homogeneously distributed in the parallel direction and the model can be reduced to the two-dimensional cross-section of the mask and a one-dimensional mask-surface a_M. In this case, Eq. (5.2) transforms to

$$F_{i+1}(\mathbf{r}, t+\tau) = \int_{a_M} (1 - s(\mathbf{r}', t)) F_i(\mathbf{r}', t) Z(\mathbf{r}, \mathbf{r}') \frac{(\mathbf{n}_{r'r} \cdot \mathbf{n}')(\mathbf{n}_{rr'} \cdot \mathbf{n})}{2(\mathbf{r} - \mathbf{r}')} da'. \qquad \text{(A.3)}$$

A.2 Mass conservation

When molecules are redistributed in the mask-cavity according to Eq. 5.3, part of the molecules escape through the mask aperture. However, if the surface of the apertures A_A is considered as a part of the mask-cavity A_M (by the definition $s = 1$ for $\mathbf{r} \in A_A$) the system is closed, and the total redistributed flux is equal to the total desorbed flux, which gives the equation

$$\oint_{A_M + A_A} \oint_{A_M + A_A} (1 - s) fZ \frac{(\mathbf{n}_{r'r} \cdot \mathbf{n}')(\mathbf{n}_{rr'} \cdot \mathbf{n})}{(\mathbf{r} - \mathbf{r}')^2 \pi} dA' dA = \oint_{A_M + A_A} (1 - s) fZ dA. \qquad \text{(A.4)}$$

It is reasonable to control Eq. (A.4) in the numerical analysis. For small numerical deviations, Eq. (A.4) can also be used to calculate a position-independent correction term for the integral in Eq. (5.3).

A.3 Growth rates of ZnSe

The data points in Fig. 3.5(b) represent the Zn sticking coefficient values (as a function of the atomic flux ratio) during ZnSe MBE at a substrate temperature of 300°C.[Riley96] The solid line corresponds to experimental data from Ref. [Rupp94], which, however, has been multiplied by a constant correction factor of 0.68 (=0.87/0.59). The reason for using the correction factor is to compensate for the overestimated values of Zn-sticking coefficients in the latter (RHEED oscillation) study (s_{Zn}=0.87 at p_{Se}:p_{Zn} = 1.27). The data presented in Ref. [Riley96] is more reliable because the absolute value of the atomic flux has been determined from deposition rates at a low substrate temperature (s_{Zn}=0.59 at p_{Se}:p_{Zn} = 1.27). As can be seen in Fig. 3.5(b), with the correction factor, the solid line gives an excellent fit to the data points. This curve has been used to calculate the sticking coefficients of interacting Zn and Se species, in order to obtain the steady state flux distributions within the cavity of the mask.

A.4 Surface diffusion of As molecules on GaAs.

According to Burton, Cabrera, and Frank,[Burton51] the number of sites visited during random motion on the surface of a crystal is given by $n = \exp(E_D - E_\lambda)/kT$. According to Foxon and Joyce,[Foxon75] the desorption energy E_D and the surface diffusion activation energy E_λ of physisorbed As_4 molecules on the GaAs(001) surfaces are 0.38 eV and ~0.24 eV, respectively (E_D is much smaller for As_2). Consequently, the surface migration lengths (~ $n^{1/2}$) of both As_4 and As_2 molecules are expected to be shorter than 10 nm on the GaAs(001) surface at 600 °C. Investigations by Tok *et al.* indicate that the desorption energy is smaller for (110) and (111)A surfaces, which suggests that the diffusion length is small for both As_4 and As_2 molecules.

In contrast, one group (see Ref. [Tatsuoka01]) has proposed that the diffusion length of As_4 molecules during MBE growth of GaAsP on the GaAs(114)A surface was as large as 20 µm at a substrate temperature of 600°C. This value, which appears to be unrealistic large, relies on the observation of a composition modulation of GaAsP layers (grown on a patterned substrate) measured by Energy Dispersive X-ray Analysis (EDX). This has been explained by inter-surface diffusion of As adatoms (or molecules). However, Tatsuoka *et al.* have not considered that inter-surface diffusion of Ga adatoms also affects the growth conditions (Ga surface concentration) and thus may have caused the observed composition modulation. Moreover, it has not been explained why the composition is changed only on the (114)A and not on the (001) surface, and why the As fraction is increased rather than decreased near the edge of the (114)A surface [The large diffusion length of As on (114)A implies a relative high surface concentration of As molecules and hence the effective migration of As from (114)A surface towards the (001) surface is more likely].

During this work, EDX has also been tried as an experimental technique to determine the composition profiles of non-planar structures. It has been found that the alignment of the investigated structure relative to the EDX detector may affect the results of the experiment. This may also explain the GaAsP composition modulation observed by Tatsuoka *et al.*.

Ehrenwörtliche Erklärung

*gemäß §6 Abs. 1 Ziff. 3 und 7 der Promotionsordnung
der Fakultät für Physik und Astronomie der Universität Würzburg*

Hiermit erkläre ich ehrenwörtlich, dass ich die Dissertation selbständig und ohne Hilfe eines Promotionsberaters angefertigt und keine anderen als die angegebenen Quellen und Hilfsmittel benutzt habe.

Die Dissertation wurde bisher weder vollständig noch teilweise einer anderen Hochschule mit dem Ziel, einen akademischen Grad zu erwerben, vorgelegt.

Im Frühjahr 1999 habe ich die Erste Staatsprüfung für das Lehramt an Gymnasien (Mathematik und Physik) bestanden. Weitere akademische Grade habe ich weder erworben noch versucht zu erwerben.

Würzburg, den 23. April 2004

Timo Schallenberg

Publications

P.1 Publications in peer-reviewed journals as the first author

List of my publications in peer-reviewed journals as the first author. The first author provides the main contribution.

[09] *Molecular beam epitaxy of compound materials through shadow masks*
T. Schallenberg, L.W. Molenkamp, and G. Karczewski
Physical Review B (*in print*)

[08] *In situ area-controlled self-formation of InAs nanostructures*
T. Schallenberg, L.W. Molenkamp, S. Rodt, R. Seguin, D. Bimberg, and G. Karczewski
Applied Physics Letters **84**, 963 (2004)
\+ Virtual Journal of Nanoscale Science & Technology

[07] *In situ size-control of CdZnSe nano-islands using shadow masks*
T. Schallenberg, T. Borzenko, G. Schmidt, L.W. Molenkamp, S. Rodt, R. Heitz, D. Bimberg, and G. Karczewski
Journal of Applied Physics **95**, 311 (2004)

[06] *Selected area growth of II-VI nanostructures using shadow masks*
T. Schallenberg, C. Schumacher, K. Brunner, and L. W. Molenkamp
Physica Status Solidi B **241**, 564 (2004)

[05] *In situ lateral growth control of optically efficient quantum structures*
T. Schallenberg, W. Faschinger, G. Karczewski, V. Türck, S. Rodt, R. Heitz, D. Bimberg, M. Obert, G. Bacher, A. Forchel, and L.W. Molenkamp
Applied Physics Letters **83**, 446 (2003)
\+ Virtual Journal of Nanoscale Science & Technology

[04] *Controlled self-assembly of semiconductor quantum dots using shadow masks*
T. Schallenberg, T. Borzenko, G. Schmidt, M. Obert, G. Bacher, C. Schumacher, G. Karczewski, L. W. Molenkamp, S. Rodt, R. Heitz, and D. Bimberg
Applied Physics Letters **82**, 4349 (2003)
\+ Virtual Journal of Nanoscale Science & Technology

[03] *Projective techniques for the growth of compound semiconductor nanostructures*
T. Schallenberg, C. Schumacher, and L. W. Molenkamp
Physica Status Solidi A **195**, 232 (2003)

[02] *In situ structuring during MBE regrowth with shadow masks*
T. Schallenberg, C. Schumacher, and W. Faschinger
Physica E **13**, 1212 (2002)

[01] *Shadow mask technology*
T. Schallenberg, C. Schumacher, S. Gundel, and W. Faschinger
Thin Solid Films **412**, 24 (2002)

P.2 Publications in peer-reviewed journals as Co-author

List of my publications in peer-reviewed journals due to my work in the SFB410 project A1 of the Deutsche Forschungsgemeinschaft (1999-2004) and in the FOROPTO project (*) of the Bayerische Forschungsstiftung (1998).

[>15] *A few other publications due to my contribution in fruitful collaborations with other research groups in the frame of the SFB410, are under preparation.*

[15] *Valence band electronic structure of ZnSe(001): Theory and Experiment*
L. Plucinski, R. L. Johnson, A. Fleszar, W. Hanke, W. Weigand, C. Kumpf, C. Heske, E. Umbach, T. Schallenberg, and L. W. Molenkamp
Physical Review B (*in print*)

[14] *X-ray Diffraction study and Monte Carlo Simulation of the relaxation behaviour of epitaxially grown wire structures*
C. Schumacher, A. S. Bader, T. Schallenberg, N. Schwarz, W. Faschinger, L. W. Molenkamp, and R. B. Neder
Journal of Applied Physics **95**, 5494 (2004)

[13] *Structural investigation of the ZnSe(001)-c(2x2) surface*
W. Weigand, A. Müller, L. Kilian, T. Schallenberg, P. Bach, G. Schmidt, L. W. Molenkamp, O. Bunk, R. L. Johnson, C. Kumpf, and E. Umbach
Physical Review B **68**, 241314 (2003)

[12](*) *High-sensitivity p-i-n-detectors for the visible spectral range based on wide-gap II-VI materials*
W. Faschinger, M. Ehinger, and T. Schallenberg
Journal of Crystal Growth **214/215**, 1138 (2000)

[11](*) *High response photodiodes based on Be-chalcogenides*
J. Siess, G. Reuscher, P. Grabs, H.-J. Lugauer, T. Schallenberg, M. Ehinger, A. Waag, and G. Landwehr
Journal of Crystal Growth **201/202**, 965 (1999)

[10](*) *High-efficiency p i n detectors for the visible spectral range based on ZnSTe/ZnTe superlattices*
W. Faschinger, M. Ehinger, T. Schallenberg, and M. Korn
Applied Physics Letters **74**, 3404 (1999)

P.3 Other publications

- *Asymmetry in the surface electronic structure of ZnSe(001)-c(2x2) surfaces*
  L. Plucinski, R. Kosuch, W. Weigand, C. Kumpf, C. Heske, A. Fleszar, T. Schallenberg, W. Faschinger, L. Molenkamp, E. Umbach und R.L. Johnson,
  Proc. ICPS-26, Edinburgh, p. 29 (Aug. 2002)

- *Wellenlängenselektive Photodioden aus II-VI Halbleiter mit großer Bandlücke*
  T. Schallenberg,
  Examensarbeit, Physikalisches Institut, EP-III, Universität Würzburg (Oct. 1998)

Acknowledgements

Finally comes the most difficult part of writing a thesis: All the work and their outcomes (or mere gibberish!), which I described in the previous chapters would have been impossible without the cooperation, guidance, inspiration, and encouragement of a lot of people. I wish I make justice in giving credit to all of them.

First and foremost, I take this opportunity to express my sincere gratitude to my research supervisor, Professor Dr. Wolfgang Faschinger, who by initiating the SFB410 project, made this work possible. My heartfelt thanks are due to him, all the more, for his valuable suggestions and for providing an excellent working ambient for research. I express my deep regret and sorrowfulness for his tragic demise in 2001.

My sincere acknowledgements are due to Professor Dr. Laurens W. Molenkamp, who subsequently took the responsibility of the research project. I treasure his support and guidance, and also the liberal research environment which he provided me with.

I consider myself fortunate to have had the critical, yet constructive, supervision of Professor Dr. Grzegorz Karczewski ("Greg") from the Polish Academy of Sciences, Warsaw. I greatly acknowledge his valuable suggestions and immense inspiration during the course of my work, which resulted in a number of publications in recognized journals. I also thank Professor Dr. Karl Brunner, my advisor in the final stages of the work, for his valuable suggestions and critical comments during the preparation of this thesis.

My thanks are due to all my co-workers in the MBE lab and the clean-room facility. Firstly I thank Claus Schumacher, my fellow worker in the SFB410(A1) project, for introducing me to the experimental techniques, which I subsequently used extensively during the course of my work. Moreover, I would like to thank him and Dr. Charles Becker ("Charlie") for helping me manage the turbulent time after the sudden death of my supervisor. I also thank Armin Bader († 2003), Frank Reuss, Lars Hansen, Peter Bach, Peter Grabs, Suddhasatta Mahapatra ("Suddho"), Jochen Nürnberger, Volker Daumer, and Wolfgang Weigand for their friendly and enriching company at the university as well as outside. I, especially thank Suddho and Charlie, who took up the pain-staking task of proofreading this thesis. I am grateful to Tanja Borzenko, Jian Liu, and Georg Schmidt for the fruitful technical discussions and the assistance in lithography processes.

This work would not have been possible without the professional support of the technical staff of EP3. I would like to thank Anita Gebhardt, Petra Wolf-Müller, and Volkmar Hock for all the technical assistance, and Alfred Schönteich and Rainer Brauner for maintaining the MBE system. I am also grateful to the secretary of the department, Anja Brück. The long-term professional experience of these people and their contribution to a friendly working atmosphere are forsooth invaluable.

In the course of my work, I had been fortunate to have a number of collaborations at Würzburg University from which I have benifited extensively. Important for this thesis was, in particular, the photoluminescence results provided by Michael Obert from the group of Professor Gerhard Bacher. In addition, I sincerely thank Professor Dr. Alfred Forchel, Anatoliy Slobodskyy, Charles Gould, Christian Kumpf, Christian Rüster, Daniel Supp, Dirk Keller, Professor Dr. Eberhard Umbach, Georgy Astakhov, Gisela Schott, Professor Dr. Gottfried Landwehr, Professor Dr. Hartmut Buhmann, Idris Chado, Professor Jean Geurts, Joachim Wagner, Markus König, Michael Lentze, Michael Leufgen, Priv. Doz. Dr. Michael Biehl, Professor Dr. Reinhard Neder, Roland Ebert, Roland Fiederling, Taras Slobodskyy, Tobias Muck, and Prof. Dr. Wolfgang Ossau, who contributed to this work in their own ways. My special thanks are due to all other co-workers and staff members of the institute for their cooperation and sociability.

Without the timely cooperation of Florian Beil, from the group of Professor Jörg P. Kotthaus at LMU München, some of the most important results of this work would not have existed. I sincerely acknowledge his help and, also thank Stefan Malzer from Universität Erlangen-Nürnberg, for providing Florian´s personal contact.

I gratefully acknowledge Professor Dieter Bimberg, from Technical University Berlin, and his colleagues, Robert Heitz († 2003), Robert Seguin, Sven Rodt, and Volker Türck, for providing the cathodoluminescence results. I particularly enjoyed the fruitful collaboration with Sven Rodt and the nice time we had at the Nara conference.

I also thank Dr. Sebastian Mackowski, University of Cincinnati, for his interest in a few of my samples.

The past four years have been rich with experience; incurring the development of many friends and acquaintances who have, in numerous contexts, helped me by their myriad contributions, suggestions, timely distractions, and by keeping my world beyond physics, jovial and vivacious. I, especially thank Flo, Holger, Katrin, and Michi, my best friends over the last decade. I also thank all other close friends and living community members from Coburg and Würzburg, for making my life this exciting.

Last, but not the least, I express my sincere gratitude to my parents and thank my sister for their love, affection, and absolute confidence in me.